Total scattering applied to the study of nanomaterials

Serena Ada Maugeri

Submitted in partial fulfillment
of the requirements of the Degree of
Doctor of Philosophy

2 Aug 2017

School of Physics and Astronomy
Queen Mary, University of London

Queen Mary
University of London

Statement of originality

I, Serena Ada Maugeri, confirm that the research included within this thesis is my own work or that where it has been carried out in collaboration with, or supported by others, that this is duly acknowledged below and my contribution indicated. Previously published material is also acknowledged below.

I attest that I have exercised reasonable care to ensure that the work is original, and does not to the best of my knowledge break any UK law, infringe any third party's copyright or other Intellectual Property Right, or contain any confidential material.

I accept that the College has the right to use plagiarism detection software to check the electronic version of the thesis.

I confirm that this thesis has not been previously submitted for the award of a degree by this or any other university.

.....

Serena Ada Maugeri

2 Aug 2017

Parts of chapter 3 [1] and 5 [2] have been previously published. This research utilised the programs `RMCProfile`, `PDFgui`, `DL_Poly_4` and the Queen Mary's MidPlus computational facilities, supported by QMUL Research-IT and funded by EPSRC grant EP/K000128/1. For the molecular dynamics in section 3.3.4.2 I made use of the HPC-Midlands-Plus Tier-2 computing system, supported by the research computing staff of Queen Mary University of London and Loughborough University, and funded through EPSRC e-infrastructure grant EP/P020232/1.

Acknowledgement

It is with great pleasure that I express my deep gratitude to my supervisors Martin T. Dove and Anthony E. Phillips (Queen Mary University of London, QMUL). I consider it a privilege to have had the chance to work with you and have been exposed to your vast and inspiring knowledge. Your passion for crystallography and the study of materials has contributed to generate in me an even stronger curiosity for the subject.

In particular, I would like to thank: Martin T. Dove for the trust granted to me from the beginning and for always pushing me to reach my full potential, as well as for strongly contributing to my research and understanding of the field of total scattering, and crystallography as a whole, with fruitful discussions and insightful observations; Anthony E. Phillips who has supported me in many ways, through enriching and stimulating conversations, providing his prompt help in structuring and planning my research to work towards a goal, nourishing my knowledge of the field, as well as expanding it in other areas such as chemical synthesis and programming.

This work would have not been possible without the crucial support of my second supervisor, David A. Keen, at the ISIS neutron and muon source, to whom I wish to express my sincere gratitude. Your deep knowledge of the total scattering technique has helped me to overcome the obstacles encountered in the analysis of the data and in the understanding of its theoretical basis.

I wish to thank my collaborators, whom I had the opportunity to work with on cutting-edge research projects: Marx Baxendale (QMUL), Filippo S. Boi (Sichuan University) and Ibrar Muhammad (QMUL), who have contributed to the research work performed in the field of multi-walled carbon nanotubes filled with iron; Matthew T. Dunstan and Claire Gray (University of Cambridge), whom I had the pleasure to work with in the study of the CaO and $CaCO_3$ nanoparticles systems for CO_2 capture.

I would like to thank the beam scientists at the ISIS neutron and muon source, Daniel T. Bowron and Tristan G. A. Young, who have helped me in performing the neutron total scattering experiments and in the analysis of the data.

I wish to thank Isaac Abraham, Majid Motevalli and Rory M. Wilson at QMUL for their friendly support during my PhD, for their help in performing the X-ray total scattering measurements and for sharing their knowledge of X-ray diffraction.

Thank you to the staff of the School of Physics and Astronomy at QMUL and in particular Terry Arter, Lucie Bone, Sarah Cowls, Jessica Henry, Tom Horner, Predrag Micakovic, Jazmina Moura, John Sullivan and Karen Wilkinson for being always helpful, supporting and friendly. Thank you to Geoff Gannaway, George Nevill and Ken Scott for helping me in running experiments smoothly.

I wish to thank the academic staff at QMUL and in particular Alan Drew, Theo Kreouzis, Alston Misquitta, Andrei Sapelkin and Kostya Trachenko for the numerous enriching conversations and for the friendly support provided throughout.

Thank you to all the colleagues at QMUL for making the workplace a cheerful one and for the inspiring moments of exchange of ideas. In particular I wish to thank: Carlos Aristizabal, Juan Du, Helen Duncan, Osman Ersoy, Rory Gilmore, Rodrigo Gamboa, Jelena Gorbaciova, Shuo Han, James Kneller, Emanuele Moscato, Prashantha Murahari, Andres R. Morales, Ali Shehu, Jack W. Skinner, Ke Wang, Mark G. L. Wilkinson, Chenxing Yang, Zhengqiang Yang, Yuanpeng Zhang and Tingting Zhang.

A big thank you goes to my QMUL colleagues and dear friends Eleftherios Andritsos, Asmi Barot, Min Gao, Sophia Goldberg, Ying Liu, Brenda Penante, Manting Qiu, Domenico Trotta and Lei Wang, who have been my travel companions during my years as a PhD student.

Thank you to all my dear friends (old and new) who have been on my side in many ways during these years. In particular, a deep thank you goes to Paloma Arenas Guerrero, Marzia Buscema, Pierrick Clement, Ayantika Dhara, Giovanni Gagliano, Cristina Profeti, Erica Russo and Ollie Smallwood.

Last but not least, I wish to thank my beloved family: my parents, my brother, Alessio, my sisters, Alida and Nilde, and our dog, Becks. My deepest thank you goes to my mom and dad, my solid pillars, who have always supported me with all their means in overcoming the obstacles encountered during my PhD and beyond.

Abstract

Total scattering can be used to study crystalline materials, whose structure presents a periodic arrangement of atoms, as well as disordered materials, such as liquids, glasses or nanomaterials. This thesis work reports three experimental case studies in which different analysis methods were chosen as appropriate on a case-by-case basis. This study demonstrates that total scattering combined with modelling and complementary experimental techniques can guide the understanding of the structure of complex nanostructures.

X-ray and neutron total scattering data were collected on multi-walled carbon nanotubes continuously filled with iron and analysed using the program `PDFgui` for refinement of the pair distribution function and molecular dynamics simulations using the program `DL_Poly_4`. The analyses show that the iron core is mainly composed of α-Fe and confirms the dependence of the local ordering on the orientation of the crystallographic axes of iron with respect to the nanowire axis.

Prussian blue ($Fe_4[Fe(CN)_6]_3 \cdot nH_2O$) was synthesised in bulk and nanoparticulate phases using deuterated chemicals; the amount of D_2O and H_2O in the pores and vacancies, as well as polyvinylpyrrolidone remaining in the nanoparticle samples, were estimated, using an ad hoc modelling procedure of the first few peaks in the neutron PDF function. Models of the structure were refined using the programs `PDFgui` and `RMCProfile`. In the last case, a 50 Å supercell of the bulk structure with randomly distributed stoichiometric vacancies and D_2O and H_2O molecules occupying both the pores and the vacancies was used as starting atomic configuration.

The $CaO/CaCO_3$ family of materials consists of a series of samples that have undergone carbonation and/or calcination. The X-ray and neutron pair distribution function data were compared to the theoretical PDF of the CaO and $CaCO_3$ phase, generated using the program `GULP`, that produces PDF functions based on the spectrum of phonon frequencies of the material. The analysis shows that the carbonation is almost completed already after 2 minutes of carbonation and the structure remains stable under further carbonation.

Contents

Chapter 1

Introduction

1.1 What are nanomaterials: a brief history

The term nanomaterial refers to any material that comprises particles (nanoparticles) whose size falls in the range 1 nm and 100 nm [5, 6]; a nanoparticle can be considered as the building unit of a nanomaterial. Systems with dimension below 1 nm can be generally classified as molecular structures [7, 8] rather than nanomaterials, and their properties are studied at a molecular level [5]; the upper limit of 100 nm, chosen to mark an approximate separation between the realms of nano and non-nanomaterials, is not equally well defined; this limit is sometimes considered to be 1000 nm [9]. A more quantitative way of defining this demarcation line is based on the emergence, as one move down from microscopic to nanoscopic dimensions, of structural, optical, electrical or mechanical properties that deviate from those of the equivalent bulk material and are in between those of a macroscopic and a molecular (or atomic) system [10]. The term bulk designates, on the other hand, a material that does not exhibit size-dependent properties and whose structure is (in the case of crystalline materials) constituted by a regular arrangement of atoms, distributed periodically for lengths of the order of at least microns inside the material.

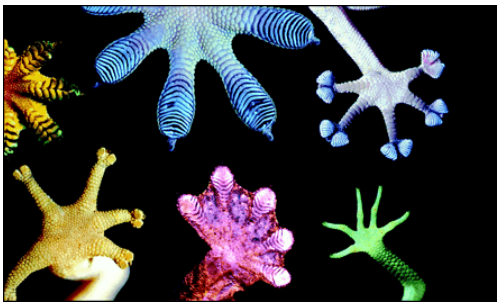

Figure 1.1: Geckos have millions of adhesive hairs (setae) on their feet that allow them to stick to any surface. The setae present a hierarchical structure, with micrometer stalks branching into smaller components; the smallest units have diameter between 100 nm and 200 nm and leaf-like plates at their tips [3]. The adhesive properties of the setae are a result of the shape and size of their nanometric tips, that interact with any surface by means of Van der Waals forces. The physics of geckos' setae has been source of inspiration for the creation of new nanostructures [4].

The big family of nanomaterials does not comprise only man-made synthetic materials. They also exist in nature [5, 6] and can be found in interplanetary dust [13], planetary surfaces and in the biosphere in volcanic ashes [14], ocean spray, natural water [15, 16], insects and geckoes feet

(a) (b)

Figure 1.2: The Lycurgus cup is a stunning decorative Roman glass vessel from AD 400, depicting the legend of king Lycurgus [11]. The cup owes its extraordinary and unusual optical properties to the presence of silver-gold alloy nanoparticles [12]. (a) The colour of the cup turns from a jade-green to a translucent ruby colour, when the glass is observed in reflected or transmitted light, respectively. The metallic nanoparticles present characteristic plasmonic resonance frequencies that affect the optical properties of the material, causing only the red light to be scattered and the other visible frequencies to be absorbed. (b) Transmission electron microscopy (TEM) of a silver-gold alloy particle found inside the glass of the Lycurgus cup [12].

[3, 4, 17] (figure 1.1) and, more generally, any living organism is made up of nano-components: animal and plant cells and their components as well as proteins, lipids, bacteria, viruses and so on. Moreover, man-made nanomaterials are often engineered taking inspiration from nanomaterials existing in nature [4] or using biological components as part of a synthetic system. The latter is the case of a study by Buscema et al., where biological units (liposomes) acting as nano-carriers of cardiovascular drugs, are modified to have mechano-sensitive properties in order for the drugs to be released in correspondence of arterial vasoconstrictions [18, 19].

Nanomaterials were also inadvertently used in ancient times in the manufacturing of objects and materials with specific features or functionalities. Expert Egyptian cosmeticians, Roman glass-makers and Mayan architects exploited nanoparticles or nanoporous materials for improving the quality, beauty or durability of their products and artefacts (figures 1.2 and 1.3a) [11, 12, 20, 22].

Despite the ubiquitous existence of nanoparticles, we have become more aware of them and their properties, when we have started being able to “see” them. The advent of more powerful imaging techniques, such as scanning transmission electron microscopy in 1969 by Albert Crewe [23], scanning tunnelling microscopy in 1981 by Ernst Ruska, Gerd Binig and Heinrich Rohrer

Figure 1.3: (a) A Greco-Roman text reports a hair-dyeing recipe, consisting of a mixture of PbO, $Ca(OH)_2$ and some water. The recipe was already known at Egyptian times, when more than 4000 years ago it was used to obtain the intense black hair colour, well-known from Egyptian art. Walter et al. [20] repeated the chemical preparation in their lab and observed the formation of PbS nanocrystals with size of $\approx 4.7\,\mathrm{nm}$. The growth of the nanocrystals is remarkably controlled by the supramolecular organisation of keratins in the hair. The figure is an electron microscopy of the $2\,\mu\mathrm{m}$-thick transverse cross section of a 6 h treated hair, showing the nanoparticles accumulation in the cortex and cuticles. (b) One of the gold colloids samples synthesised by Faraday. They are still optically active being over 150 years old, which is very unusual since most nanoparticle colloids wouldn't last for more than a year [21].

(Nobel Prize for Physics in 1986) [24] and atomic force microscopy by Gerd Binig, along with Calvin Quate and Christoph Gerber, 1986, marked the start of the era of nanotechnology [25].

Nevertheless, the scientific community started putting the foundation for the concepts that have determined the advent of nanotechnology in the previous decades. Michael Faraday was the first to report a scientific experimental observation on nanoparticles, having synthesised by accident a colloidal solution of gold. He understood that the ruby colour was due to the size of the gold particles (figure 1.3 b), that he called "*activated gold*" [21, 26] and caused the frequencies corresponding to red light to be scattered, altering the visible colour of the solution. This is effect was also observed by Tyndall and it is thus known as Faraday-Tyndall effect, which occurs in colloidal solutions as a consequence of the scattering of light by particles of dimensions comparable to the wavelengths of visible light (400 nm–700 nm) [27, 28].

The progress that science would make in the field of nanotechnology was anticipated by R. Feynman in his famous talk "*Plenty of Room at the Bottom*" [29, 30], presented to the American Physical Society in Pasadena in December 1959. Feyman envisaged the possibility of controlling matter at the atomic scale and store information in a "*very small space*". He anticipated the concept of digital memory storage: "*all of the information that man has carefully accumulated in all the books in the world can be written in this form in a cube of material one two-hundredth of an inch wide, which is the barest piece of dust that can be made out by the human eye. So there is plenty of room at the bottom!*". The advent of new powerful microscopes: "*I would like*

to try and impress upon you the importance of improving the electron microscope by a hundred times". And the idea of nanotechnology: "*A biological system can be exceedingly small. Many of the cells are very tiny, but they are very active... Consider the possibility that we too can make a thing very small which does what we want, that we can manufacture an object that manoeuvres at that level!*".

Most of the concepts Feynman mentioned in his lecture have become, in part, reality in the past three decades [9], although there is still a high margin of improvement in most fields (e.g. quantum information technology, drug delivery, data storage etc.). The most fundamental questions to address in the field, in order to be able to achieve these improvements, concern the ability to design, control and predict the properties of materials down to the atomic level [10]. Nanotechnology is relatively young and one can probably say that there is still plenty of room to discover at the bottom.

1.1.1 Properties of nanoparticles

1.1.1.1 Size is crucial

Everything that in nanomaterials differs from bulk materials arises as a consequence of their size [4]. The small scales that characterise the domain of nanomaterials determine the emergence of new chemical and physical phenomena, not observed at the bulk level [10]. Citing another passage from Feynman's lecture: "*Atoms on a small scale behave like nothing on a large scale, for they satisfy the laws of quantum mechanics...I can hardly doubt that when we have some control of the arrangement of things on a small scale we will get an enormously greater range of possible properties that substances can have, and of different things that we can do*".

In fact moving along an imaginary line towards decreasing nanometric dimensions, the appearance of properties linked to the increase of surface-to-volume ratio is observed; when sizes of approximatly 10 nm and below (e.g. in quantum dots) are reached, phenomena caused by the quantum confinement of electronic states occur [31] , having drastic impact on the optical and electronic properties of the system. These properties are what makes nanomaterials so interesting, opening a whole world of possibilities when it comes to their application.

1.1.1.2 Properties

As already mentioned, one of the main differences between nanoparticles and crystalline bulk materials arises from the higher surface-to-volume ratio. As the size of the grains reduces, the available surface area increases, so that a larger fraction of the atoms will be found on the surface. This gives rise to the presence of so-called dangling bonds on the surface, which is one of the reason why nanoparticles present an enhanced chemical reactivity compared to their bulk counterpart, making them particularly suitable for applications in catalysis [32–35].

When the size of the nanoparticles is smaller than a critical dimension, the density of states near the band-edges changes, reflecting quantum confinement [36]. In the case of semiconductor the critical parameter is given by the Bohr radius and the confinement causes a widening of the band gap as the size of the nanoparticle decreases, resulting in a blue-shift in the absorption and emission spectrum. The electronic band structure of nanoparticles is in this case in between that of a crystalline material and an atomic/molecular system and it can be modified by changing size and composition of the nanoparticles, with consequent ability to tune their electronic and optical properties.

Another phenomena of great interest for its many implications in technological applications is that of surface plasmon resonances, that greatly affect the optical properties of nanoparticles (this is also why the the Lycurgus cup in figure 1.2 appears of a ruby colour under transmitted light). Metal nanoparticles present strong electric fields at the surface, which cause a strong enhancement of the absorption and scattering of electromagnetic radiation. Moreover, the frequencies of resonance are affected by the shape, size, dielectric properties and environment of the nanoparticles [37], implying that the optical response to an applied electro-magnetic field can be tuned accordingly. Nanoparticles with tuneable plasmon resonances can be used in optics, magneto-optics, photonics, as well as chemical and biosensing applications [38].

Size has also a critical impact on the thermal and mechanical properties. The strength of a particle increases inversely with the square-root of its size, where it becomes soft when it reaches dimensions of $\approx 10\,\text{nm}$ (this is known as the inverse Hall-Petch relationship) [10]. Finally, the melting points of most materials decrease with particle size.

1.1.1.3 0D, 1D and 2D nanomaterials

Nanoparticles are generally also classified in three categories, 0D, 1D and 2D, depending on whether either all of the three, two or one of the dimensions are in the above specified range (between 1 nm and approximately 100 nm), respectively. Some examples are given below to show how the properties of these different classes of materials can be used in applications and how they are different from their bulk equivalents.

Canonical examples of 0D nanomaterials are fullerenes [39] or quantum dots, whose dimensions in all three directions are typically below 10 nm. Some promising applications of fullerenes are in the field of quantum information processing and drug delivery [40]: endohedral fullerenes can act as cages for atoms, ions or clusters, and then be used as qubits of a quantum computer [41]; water-soluble amphiphilic fullerenes, consisting of C_{60} molecules modified with the addition of hydrophilic component, can be used as nanocarriers of drugs for application in cancer therapy [42].

Semiconductor quantum dots have optical properties that can be tuned by changing the size and the structure, owing to quantum confinement [43, 44]. This makes them suitable

for applications in optics such as photodetection [44], computing, photovoltaic devices, light emitting device, photocatalysis. These materials play also a crucial role in advances in the area of detection and sensing of biological systems, since their fundamental units (membranes, nucleic acids, enzymes etc.), all comprise complex nanoscale components [45–47]. For these reasons quantum dots with specific tuneable optical, magnetic and electronic properties act as perfect probes for obtaining focused and localised responses in these systems at a molecular level [45].

Archetypes of 1D nanomaterials are carbon nanotubes (CNTs) (with tube diameter generally smaller than 50 nm); they were discovered in 1990 by Ijima [7] and from then have constituted a constant focus of research [48–50]. CNTs exist either as single-walled carbon nanotubes (SWCNTs) or multi-walled carbon nanotubes (MWCNTs). CNTs are often used in conjunction with other materials, to obtain specific properties. As an example, TiO_2 nanoparticles and MWCNTs composite layers deposited on $Pt/SiO_2/Si$ substrates can be used in photocatalysis applications for water purification [51]; the use of composite nanostructures solves the problem of fast electron-hole pair recombination encountered when using only semiconductor oxides: the pair lifetime is in fact increased owing to the trapping of electrons in the MWCNTs, resulting in an improved photocatalytic efficiency.

CNTs are naturally apt for use as nano-containers, due to to their hollow cylindrical shape. In a study by Benjamin et al., peapod type structures, consisting of SWCNTs filled with $N@C_{60}$ molecules (a nitrogen atom in a C_{60} cage), are proposed for use in quantum computing [52]. Other studies (among them part of the work done in this thesis and presented in chapter 3) have focused on the synthesis of CNTs filled with transition metals: these systems effectively constitute nanomagnets, protected from oxidation by the carbon capsule [1, 53]. These features make them suitable for application in magnetic data storage, hyperthermia cancer therapy, exchange bias systems and others.

For the 2D category the most well-known material is graphene [54], produced for the first time in a stable form in 2004 by Geim and Novoselov [55] (who were awarded the Nobel Prize in 2010 for their findings). Graphene owes its unusual mechanical, optical and electronic properties to the delocalisation of the *p*-orbital electrons at the surface. Graphene behaves as a zero-gap semiconductor, where the energy of the conduction and valence bands touch at isolated points in the first Brillouin zone [56, 57]. It has very high chemical reactivity, since every single atom in a graphene sheet can be involved in a chemical reaction owing to the two dimensionality of the structure [58]. There are also other examples of ultrathin materials, such as molybdenum disulfide or boron nitride [59] and the more recently developed inorganic equivalents of graphene [60].

1.1.2 The study of the structure of nanomaterials

In order to achieve high and accurate control of the properties of nanomaterials it is necessary to understand their atomic structure. The properties and behaviour of a nanoparticle in a specific chemical/physical environment are in fact intimately connected with the structure: on one hand they are determined by the structure and on the other, the response of a material to a specific stimulus can result in a change of the structure and a consequent modification of its behaviour and properties.

Although these two concepts may seem analogous there is a subtle difference between them. The first implies that one can govern, control, design the properties of a nanomaterial if one is able to achieve an accurate understanding of the structure at the local level (a real-space resolution of the order of approximately 0.1 Å). The second implies that in many cases the structure, and hence the properties, of a nanomaterial are not necessarily stable and can change dramatically under certain conditions.

An interesting example is a study by Zhang on ZnS nanoparticles with a diameter of 3 nm [61], belonging to the class of II-VI semiconductor quantum dots. The effect of desorption and subsequent absorption of methanol on the structure is studied in two different environments. In presence of liquid methanol, the structure transforms from a distorted four-coordinated structure to an unidentified phase after evaporation of the methanol. The addition of a small fraction of water to the methanol solution has a drastic effect on the structural transition: the change in the surface environment, as a consequence of water binding, leads to an increase in crystallinity with the resulting atomic ordering corresponding to that of the sphalerite structure [61]. Interestingly, the interaction between water and ZnS has the effect of reducing the interfacial energy, owing to the polarisation of water molecules. This induces a stabilisation effect on the structure and cause a transition from a more disordered to a crystalline configuration, being the latter energetically favourable. Hence, it is clear that the interaction between a nanoparticle and the environment deeply affects and determines the structure and, on the other hand, we would not be able to understand the behaviour of the nanoparticle in that environment, if we did not understand the structure.

As an example, achieving a clear understanding of the structure of a nanoparticle and how it is affected by the environment in which it is found is fundamental for predicting how it would evolve in and interact with a biological system [62]. This point is crucial for determining the suitability of a given nanomaterial for medical applications or for evaluating the harm it could cause when realised in the biosphere.

1.2 Determining the structure of nanomaterials

1.2.1 Experimental techniques

1.2.1.1 Imaging

The main imaging techniques used for characterising nanomaterials are scanning electron microscopy (SEM) [63], transmission electron microscopy (TEM) [24, 64] and atomic force microscopy (AFM). These techniques are used to access a localised area in the sample and obtain information about the size, shape, surface and local composition of the nanoparticles. Their use is fundamental in order to access a preliminary and qualitative understanding of the nanoparticles under study.

1.2.1.2 Spectroscopy

The main spectroscopy techniques in use include: vibrational spectroscopy (infrared and Raman), UV-visible absorption spectroscopy, fluorescence, dynamic light scattering (DLS), nuclear magnetic resonance (NMR) and X-ray absorption spectroscopy (XAS).

Infrared (IR) spectroscopy is sensitive to vibrational modes associated with a change in dipole moment [65]. Raman spectroscopy is instead sensitive to vibrational modes associated with a change in the polarisability of the molecule [66]. Vibrational spectroscopy can thus be used to identify the presence of specific functional groups to which characteristic absorption bands are associated. IR and Raman are complementary, since functional groups that are IR active are often not Raman active, owing to the different selection rules that apply in the two cases.

UV-vis absorption measures the absorbance of wavelengths in the visible region as a result of localised surface plasmonic resonance, thus providing information about the geometry of the nanoparticles. DLS correlates the brownian motion of nanoparticles in suspension or solution to their size. In particular, it gives an estimate of the hydrodynamic radius, through application of the Stokes-Einstein equation and calculation of the translational diffusion coefficient [67].

In NMR the interaction between the nuclear spins in the material analysed and an external applied magnetic field is used to study the composition of the sample [68, 69]. The technique has been used in studies of nanoparticles for magnetic resonance imaging applications [70] and to study their properties [71, 72].

The XAS signal [73, 74] includes extended X-ray absorption fine structure (EXAFS) and X-ray absorption near-edge structure (XANES); EXAFS can give a crucial contribution in studies of the local structure. This technique can be used to access information about the first few coordination shells in a material. Moreover due to its site selectivity, different atomic species in a sample can be probed individually. However, EXAFS has some limitations in determining the

local symmetry and the medium range order, which is where XANES can provide complementary information.

1.2.1.3 Diffraction

Diffraction techniques make use of three different probes: X-rays, neutrons or electrons. The main techniques in use are Bragg diffraction [75], total scattering [76], TEM diffraction [77] and small angle scattering (SAS) [78].

Compared to XAS, Bragg and total scattering can access more information about the medium and long range order in the structure. However, while Bragg can only provide information about the periodic arrangement of atoms inside the material (i.e. the long range order), the total scattering technique encompasses the average periodic ordering and the local deviation of the structure from this average (i.e. long, medium and local range order) in one function. The two techniques will be discussed in more details in the following section and in chapter 2.

TEM diffraction probes a selected area of the sample of as little as few nano-meters in diameter, thus offering the advantage of providing site-specific information. However this implies that one cannot access information about the totality of the sample, being able to sample only a limited region of the material. Finally, while the previous techniques provide structural information, SAS is used to characterise the geometry and surface of the nanoparticles.

1.2.2 Challenges

Periodicity is, from the structural point of view, the most eminent and universal property of crystals. The whole formalism of traditional crystallography, that is used to understand the structure of crystalline materials, stems from the assumption of periodicity of the atomic structure. The structure of a crystalline material is defined in terms of a unit cell, identified by six lattice parameters (three edges and three angles), from which the structure is generated by translational symmetry operations. Starting from this premise, the lattice parameters can be determined and the atomic structure unveiled by means of Bragg diffraction [75]. In the case of powder samples, this is done by means of the Rietveld refinement method [79]. This concept and the theory of Bragg diffraction have been pivotal in deepening the knowledge of materials and the correlation between their macroscopic and microscopic properties and their atomic structure.

However, traditional crystallographic methods have some limitations when applied to study of the structure of nanomaterials. When it comes to nanomaterials, describing the whole system in terms of a unit cell is often inappropriate, owing to the lack of long-range order [80].

The structure of nanomaterials is inherently different from that of crystalline materials for a series of reasons. This is often inhomogeneous, presenting variations between the core and the surface of the nanoparticle: the core is more crystalline, while the structure of the first

few atomic shells at the surface is usually more disordered or amorphous [61, 81]. Moreover, nanomaterials of technological interest are often composite materials, comprising several phases with one or more of them having dimensions in the nanorange [1, 2]. This is the case of CNTs filled with transition metals, one of the materials analysed in this thesis, usually synthesised as MWCNTs filled with one or more phases of one or more metals [1].

Even when it is possible to identify a unit cell, as in the case of highly crystalline nanoparticles [82–84], the limited size of the particles implies that the structure cannot be assumed to be infinitely periodic, thus causing an intrinsic flaw in the Bragg diffraction formalism. This reduces the amount of information deducible from analysis of the Bragg diffraction data. Moreover, the size of the nanoparticles affects the diffraction pattern causing a broadening of the the peaks or in the case of highly disordered structures Bragg peaks are almost absent or present in limited number, thus making it hard to infer precise considerations about the structure. The broadening of the Bragg diffraction peaks can be used to estimate the size of the nanoparticles [85–87]: however quite often this estimate is not correct, since the broadening only takes into account size contribution neglecting other contributions arising from internal strain forces. In the above mentioned study on ZnS nanoparticles, the estimated diameter of the particles is 1.4 nm, if calculated using X-ray diffraction (XRD) and the Scherrer equation [85], while is estimated to be approximately 3 nm, based on UV-vis absorption and TEM analysis. The latter is in agreement with the results from molecular dynamics (MD) simulations [61].

Another problem encountered in studies of the structure of nanoparticles concerns the lack of prior knowledge of the composition and density. Even when the composition of the nanomaterial can be almost exactly determined, as in the case of materials comprising only one phase of a material or a compound, and it is possible to identify a bulk equivalent of the structure, still the density is not necessarily equal to that of the bulk. Strain and surface tension in the nanoparticle are in fact going to affect and alter the density. Moreover the presence of empty space or a matrix between one nanoparticle and another makes the definition of density used in the context of bulk materials inappropriate when applied to the case of nanoparticles.

1.2.3 Local and medium range probes

In order to overcome the limitations and issues just mentioned, the use of techniques that are sensitive to the local ordering and local fluctuations of the structure from the average becomes crucial. The total scattering technique in particular has been increasingly used in studies of nanomaterials [30, 88, 89], owing to its capability to access information about the local and the long range inside a material simultaneously.

Bragg scattering gives a discrete signal at values θ_{hkl} corresponding to symmetry planes inside the material characterised by inter-planar distance d_{hkl}, according to Bragg's law $\sin\theta_{hkl} =$

$\lambda/2d_{hkl}$, thus providing information about the average structure.

On the other hand, the total scattering technique makes use of a continuous signal of scattered intensities, that encompass information concerning both the average structure of the material and the deviation of the latter from the average [90, 91].

The wavelengths of the radiation used in total scattering experiments are a fraction of interatomic distances, small enough to be sensitive to local fluctuations [83, 92]. The diffuse scattering, which appears in the total scattering function as a background signal, is what contains the information about the local disorder, that are not accessed in traditional crystallography, but can unveil details about the structure of materials and their properties. In Bragg diffraction studies the diffuse scattering is in fact treated as background and subtracted from the data, prior to analysis.

The total scattering function is usually studied in conjunction with its Fourier transform, the pair distribution function (PDF). The PDF is calculated from the experimental total scattering function, which is what is measured in a total scattering experiment. Both functions contain effectively the same information, in one case observed in reciprocal space (Q-space) and in the other in real space (r-space). However the PDF function gives a more direct and intuitive view on the atomic structure, since it is essentially a distribution of real space atomic distances, representing the weighted probability of finding an atom at a given distance from another atom (see equation 1.2). More precisely, a peak in the PDF provides information about a specific pair of atoms at a given distance: the mean of the peak corresponds to their average distance, its integral is proportional to the coordination number and the width and shape give information about the distribution of distances around the average.

Other techniques that can provide information about the local structure are nuclear magnetic resonance (NMR) and extended x-ray absorption fine structure (EXAFS). They provide information about the first few coordination shells but are not sensitive to the medium and long range order in materials. However a structural model that provides a good description of the short range order is not necessarily equally good at describing the long-range order. As a consequence, a technique that only gives information about the short range order does not always allow a global and comprehensive understanding of the structure. On the other hand the PDF method provides a description of the structure of materials that is self-consistent across multiple length scales [93]; hence a theoretical structural model, that matches the PDF data equally well on several length scales, is a coherent and comprehensive representation of the structure.

Knowledge of the short range order alone (even though of fundamental importance), as that acquired through EXAFS, may not provide an exhaustive picture of the material and its properties, lacking the complementary information about the long-range order. A study on ferrihydrite nanoparticles by Harrington et al. [94] is an example of how a structural model valid in the short-range may not be consistent with the medium and long-range order: Figure

1.4 shows a fit of the PDF of a sample of ferrihydrite nanoparticles against a goethite structural model; even though the latter is consistent with the first few peaks, it does not provide a good representation of the long-range data.

On the other hand EXAFS presents also some advantages, as it is element specific and sensitive to low concentration [94] while PDF is not; EXAFS and total scattering can be considered, for this reason, as complementary rather than competing techniques.

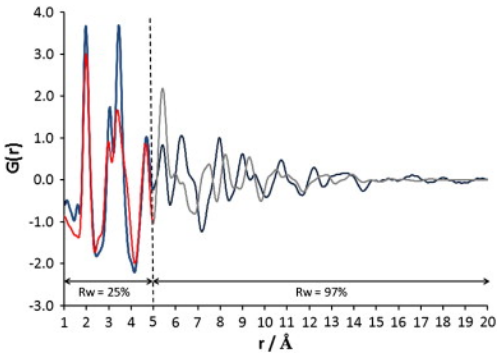

Figure 1.4: PDF of ferrihydrite, split into short and medium range structure (light and dark blue respectively) and the PDF of the calculated phase of goethite (red and grey) [94]. Here the PDF is defined as $G(r)$, but it is called $D(r)$ in the formalism that I use (see equation 1.2).

1.2.4 Modelling techniques

The PDF function is a very powerful tool for the analysis of the structure of materials, since it is a direct representation of the interatomic distances between atoms. The PDF gives a wealth of information: average interatomic distances of the first nearest neighbours, coordination numbers from the integral of the peaks or correlated motion of atoms from the peaks width. However, in order to achieve a better understanding of the structure and obtain more quantitative information, it is desirable to generate a structural model to be used as a comparison or to refine against the experimental data [91, 92]. The PDF from such a model can be generated using the following relation

$$D_{\text{calc}}(r) = \frac{1}{r}\sum_{i,j}\left[f_i f_j \delta(r - r_{ij})\right] - 4\pi r\rho_0 \tag{1.1}$$

where f_i and f_j are not dependent on the scattering vector Q. The PDF function is defined as

$$D(r) = \frac{2}{\pi}\int_0^\infty Qi(Q)\sin(Qr)\mathrm{d}Q \tag{1.2}$$

where $i(Q)$ is the total scattering function. The mathematical derivation will be discussed in more details in section 2.3.

1.2.4.1 RMCProfile and PDFgui

In this thesis work, the programs `RMCProfile` [95, 96] and `PDFgui` [91, 97] are used for refinement of theoretical starting configuration against the data. The main differences between these refinement techniques stems from two main points: the size of the configuration used in the refinement process and the space in which the refinement is performed.

RMCProfile is based on the Metropolis Monte Carlo algorithm and performs what is called "big box modelling" since the data can be refined against a supercell, of size specified by the user, on which periodic boundary conditions are applied; in a typical calculation the configuration is a cube with edge of $\approx 50\,\text{Å}$. Such box, assuming there is an atom per $18\,\text{Å}^3$), would contain 6944 atoms.

In contrast with RMCProfile, PDFgui performs what is called small box modeling. In this case the data are refined based on a few unit cells (containing approximately 100 atoms) instead of using a big box of atoms. The program applies periodic boundary conditions to a small structural model in order to calculate the quantities of interest, such as lattice parameters, atom-atom distances, anisotropic ADPs up to large real space vectors. It can also be used to create structural models of multiphase systems [91], including multiple structures in the fitting procedure; in this case phase scale factors can be refined to determine the abundance of each phase. It also contains functionalities for sequential fitting, so that a given fit can use the results of a previously performed fit as starting parameters.

In RMCProfile both real space and reciprocal space data are refined against the theoretical configuration, while in PDFgui the refinement is only performed in real space. In PDFgui the structural parameters are refined in a way that might look similar to what done in a Rietveld refinement; however the difference lies in the fact that the model is only valid in the r-range used for the refinement [91], while the Rietveld theory is based on the assumption of infinite periodicity.

These differences between the two strategies imply that big box modelling is generally more suitable for taking into account the long range order in a structure, that arises also as a consequence of (or in conjunction with) local ordering. However there is another way of accounting for differences between short and long range order in PDFgui, since it can analyse the parameters as a function of the length scale, by varying the r-range on which the refinement is performed [91].

PDFgui offers among the functionalities the options to apply a spherical shape function to the PDF of the equivalent bulk structure, to account for effects arising as a consequence of the size and shape of spherical nanoparticles. This method is very useful for modelling mono-phase spherical nanoparticles, but it is not robust when applied to more complex nanostructures with different shapes or containing several phases.

The RMC method does not contain yet specific functionalities for refining nanoparticle data, although some preliminary work in this direction has been conducted as part of this project. A study by Funnell et al. adopts a bespoke solution to address this problem [59]. In the study, a model of a Zn_2Al-borate layered double hydroxide nanosheet was refined against X-ray total scattering data using RMCProfile. Corrections that account for the density difference between the real system and the RMC configuration and for unstructured pair correlations between

atoms in the nanosheet and in the surrounding material were applied.

1.2.4.2 Molecular dynamics simulations

The program `DL_Poly_4` is used to perform molecular dynamics simulations (MD) of nanoparticles configurations to compare with the data. The molecular dynamics (MD) method simulates the behaviour of atomic configurations in specific physical conditions. In a MD simulation the atoms interact *via* interatomic potentials that are specified and chosen by the user depending on the system. The length of the simulation can be specified in terms of number of steps and duration of each step; after each interval a new set of coordinates and velocity is generated for each atom in the system based on the previous steps. It is possible to set temperature and pressure to values specified by the user.

In the framework of total scattering studies this represents an extra source of information since the MD can be used to produce configurations and observe their response under certain conditions. The PDF and total scattering functions can be calculated from these configurations and used as a comparison to the data or even as starting configuration for a RMC refinement.

1.3 Overview of the thesis

In this thesis, the total scattering technique is applied to the study of three classes of novel nanomaterials, answering important questions that concern their structure. These nanostructures are, from the structural and compositional point of view, more complex than other nanomaterials previously studied [82, 83, 89, 98–101], thus placing this work at the forefront of the study of the structure of nanomaterials. This work aims at pushing the boundaries of research in the field using a combination of experimental and modelling techniques.

The thesis is organised as follows. In chapter 2 the experimental techniques, alongside the analysis and atomic modelling approaches used are described. Some of the methods that are specific to only one among the materials studied are described in the respective result chapters.

Chapter 3 concerns the study of the structure of MWCNTs continuously filled with iron, where the X-ray PDFs are used to analyse the iron core structure and the role played by preferential orientations. Chapter 4 describes the study of the structure of Prussian blue in nanoparticulate and bulk form. Preliminary analysis, such as infrared spectroscopy and a bespoke modelling procedure of the low-r region of the PDF, are used for optimising the data correction and guiding the making of the starting atomistic configurations, used the `RMCProfile` analysis. The study of CaO nanoparticles with different degrees of carbonation is discussed in chapter 5. Finally chapter 6 presents the broad conclusions of my work and possible future work that could be performed on these nanomaterials.

The appendix contains details of some of the codes used in this thesis work, written in `Fortran`, `Matlab` and `Python`.

Chapter 2

Methods and theoretical background

The nanomaterials presented in this thesis were all studied by means of X-ray and neutron total scattering and PDF analysis. There are numerous theoretical tools and modelling approach that can be taken when analysing total scattering and PDF data and the choice is very much dependent on the characteristics of the material.

The modelling techniques used were chosen on an *ad hoc* basis depending on questions addressed case by case. The data were refined with respect to a starting configuration, using either the program `PDFgui` or `RMCProfile`. Models to compare with the data were generated by means of MD simulations, using the program `DL_Poly_4`. For some of the systems studied, the PDFs of single phases were calculated from the spectrum of phonon vibrational frequencies, using the program `GULP`. In some cases, bespoke programs have been written to build nanoparticle configurations with specific features or to address questions (e.g. relative to the composition of the nanoparticles) that could not be easily solved by means of other analysis techniques.

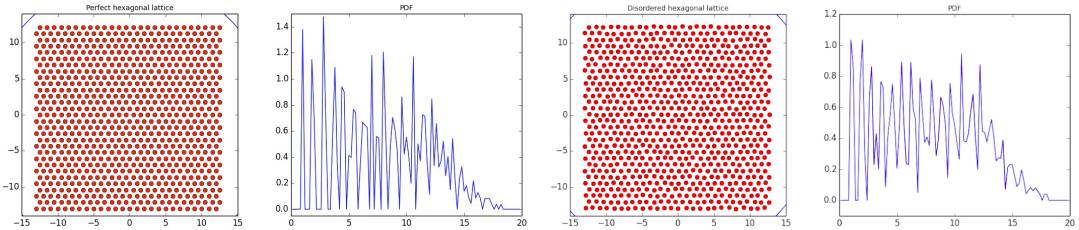

Figure 2.1: An example to show how the PDF encompasses information about the local disorder in the structure. The 2D hexagonal lattice is perfectly ordered in (a), while some random disorder was added in (b), which is reflected by the appearance of new peaks and broadening of others in the PDF.

2.1 Total scattering and pair distribution function

It was mentioned that the choice of the total scattering technique was motivated owing to its ability to determine simultaneously the local and medium range order inside a material. The technique plays an important role in the study of the atomic structure of nanomaterials, since even small changes in the local atomic arrangement have an impact on the properties of materials [84, 102].

Figure 2.1 shows the last frames of two movies (attached in the electronic appendix) that was created to show how the disorder is reflected by the PDF; in the movie, a circle of increasing radius expands over the lattice, departing from the centre and a count is added to the PDF function for each atom hit by the circle at a given distance r from the centre. Figure 2.1 a shows a perfectly ordered hexagonal lattice, while in b some random disorder was added to the structure. This simple example shows clearly that the PDF carries information about the disorder: the peaks are in the case of the latter broader and few new features arising from the disorder have appeared (see e.g. peak at approximately 3 a.u. in figure b). Moreover the 2D lattice was purposely made with finite size, to mimic the features that the PDF of an object of limited size (such as a nanoparticle) would have: there are not any peaks after 18 a.u., corresponding to the half-diagonal of the square, indicating that no correlation between pairs of atoms is recorded beyond this distance. This also shows how the PDF provides an indication about the size of the regions where correlation in the distribution of interatomic distances is present.

2.1.1 History and applications

The theory of total scattering scattering saw its dawn in 1915, when P. Debye sent a paper entitled *Zerstreuung von Röntgenstrahlen* [Scattering of X-rays (Debye, 1915), English version in Debye (1988)] to the editors of the journal *Annalen der Physik* [104, 105]. In the paper Debye postulated for the first time that the interaction of X-ray radiation with the electrons cloud surrounding the atoms in randomly oriented aggregates produces an interference pattern that reflects is some way the arrangement of atoms inside the material: "*we must expect the atoms themselves to show occasional interference patterns when irradiated with X-rays; these interference patterns cannot be obliterated entirely even though the atoms have random orientation in the space*" [106]. The Debye equation, that is used to calculate the intensity of the radiation scattered by a randomly oriented aggregate of atoms, was published in its modern form (that includes the atomic form factors) in 1930 [107]; the equation, which still constitutes the foundation of total scattering theory, has the following form :

$$I(Q) = \sum_{i,j} f_i(Q) f_j(Q) \frac{\sin(Qr_{ij})}{Qr_{ij}} \tag{2.1}$$

where the sum is over pairs of atoms i and j, r_{ij} is the distance between the atoms, Q is the scattering vector, $f_i(Q)$ the X-ray atomic scattering factor of atom i.

The formalism of the pair correlation function was introduced by Zernike and Prins [108], who in 1927 established the relationship between the isotropically averaged scattering function (equation 2.1) and the relative positions of pairs of atoms in a material [109]. Despite the absence of high-speed computing, the approach was applied already in 1930 by Debye and Menke to study the structure of liquid mercury [83]. Since that moment onwards the technique has been extensively applied to the study of liquid initially and then glasses.

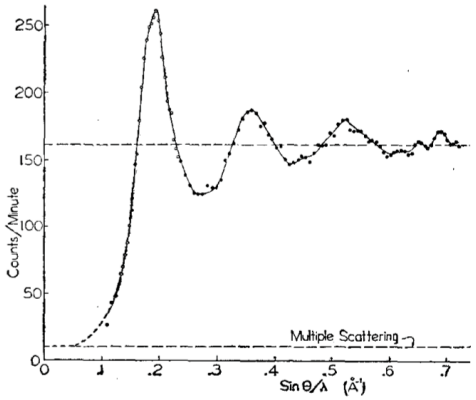

Figure 2.2: Neutron total scattering function of liquid mercury from a paper dating back to 1954 [103], reviewing the original study of the structure made by Debye and Menke in 1930. The data, collected at the Brookhaven reactor, are the circles (solid, 20 minutes counting period, open, 10 minutes) and the dotted line represents a fit to the data.

Total scattering was in fact originally conceived starting from the need for a tool to study the structure of amorphous materials, such as liquids and glasses. A typical scattering pattern from an amorphous material presents only few broad Bragg peaks or none at all, owing to the lack of long range order (figure 2.2). Correlation between atomic pairs is observed only up to second or third nearest neighbours and a typical PDF function of an amorphous material is characterised by few sharp peaks in the low r region, corresponding to the first few coordination shells, very broad features at intermediate r and none at all at high r. In other words total scattering has been firstly used to study the structure of materials lacking any sort of long range order, where the diffraction pattern is characterised only by broad features arising from diffuse scattering.

In subsequent times, the technique started to be applied also to the study of crystalline materials. Contrarily to amorphous materials, the diffraction pattern from a crystal is characterised by sharp Bragg peaks, arising from the periodic arrangement of atoms in the material. However, despite its periodicity, a crystal may (and usually does) present a degree of local disorder. This disorder is what often determines the behaviour and the properties of a material and it is for these reasons a fundamental bit of information [102]. Since Bragg diffraction gives by definition only information about the average ordering, an understanding of the local disorder is unreachable through the sole analysis of Bragg peaks. The local disorder is detectable only by taking into account the diffuse component of the scattering.

Figure 2.3 shows the total scattering function obtained from SiO_2 at 300 °C: this high temperature phase of silica is called β-cristobalite and we can observe that its diffraction pattern

presents a high degree of disorder, as it is deducible from the presence of broad features (diffuse scattering) characterising the diffraction pattern. These features arise from the local ordering of the structure or, in other words, from the local deviations of the atomic positions from the average ordering, as will be discussed in more details in the following section.

The point that should be appreciated at this stage is that the total scattering was at its origin conceived as a tool for analysis of structural features whose signature is in the diffuse scattering; hence, total scattering was and is in a sense the quintessential diffuse scattering analysis tool, since it offers a direct and preferential view on the local order or disorder of a material. And while no one had originally thought about its importance in studies of crystalline materials, it has been the need to understand their properties that has led to the technique being increasingly used in studies of their crystalline structure.

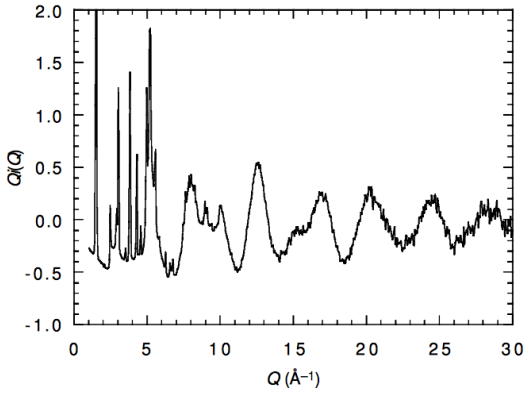

Figure 2.3: Total scattering function from the β-cristobalite phase at $300\,^{\circ}\mathrm{C}$. Bragg peaks are visible only at low-Q value, while they become broader at larger value of Q, until any Bragg component is effectively lost beyond approximately $11\,\mathrm{Å}^{-1}$, where only a diffuse scattering signal is detectable (figure taken from [76]).

As an example, the above mentioned β-cristobalite phase of SiO_2 exhibits local disorder. Incidentally, the macroscopic thermal expansion properties of this material are a consequence of the local deviation of the structure from its average. Such understanding has been achieved analysing the diffuse scattering [76].

The increasing level of accuracy and details reachable in the knowledge of the local atomic structure, owing to the advances in crystallographic techniques, has been at the heart of many of the developments in material chemistry and functional materials applications [93]. The information encompassed in the diffuse scattering are crucial for tuning and controlling the properties of materials. Effectively a combined knowledge of both short-range order and long-range order is needed.

In this sense, the mathematical and physical beauty and utility of the total scattering technique lies in the already mentioned ability to provide a picture of the structure that is coherent across multiple length scales, embracing both Bragg and diffuse scattering in one unique function.

If one could trace an imaginary line departing from crystalline materials, passing through disordered crystalline materials and ending on amorphous materials, nanomaterials would be located somewhere in between the disordered crystalline and amorphous ones. Where a specific nanomaterial will be exactly located on this line (either closer to amorphous or

crystalline materials) will depend on specific features and factors such as size, shape, environment, composition etc., that determine the degree of disorder of the nanoparticles. It is then clear that, if a combined understanding of both Bragg and diffuse scattering is important in studies of crystals, it is equally (or even more) crucial when the materials under analysis are nanomaterials. It is for this reason that, as the interest of the scientific community towards nanomaterials has increased, the total scattering technique has been increasingly used as a tool of analysis of their structure [82, 83, 89, 98–101, 110–112].

An interesting example of total scattering applied to nanomaterials is the study of the fullerene molecule, C_{60} [91]. At room temperature C_{60} behaves as a plastic crystal [113–116], since the molecules are randomly oriented with respect to each other and tumble around their position rotating freely [117]. The dynamic orientational disorder has its signature in the diffuse scattering component [117], which is reflected by broad features in the PDF function. Depending on the length scale analysed in the PDF, one can either probe a single domain (a bucky ball) individually, focussing on the low r region, or domains interaction, looking at the medium and high r.

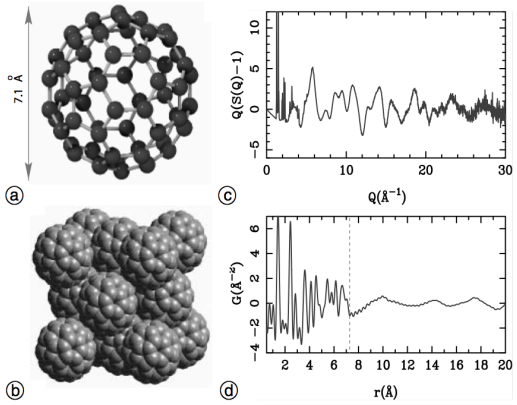

Figure 2.4: (a) a single domain and (b) several neighbouring domains of C_{60}, (c) its normalised neutron diffraction pattern, (d) the PDF with the dotted line corresponding to the diameter of the ball, 7.1 Å [91].

The diameter of C_{60} is 7.1 Å, so the sharp peaks observed at r lower than this value (figure 2.4) are due to intramolecular distances in a single domain, while when $r > 7.1$ Å the features become much broader, corresponding to intermolecular distances between atoms. The lack of well defined correlation between interatomic distances beyond the diameter of a single domain, arising as result of the plastic behaviour of C_{60}, is reflected by the loss of sharp peaks.

2.1.2 Bragg diffraction: Differences and advantages

Traditional crystallographic techniques treat Bragg and diffuse scattering separately. The position of the Bragg peaks is used to determine the lattice parameters, while their intensity gives information about the average position of the atoms [76]. A polynomial fitting procedure is generally applied to eliminate the diffuse scattering component, which is normally neglected and subtracted together with the instrumental background. What this means in practice is that Bragg scattering contains only information about the distance between the average positions of individual atoms $< r_2 > - < r_1 >$. The total scattering, which includes both Bragg and diffuse

scattering, contains instead information about the average distance between instantaneous positions of atoms $< r_2 - r_1 >$, which is enclosed in the two-particle correlations terms. This subtle divergence is the key difference between the two techniques and is what determines the ability of total scattering to detect deviations of the structure from the local average.

This point can be also observed mathematically, starting from the equation of the intensity of the scattering from an ensemble of atoms:

$$S(\mathbf{Q}) = N \left\langle |F(\mathbf{Q})|^2 \right\rangle = \frac{1}{N} \sum_{i,j} f_i f_j \left\langle \exp\left[\mathrm{i}\mathbf{Q} \cdot (\mathbf{r}_i - \mathbf{r}_j)\right] \right\rangle_t \quad (2.2)$$

where $\mathbf{Q} = \mathbf{k}_i - \mathbf{k}_f$ is the scattering vector ($\mathbf{k}_i$ and $\mathbf{k}_f$ are the incident and scattered wavevector, respectively), $F(\mathbf{Q})$ is the structure factor, N is the number of scatterers or particles and the sum is over atom pairs, where f_i and r_i are the scattering length (or factor) and the position of particle i respectively. The exponential is averaged over time.

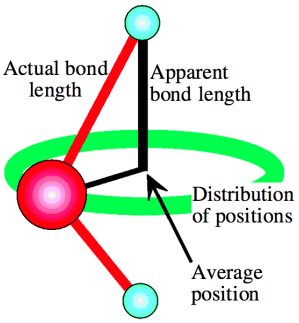

Figure 2.5: Apparent and actual bond length of the Si-O bond in β-cristobalite [90].

If we separate this equation into two parts, one arising from the Bragg scattering and the other from the diffuse scattering, as:

$$S(\mathbf{Q}) = S_{\mathrm{Bragg}}(\mathbf{Q}) + S_{\mathrm{Diffuse}}(\mathbf{Q}) \quad (2.3)$$

the Bragg term can be effectively written as the single particle correlation

$$S_{\mathrm{Bragg}}(\mathbf{Q}) = N \left\langle |F(\mathbf{Q})| \right\rangle^2 = \frac{1}{N} \left\langle \left| \sum_i f_i \exp\left[\mathrm{i}\mathbf{Q} \cdot \mathbf{r}_i\right] \right| \right\rangle^2 \quad (2.4)$$

that does not retain any information about relative positions of pair of atoms. The diffuse scattering is then given by the difference between the two terms (total and Bragg scattering)

$$S_{\mathrm{Diffuse}}(\mathbf{Q}) = N \left\langle |F(\mathbf{Q})|^2 \right\rangle - N \left\langle |F(\mathbf{Q})| \right\rangle^2 \quad (2.5)$$

Bragg reflections are only observed when $\mathbf{Q}$ is equal to a reciprocal lattice vector, $h\mathbf{a}^* + k\mathbf{b}^* + l\mathbf{c}^*$. This can be reduced to a relationship between the scattering angle θ, the incident wavelength λ and interplanar spacing d, known as Bragg's law:

$$2d_{hkl} \sin\theta_{hkl} = \lambda \quad (2.6)$$

where the subscripts *hkl* are the Miller indices that identify a given set of planes and where:

$$Q = |\mathbf{Q}| = \frac{2\pi}{d} = \frac{4\pi \sin\theta}{\lambda} \tag{2.7}$$

An important consequence of this is that Bragg peaks will only be observed for materials that posses long-range order, characterised by an averagely ordered and periodic arrangements of atoms. In fact an aperiodic and highly disordered structure does not present sets of evenly spaced planes, so that, even in the presence of diffraction from localised planes of atoms, the diffraction pattern will not contain Bragg peaks.

On the other hand, for crystalline materials, Bragg's law (combined with data analysis procedures such as Rietveld refinement) can be used to identify and classify, with an elegantly simple formalism, the structure of crystalline materials. From the Bragg diffraction pattern we can obtain information about the unit cell of the material and hence the overall symmetry properties of the system.

If it is true that diffuse scattering holds information that is crucial for understanding the structure and the properties of materials, it is also true that (except for the case of amorphous materials) the diffuse scattering and hence the local structural information become meaningful when put in the context of the overall average structure of the system.

The already cited example of the SiO_2 and its high temperature phase, β-cristobalite [76], can be used to illustrate this point. The structure of SiO_2 consists of an infinite framework of corner sharing SiO_4 tetrahedra at an angle between each other [118]. Linear Si−O−Si linkages are not energetically favourable, so the SiO_4 tilt with respect to each other, generating a tetragonal structure with bent Si−O−Si linkages. While at room temperature this occurs by means of a phase transition to a tetragonal structure, at high temperature it is a dynamic process where the tetrahedra perform large amplitude rotations around the average positions determined by the face centred cubic (fcc) symmetry.

In the case of the high temperature phase, the information obtained through the analysis of the Bragg peaks would lead to the conclusion that the Si−O−Si bond is straight with the O atom sitting in the midpoint between the two silicon atoms; the average position of the oxygen atom is the midpoint of its distribution of positions. On the other hand the analysis of diffuse scattering shows that the bond is instead bent, with the O atoms slightly displaced normally to the Si−Si vector (figure 2.5).

The Bragg scattering would lead to an interpretation, that does not describe correctly the behaviour of the material; what is indeed recorded through Bragg scattering is the average position of the O, located in the mid-point between Si atoms. Contrarily, the O can be found with equal probability in an annulus surrounding the average position. The sole analysis of Bragg scattering would lead to the conclusion that the Si-O bonds shorten as the temperature raises,

while the total scattering technique is able to identify the real origin of the negative thermal expansion of β-cristobalite in the displacement of the O atoms along the direction normal to the Si-Si distance.

Still without the information about the average structure, which is found to be fcc with linear Si−O−Si bonds, one would not be able to value the information obtained from diffuse scattering, by interpreting them as local deviations of the structure from the average symmetry.

2.2 Total scattering probes

2.2.1 Neutrons and X-ray

2.2.1.1 Neutrons

Neutrons interact with the nuclei inside the material of interest by means of the strong nuclear force (nuclear scattering), as well as, where present, with the magnetic moment of the atoms arising from unpaired electrons in the outer shells (magnetic scattering) [119].

The scattering process can be either elastic, if the energy transfer is zero, or inelastic, when there is energy transfer. Elastic scattering arises from the static component of a structure (i.e. the time-averaged structure), while the second contains information about time-dependent processes (i.e. the dynamical behaviour) [119, 120].

Each isotope is characterised by a constant (Q-independent) scattering length b (units of length, in the order of fm), reflecting the strength of the nuclear interaction for a given isotope. The scattering cross section (units of area) from the same element has different values depending on the isotopic or nuclear spin state. This gives rise to two different types of nuclear scattering: coherent and incoherent [120]. The scattering cross sections are given by:

$$\sigma_{\text{coh}} = 4\pi b_{\text{coh}}^2 = 4\pi \bar{b}^2 \tag{2.8}$$

$$\sigma_{\text{inc}} = 4\pi b_{\text{inc}}^2 = 4\pi(\overline{b^2} - \bar{b}^2) \tag{2.9}$$

for coherent and incoherent scattering processes respectively [120], where the overline denotes an average . The coherent part of the scattering depends on the average of the scattering length, thus containing information about coherent (i.e. correlated) processes, while the incoherent part accounts instead for differences in both isotopic and nuclear spin states, thus containing the dynamic information for individual atoms. The incoherent scattering component is significant in cases where either the samples contain a relatively high percentage of two or more isotopes of the same element or when, even in the presence of one unique isotope, the fluctuations of the nuclear spin states interact strongly with the neutrons in the scattering process.

Diffraction techniques make use of the coherent elastic part of the scattering. The incoherent

part of the scattering is not useful for diffraction studies, so the sources of incoherent scattering are usually minimised and the residual contribution subtracted during the data correction procedure. In most cases the coherent cross section is much larger than the incoherent one, especially since among the isotopes of one element there is usually one that is naturally more abundant than the others. However, in the case of incoherent scattering arising from nuclear spin contributions, there is one well known and experimentally relevant example and it is the case of the most abundant isotope of hydrogen, ^{1}H. Hydrogen is peculiar in two ways in fact: it has a negative coherent scattering length, -3.74 fm, and a large incoherent one, 25.27 fm. The latter gives a strong contribution to the scattered intensities over all values of Q. For this reason, in case of hydrogen-containing samples, isotopic substitution is usually performed, using deuterium, ^{2}H, instead of ^{1}H in the synthesis of the samples. Moreover deuterium has also a larger coherent scattering length, 6.67 fm, implying that its contribution to the diffraction pattern will have a stronger intensity compared to ^{1}H. The Prussian blue series of samples studied in this thesis (chapter 4) were synthesised in deuterated form, to avoid, as much as possible, the presence of ^{1}H in the pores and vacancies of the structure.

The magnetic scattering due to the interaction between the neutron spins and the magnetic moments of the atoms produces an extra scattering contribution that adds on to the nuclear scattering. The density of the magnetisation of the atom extends across the same length scale of the electron cloud or charge distribution [120]. Hence, as for X-rays, the intensity of the scattering is not modulated by a constant scattering length dependent on the isotope, but rather by a Q-dependent atomic form factor, that falls off to zero at large Q values.

2.2.1.2 X-rays

X-rays are electromagnetic waves with wavelength between 0.1 Å and 100 Å. They interact with the electronic density distribution around the nuclei.

In the X-ray scattering process each atom is characterised by a Q-dependent atomic form factor, generally denoted as $f(Q)$ [121]. Its value at $Q = 0$ is equal to the number of electrons ($= Z$ for a neutral atom) and it falls off to zero for large values of Q, in a similar way to the magnetic component in neutron scattering. As a consequence, the intensity of the X-ray scattered from a given element is dependent on its size or atomic number.

2.2.1.3 Form factors and complementarity of the two techniques

Owing to the the differences between the scattering phenomena involved in neutron and X-ray diffraction, it can be often useful to collect data using both sources.

As already mentioned, neutrons are scattered by each isotope with an intensity that is proportional to b^2_{coh}. The value of this quantity does not have any direct correlation with the

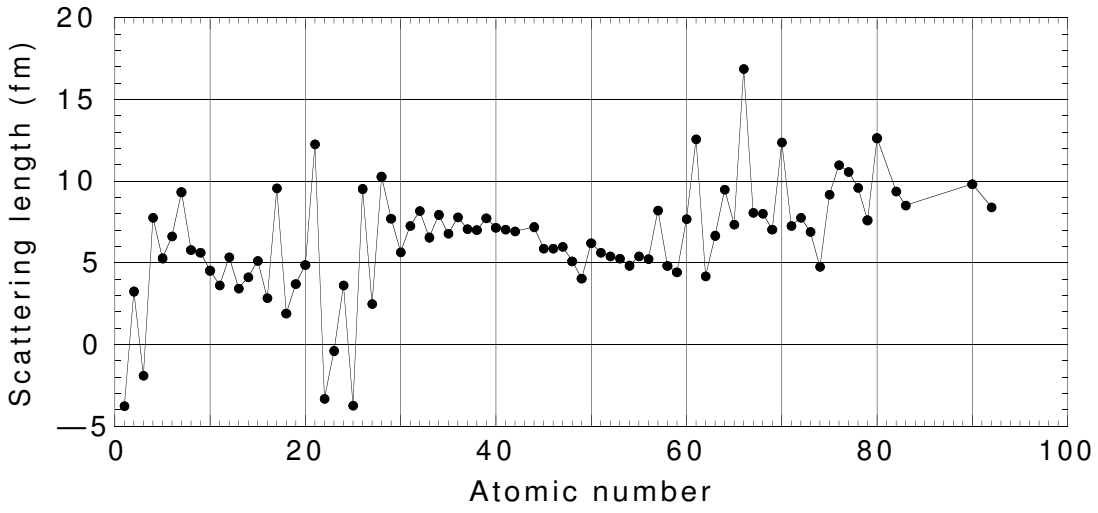

Figure 2.6: Coherent neutron scattering length as a function of the atomic number of the most naturally abundant isotope of a given element [90].

size of the nuclei or its atomic number. This can be observed in figure 2.6, that shows the values of the coherent scattering length for the various atomic species. On the other hand, the X-ray scattering intensity is proportional to the atomic number and is Q-dependent.

There are several implications to these differences. First of all, since the X-ray scattered intensities decrease with increasing scattering angle, to an extent that is inversely proportional to the size of the nuclei, while for neutrons these are constant, the latter are often to be preferred when one is interested in studying the details about the short-range order of the material. Real space resolution is in fact proportional to $Q_{\max}$, the maximum Q that contains useful structural information, as will be discussed in more details later.

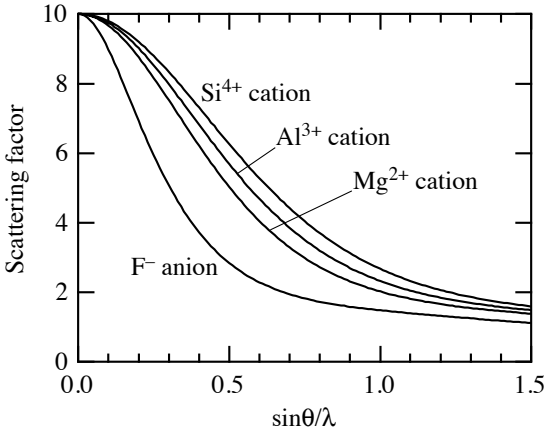

Figure 2.7: X-ray atomic scattering factors of atoms with the same number of electrons (10 in this case, so that $f(0) = 10$), but different atomic numbers, which is reflected by the faster or slower fall of f for increasing Q [90]. The higher is the nuclear charge the denser is the electrons distribution around the nuclei, resulting in slower fall-off in reciprocal space.

Second, in the presence of a sample containing some elements that are significantly heavier than others, X-rays can be used to isolate the contribution to the scattering arising from the heavier elements. On the other hand, neutrons are sensitive also to lighter elements. So effectively the combined use of the two techniques turns out to be very useful in cases whereby a material comprises several atomic species, whose scattering contributions is desirable to separate.

This is the case of all the nanomaterials studied in this thesis, where the combined used of the two probes is useful in differentiating the contribution and structural features of different phases contained in the samples, especially in the case of the MWCNTs continuously filled with iron (chapter 3).

Another situation in which the use of neutrons combined with X-rays may help is the case of a sample containing different elements with the same or very similar number of electrons as illustrated in figure 2.7. On the other hand there may be also an inverse situation where the atoms contained in the samples have different atomic numbers, but very similar neutron scattering lengths. In this case the use of X-rays can help discerning the contribution arising from different atoms.

Moreover the scattering from hydrogen is almost invisible using X-rays as a probe while it has intensity comparable to that of the other atoms in the case of neutrons and gives a strong incoherent contribution, as previously observed. Finally, as already mentioned, information about the magnetic moments inside a material, arising from aligned unpaired electrons in the partially filled energy levels, can only be accessed by means of neutron scattering.

2.2.2 Production and sources

2.2.2.1 ISIS and Nimrod

Neutrons can be generated into two main ways: by a nuclear reactor or spallation source. All the neutron experiments performed in this thesis were conducted at ISIS, where neutrons are produced by spallation. Protons are accelerated through a synchrotron to energies of the order of 800 MeV and finally collide with a tungsten target, driving neutrons from the nuclei of the target atoms (see figure 2.8) [122]. The neutrons are then slowed down by moderators (hydrogen, methane or water) surrounding the target, in order to achieve a speed useful to study and explore properties of materials. Moderators at different temperatures can be used to produce a spectrum of neutrons with different wavelengths, e.g. a liquid hydrogen moderator for longer wavelengths and a water moderator for shorter wavelengths.

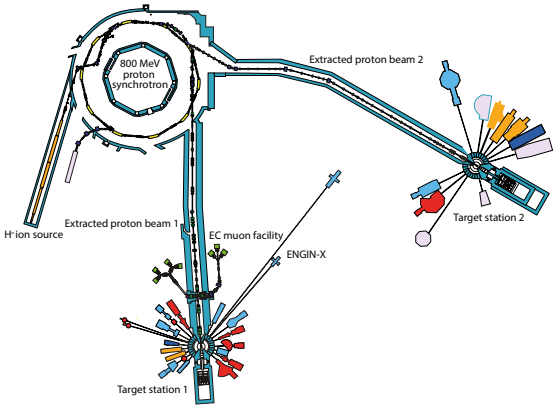

Figure 2.8: A map of ISIS, showing the proton synchrotron and the two target stations with the beamlines (instruments) shown in different colours and departing radially from the respective target stations [122].

Pulsed or spallation neutron sources present some advantages with respect to reactor sources; they are safer, as they do not produce radioactive and toxic waste, and, if the proton pulses are

short enough, the neutrons leave (to first approximation) the target all at the same time, which means that the energy can be measured by the time-of-flight to the detector. More importantly, improving reactor sources beyond the current state of performances is not economically feasible.

The instrument used for the neutron total scattering experiments carried out in this thesis is the Near and InterMediate Range Order Diffractometer (NIMROD), figure 2.9 a. NIMROD is an instrument located in the second target station at the ISIS facility, optimised for the study of disordered materials, liquid and nanostructured materials [123]. It bridges the gap between small angle and wide angle scattering, using a common calibration procedure for the whole length scale.

The instrument has 25 banks of detectors, from $\theta = 0.5°$ to $\theta = 40°$, and is able to measure the scattering from $Q_{\text{max}} = 50\,\text{Å}^{-1}$ to $Q_{\text{min}} = 0.01\,\text{Å}^{-1}$, which corresponds, respectively, to a length scale in real space that ranges from $< 1\,\text{Å}$ to $> 300\,\text{Å}$. These requirements are met owing to the characteristics of ISIS second target station, where the neutrons pulses are separated by 100 ms time intervals, allowing to exploit neutrons over a broad spectral range (wavelengths from 0.05 Å to $> 12\,\text{Å}$).

The use of a water moderator coupled with a methane/liquid hydrogen moderator is what allows the production of two distinct fluxs of neutrons, that are delivered to the sample and the detectors with each pulse. The time-of-flight neutron spectrum is shown in figure 2.9 b: the first peak at approximately 4900 µs corresponds to neutrons with wavelength 1.3 Å delivered from the water premoderator, while the second at 10 800 µs corresponds to neutrons with wavelength 2.9 Å delivered from the hydrogen moderator.

This instrument has played a particular role in this research as its characteristics make it particularly suitable for study of total scattering from nanomaterials.

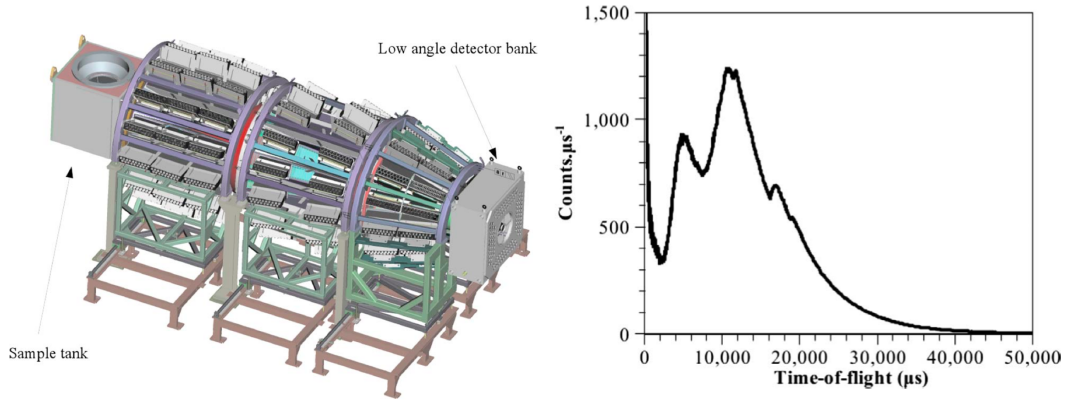

(a) **(b)**

Figure 2.9: (a) Overview of the distribution of the full complement of detector modules that can be mounted on NIMROD, covering angles that range from $0.5°$ to $40°$ [123]. (b) Time-of-flight neutron spectrum measured on NIMROD using an incident beam monitor placed 15.26 m from the moderator face. [123].

2.2.2.2 Ag-anode X-ray source

X-rays can be produced into two main ways: with lab-based x-ray tubes or with synchrotron sources. In order to measure total scattering, in the context of lab-based sources, Ag anode sources are preferred, as the mean $K\alpha$ radiation produced has a wavelength of 0.5609 Å, which allow to reach higher maximum Q values [121]. It should also be noted that, although in total scattering experiments one tries to maximise the value of $Q_{\max}$, the falls off of the scattering factors at high-Q makes the use of very high Q values unnecessary.

Figure 2.10: The PANalytical Empyrean Ag-anode X-ray diffractometer, located in Queen Mary. The wavelength of the X-ray is $\lambda = 0.5609\,\text{Å}$, the diffraction angle $2\theta = 156°$, which corresponds to $Q_{\max} = 21.9\,\text{Å}^{-1}$.

The diffractometer used along the course of this research project is a PANalytical Empyrean Ag-anode X-ray diffractometer, located in Queen Mary 2.10. It reaches a maximum scattering angle of 156°, which corresponds to $Q_{\max} = 21.9\,\text{Å}^{-1}$. The $K\alpha$ wavelength of Mo-anode x-ray source is also in the order of interatomic distance (0.709 Å) . However, for the same maximum angle, this wavelength corresponds to $Q_{\max} = 17.3\,\text{Å}^{-1}$, which would not be enough to resolve details in the short-range order. Lab based sources present in general some drawbacks, i.e. the fact that the X-rays production is not very efficient as large part of the energy of the electrons is lost as heat; also the energy of the x-ray is fixed by the target material used. On the other hand, synchrotron sources, such as Diamond, have represented a huge stepforward [90] in the study of materials.

2.2.2.3 Wavelengths and resolution

The main factors that determine the choice of the instrument to be used in total scattering experiments are the resolution in real space and the resolution in reciprocal space [92]. The first is determined by the highest possible value of $Q_{\max} = 4\pi/\lambda$ (as a consequence of equation 2.7, assuming $2\theta = 180°$) and is improved by choosing instruments that are capable of delivering short-wavelength neutrons or X-rays. This factor is very important, because the ability of recording information about the local structure is dependent upon this. Figure 2.11 a shows the effects of the use of two different values of $Q_{\max}$ on the room temperature data of the Prussian blue solid nanoparticles sample (chapter 4). The use of a $Q_{\max} = 17\,\text{Å}^{-1}$ causes the loss of the features at 0.96 Å and 1.2 Å, that become merged in one peak at 1.08 Å. Similarly several other features in the range $2 < r < 6$ Å are lost. Incidentally, as will be discussed in chapter 4, the ability to distinguish the two peaks at 0.96 Å and 1.2 Å is of crucial importance for the analysis. Figure 2.11 b (insets b and c) shows another example from the literature [92] where the use of

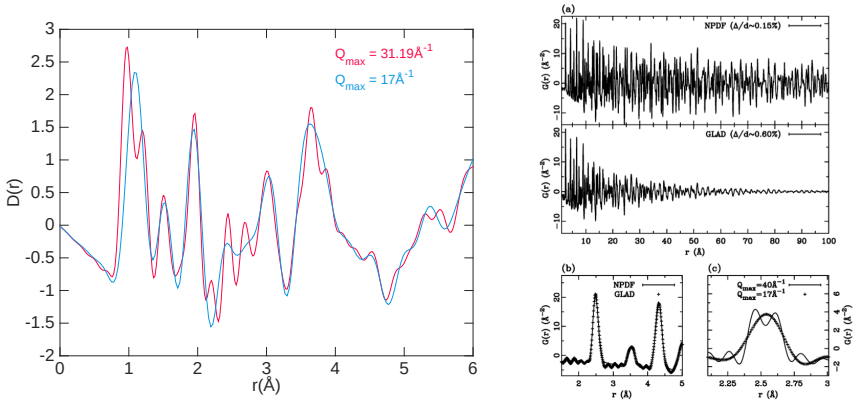

Figure 2.11: The $D(r)$ in figure (a) is the room temperature PDF of my solid nanoparticle sample (chapter 4). The use of different $Q_{\max}$ has drastic effects on the PDF resolution. (b) Data collected on nickel powder. Inset a shows the comparison of two PDFs, calculated from total scattering data collected on different instruments with the same $Q_{\max}$ but different reciprocal space resolution, causing a damping effect on the high r section of real space data. The top PDF was calculated from data collected on NPDF and the one below on a lower resolution instrument, GLAD, at the Lujan Neutron Scattering Center). Inset and c shows an effect of the finite cut-off of Q on the near-neighbour region [92], analogously to what observed in figure (a). The lower $Q_{\max}$ leads to the disappearance in the GLAD instrument data of the peak splitting at $2.5\,\text{Å}$.

instruments with different $Q_{\max}$ affects the ability to detect variations in the local range order of the PDF. The feature at 2.5 Å (inset b) appears as one unique peak in the data collected on the GLAD diffractometer ($Q_{\max} = 17\,\text{Å}$) and is split into two peaks in those collected on the NPDF diffractometer ($Q_{\max} = 40\,\text{Å}$).

The cutoff at finite Q has also the inevitable consequence of causing the appearance of the so-called termination ripples, whose effect is that of masking local features of the structure. The termination ripples can be reduced during the correction of the data, by applying a smoothening function and other empirical solutions. These will be discussed in section 2.3.3.

The second factor is the Q resolution, that is ΔQ, which has the effect of dampening the PDF at high r. This is important when we are interested in collecting information about long-range order as well as short-range order. Figure 2.11 a shows the effect that the lowering of reciprocal space resolution has on the real-space PDF.

Finally the ability of measuring large correlation lengths (encompassed in the small angle scattering signal) is determined by the $Q_{\min}$ value. In our case e.g. the data collected on the instrument NIMROD contain a portion of the small angle scattering which can be used as a source of complementary information in studies of nanomaterials [123].

2.3 Scattering theory

Following the formalism in [90, 120, 124], the structure factor $F(\mathbf{Q})$ is given by:

$$F(\mathbf{Q}) = \sum_i f_i \exp\left[i\mathbf{Q}\cdot\mathbf{r}_i\right] \tag{2.10}$$

and represents the scattering from a monoatomic sample, where f_i is the scattering length (b for neutrons) or form factor ($f(Q)$ for X-rays), $Q = |\mathbf{Q}| = 4\pi\sin\theta/\lambda$ for elastic scattering, 2θ is the scattering angle and λ is the wavelength of the radiation used. The function $F(\mathbf{Q})$ is the Fourier transform of the number density of the sample, weighted by the scattering length, i.e. $\sum_i f_i\delta(\mathbf{r}-\mathbf{R_i})$, where an atom i at distance R_i from the origin is approximated by a Dirac delta function.

Scattering experiments measures the scattered intensity per unit atom, $S(\mathbf{Q})$, which is related to $F(\mathbf{Q})$ by:

$$S(\mathbf{Q}) = \frac{1}{N}|F(\mathbf{Q})|^2 = \sum_{i,j} f_i f_j \exp\left[i\mathbf{Q}\cdot\mathbf{r}_{ij}\right] \tag{2.11}$$

This is valid for a multicomponent system and was anticipated in equation 2.2 and comprises a Bragg and a Diffuse scattering component.

In total scattering studies the reverse Fourier transforms of both $S_{\text{Bragg}}(\mathbf{Q})$ (equation 2.4) and $S_{\text{Diffuse}}(\mathbf{Q})$ (equation 2.5) are calculated. While the transformation of the first has been a standard and well established process, these are relatively early days for total scattering. For an isotropic sample, such as a glass, a liquid or a polycrystalline material, there is not a preferential orientation, so we have to perform an average over all the possible orientations. Hence, an expression in terms of Q rather than $\mathbf{Q}$ is obtained:

$$S(Q) = \frac{1}{N}\sum_{i,j} f_i f_j \left\langle \exp\left[i\mathbf{Q}\cdot(\mathbf{r}_i-\mathbf{r}_j)\right]\right\rangle_\Omega = \frac{1}{N}\sum_{i,j} f_i f_j \frac{\sin(Qr_{ij})}{Qr_{ij}} \tag{2.12}$$

with $r_{ij} = |\mathbf{r}_i - \mathbf{r}_j|$ and Ω the solid angle . The fact that the scattering function is reduced to a function of Q, shows that it depends on the distribution of distances between atoms, where the directional informationis lost since they are not expressed as vectors but as distances.

As the scattering law involves a sum over atom pairs, it is convenient to introduce the function $g_{m,n}(r)$ which represents the distribution of atoms of type n with respect to an atom m at the origin, as a function of distance. If an atom of type m is the reference atom, the number of atoms of type n lying within a spherical shell with a thickness dr and inner radius r centred on the atom m is given by: $\mathrm{d}\mathcal{N}_{m,n}(r) = 4\pi\rho_n g_{m,n}(r) r^2 \mathrm{d}r$ with $\rho_n = \mathcal{N}_n/V$, where ρ_n is the average density of atoms of type n (with $\mathcal{N}_n$ number of atoms of type n in volume V). The function $g_{m,n}(r)$ is expected to be equal to 0 for values of r that fall below the smallest interatomic distance and to go to 1 in the limit $r \to \infty$, as the atoms of type m and n have no

correlations at large distances.

In particular, considering a bond with a spread of distances $R \pm \delta R$, the coordination number will be given by:

$$\mathcal{N}_{m,n} = 4\pi\rho c_n \int_{R-\delta R}^{R+\delta R} g_{m,n}(r) r^2 \mathrm{d}r \tag{2.13}$$

where c_n is the fraction of atoms of type n and can also be expressed as $c_n = \rho_n/\rho$. Now, the scattering function can be separated into two terms, one arising from the self-scattering and the other due to interaction between different atoms

$$S(Q) = i(Q) + \frac{1}{N}\sum_i {f_i}^2 = i(Q) + \sum_m c_m {f_m}^2 \tag{2.14}$$

where N is the overall number of atoms. Using the formalism of the pair distribution function $i(Q)$ can be written as

$$i(Q) = 4\pi\rho \sum_{m,n} c_m c_n f_m f_n \int_0^\infty r^2 g_{m,n}(r) \frac{\sin(Qr)}{Qr} \mathrm{d}r \tag{2.15}$$

which is the total scattering structure factor. Since the function $g_{m,n}(r) \to 1$ as $r \to \infty$, $i(Q)$ diverges at $Q = 0$. The function can be separated into two parts

$$i(Q) = 4\pi\rho \sum_{m,n} c_m c_n f_m f_n \int_0^\infty r^2 [g_{m,n}(r) - 1] \frac{\sin(Qr)}{Qr} \mathrm{d}r \tag{2.16}$$

$$+ 4\pi\rho \sum_{m,n} c_m c_n f_m f_n \int_0^\infty r^2 \frac{\sin(Qr)}{Qr} \mathrm{d}r. \tag{2.17}$$

It can be seen that the second term is non zero only when $Q = 0$ which is experimentally inaccessible and therefore can be ignored. Then just the first term remains, which can be written as

$$i(Q) = \int_0^\infty D(r) \frac{\sin(Qr)}{Q} \mathrm{d}r \tag{2.18}$$

where $D(r) = 4\pi\rho r \sum_{m,n} c_m c_n f_m f_n [g_{m,n}(r) - 1]$ is the PDF. This leads to the following transformations:

$$D(r) = \frac{2}{\pi}\int_0^\infty Qi(Q)\sin(Qr)\mathrm{d}Q \tag{2.19}$$

$$Qi(Q) = \int_0^\infty D(r)\sin(Qr)\mathrm{d}r \tag{2.20}$$

The two functions $D(r)$ and $Qi(Q)$ are the Fourier transform of each other. If we consider that $g_{m,n}(r) \to 0$ for value of r smaller than the location of the first peak in the PDF, we observe that $D(r) \to -4\pi\rho r\sum_{m,n} c_m c_n f_m f_n$. Similarly $D(r) \to 0$ for large values of r, as $g_{m,n}(r) \to 1$. Another function that is often used is $G(r)$, related to $D(r)$ by the following equation:

$$G(r) = \frac{D(r)}{4\pi\rho r} \tag{2.21}$$

which represents the weighted linear combination of the individual $g(r)$ functions. It is also common to use the following function

$$T(r) = D(r) + 4\pi\rho r\left(\sum_j c_j f_j\right)^2 \tag{2.22}$$

which will fall to 0 for values of r smaller than the shortest interatomic distance and will tend towards a linear function at large r.

It should be noticed that while in theory the total scattering function and PDF are continuous and can be sine-Fourier transformed by integration, experimental and model data have always discrete values. Thus, what is effectively performed, is the discrete sine-Fourier transform of the data. The integrals in equations 2.19 and 2.20 written in the discrete form are:

$$D(r_k) = \frac{2}{\pi}\frac{1}{L}\sum_{n=0}^{L-1} Q_n i(Q_n)\sin(2\pi kn/L) \tag{2.23}$$

$$Q_n i(Q_n) = \frac{1}{L}\sum_{k=0}^{L-1} D(r_k)\sin(2\pi kn/L). \tag{2.24}$$

where L is the size of r and Q, now considered as vectors of evenly sampled values, with $1 \leq n$ and $k \leq L$. This needs to be taken into account when performing the Fourier transform of the PDF and total scattering function, since ΔQ and Δr (depending on the space in which the Fourier transform is performed) are not explicitly defined. These intervals have to be calculated starting from the size L of r or Q, respectively, as will be discussed in chapter 5 (section 5.4.1).

It is worth noting that the formalism used in the literatures is very varied and will differ from one community to another. The notations here used are the ones mainly preferred in the ISIS and Queen Mary communities [90], which is also called HHS nomenclature, from the names

of the creators [124]. The paper by D. A. Keen [124] gives an exhaustive review of the various notations currently in use.

2.3.1 The total scattering formalism from the point of view of real space

It is convenient at this point to express the formalism of the PDF starting from the function $g(r)$, the radial distribution distribution function [125], in order to point out some of the properties of this function that will be useful in some of the analysis, particularly in chapter 4.

It should be noted firstly that there is a distinction between $g(r)$ and the function $g(\mathbf{r})$, since the first is the orientational average of the second:

$$g(r) = \langle g(\mathbf{r}) \rangle_{\Omega} \tag{2.25}$$

This function, sometimes thought as the probability of two atoms being separated by a distance r, can be better understood if we start from the concept of number density of a material. Given an atom i, whose position is $\mathbf{R}_i$, the number density can be expressed as

$$n(\mathbf{r}) = \sum_i \delta(\mathbf{r} - \mathbf{R_i}) \tag{2.26}$$

In order to extract some useful information about the arrangement of the atoms inside the material with respect to each others, the autocorrelation of the density distribution has to be calculated;

$$G(\mathbf{r}) = \frac{1}{N} \int \mathrm{d}\mathbf{r}' \, n(\mathbf{r}' + \mathbf{r}) = \frac{1}{N} \sum_{ij} \delta(\mathbf{r} + \mathbf{R_j} - \mathbf{R_i}) \tag{2.27}$$

If we separate the self-contribution terms, $i = j$ (i.e. the correlation of an atom with itself), from the terms where $i \neq j$, this can be written as:

$$G(\mathbf{r}) = \delta(\mathbf{r}) + \frac{1}{N} \sum_{i \neq j} \delta(\mathbf{r} + \mathbf{R_j} - \mathbf{R_i}) = \delta(\mathbf{r}) + \rho g(\mathbf{r}) \tag{2.28}$$

from which $g(\mathbf{r})$ is formally defined. Given an atom at position $\mathbf{R}_i$, the autocorrelation tells how many atoms there are at a displacement $\mathbf{r}$ away from the atom i and converts this number to a density. So rather than as a probability, it is more correct to describe this function as a distribution of local density with respect to the average. The autocorrelation is another way of expressing the pair distribution function, as given in equation 2.21. However, while in section 2.3 the focus was on the link between PDF and the the total scattering from a collection of atoms (and hence on the connection between the measured reciprocal space data and the real space data, calculated from those), here this function is described from a different perspective to better understand its meaning in real space.

Since at large r the distribution of particles becomes uniform, no correlations will be observed, resulting in $G(\mathbf{r}) = \rho$ (i. e. $g(\mathbf{r}) = 1$), so we can rewrite the equation as

$$G(\mathbf{r}) = \delta(\mathbf{r}) + \rho(1 + h(\mathbf{r})) \tag{2.29}$$

where $h(\mathbf{r}) = g(\mathbf{r}) - 1$ and $D(r) = 4\pi\rho r h(r)$.

In the case of a system composed of different particles (i.e. several atomic species) it is convenient to split the pair correlation function into several terms, arising from the contribution of individual pairs of atoms; hence, we can define $g_{mn}(\mathbf{r})$ which represents the pair correlation function between atoms of type m and n. It is worth noticing that it does not matter in which order the atoms are listed, since

$$g_{mn}(\mathbf{r}) = g_{nm}(-\mathbf{r}) \tag{2.30}$$

from which

$$g_{mn}(r) = g_{nm}(r) \tag{2.31}$$

From this the full autocorrelation function of the system (equation 2.28) can be expressed, in terms of the contribution from individual pairs of atoms:

$$G(\mathbf{r}) = \sum\nolimits_m c_m \delta(\mathbf{r}) + \rho \sum_{m,n \geqslant m} (2 - \delta_{mn}) c_m c_n g_{mn}(\mathbf{r}) \tag{2.32}$$

From this it can be seen explicitly that each atom pair will contribute two identical terms to the sum, when $m \neq n$, and only one otherwise. In a total scattering experiment, since powder samples composed by grains with random orientations of the crystallographic axis are used, $g_{mn}(\mathbf{r})$ is isotropic and can be replaced by $g_{mn}(r)$ (as defined in 2.25), so that also equation 2.31 applies.

At this point, it is useful to recall the relationship between $g_{mn}(\mathbf{r})$ and the coordination number $\mathcal{N}$ (whose definition was anticipated in section 2.3). Consider for the moment a monoatomic system. Since the radial distribution function holds information about the density distribution in a material, it follows that the total number of atoms at distances between $r_{\min}$ and $r_{\max}$, defined with respect to a given atom located at the origin is given by

$$\mathcal{N}(r_{\min}, r_{\max}) = \rho \int_{r_{\min}}^{r_{\max}} g(\mathbf{r}) d(\mathbf{r}) = 4\pi\rho \int_{r_{\min}}^{r_{\max}} r^2 \, g(r) \, \mathrm{d}r \tag{2.33}$$

and in other words this tells how many atoms at a given distance are coordinated to the atom chosen as origin. The formalism can then be extended to the case of a multicomponent system, where, out of the overall number of coordinated atoms, $\mathcal{N}$, only the atoms of type n coordinated

to an atom of type m at the origin are selected.

$$\mathcal{N}_{mn}(r_{\min}, r_{\max}) = 4\pi\rho_n \int_{r_{\min}}^{r_{\max}} r^2\, g_{mn}(r)\,\mathrm{d}r = 4\pi c_n \rho \int_{r_{\min}}^{r_{\max}} r^2\, g_{mn}(r)\,\mathrm{d}r \tag{2.34}$$

In general $\mathcal{N}_{mn} \neq \mathcal{N}_{nm}$, however from 2.31 and 2.34 it can be seen that the following relationship holds:

$$\mathcal{N}_{nm}(r_{\min}, r_{\max}) = \frac{c_m}{c_n}\mathcal{N}_{mn}(r_{\min}, r_{\max}). \tag{2.35}$$

2.3.2 Data collection

In each neutron and X-ray total scattering experiment three different sets of measurements need to be performed: sample, empty container and empty diffractometer. The neutron experiments require two additional measurements for the empty sample environment and a vanadium standard measurement.

Sample measurement. In a typical experiment the data are not collected in one run, but split into several measurements. In the case of neutron the length of a measurement is defined by the total proton beam charge measured in µA h. At target station 2 in ISIS, where NIMROD is located, 40 µA h corresponds approximately to a measurement time of one hour. Hence, a single scan is typically stopped and saved after the beam charge of 40 µA h is reached. For each sample, between 2 and 8 such scans were performed (corresponding to a total collection time between approximately 2 and 8 hours or 80 µA h and 320 µA h).

In the case of X-rays, it was also decided to split a measurement into several scans, in order to improve the statistics. Specifically, 5 scans, each of approximate duration of 5 hours and spanning the angles from $\theta \approx 1.5°$ and $\theta \approx 74°$, were collected for each sample. The voltage and current used are 45 kV and 40 mA, respectively.

Empty container. As previously mentioned, in a total scattering experiment, the samples are in powder form. The sample measurement is thus performed placing the powder sample inside a container (usually a can, flat or cylindrical, or a capillary). Hence an empty container measurement is required, in order to subtract its contribution to the scattering intensities from the sample measurement data.

A typical neutron sample container is made of a material which is a very weak scatterer, having a relatively small value of the scattering length. A commonly used material for this purpose is vanadium, which has a negligible coherent scattering length of -0.402 fm and a weak incoherent scattering contribution of 6.35 fm. Some more recently developed types of containers are made of an alloy of TiZr, that forms a null matrix with virtually null scattering contribution. The experiments performed in this work made use of 6 mm diameter V cylindrical cans (materials in chapter 3 and 4) and 2 mm thick TiZr flatplate cans (chapter 5).

The Ag-anode machine uses a cylindrical geometry that requires the use of capillaries. In this thesis measurements kapton (polyimide, Cole-Parmer) tubes of 1 mm diameter were used for their versatility and good performances.

Since the scattering arising from the container is weak, the measurement in the case of the neutron data is usually performed for 40 µA h or 80 µA h. In the case of the X-ray data the measurements were collected for the same time as the sample measurements (i.e. 5 scans). This was done in order to collect empty container data with the same statistics as the sample data. Moreover the empty container data for the X-ray machine usually are not collected at each new experiment (as in the case of neutron), but periodically (i.e. once a month), thus a longer measurement does not involve a great loss of sample measurement time.

Empty diffractometer. This measurement is required in order to subtract the empty diffractometer contribution from the scattered intensities of the sample measurement. In the case of neutrons, this measurement is usually performed for 40 µA h.

Empty sample environment. In the case of the neutron measurements, the low temperature data were collected in CCRs. Thus a measurement is required to correct for the attenuation and spurious scattering arising from the contribution of the sample environment. This measurement was performed for 40 µA h or 80 µA h.

Vanadium standard. In order to put the data on an absolute scale, it is necessary to determine the calibration constants. In a neutron experiment this is done measuring the differential cross section using the same beamline conditions as for the sample of a vanadium standard. Depending on the geometry of the sample container used, the vanadium standard can have either cylinder or flat-plate shape (and same size as the container). Vanadium is the material of choice since its very low coherent scattering cross length implies that the differential cross section is dominated by the single atom scattering; moreover the inelasticity effects are small due to the mass of vanadium, and it is a solid metal with known density [125]. The measurement is usually performed for 40 µA h.

2.3.3 Data correction

When neutron and X-ray scattering data are collected they are generally in a crude form, expressed as counts per detector. In fact they are called raw data and in order to be meaningful they need to undergo a treatment by means of specific programs written for this purpose. The are several programs that can be used for data correction and to perform the Fourier transform of the neutron and X-ray total scattering data. However the two probably more widely used are `PDFgetN/X` and `GudrunN/X` [97, 125]. The data presented in this thesis were corrected using the latter.

`Gudrun` was written and is still maintained by Alan Soper at ISIS and it has been mainly

developed for use in correction of data collected on the instruments at ISIS. The differential cross section is extracted from the number of radiation counts, measured in the detector/s, and the total scattering function $Qi(Q)$ is from this calculated. The latter is then Fourier transformed to calculate the PDF $D(r)$. The program makes use of a GUI from which it is possible to set parameters and upload sample and background data. The GUI is divided in tabs that classify the information needed for the treatment of the data in few main sections: instrument, beam, normalisation, sample background, sample and container. At the beginning of the correction procedure, `Gudrun` combines the multiple datasets collected into one spectrum.

X-ray data corrections need to take into account the contributions arising from Bremsstrahlung, Compton scattering, multiple scattering and fluorescence. These functionalities are all available in `GudrunX` [121]. Of these, only multiple scattering is present also in the case of a neutron experiment and its effect is corrected for in `GudrunN`.

The user has to provide input such as container geometry, density and composition, as well as sample composition, density and height. Moreover a parameter called tweak-factor, that is effectively the inverse of the packing fraction, has to be specified. This can be calculated as the ratio of the measured density of the sample inside the container to the theoretical density of the sample. The tweak factor is needed in order to evaluate the number of atoms in the beam, which the data have to be divided by to calculate the differential cross section per atom in the sample [125]. The value of the tweak-factor specified by the user is estimated with an uncertainty depending on how accurate the measure of the volume occupied by the sample is and how close to the real value the theoretical density is. When dealing with neutron data, the value of the tweak-factor can be corrected so that the high-Q limit of the differential scattering cross section matches the expected limit (calculated based on the composition).

In the previous section we mentioned that in a neutron experiment a vanadium standard measurement is used for calculating the calibration constant. For X-rays the procedure is more complicated. There is not a reference standard material that can be used for normalisation, thus the calibration constants are calculated during the data correction process. The calibration constant is determined iteratively at each step during the data correction. In any case, both X-ray and neutron data are put on an absolute scale of cross section, dividing by the calibration constant (calculated or measured, respectively) [125].

As previously mentioned, the truncation of the reciprocal space data at a finite $Q_{\max}$ produces often a series of spurious peaks (or ripples) in the real space data, that can be identified and distinguished from real peaks owing to their oscillatory and regular nature. Hence, it is often necessary to apply corrections aimed at cleaning the real data from such termination ripples. This is usually done through application of a function, the Lorch function, whose effect is that of smoothing the reciprocal space data in the high-Q region.

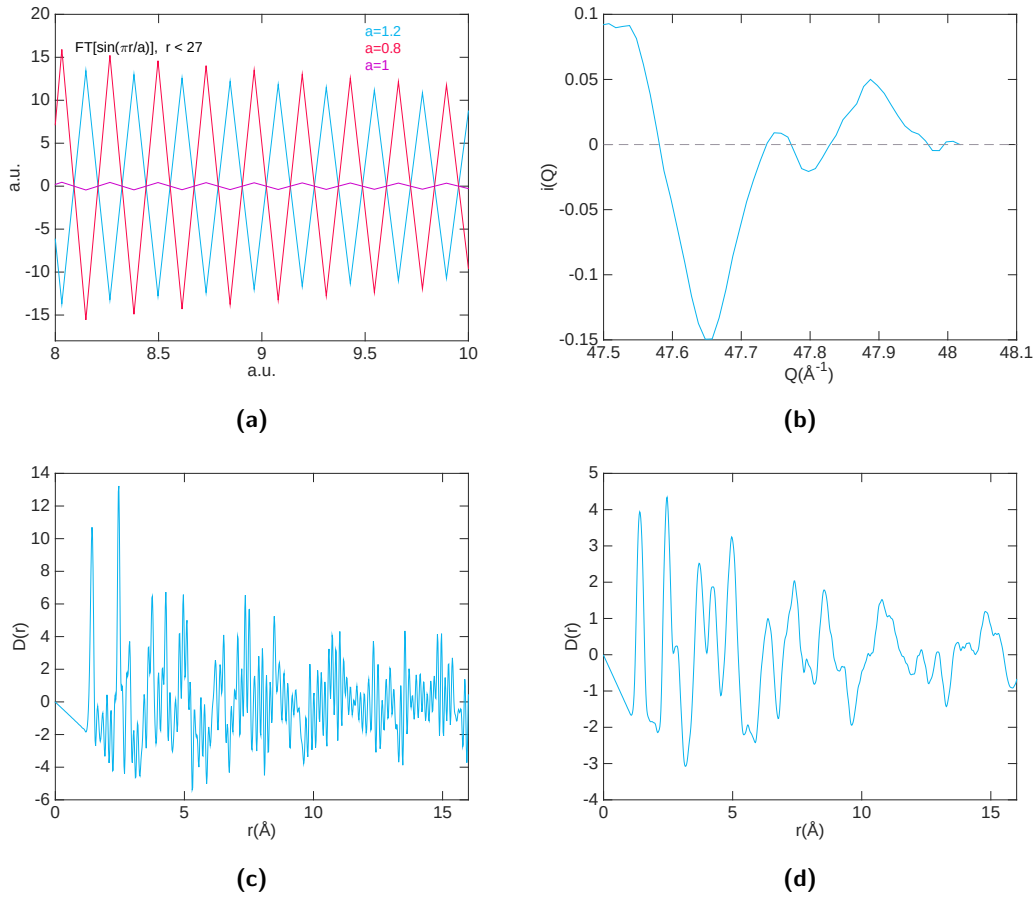

Figure 2.12: (a) Sine Fourier transform of the function $sin(\pi r/a)$ terminated at $r = 27a.u.$, using three different values of a. (b) At the maximum Q chosen as cut-off for this neutron set of data, the $i(Q)$ is very close to zero. The pdf functions $D(r)$, calculated from the total scattering data in (b), (c) before and (d) after application of the Lorch corrections. The parameters used in this case are $\Delta_0 = 0.1$ Å and $\beta = 0.2$.

`Gudrun` uses a revised version of the traditional Lorch function, that has the form

$$L'(Q,\Delta) = \frac{3}{(Q\Delta)^3}(\sin Q\Delta - Q\Delta\cos Q\Delta) \tag{2.36}$$

where $\Delta = \Delta_0(1 + r^\beta)$ and the parameters Δ_0 and β are specified by the user. The linear term Δ_0 is effectively the distance between the maxima of two contiguous termination ripples in the PDF function at $r = 1$ Å and can be approximately determined by observation of the function prior application of the Lorch correction (equivalent to setting the two parameters to zero). The term β can be determined from the first by

$$\beta = \frac{\log(\frac{\Delta(r)}{\Delta_0} - 1)}{\log r} \tag{2.37}$$

where $\Delta(r)$ is the distance between ripples at large r.

The application of the Lorch function comes however with some drawbacks, since one may

run into the risk of suppressing some real (i.e. structural) peaks while trying just to eliminate the spurious ones. There are few practical rules that can help in this situation and that it is always best applying before using the Lorch function (to avoid throwing some precious data out before even realising it).

Firstly the cut-off, $Q_{\max}$, must be chosen so that the value of the $Qi(Q)$ function at that point is as close as possible to zero. To visualise the effect that this has on the Fourier transform, one can consider the example of the Fourier transform of a sine function defined as $sin(\pi r/a)$. If a value of a such that the function approaches zero at the maximum value of r considered is chosen, the termination ripples generated in the Fourier transform are minimised, compared to the case where, at the maximum r, a is such that the function approaches 1 or other values different from zero. This is shown in figure 2.12 a, where for $r < 27$ and $a = 1$ (i.e. $\sin(27\pi) = 0$) the termination ripples are minimised. The other two functions, calculated using $a = 0.0806$ and $a = 1.2$, present significantly more pronounced termination ripples since $\sin(27\pi/0.806) = -1$ and $\sin(27\pi/1.2) = 1$, respectively.

The second approach is that of checking the resulting PDF against a theoretical model to confirm which of the peaks in the experimental function are expected to be there.

An example of the result of the application of the Lorch function to neutron data collected on NIMROD, is given in figure 2.12 c shows the $D(r)$ calculated setting Δ_0 and β to zero (i.e. no smoothening is applied). Care was taken to reduce the termination ripples in the Fourier transform prior to the application of the smoothing function, by selecting only the banks of detectors with low level of noise and by choosing a maximum Q cut-off, such that the total scattering function approaches zero at that point, figure 2.12 b (for the reasons explained above). However, a significant level of noise is still observed in the $D(r)$, figure 2.12 c, thus requiring the use of the Lorch corrections. The truncation ripples can be distinguished from real structural peaks, because the first are equally spaced and present a symmetric shape, creating a regular periodic oscillatory pattern superimposed to the real data. Moreover, usually the distance between the maxima of two neighbouring truncation ripples, in the low-r region is of the order of 0.1 Å or less. It should also be noted that for an instrument that reaches $Q_{\max} = 50\,\text{Å}^{-1}$, the maximum resolution achievable in real space is $\Delta r = 2\pi/Q_{\max} = 0.1257\,\text{Å}$; so, as long as one chooses $\Delta_0 < \Delta r$, no structural features should be suppressed by the application of the Lorch function (criteria hence met by the example just given).

In a neutron experiment, in the case of hydrogenous samples, the user can specify parameters for up to five exponential functions that the software uses to subtract the residual low-Q behaviour, due to the inelastic scattering component, that is not removed by the top hat function. This background function is defined as $B(Q) = \sum_i A_i \exp(-Q/\gamma_i)$, where the sum is over the number of exponentials specified, A_i is the amplitude (positive or negative) and γ_i the decay constant for each exponential. The choice of the exponential parameters to use is not

trivial, but it can be guided through observation of the resulting low-Q limiting value of $i(Q)$, i.e. $\lim_{Q\to 0} i(Q) = \sum_{i=1}^{n} c_i \bar{b}_i^2$ [124].

2.4 Modelling and data refinement

2.4.1 MD simulations

The MD simulations in this thesis work were performed using the program `DL_Poly_4` [126]. A typical MD simulation involves the use of a starting atomic configuration, where atom types and coordinates are specified, that is used as starting point of the simulation. The user has to specify interatomic potentials that describe the interactions of the various types of atoms comprised in the systems. These are differentiated in intramolecular and intermolecular potentials. The most common types of potentials are implemented (such as harmonic, Morse, 12-6 potential, Lennard-Jones etc.); if not implemented the user has the choice to tabulate the desired potential.

The user has also to specify a time step, treated as the interval of time Δt, that separates two consecutive snapshots of the system. The positions and velocities of the atoms at time $t + \Delta t$ are determined from their values at time t, depending on the force field that regulates the interaction between atoms.

The force $\mathbf{f}(t)$ acting on a particle of mass m, with position $\mathbf{r}(t)$ at time t is treated according to basic Newton mechanics as

$$\mathbf{f}(t) = m\frac{\partial^2 \mathbf{r}(t)}{\partial t^2}. \tag{2.38}$$

Performing a Taylor expansion of the coordinates as a function of time, in both forward (time $t + \Delta t$) and backwards (time $t - \Delta t$) direction we can obtain two expressions that relate the positions of the particles at time $t + \Delta t$ to the positions and forces of the two previous snapshots and the velocities to the positions of the previous and subsequent snapshots. The Taylor expansions can be written as:

$$\begin{aligned} \mathbf{r}(t+\Delta t) &= \mathbf{r}(t) + \frac{\partial \mathbf{r}(t)}{\partial t}\Delta t + \frac{1}{2}\frac{\partial^2 \mathbf{r}(t)}{\partial t^2}(\Delta t)^2 + \dots \\ &= \mathbf{r}(t) + \mathbf{v}(t) + \frac{\mathbf{f}(t)}{2m}(\Delta t)^2 + \dots \end{aligned} \tag{2.39}$$

$$\begin{aligned} \mathbf{r}(t-\Delta t) &= \mathbf{r}(t) - \frac{\partial \mathbf{r}(t)}{\partial t}\Delta t + \frac{1}{2}\frac{\partial^2 \mathbf{r}(t)}{\partial t^2}(\Delta t)^2 + \dots \\ &= \mathbf{r}(t) - \mathbf{v}(t) + \frac{\mathbf{f}(t)}{2m}(\Delta t)^2 + \dots \end{aligned} \tag{2.40}$$

Adding and subtracting the two equations leads to

$$\mathbf{r}(t+\Delta t) = 2\mathbf{r}(t) - \mathbf{r}(t-\Delta t) + \frac{\mathbf{f}(t)}{m}(\Delta t)^2 + O(\Delta t)^4 \tag{2.41}$$

$$\mathbf{v}(t) = \frac{\mathbf{r}(t+\Delta t) - \mathbf{r}(t-\Delta t)}{2\Delta t} + O(\Delta t)^3 \tag{2.42}$$

which is known as the Verlet integration algorithm. It can be observed that the accuracy on the calculated velocity is an order lower than that of the position. Moreover the velocity is always Δt behind the calculated position. This problem can be overcome, writing the velocity at time $t + \Delta t/2$ as a Taylor expansion again giving

$$\mathbf{v}(t + \Delta t/2) = \mathbf{v}(t) + \frac{1}{2}\frac{\partial^2 \mathbf{r}(t)}{\partial t^2}(\Delta t) \tag{2.43}$$

that combined with equation 2.39 gives

$$\mathbf{r}(t + \Delta t) = \mathbf{r}(t) + \mathbf{v}(t + \Delta t/2)\Delta t. \tag{2.44}$$

Thus at time $t + \Delta t$ the velocity is given by:

$$\mathbf{v}(t + \Delta t) = \mathbf{v}(t + \Delta t/2) + \frac{1}{2}\frac{\partial^2 \mathbf{r}(t + \Delta t)}{\partial t^2}(\Delta t) \tag{2.45}$$

which is effectively an expansion around time $t + \Delta t$ in steps of $-\Delta t/2$. Substituting equations 2.43 and 2.38 gives

$$\begin{aligned} \mathbf{v}(t + \Delta t) &= \mathbf{v}(t) + \frac{1}{2}\left(\frac{\partial^2 \mathbf{r}(t + \Delta t)}{\partial t^2} + \frac{\partial^2 \mathbf{r}(t)}{\partial t^2}\right)\Delta t \\ &= \mathbf{v}(t) + \frac{1}{2}\left(\frac{f(t + \Delta t)}{m} + \frac{f(t)}{m}\right)\Delta t \end{aligned} \tag{2.46}$$

which is the final expression used in `DL_Poly_4` in the calculation of the velocity.

The trajectories are generated in the microcanonical ensemble (NVE) so that the total energy (potential plus kinetic) is conserved. However, if it is desired to keep the system close to a chosen temperature, the equations of motion are modified and the system does not directly sample the canonical ensemble anymore, but trajectories in the canonical (NVT) ensemble, where volume and temperature are kept constant. The NVT is the ensemble used in the MD reported in chapter 3. In particular, among the seven different thermostats available in `DL_Poly_4` the Nosé-Hoover thermostat was used. Compared to the other algorithms implemented, the method introduced by Nosé has more robust statistical mechanics basis since it generates trajectories that are consistent with the canonical ensemble [126].

2.4.2 Big and small box modelling

2.4.2.1 RMCProfile

As the total scattering technique evolved and the computer power increased, programs for the modelling and interpretation of the data started being created. The Reverse Monte Carlo (RMC) method was originally developed in 1988, in the framework of the `RMCA` code [127], to model

the structure of liquids and glasses [128, 129]. Only later the program started being used for analysis of crystalline materials [128, 130].

The refinement procedure is based on the Metropolis Monte Carlo algorithm [96, 129, 131]. Configurations comprising large number of atoms ($\sim 10^3$) are refined against the data and for this reason this approach is also called large box modelling [92].

The RMC method differs from the traditional Monte Carlo method since the simulation is driven by experimental data, rather than parametrised equations [129]. Monte Carlo methods generally produce models of idealised systems, based on interatomic potentials, but they do not require real data and in general the model may not agree with experimental data.

On the other hand, in the RMC method, a model atomic configuration (an initial guess of the atomic structure of the material studied) is refined against both reciprocal total scattering data and real space PDF data. At every step of the simulation an atom is moved at random. At each move the program generates a calculated total scattering structure factor $i_{\mathrm{calc}}(Q)$, a calculated PDF $D_{\mathrm{calc}}(r)$ and Bragg profile $I_{\mathrm{calc}}(t_i)$. The function $i_{\mathrm{calc}}(Q)$ is calculated as the Fourier transform of $D_{\mathrm{calc}}(r)$. The latter, however is computed only in a range limited by the size of the RMC configuration and as a consequence the peaks in $i_{\mathrm{calc}}(Q)$ will be broadened. In order to make the experimental data comparable to the model, they are convolved by a box function with size $L/2$, determined by the smallest dimension L of the configuration, as follows

$$i_{\mathrm{box}}(Q) = \frac{1}{\pi} \int_{-\infty}^{\infty} i_{\mathrm{exp}}(Q') \frac{\sin\, L(Q-Q')/2}{Q-Q'} \mathrm{d}Q' \tag{2.47}$$

It will be then this function and not the original i_{exp} to be used in the refinement of the model [96].

At each move, a goodness-of-fit parameter is calculated for both the calculated total scattering and PDF functions, comparing them to the experimental data, in the following way:

$$\chi^2_{i(Q)} = \sum_i \frac{\left[i_{\mathrm{calc}}(Q_i) - i_{\mathrm{box}}(Q_i)\right]^2}{\sigma^2_{i(Q)}(Q_i)} \tag{2.48}$$

$$\chi^2_{D(r)} = \sum_i \frac{\left[D_{\mathrm{calc}}(r_i) - D_{\mathrm{box}}(r_i)\right]^2}{\sigma^2_{D(r)}(r_i)} \tag{2.49}$$

where the sums is over i experimental points, σ is the standard error on individual data values and the minimum Q_i value used should be larger or equal to $2\pi/L$. Analogously, the goodness-of-fit parameter for the Bragg profile is given by:

$$\chi^2_{\mathrm{Bragg}} = \sum_i \frac{\left[I_{\mathrm{calc}}(t_i) - sI_{\mathrm{exp}}(t_i)\right]^2}{\sigma^2_{\mathrm{Bragg}}(t_i)} \tag{2.50}$$

In this case the parameter is calculated with respect to $I_{\mathrm{exp}}(t_i)$, i.e. the intensity of the experimental Bragg profile for a given neutron time of flight. The contribution from all detector banks are merged using the program `GSAS`. `GSAS` provides also information about the background and peak shapes parameters, that are used in the RMC calculations of the $I_{\mathrm{calc}}(t)$. A scaling factor s is required, since the scale is not as well defined as in the case of the $D(r)$ function and the function is not corrected using the box function to account for the size of the model.

Often the user may want to apply interatomic bond stretching or angle potentials to prevent the program from generating unphysical models. A Morse type potential is implemented in `RMCProfile` for the bond stretching term and is written as:

$$E = D\left[1 - e^{\alpha(r_{ij} - r_0)}\right]^2 \tag{2.51}$$

where D, the bond energy, and r_0, the equilibrium bond length, are specified by the user and α is set to $2.55\,\text{Å}^{-1}$. The bond angle potential is a simple harmonic cosine potential:

$$E = \frac{1}{2}K(\cos\theta - \cos\theta_0)^2 \tag{2.52}$$

where θ is the angle at a given step in the simulation and K and θ_0 are specified by the user.

Hence, an overall goodness-of-fit parameter χ^2_{RMC} is computed at every move. This is given by:

$$\chi^2_{\mathrm{RMC}} = \chi^2_{i(Q)} + \chi^2_{D(r)} + \chi^2_{\mathrm{Bragg}} + \frac{\Delta E}{k_{\mathrm{B}}T} \tag{2.53}$$

where the change in energy ΔE is calculated with respect to the specified interatomic potential and T is the temperature, specified by the user, at which the experimental data were collected.

The χ^2_{RMC} term is then used to determine whether an atom move improves or not the agreement of the model with the data. If the move results in an improvement, i.e. $\Delta\chi^2 < 0$, it is accepted; otherwise, it is accepted with a probability $P = \exp(-\Delta\chi^2/2)$.

Finally, the user can also apply restraints: those used in this thesis work are minimum distances to prevent atoms from getting too close or distance windows to force a pair of atoms not to move above or below a specified range of distances. Other restraints can be applied and can be found in the `RMCProfile` manual [132].

2.4.2.2 PDFgui

In contrast with `RMCProfile`, the `PDFgui` approach is called small box modelling, whereby the refinement is performed based on the structure of a unit cell. For this reason it is sometimes also called real space Rietveld refinement [97, 133, 134].

`PDFgui` provides the capabilities for refining both structural and experimental parameters. Among the first are lattice parameters, anisotropic displacement parameters, occupancies, atomic

positions and two parameters for correlated atomic motion. The experimental parameters include instead broadening and damping factors due to finite Q resolution.

Among the functionalities that `PDFgui` offers are the ability of using a shape function for the refinement of spherical nanoparticles and that of refining data against several phases. A scale factor can be specified for the data set and for each phase included in the fit and refined against the PDF function. While the experimental scaling does not have a specific physical meaning (i.e. it only depends on the way the data have been corrected and Fourier transformed), the phases' scale factors do in principle provide an estimate of the fraction of each phase contributing to the PDF (and hence of the atomic abundances of the phases in the sample).

For details of the algorithms used in `PDFgui` the reader is referred to appendix A of the manual [134]. I present here few salient features.

`PDFgui` convolves the model PDF function by a factor $S(r)$, dependent on $Q_{\max}$, which is the Fourier transform of the step function. This is given by:

$$S(r) = \frac{\sin(Q_{\max} r)}{r} \tag{2.54}$$

The parameters used to estimate the goodness-of-fit are the R_w (weighted R-value)

$$R_w = \sqrt{\frac{\sum_{i=1}^{N} w(r_i)[G_{\text{obs}}(r_i) - G_{\text{calc}}(r_i)]^2}{\sum_{i=1}^{N} w(r_i) G_{\text{obs}}^2(r_i)}} \tag{2.55}$$

where the sum is over the data points N, $G_{\text{obs}}(r_i)$ is the experimental value of $G(r)$ at point r_i and $G_{\text{calc}}(r_i)$ the calculated value at the same point. We recall that in the `PDFgui` the function $G(r)$ is what in this thesis work (and generally in the `RMCProfile` and ISIS community) is defined as $D(r)$ (equation 2.19).

The width of the peaks is modelled accounting for contributions from both thermal and static disorder [133]. The width is given by:

$$\sigma_{ij} = \sigma'_{ij} \sqrt{1 - \frac{\delta_1}{r_{ij}} - \frac{\delta_2}{r_{ij}^2} + Q_{\text{broad}}^2 r_{ij}^2} \tag{2.56}$$

where the index ij refers to the pair of atoms i and j, σ'_{ij} is the peak width without dependence on atomic correlations (i.e. determined by the the anisotropic displacement parameters) and Q_{broad} is the broadening arising as a consequence of the resolution in Q-space of the diffractometer.The two factors δ_1/r_{ij} and δ_2/r_{ij}^2 accounts for correlated atomic motion at low-r. The former is used to describe the low temperature behaviour and the latter for high temperature. It is advisable to refine only one of these two parameters since they are highly correlated.

Chapter 3

Multi-walled carbon nanotubes continuously filled with iron

This chapter concerns a novel class of nanostructures consisting in multiwall carbon nanotubes (MWCNTs) continuously filled with iron. The first section is a review of the main properties of filled CNTs and in particular of iron filled MWCNTs, focussing mainly on their magnetic properties and numerous potential application. The difference between the iron filled MWCNTs analysed in this thesis and those previously reported in the literature stems predominantly from the continuity of the iron core, together with the ability to control its phase composition through a careful optimisation of the synthesis parameters.

The following section contains a description of the samples analysed, outlining the differences between them, particularly in the iron composition and morphology. The synthesis technique used in the production of two of them are subsequently exposed.

The third section is divided into two main parts. The first is focused on the total scattering data and their qualitative differences, the second on the various modelling approaches used. The total scattering data of some of the samples studied will be described, with particular focus on the main differences observed between neutron and X-ray data and the overall qualitative information that can be obtained through careful observation of the corrected data. These include main phases detectable in the samples, size of the iron nanowire, relative contribution to the the X-ray and neutron scattering signal arising from the iron and carbon content. Details of specific considerations and strategies applied in the correction of the data are also presented. Subsequently, the analysis of the structure performed using different modelling techniques are described. Firstly, X-ray Bragg data modelled through Rietveld least-square refinement method are discussed, focusing on their contribution to the analysis as well as limitations. Other techniques such as PDFgui real space refinement are adopted to get more insight about the phase content, as well as average lattice parameters and atomic displacement parameters. Recognising the limitations of the first two approaches MD simulations are used to build models of the

iron core to compare with the X-ray total scattering data, as well as iron filled CNTs models for comparison to both X-ray and neutron data to better understand the role played by the spacial confinement. Particular focus is devoted to deviations from the bulk structure observed depending on the orientation of the crystallographic axis with respect to the nanowire axis.

In the last section, the conclusions of this work are outlined, showing in particular the wealth of understanding that was achieved through the use of X-ray and neutron total scattering combined with theoretical modelling and other prior information from traditional experimental techniques. Further studies that can be performed on these materials, aiming at a complete knowledge of their structure and properties, are proposed.

3.1 Properties, applications and previous studies

Since the discovery of CNT [7] in 1991, numerous studies have focused on the development of new methods for the synthesis of nanotubes filled with a variety of materials, such as metals, alloys, fullerenes, solvents, ionic and non-ionic compounds and biomolecules [135]. Regardless of what the filling is made of, these structures all have the common feature of presenting a nano-dimensional functional core, passivated and isolated from the external environment by the carbon capsule around it. The properties of such core/filling are affected by the spatial confinement and, in some cases, by the strong exchange interaction with the innermost CNT layer. In fact, these nanostructures present the peculiarity of a very large interfacial area, that often results in changes in the structural and surface properties of the encapsulated materials. The applications are vast and include measurement of temperature at the nanoscale, nano-spot welding, storage and delivery of extremely small quantities of materials and others [135].

This thesis focus on MWCNTs filled with iron (sometimes referred to as Fe@MWCNTs). The work carried out by the collaborators Filippo Boi (SCU, China) and Mark Baxendale (QMUL) [49, 136, 137] led to the development of improved synthesis techniques for the production of MWCNTs continuously filled with iron. TEM and SEM analysis have shown that the MWCNTs are filled continuously for length of the order of several microns. To our knowledge, a similar result has not been previously reported in the literature; in other analogous studies the filling is in fact observed to be discontinuous and irregular, presenting large empty regions in the MWCNTs core [138]. Moreover, owing to the accurate control of the synthesis parameters, it was possible to tune the composition of the filling to obtain a core containing mainly one single phase of iron and very small fraction other phases.

Hence, the core can be effectively regarded as a thin nano-magnet of micrometer length, that is chemically passivated by the MWCNTs, ensuring protection against oxidation and mechanical degradation. The composition and phase distribution, length, confinement of the iron filling and alignment of the MWCNTs with respect to each other all contribute to the anomalous magnetic

properties of these nanostructures [139]. The saturation magnetisation [140, 141] and coercivity [1, 49, 138, 139, 142] have values largely beyond those reported previously in the literature.

The magnetic properties of these nanostructures are due to several factors. Firstly, the magnetic shape anisotropy leads to an enhancement of the magnetisation along certain preferential direction, in this case corresponding most likely to the long axis of the wire [143, 144] (in our work this is generally aligned along the orthogonal z-direction). The magnetisation easy axis for bulk (or isotropic) α-Fe (ferromagnetic, space group $Im\bar{3}m$), one of the major components of the core, is along the $\langle 100 \rangle$ crystallographic direction, owing to the intrinsic magneto-crystalline anisotropy properties with characteristic energy gap $\Delta E = E_{100} - E_{111} = -1.4\,\mu\text{eV/atom}$ [144], where E_{hkl} is the total energy of the system when the magnetisation is pointing along hkl. However the direction of the magnetic easy-axis can be affected by the size and shape of the material [49], causing the magnetic easy axis to point along the $\langle 111 \rangle$ or $\langle 110 \rangle$ directions.

Secondly, phenomena due to exchange interaction are expected to occur at junctions between the α-Fe ferromagnetic phase and γ-Fe (antiferromagnetic at $T < 130\,\text{K}$, paramagnetic at $T > 130\,\text{K}$, space group: $Fm\bar{3}m$). The latter of the two phases was detected in smaller fractions compared to the first at bending points or extremities inside the MWCNTs. Ibrar Muhammad (QMUL) has performed syntheses aimed at maximising the fcc Fe content in the core. In his samples, he has observed bcc/fcc Fe junctions through TEM imaging and diffraction and has recorded a shift of the magnetic hysteresis loop that can be probably attributed to the exchange bias between the two phases. This was also observed previously by Prados et al [145].

Finally the diameter of these nanowires is usually between 10 nm and 40 nm, below the critical magnetic single domain diameter of Fe_3C and α-Fe (approximately 60 nm). Previous work [146, 147] has in fact shown that these nanowires present a single magnetic domain arrangement, as also confirmed by the very high value of coercivity.

These properties make Fe@MWCNTs suitable for a large number of applications, such as magnetic hyperthermia cancer therapy [148, 149], thermoelectric materials, magnetic data storage [138, 139], microwave absorption [150], magnetic force microscopy [151], artificial muscles [138] and so on.

An interesting study exploits the magnetic properties of Fe@MWCNTs and their ability to act as scaffolds for drug delivery for application in magnetic fluid hyperthermia cancer therapy (the drug used is a monoclonal antibody, mAb) [149]. The experiments on electromagnetically irradiated cancer cells with addition of the bioconjugate Fe@MWCNTs-NHCO-Ab show that 25% of the cells are killed after the exposure. However, the authors comment that "*the moderate overall killing efficiency suggests that an improvement of the structural properties of the CNTs in terms of both Fe content and homogeneity of Fe distribution in the CNTs is necessary to engineer a full operative theranostic tool*", where theranostic refers to the use of these nanostructures as both therapeutic and diagnostic tool.

This study is only one of many possible examples where the ability to achieve a high rate of the Fe filling and control upon the magnetic and structural properties of this material is pivotal for their successful application, thus showing the importance of the results obtained through the synthesis work developed by Boi et al.

Studies of the morphology and structural properties of these materials are generally performed by means of SEM, TEM imaging and diffraction, magnetometry and Bragg diffraction combined with Rietveld refinement, as in the case of the analysis carried out by Boi et al. [49, 136, 137, 150]. This work is the first attempt to study Fe@MWCNTs by means of total scattering. Indeed, no previous reports of total scattering studies of any filled carbon nanotubes was found. This work fills therefore a gap in the literature of these nanostructures. However, this class of materials is also relatively new and equally new is the application of total scattering to the study of nanomaterials, as mentioned in the previous chapters. Hence, despite the insight that the technique can provide in the understanding of the structure and properties of these materials, there are several factors that make its use not trivial, as discussed in the following sections.

3.2 Samples: Urchin, Flowers and Carpet structures of multiwalled carbon nanotubes continuously filled with iron

The samples studied in this thesis work were all synthesised by means of chemical vapour deposition (CVD). The collaborators Baxendale, Boi and Ibrar Muhammad implemented improved CVD synthesis routes [1, 49, 136, 152] that led to a great control upon the composition, size and continuity of the iron filling and the concentration of impurities (such as oxides and graphitic onions).

The samples can be classified in four main categories, depending on the morphology and estimated composition of the iron core: 1. α-Fe based flower structures (figure 3.1 a and c), 2. α-Fe based urchin with small fractions of γ-Fe and Fe_3C (figure 3.1 b and d), 3. MWCNTs buckypapers filled with Fe_3C (carpet structures) and 4. α-Fe based urchin with γ-Fe junctions. All these structures present a very high filling rate that is observed to be continuous for several micrometers, figure 3.2. Other numerous examples of TEM, SEM and backscattered electron images showing the filling of the MWCNTs, produced following the same synthesis route, can be found in the work of Boi et al. [1, 49, 136, 152].

The α-Fe based flower structures were synthesised following a procedure (see following section) aimed at achieving a Fe filling almost exclusively formed by α-Fe. Depletion of the other phases leads in fact to an increase of the saturation magnetisation owing to the ferromagnetic properties of the α phase [49, 141, 153]

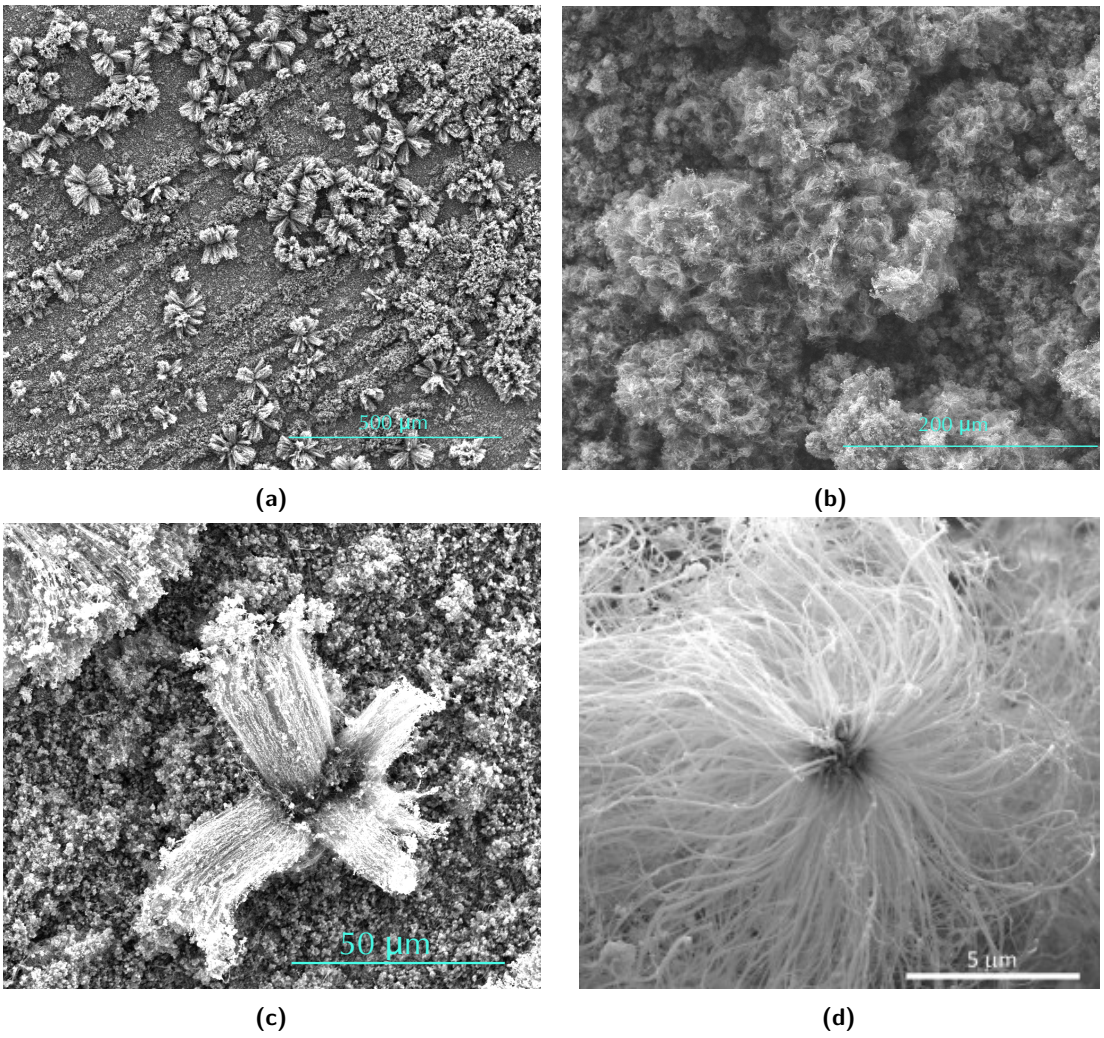

Figure 3.1: Scanning electron micrographs of sample 1. and 2. showing in (a) the very high density growth of flower like structure departing from a Si substrate and in (b) urchin structure formed in the vapour and deposited on a Si substrate. (c) and (d) show a typical single flower-like and urchin structure respectively. Figure (d) was taken from [136].

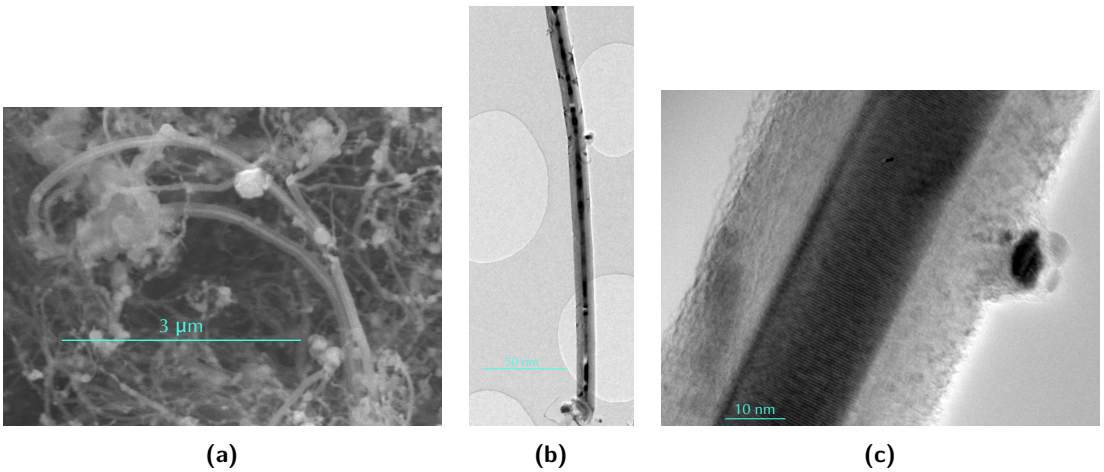

Figure 3.2: Scanning electron micrograph (a) and transmission electron microscopy images (b)-(c) showing the continuity of the iron filling inside the MWCNTs. (b) and (c) were taken by Boi.

3.2.1 Synthesis method

The α-Fe based flower structures (sample 1) and α-Fe based urchin (sample 2) were synthesised with the collaboration of Boi, while the sample 3 was synthesised by Boi with his group and sample 4 by Ibrar.

The synthesis routes of samples 1 and 2 are reported below, while details of the synthesis of sample 3 can be found in the work by Boi et al. [154] and of sample 4 have not yet been published.

Metal catalyses the formation of CNTs [135] so it is possible to tailor the synthesis to fill the CNTs with the same material. Usually the synthesis of CNT filled with metal and alloys is performed by means of high-temperature CVD. The conventional CVD synthesis route for production of Fe@MWCNTs involves the pyrolysis of ferrocene, $Fe(C_5H_5)_2$, in a laminar vapour flow with the nanostructures forming on a supporting substrate in the hot region of the furnace in steady state conditions. This procedure generally leads to discontinuous filling with typical Fe nanowires length of the order of one micrometer or less.

The synthesis of the α-Fe based flower structures involves the use of a novel two stage approach: a perturbed-vapour method followed by a heat treatment at lower temperature. The synthesis was performed in a one-zone electrical furnace. Ferrocene powder, 80 mg, was sublimated and pyrolysed in an Ar flow at 12.5 cm^3 min^{-1} at 180 °C, by means of a coil preheater, inside a quartz tube (length: 2 m, outer diameter: 22 mm, inner diameter: 18 mm) at atmospheric pressure. A 2 cm long quartz substrate was placed in the region of the furnace at 990 °C. The substrate was characterised by either of two geometries, both aimed at creating localised perturbations in the vapour flow. One of the two types of substrates presented a discontinuity created performing a rectangular hole (1 mm depth and width) along the shorter edge of the substrate; the other consisted of two smooth substrates placed symmetrically in front of each other with the convex side leaning on the inner walls of the tube, forming a V-shaped geometry. After the complete pyrolysis of the precursor, 4 minutes were allowed for the synthesis. The sample was subsequently annealed for 13.5 hours by reducing the furnace temperature at 500 °C. Annealing the sample at this temperature allows the γ-Fe and Fe_3C phases to decompose into α-Fe. After the annealing the sample was left to cool down to room temperature at the cooling rate of the furnace and was mechanically removed from the surface.

The mechanism of formation of the flower-like nanostructures, proposed by Boi et al., is based on the homogeneous nucleation of nanoparticles in the vapour [49]. Key synthesis parameters are the quantity of ferrocene and the very low vapour flow rate that contribute to the very high density of concentration of Fe and C atoms, leading, in presence of the substrate geometry induced perturbations, to the homogeneous nucleation of nanoparticles in the vapour (these have larger dimensions compared to typical nanoparticles heterogeneously nucleated on the

substrate). Once a critical mass is reached, the particles deposit on the substrate and the filled MWCNTs start forming departing from these, thus conferring the peculiar morphology. The size of the initial particles and the concentration of Fe and C species are key for the formation of MWCNTs longer than those observed in previous studies (figure 3.1 c) and to the achievement of a continuous Fe filling.

The synthesis of the α-Fe based urchin (sample 2) exploits random fluctuations in the viscous boundary layer between a laminar vapour flow and a surface to produce self-organised nanostructures, comprising MWCNTs continuously filled with iron, departing from a central nucleating particle [1, 136]. Ferrocene powder, 60 mg, was sublimated and pyrolysed in an Ar flow at 12.5 cm^3 min^{-1} at 180 °C by means of a coil preheater, inside a quartz tube (same dimensions as above) at atmospheric pressure. As above the pyrolysed components are transported by the argon flow in the reaction zone of the furnace at 990 °C. A 2 cm quartz subtrate characterised by surface roughness was previously placed in correspondence of the reaction zone inside the quartz tube. The substrate multi-scale roughness with peak-to-valley distance of approximately 100 µm was obtained by roughening a smooth quartz substrate using a conventional diamond cutting tool. After the complete pyrolysis of the precursor, 4.5 minutes were allowed for the synthesis. The sample was then left to cool down to room temperature at the natural rate of the furnace (i.e. no annealing was performed in this case). The sample was mechanically removed from the surface.

The three-stage formation mechanism, proposed by Boi et al., involves: the homogenous nucleation of graphite encapsulated Fe_3C particles in the boundary layer between the rough surface and the global laminar flow, the agglomeration of the nanoparticles in clusters and the growth of filled nanotubes from elongated peripheral particles of the cluster owing to the temperature gradient. The urchin structures deposit on the substrate where the isothermal substrate causes the interruption of the growth (thus fixing the length of the nanotubes). The reaction is self-sustained since the random fluctuations keep occurring once the urchins deposit on the substrate, since their dimension and overall roughness is comparable to that of the quartz substrate. More details about the synthesis procedure and mechanism can be found in [136]. As in the case of the flower-like structure one of the key parameters is the C to Fe ratio in the vapour and its pathway in the reactor as a function of temperature. The urchin structures present a slightly higher concentration of other Fe phases (γ-Fe and Fe_3C), compared to the flower-like structures.

It should be noted that the mass of the sample used in one synthesis is not sufficient for neutron experiments, so that the sample 1 and 2 used in the total scattering measurements were effectively a collection of the yield of 10 such syntheses. Each individual substrate was firstly analysed by means of SEM to confirm the correct geometry and filling had been achieved and subsequently gently removed from the substrates with a spatula and collected in the form of a

powder, ready for the scattering experiments.

3.3 Studies of the local structure

In the study of these nanostructures we use neutron and X-ray total scattering measurements, combined with PDFgui structural refinement and MD simulations.

The PDFgui method is generally not appropriate for describing the structure of such complicated nanosystems, comprising several phases, with structural changes expected at the interfaces between those. However, since the X-ray and neutron data are most sensitive to the iron and carbon content, respectively, PDFgui modelling can be useful for obtaining information such as the Fe phases content of the core and the MWCNTs separately.

MD simulations are instead used for understanding the role played by the spatial confinement and hence properties more distinctly linked to the nanosized dimensions of the systems and the interaction between different phases in interfacial regions.

3.3.1 X-ray and neutron total scattering measurements

The combined use of both probes, neutron and X-rays, proves to be a particularly powerful approach in the study of this class of nanostructures. Using X-rays is equivalent to make use of a magnification lens focused mainly on the iron core, while, using neutrons, the attention is shifted on the carbon nanotubes.

The X-ray total scattering data and the respective PDF functions of the flower and urchin structures are shown in figure 3.3, while the neutron data are shown in figure 3.4. Figure 3.5 shows the first reflections observed in both X-ray and neutron data, labeled with the corresponding phases and indexes, as well as the first few peaks of the PDF functions.

The X-ray data show some relatively strong and sharp reflections in the diffraction pattern. The most intense reflections are due to the bcc phase of iron encapsulated in the core of the MWCNTs. This phase must be encapsulated inside the MWCNTs, since the iron forms oxides when exposed to air, thus losing the bcc ordering. Moreover this is also confirmed by numerous previous studies performed by the collaborators Boi and Ibrar on the same class of materials (produced following the same or an analogous synthesis technique) [1, 49, 136, 137]. These have shown, by means of TEM diffraction localised on single nanotubes, that the core comprises Fe predominantly in the bcc (also called α) phase and more rarely in its fcc (or β) phase or as iron carbide, Fe_3C. In the same studies, Rietveld refinement of Cu-anode X-ray Bragg diffraction also confirms the observation of a strong α-Fe component in the samples. The α-Fe is in fact the most stable at room temperature among the iron phases. What is not common, instead, is finding the γ phase at room temperature, since this is generally observed at high temperatures and pressure. Still, a small percentage of γ Fe is often detected, especially at the tip of the tube

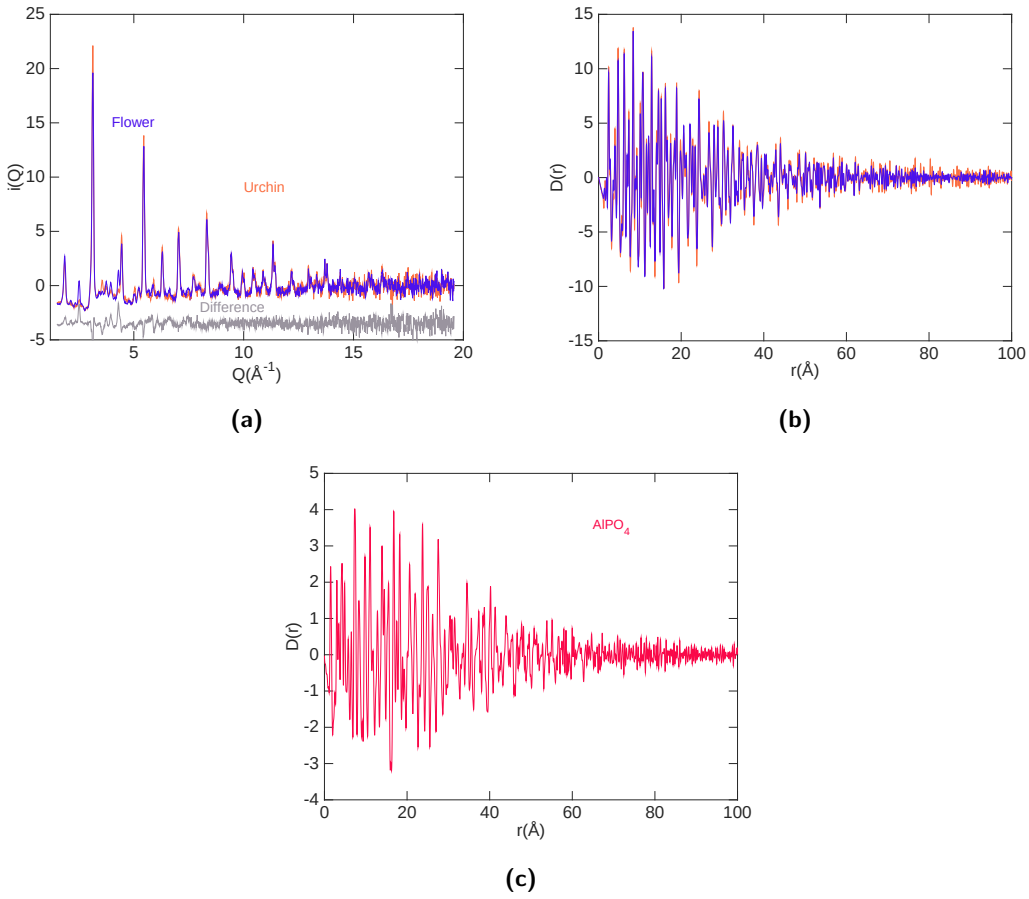

Figure 3.3: (a) X-ray total scattering function of the flower and urchin structure (blue and orange curves, respectively). The Q_{max} used is $19.98\,\text{Å}^{-1}$ and $20.88\,\text{Å}^{-1}$ respectively. The difference between the two set of data is the grey curve. (b) The corresponding PDF functions, showing the lack of long range order beyond approximately 70 Å. (c) The same is observed in the case of the PDF of $AlPO_4$, implying that the effect is a consequence of instrumental resolution.

and in points of constrictions or bending [49, 136]. These regions is where local conditions such as increased pressure and spatial confinement can allow the Fe to retain the γ phase even at room temperature, contrary to what is observed in standard conditions in bulk iron. In any case, the diffraction pattern does not show any strong reflection that could be associated with the γ phase; this is, however, not surprising since this phase is usually observed in segregated regions of the structure, of size of the order of few nanometers and, as a consequence, its signature is expected to be found in the diffuse scattering rather than in sharp crystalline components of the diffraction pattern. The asymmetry of the 011 reflection of α-Fe that is observed in the X-ray total scattering data (figure 3.5 a), could be partly due to a very broad contribution from the 111 reflection of γ-Fe.

The X-ray PDF of both the flower and urchin shows a lack of correlations for interatomic distances beyond approximately 70 Å (figure 3.3 b). This is likely a consequence of the instrumental resolution, as can be inferred through comparison with the PDF calculated from the

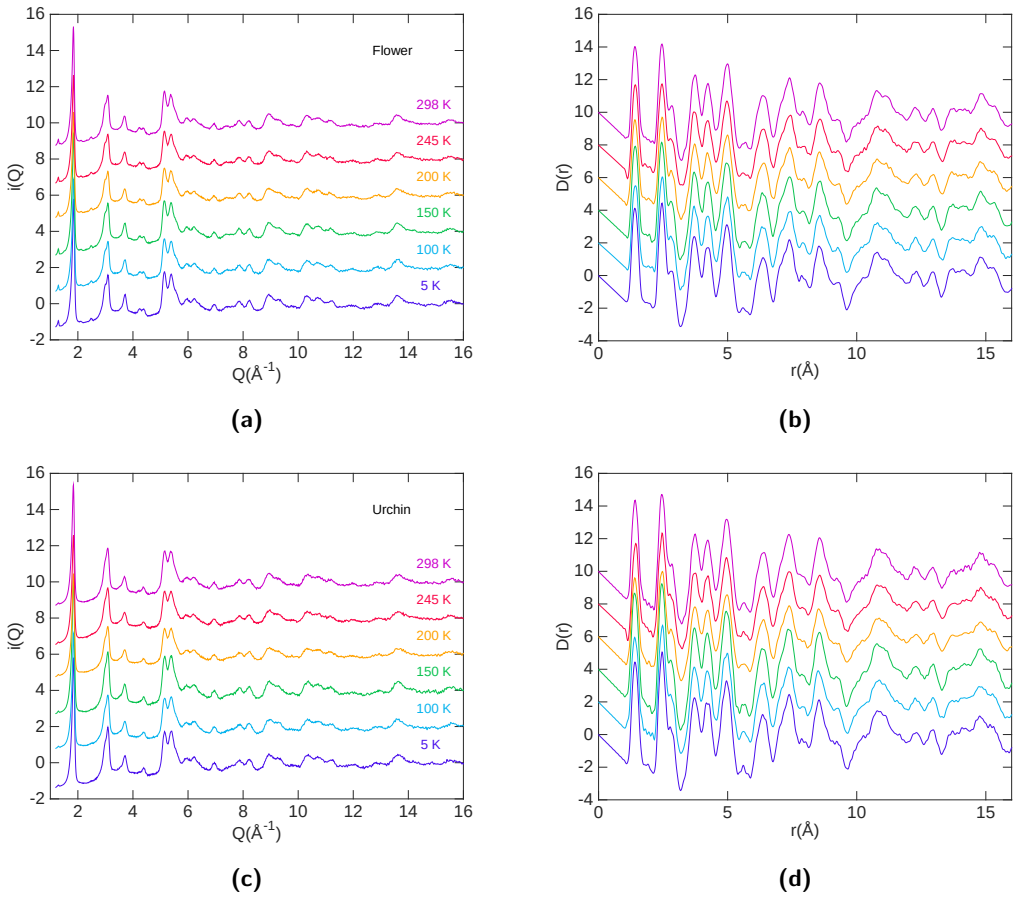

Figure 3.4: The neutron data of the flower, (a) and (b), and urchin, (c) and (d), structures. The different curve refers to the temperature of the measurements as specified by the colours and labels. There are not any visible differences between the various temperatures and the two samples.

total scattering data collected from a crystalline powder sample of $AlPO_4$ (figure 3.3 c) using the same diffractometer. The PDF of $AlPO_4$ shows a dampening of the high-r peaks, analogously to what is observed in the flower and urchin data.

The 002 graphitic reflection shows that a certain regularity is retained in the inter-planar distance between neighbouring concentric CNTs. This reflection is also observed by TEM diffraction of single nanotubes and Cu-anode X-ray diffraction [49, 136]; this confirms that the graphitic ordering is preserved in the MWCNTs. Nevertheless the broad width of the peak implies a high level of disorder, which can arise as a consequence of the tortuosity of the MWCNTS presenting irregularities and constrictions, rather than being straight cylindrical objects with perfectly ordered and homogeneously spaced graphitic planes. Moreover, an interesting study by Leven et al. has reported the influence of the chirality angles of adjacent layers on the appearance of circumferential faceting in MWCNTs, that affects as a consequence the inter-planar spacing between layers [155]. Thus, even when perfectly straight, MWCNTs are not expected to preserve a perfectly graphitic stacking and interlayer spacing, since these are locally affected by chirality

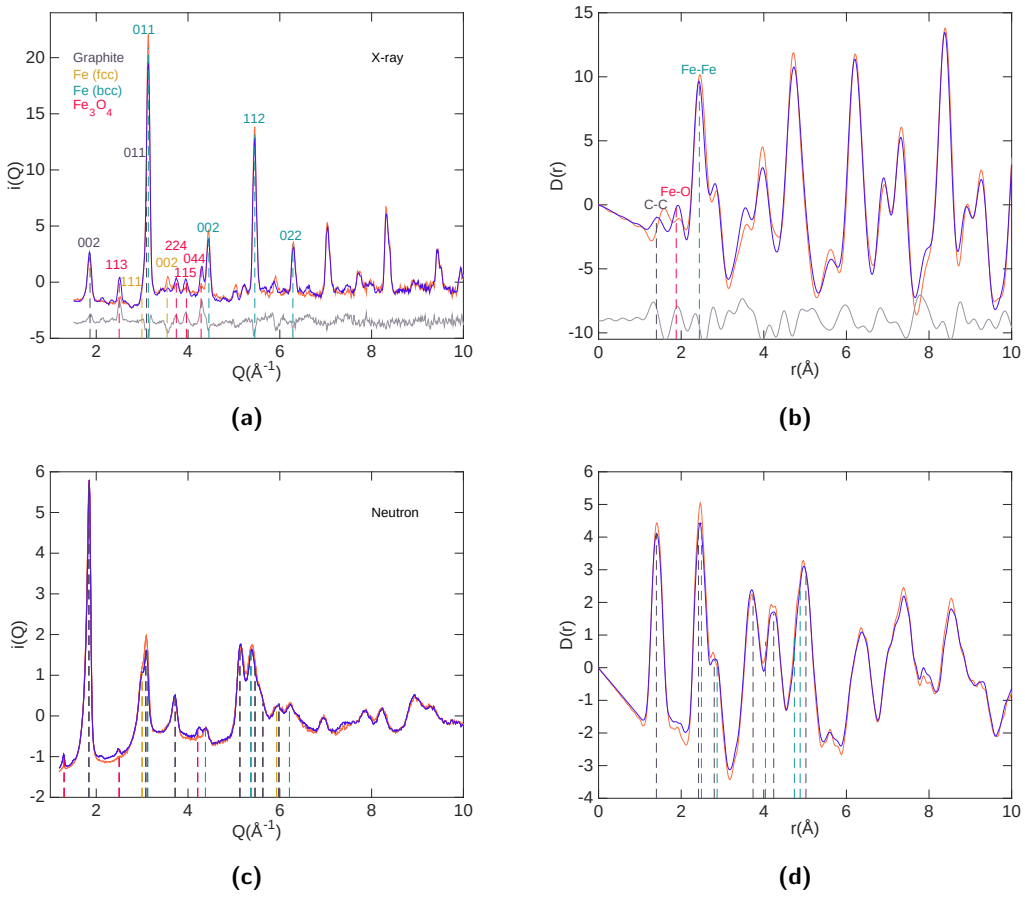

Figure 3.5: X-ray (a and b) and 5 K Neutron data (c and d). As before in blue are the flower data and orange the urchin. The main reflections in the reciprocal space data and interatomic distances in the real space data are marked by dashed lines: in grey those corresponding to graphite, sand to the fcc phase of iron, teal to the bcc phase of iron and red to magnetite, Fe_3O_4. (a) The main differences between the X-ray patterns of the two samples are due to a slightly higher concentration of the iron oxide in the flower samples. The strongest intensities are due to the Fe content. (b) The short range order, showing that not great difference is observed between the two pdf functions. In particular the small peak at around $1.85\,\text{Å}$, sharper in the flower sample, does probably correspond to the first interatomic distance of magnetite (as reflected by the corresponding reflections in Q-space). The other two dashed lines identify the first peaks to be attributed to the first C–C distance and the first Fe–Fe, showing how weak the contribution to the PDF from the C is compared to Fe one.

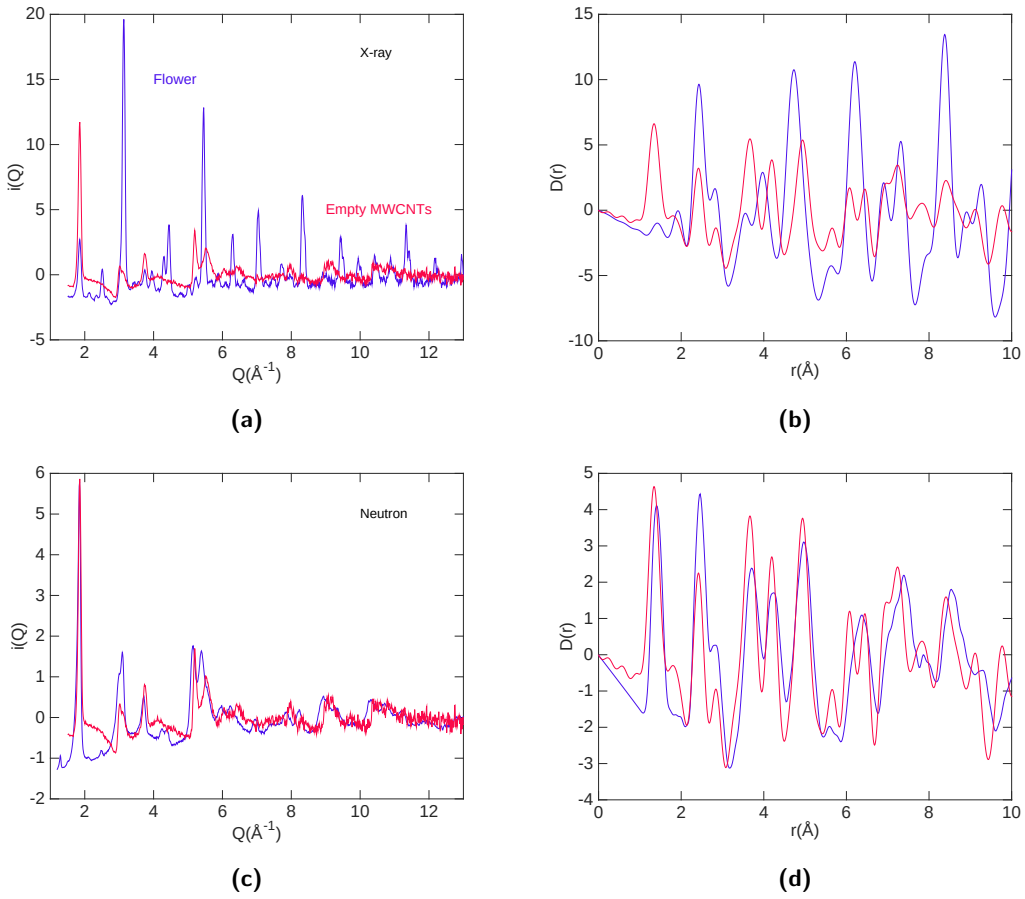

Figure 3.6: (a) Comparison between the X-ray total scattering function of the flower structure and empty MWCNTs. The corresponding PDF functions are shown in (b). (c) Comparison between the neutron total scattering function of the flower structure and the X-ray total scattering function of the empty MWCNTs, normalised with respect to the first peak, the 002 reflection, of the neutron data. The corresponding PDF functions are shown in (d).

and size.

In order to further investigate the MWCNTs contribution, X-ray total scattering data were collected on a sample of empty MWCTNs. The scatterers in this sample are hence only C atoms (assuming negligible impurities), thus providing a reference for the scattering intensities expected from a sample of empty MWCNTs. Figure 3.6 a) and b) shows a comparison between the empty MWCNTs and the flower data. The 002 graphitic peak is the only sharp feature observed in the diffraction pattern of the empty MWCNTs. The peak, even though present in the X-ray flower data (figure 3.6 a), is significantly less intense than the first α-Fe peak, the 011 reflection. This confirms that the iron contributes to the X-ray scattering intensities much more significantly than the MWCNTs; thus also the real space data are dominated by the Fe contribution. This last point is evident in the PDF observing the first C–C peak at approximately 1.4 Å, whose intensity is minimal in the flower data (figure 3.6 b). The other two peaks at approximately 2.4 Å and 2.8 Å, although very similar to those observed in the MWCNTs, are predominantly determined

by the first two nearest neighbours distances of α-Fe. These are in fact by coincidence almost identical in positions, as well as comparable in relative intensities, to the second and third intra-layer graphitic distances. Hence, although a C–C contribution to these two peaks is going to be present, it is expected to be minimal (relative to the iron): its intensity will be comparable to (or even weaker than) the one of the first C–C peak at 1.4 Å. This implies that the MWCNTs can be considered almost negligible, making X-rays the source of choice for analysis of the iron core. This point is analysed in more details in section 3.3.2.2.

Finally, the X-ray PDF of the two samples do not show significant differences. This is probably due to the fact than in both samples the α-Fe phase is the major component of the core. Some small variations in the region below the first Fe-Fe distance are probably due to the slightly higher content of Fe_3O_4 in the flower sample compared to the urchin.

Contrarily to the X-ray data, the neutron data are dominated by the C contribution, as evident from the intensity of the first graphitic reflection 002 in the scattering data and the first C–C nearest neighbour distance in the PDF (figure 3.5 c and d, respectively). It is difficult to identify peaks in the PDF function that can be attributed to phases other than the CNTs or some weak α-Fe contribution (grey and cyan dotted lines, respectively). Some very weak reflections in the total scattering function, present in the flower and absent in the urchin data, can be attributed to the higher Fe_3O_4 content (marked by the red dotted lines), as already observed in the case of the X-ray data (figure 3.5 a). Some of the γ-Fe theoretical reflections are also marked where they could be giving a very minor contribution to the scattering intensities.

To better show and confirm to what extent the neutron data are dominated by the C contribution, these were also compared to the empty MWCNTs X-ray data. The two sets of data are not directly comparable since the scattering intensities are obviously proportional to the respective neutron scattering lengths and X-ray scattering factors. However the position and relative intensities of the peaks in each of the two functions are comparable. So, it is sufficient to scale the X-ray data manually, using the first peaks (the 002 reflection in the total scattering data and the C–C first nearest neighbour in the PDF) as reference.

Contrary to the X-ray case (figure 3.6 a and b), the neutron total scattering data (figure 3.6 c) present a remarkable similarity with the empty MWCNTs data. The same observation can be made for the real space data (figure 3.6 d). Since the neutron scattering lengths of carbon and iron are comparable ($b_C = 6.646$ fm and $b_{Fe} = 9.540$ fm, respectively), the stronger intensity of the C peaks compared to the Fe can be only justified based on the relative composition of the sample. In fact, as explained in more detail in section 3.3.1.1, the samples contain C and Fe atoms in a ratio of 10:1 approximately. Based on this concentration, the ratio x between the

neutron scattering intensities arising from C and Fe, respectively, is proportional to:

$$x = \frac{c_{\mathrm{C}}^2 b_{\mathrm{C}}^2 n_{\mathrm{C}}}{c_{\mathrm{Fe}}^2 b_{\mathrm{Fe}}^2 n_{\mathrm{Fe}}} = 18.199 \tag{3.1}$$

where c_{C} and c_{Fe} are the concentrations of Fe and C, respectively, and $n_{\mathrm{C}} = 3$ and $n_{\mathrm{Fe}} = 8$ are the number of nearest neighbours of graphite and α-Fe, respectively.

Based on the predominance of the C signal, it is possible to explain why strong variations in the total scattering and PDF functions are not observed at different temperatures (figure 3.4). While the local structure of the MWCNTs is not expected to undergo any transition with changing temperature, the iron can be affected more significantly. In particular the γ-Fe phase exhibits an antiferromagnetic to paramagnetic phase transition at approximately 125 K; moreover, evidence from other magnetic measurements from collaborators pointed out that another unknown phase transition, related to the previous, may occur in these nanostructures at 230 K, owing to the exchange bias interaction between different iron phases. However as already mentioned the γ-Fe constitutes (if any) only a small percentage of the iron core, thus is very hard to detect changes due to the magnetic scattering (even more because this is Q-dependent).

3.3.1.1 Data corrections

In the case of crystalline or amorphous materials the composition and density (used in the data correction procedure) are usually very close to the values known from the literature, making the correction process relatively straightforward. On the other hand, for nanomaterials, the density and composition are usually not exactly known and it is often best to use some complementary experimental techniques or analysis methods to estimate these quantities.

In the case of the materials analysed in this chapter, the densities of the urchin, flower and empty MWCNTs samples were measured by means of a pycnometer. The values obtained are $(3.62 \pm 0.12)\,\mathrm{g\,cm^{-3}}$, $(3.45 \pm 0.14)\,\mathrm{g\,cm^{-3}}$ and $(2.19 \pm 0.06)\,\mathrm{g\,cm^{-3}}$ respectively. The composition was determined starting from the weight fractions obtained from the Rietveld refinement of X-ray Bragg diffraction data collected using a Xpert-Pro diffractometer with a Cu K_α source ($\lambda = 1.540\,59$ Å); all the main phases that can be found in the samples were included in the fit: α-Fe, graphite, γ-Fe, Fe_3C, Fe_3O_4 and Fe_2O_3. The atomic composition calculated from the weight fractions was found to be approximately 0.1 Fe, 1 C and 0.01 O (normalising the result to 1 C atom).

As a means of comparison and reference, we also estimated the composition of other samples, that are not studied in this thesis but were synthesised by collaborators by means of the same or analogous procedure and using the same precursor. It was found that the calculated atomic concentrations are always in agreement with the values given above within 15%. This gave further confirmation of the reliability of the result.

Moreover, a Fe to C ratio of 1:10 reflects the atomic composition of the precursor, $Fe(C_5H_5)_2$; this implies that, whether the C and Fe atoms pyrolysed in the reaction end up forming the iron filled MWCNTs or contribute to graphitic and oxides impurities, the overall composition of the sample remains consistent with that of its precursor. Part of the C and the Fe could be deposited inside the quartz tube in regions outside the substrate and thus not comprised in the sample.

Moreover the calculated atomic fractions are also in agreement with the result of the `PDFgui` refinement (section 3.3.2.2). The precursor stoichiometry is hence consistent with the values of the concentrations calculated from the results of both the Rietveld and `PDFgui` refinements. The sole use of the Rietveld refinement is not expected to provide in principle reliable information about the phase content (and the atomic composition) of these materials, since the diffraction patterns present a relatively small number of peaks compared to the many phases that one tries to fit to the data. A typical diffraction pattern from these nanostructures contains between 4 and 7 reflections and so are the number of phases that are usually refined in a fit. However the fact that most of the Fe and C atoms are generally found in the form of α-Fe and in graphitic components, is what makes the refinement and the calculated quantities relatively robust (i.e. most diffraction peaks are predominately associated with these two phases). More details about the Rietveld refinement and Bragg diffraction can be found in section 3.3.2.1.

A final point that indirectly confirmed the reliability of this result is given by its consistency with the experimentally determined density and packing fractions, as highlighted through the `Gudrun` correction procedures and outputs. More specifically, using these values returned the correct value for the average squared scattering of the sample (in a `Gudrun` output window this is what is called the merged differential cross section level).

In the case of the neutron data several of the low angles diffraction banks were discarded in the `Gudrun` correction, since they presented a very high level of noise, masking any structural feature. The other correction steps explained in the methodology section 2.3.3 were also applied.

3.3.2 Rietveld refinement and small box modelling

3.3.2.1 Why not only Bragg and Rietveld refinement

X-ray powder diffraction data were collected using a Xpert-Pro diffractometer with a Cu K_α source ($\lambda = 1.540\,59\,\text{Å}$) on the flower and urchin samples. The diffraction patterns, shown in figure 3.7 (a), are very similar (ignoring the difference in absolute intensities, which depend on the settings of the measurement and quantity of scatterers in the beam).

The presence of some sharp peaks in the diffraction pattern indicates that the samples or some of the phase comprised retain a certain degree of crystallinity. The fit of the urchin structure data is shown in 3.7 (b). This has been performed including the major phases that can

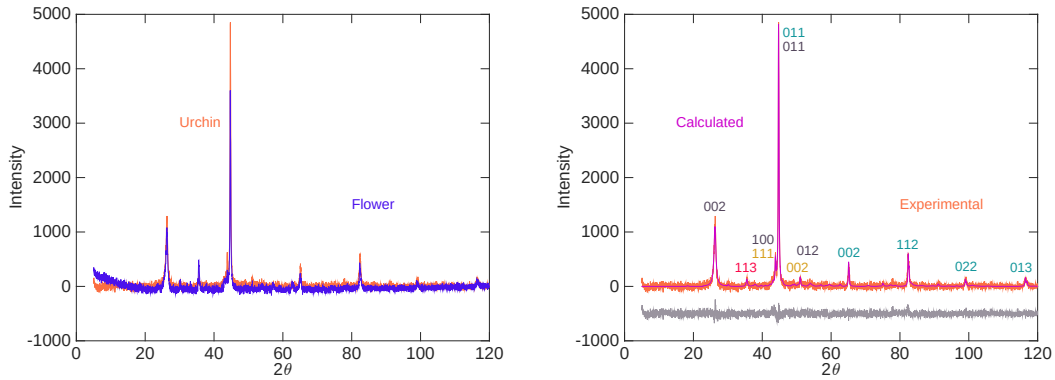

Figure 3.7: (a) X-ray powder diffraction data of the flower and urchin structures. (b) Structural refinement of the urchin data, showing very good agreement between the calculated fit and the data (the grey curve is the difference). The major reflections are labeled, using the same colour scheme as in the previous section (dark grey refers to graphitic reflections, teal to α-Fe, sand to β-Fe, red to Fe_3O_4).

be found in the sample: graphite, α and γ iron, Fe_3O_4, Fe_3C and graphitic onions (presenting a 1.5% expansion of the unit cell along c and 0.5% along a and b, compared to the the perfect graphite structure).

The weight fractions obtained from the refinement of the urchin data: 0.676 ± 0.004 graphite, 0.229 ± 0.002 α-Fe, 0.054 ± 0.006 Fe_3C, 0.024 ± 0.003 Fe_3O_4 and 0.017 ± 0.001 γ-Fe. The other phases included in the fit returned values that can be considered negligible. The respective molar concentrations, calculated from the weight fractions and normalised with respect to the graphite concentration, are: 1.000, 0.073, 0.005, 0.002 and 0.006.

The major reflections corresponding to the peaks visible in the diffraction pattern are labeled in figure 3.7 b. As previously mentioned, there are very few peaks compared to the numerous phases included in the fit (in fact the number of refined phases is higher than the number of sharp peaks visible in the pattern). However, since the graphitic MWCNTs and α-Fe phases constitute the majority of the sample (as previously mentioned) and preserve a crystalline ordering at least locally (as evident from the sharp peaks in the diffraction pattern), the refinement remains stable, leading to reliable results.

Still, the question really is how much beyond an estimate of the composition and of the average lattice parameters can we really tell based on this refinement. The Bragg data are certainly a valuable source of complementary information, but do not provide information about what occurs at the nanoscale level; they rather provide complementary information that can be used to guide further analysis.

As an example, a comparison with figure 3.5 a and 3.3 a, shows the great wealth of information contained in the X-ray total scattering compared to the Bragg diffraction data and it gives further confirmation of the added value gained when using the first in the study of this class of

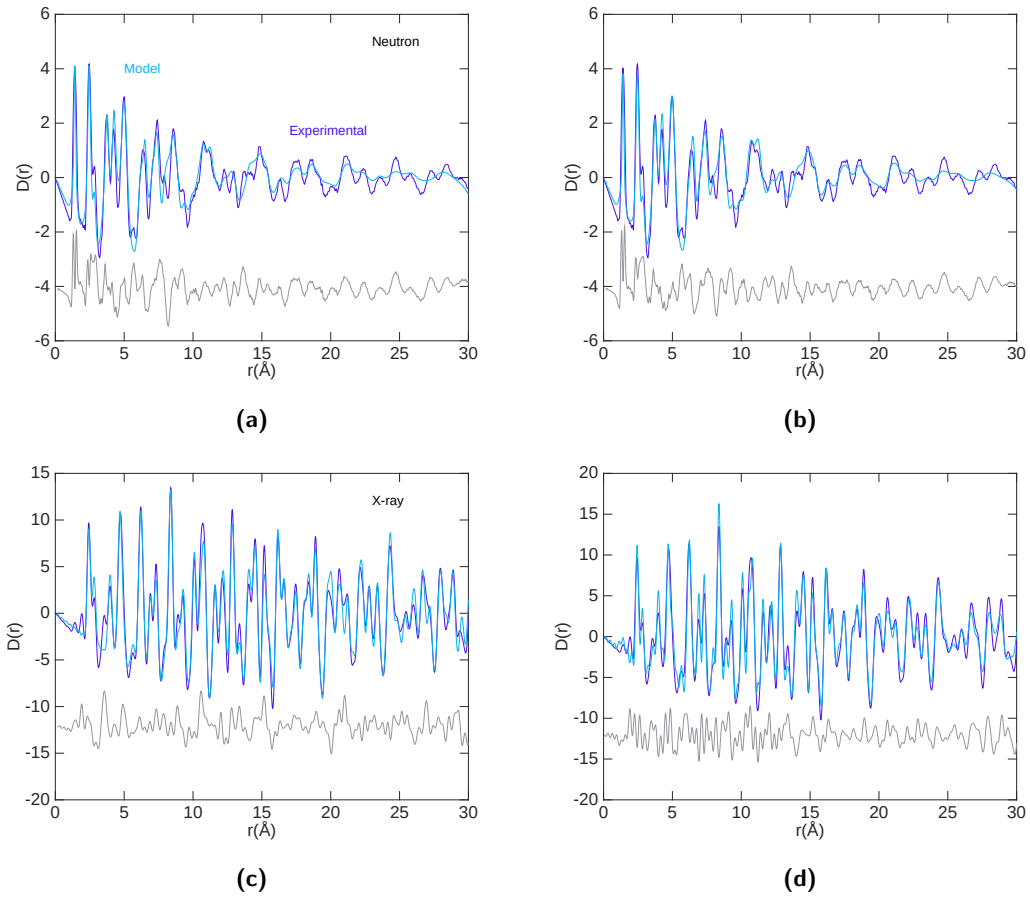

Figure 3.8: (a) (b) PDFgui refinements against the room temperature neutron flower data. In (a) the refinement is against the phase of graphite, in (b) it also includes α-Fe. (c) and (d) PDFgui refinements of the X-ray flower data. The first is with respect to α-Fe only, the second includes also the graphite phase.

materials.

3.3.2.2 PDFgui refinements

The PDFgui refinements confirmed the composition of the core, being constituted predominantly by α-Fe, and the local graphitic ordering of the MWCNTs. The parameters refined in the fit include phase scale factors, resolution dampening and broadening factors, quadratic atomic correlation factors, isotropic displacement parameters and lattice constants. The last two have been applied according to the constraints of the symmetry groups of graphite and α–Fe, $P6_3/mmc$ and $Im\bar{3}m$ respectively.

In the case of the neutron data, the refinement was first performed with respect to the graphite structure and subsequently the α-Fe phase was added to the fit. As an example, the fits to the flower data are shown in figure 3.8 a and b. The addition of the latter did not improve the fit significantly, except for few intermediate range peaks, confirming the predominance of the carbon signal in the neutron data. The minimal contribution that the iron phase gives to

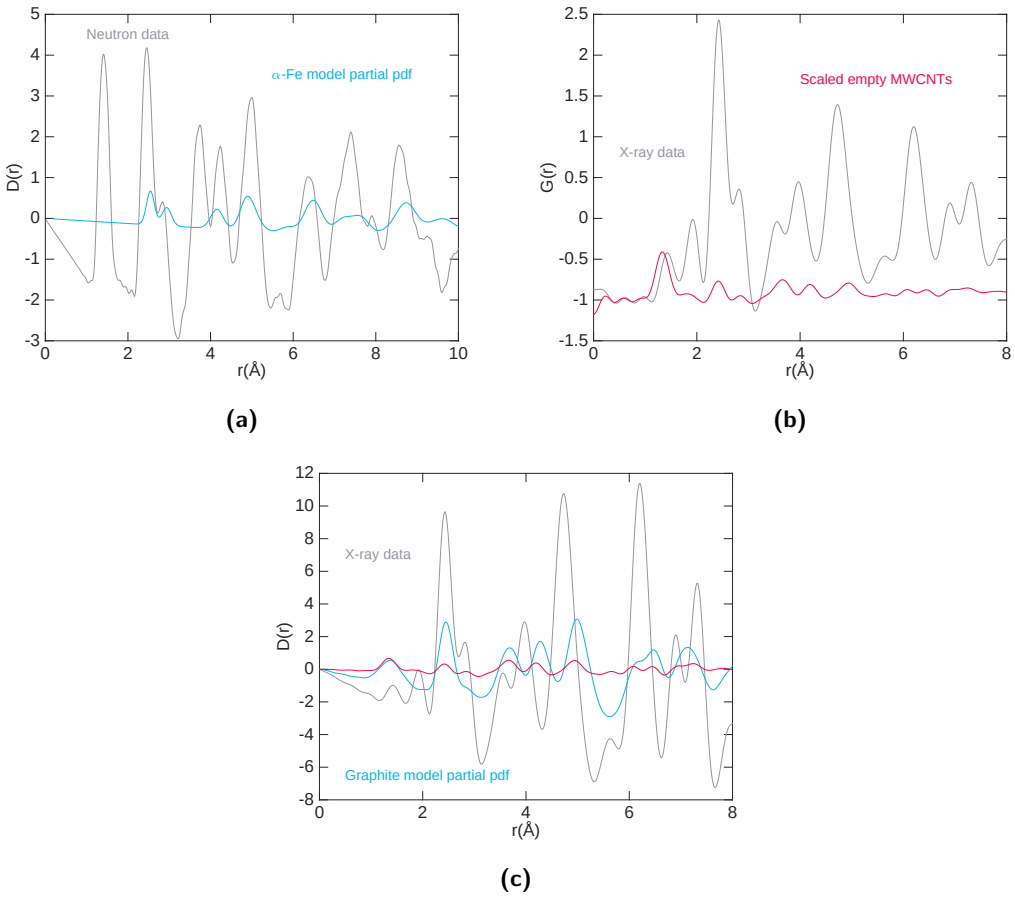

Figure 3.9: (a) α-Iron partial pdf (blue curve) from the PDFgui multiphase fit to the Neutron data (grey curve). (b) Empty MWCNTs $G(r)$ data (red curve) scaled normalising the function with respect to the integral of the first peak of the X-ray experimental data of the flower sample (grey curve). (c) Comparison between the empty MWCNTs $D(r)$ after normalisation, using the same scaling factor as in (b), and the graphite partial pdf (blue curve) from the PDFgui multiphase fit to the X-ray data.

the fit can be appreciated observing the partial PDF of the phase, figure 3.9 a.

This model manages to reproduce most of the short range order of the PDF; beyond approximately 15 Å, however, it does not capture properly the structural features observed in the PDF. We should recall, at this point, that we had already observed that a certain level of disorder is expected to be found in the MWCNTs (section 3.3.1), thus what the PDFgui refinement is telling us is that the graphite ordering is preserved locally in the first few coordination shells, but lost afterwards. It should be also considered that if interfacial Fe–C structural features are to be observed, these cannot be described by a simple model where structure is represented based on a unit cell.

Moving now the attention towards the X-ray data, the refinements were here performed in inverted order, i.e. first with respect to the α-Fe phase and then the graphite phase was added, figure 3.8 a and b (these are again the fit to the flower data). Even in this case, the inclusion of the graphite phase does not result in a substantial difference in the fit, except for few peaks in

the low-r region below 5 Å. The fact that the fit with and without graphite are not particularly dissimilar confirms the sensitivity of the X-ray data to the Fe component, despite its significantly lower concentration compared to the C.

Moreover, the X-ray PDF data of empty MWCNTs can be compared to the partial PDF of the graphite component calculated in the PDFgui fit of the X-ray data. In particular, the empty MWCNTs data are first normalised with respect to the integral of the first peak in the $G(r)$ of the X-ray flower data; the normalised function provides then an experimental estimate of what the contribution of the C component is expected to be in the PDF of the filled MWCNTs. This is shown in figure 3.9 b. As previously anticipated (section 3.3.1), the MWCNTs contribution is found to be minimal. Comparing the normalised $D(r)$ of the empty MWCNTS with the partial PDF of graphite obtained from the PDFgui fit (figure 3.9 c), it is found that, based on the experimental extrapolation, the second may be in fact overestimating the MWCNTs contribution. This point is also confirmed observing that the intensities of the peaks in the multiphase PDFgui fit below 10 Å are higher than the experimental peaks, while they match quite well the data in the fit including only the α-Fe phase (figures 3.8 d and c, respectively).

Hence, a simple model based on the unit cell of α-Fe does provide a relatively accurate representation of the X-ray data, confirming the core to be predominantly composed of this phase. The Bragg and TEM observations show the existence of extensive regions of α-Fe in the core; however the Bragg pattern does not contain enough peaks to infer this with certainty and TEM gives information about single nanowires. Using the PDF data combined with this simple modelling procedure, it can be confirmed that the totality of the heavier element component of the sample is mainly found in this phase.

Table 3.1 reports the calculated expansion percentage of the lattice parameters, from the neutron and X-ray data refinements. Both the neutron and X-ray fits return larger refined values for the lattice constant c of graphite, indicating a slight increase in the distance between graphitic planes (i.e. neighbouring concentric CNTs). Concerning the graphite lattice constant a, an expansion is observed in the case of the neutron data, while according to the X-ray fit the expansion is negative. However, for the graphite component the results from the neutron data refinements are to be considered more accurate, while for α–Fe the X-ray fit results are to be preferred, for the reasons explained above.

The calculated α-Fe to graphite ratios are $1 : 12.7$ and $1 : 6.15$ for the neutron and the X-ray fit respectively. While the first is reasonably close to the estimated Fe:C ratio of $1 : 10$, the second is significantly different. We should however notice that the $1 : 10$ ratio refers to the totality of the sample, that includes also some small percentage of other phases (while in the PDFgui refinement only α-Fe and graphite are included). Secondly, since the graphite structure, as observed, does not reproduce well the medium and long range order, the PDFgui fit result cannot give an accurate estimate of the MWCNTs content (and hence the overall C content).

Table 3.1

Number of phases in fit	Probe	a, α-Fe	$a = b$, graphite	c, graphite
1	Neutron	-	0.244%	3.375%
	X-ray	−1.620%	-	-
2	Neutron	2.672%	0.122%	3.225%
	X-ray	−1.620%	−0.122%	1.583%

Percentage of expansion of the lattice constants for the α-Fe and graphite phases calculated from the Neutron and X-ray PDFgui fit when including one or both phases.

In any case, since the neutron scattering lengths of C and Fe are comparable, the fraction calculated from the neutron data result is expected to be closer to the real value, and in fact it is reasonably close to the original estimate (section 3.3.1.1), especially considering that some of the iron phases are omitted in the fit.

Attempts to include other Fe phases in the fitting procedure were made. However this resulted in strong instability of the fit, with some of the phases' scale factors turning negative without any visible improvement of the fit.

3.3.3 Modelling the iron core with MD and GULP simulations: preferential orientations, critical size and domains

MD simulations were used to investigate the structure of the core locally and to understand the role played by the shape and high surface area of the iron nanowire.

Simulations of α-Fe nanowires of various diameters were performed, using for the Fe–Fe interaction an extended Finnis-Sinclair potential from the literature [156, 157], which accurately describes the interatomic interaction of bcc and fcc metals. This potential is in agrement with the Rose equation curve, derived from data collected through many volume-pressure experiments and generally regarded as the universal equation of state for most metals [158]. The potential can be written as:

$$U_{\text{tot}} = \frac{1}{2}\sum_{ij} V(r_{ij}) + \sum_{i} f(\rho_i) \tag{3.2}$$

where the first term is a pair potential summation and the second, $f(\rho)$, is the n-body term. These can be written as:

$$\begin{aligned} V(r) &= \begin{cases} (r-c)^2(c_0 + c_1 r + c_2 r^2 + c_3 r^3 + c_4 r^4), & r \le c \\ 0, & r > c \end{cases} \\ f(\rho_i) &= \sqrt{\rho_i} = \sqrt{\sum_{j \neq i} A^2 \phi(r_{ij})} \end{aligned} \tag{3.3}$$

where $\phi(r)$ is

$$\phi(r) = \begin{cases} (r-d)^2 + B^2(r-d)^4, & r \leq d \\ 0, & r > d \end{cases} \tag{3.4}$$

The potential parameters are $A = 0.931\,312\,\text{eVÅ}^{-1}$, $d = 4.05\,\text{Å}$, $c = 2.96\,\text{Å}$, $c_0 = 26.270\,34\,\text{eVÅ}^{-2}$, $c_1 = -24.401\,09\,\text{eVÅ}^{-3}$, $c_2 = 6.957\,871\,\text{eVÅ}^{-4}$, $c_3 = -0.303\,077\,\text{eVÅ}^{-5}$, $c_4 = -0.085\,092\,\text{eVÅ}^{-6}$ and $B = 0\,\text{Å}^{-2}$.

The substitution in the pair term of the quartic polynomial used in the original Finnis-Sinclair formalism with a sextic polynomial and the addition of the quartic term to the original quadratic term improve the performance of the potential in describing the repulsive interaction and the electronic density of metals [156]. The second point is particularly useful in the description of fcc metals, since it overcomes the electronic structure difference between the bcc and fcc metals. However, in the reference study the iron parameters are only reported for the bcc phase, since in bulk iron the fcc phase is only found at very high pressure and temperatures; thus the parameter B, i.e. the quartic term factor which accounts for the electronic difference between bcc and fcc, is set to zero.

Since the iron nanowires are not isotropic, another important variable that can have an impact on the local ordering of the atoms is the orientation of the crystallographic axis with respect to the nanowire axis. In order to be able to manipulate size and orientation of these structures easily, two subroutines (incorporated in the `RMCCreate` code) written as part of this project were used: one is used to build nanoparticles of different shapes (in solid or hollow form) and dimensions, the other to rotate the crystal axis by angles chosen by the user (see appendix A.2 and A.1 for the codes).

3.3.3.1 Iron nanowires of finite length

In a first approximation simulations of nanowires of finite length were performed, by making the edges of the box containing the nanowire significantly bigger than the dimensions of the nanowire itself. As long as the length of the nanowire is greater than its diameter (e.g. approximately 4:1 or more) the model is still expected to be a reliable representation of the encapsulated Fe core. Moreover, it can also give an indication of what is expected to happen at the extremities of the nanowires.

The MD simulations show that the local structure is very sensitive to the size and the orientation of the crystallographic axis of the starting configuration with respect to the nanowire. Figure 3.10 shows the $G'(r)$ functions calculated from the final configurations (obtained after an MD simulation in standard conditions) of nanowires of length 200 Å with diameters approximately 20 Å, 30 Å and 50 Å. The vertical axis of the tube (along the length of the tube) is chosen to be parallel to the orthogonal z aixs and the orientations of the crystallographic axis present either

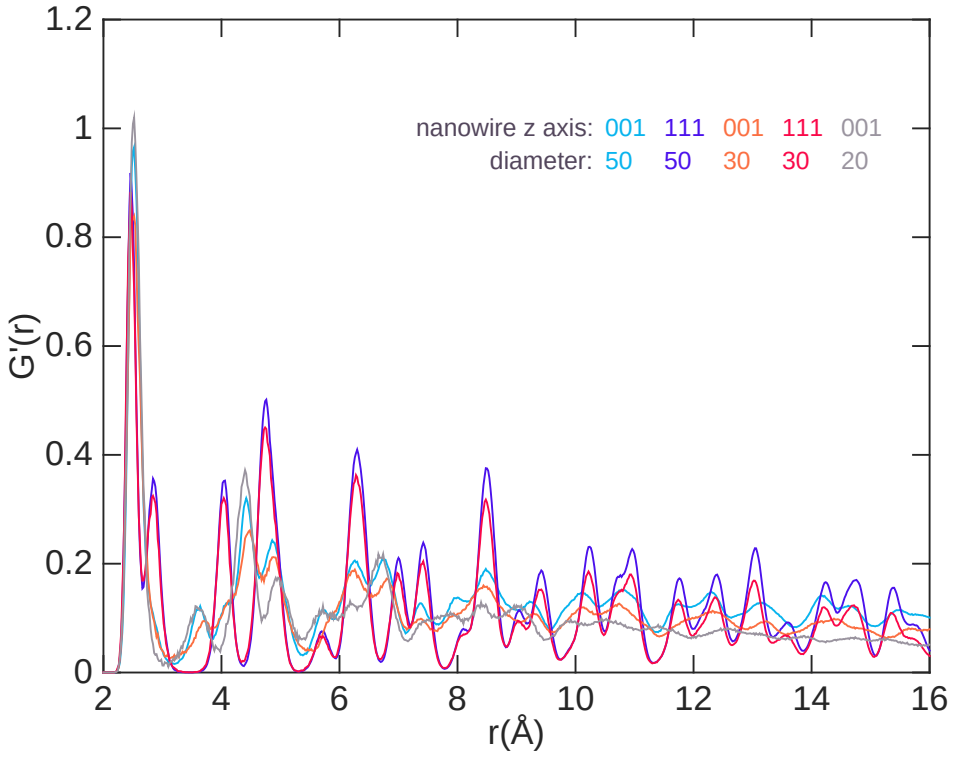

Figure 3.10: $G'(r)$ functions of iron nanowire MD models with various diameter d (20 Å, 30 Å and 50 Å as specified in the legend) and two possible orientations of the crystallographic axis hkl with respect to z ($\langle 100\rangle \parallel z$ or $\langle 111\rangle \parallel z$). The local structure is very sensitive to the orientation of the hkl directions with respect to the nanowire.

the $\langle 100\rangle$ or the $\langle 111\rangle$ direction of α-Fe aligned along the z direction.

The loss of correlations at increasing values of r, as the diameter of the tube gets smaller, is manifested in the faster fall off to zero and loss of features of the $G'(r)$ functions. This effect is purely due to the size and shape of the nanoparticles and could be well reproduced by multiplying the $G'(r)$ of a MD simulation of bulk iron performed using the same control parameters by cylindrical shape functions, using appropriate values for the radius of the cylinder.

A result that goes beyond the mere loss of coordination due to the limited size of the nanoparticles, is the drastic difference in the local structure observed depending on the choice of the orientations of the crystallographic axis previously mentioned. The nanowires with the $\langle 100\rangle$ direction aligned along z in the starting configuration, present a largely different structure: the second, third and fourth nearest neighbour distances of α-Fe have been lost completely or partially and the appearance of new peaks, absent in the other case, is observed (figure 3.10).

One of the reasons of the higher stability of the nanowire with the $\langle 111\rangle$ parallel to the z axis could be found in the distorted hexagonal ordering that is observed on the surface of the cylinder. In a bcc crystal, the distorted hexagonal ordering is effectively given by the set of

planes {110}, with the centre of each hexagon corresponding to the central atom of the bcc unit cell, figure 3.11 a. By aligning the ⟨111⟩ direction along the z axis, we maximise the surface area containing these sets of planes; in particular the (111) plane is perpendicular to the sets of planes $(10\bar{1})$, $(1\bar{1}0)$ and $(\bar{1}10)$; instead, the (100) plane is perpendicular to only two of these sets of planes: the (011) and $(01\bar{1})$. This can be observed in figure 3.11 c and d.

The pseudo-hexagonal configuration is energetically more favourable than cubic ordering, allowing the structure to retain its stability. Moreover, after the MD equilibration a decrease of the distortion of the hexagonal pattern is observed, tending towards an undistorted hexagonal lattice (figure 3.11 a and b).

The origin of the stability of this configuration compared to the other can be found in the minimisation of the surface free energy, that is achieved by the Fe atoms maximising the number of bonds formed between atoms on the surface.

A comparison between the experimental X-ray PDF and these simple models of iron nanowires show that remarkable similarities between the data and the models exist. The PDF of either of the two samples (it was previously shown that the flower and urchin PDF are very similar) shows some partial agreement with the MD models with either of the two orientations. The MD model of the nanowire with 50 Å diameter, figure 3.12 a, can be used as an example. The lack of agreement between the intensity of the peaks of the experimental function and the model beyond the first few coordination shells, is due to the size of the nanowire model, evidently too small compared to the average size of the ordered core of the Fe nanowire in the sample.

In any case, disregarding the intensity, it can be observed that most of the features of the experimental PDF find a corresponding peak in the MD model where the ⟨111⟩ direction is aligned along z, figure 3.12. However, some of the experimental peaks are not consistent with this model (some of which are indicated by the arrows), but find a corresponding peak in the other model, the nanowire with the ⟨100⟩ along the z direction. In fact, by simply adding up the $G'(r)$ of the two models (figure 3.12 b) to form a hypothetical composite model, a result similar to the data is obtained.

This finding would imply that both simulated atomic arrangements of the nanowires may coexist in the material. In this case the intensities of the model and the experimental data beyond 3 Å are comparable, since the two model data have been simply added, multiplied by a factor of 1, thus compensating for the loss of intensities at lower r due to the size of the model nanowire. At the same time, this causes the first peak of the model to have an intensity approximately twice as that of the data.

3.3.3.2 Gulp models and comparison with MD simulation of the iron core

It was observed that, regardless of the size, the MD nanowires with ⟨111⟩ along z retain a more ordered structure compared to the 100 model. The structure of the first is in fact very close

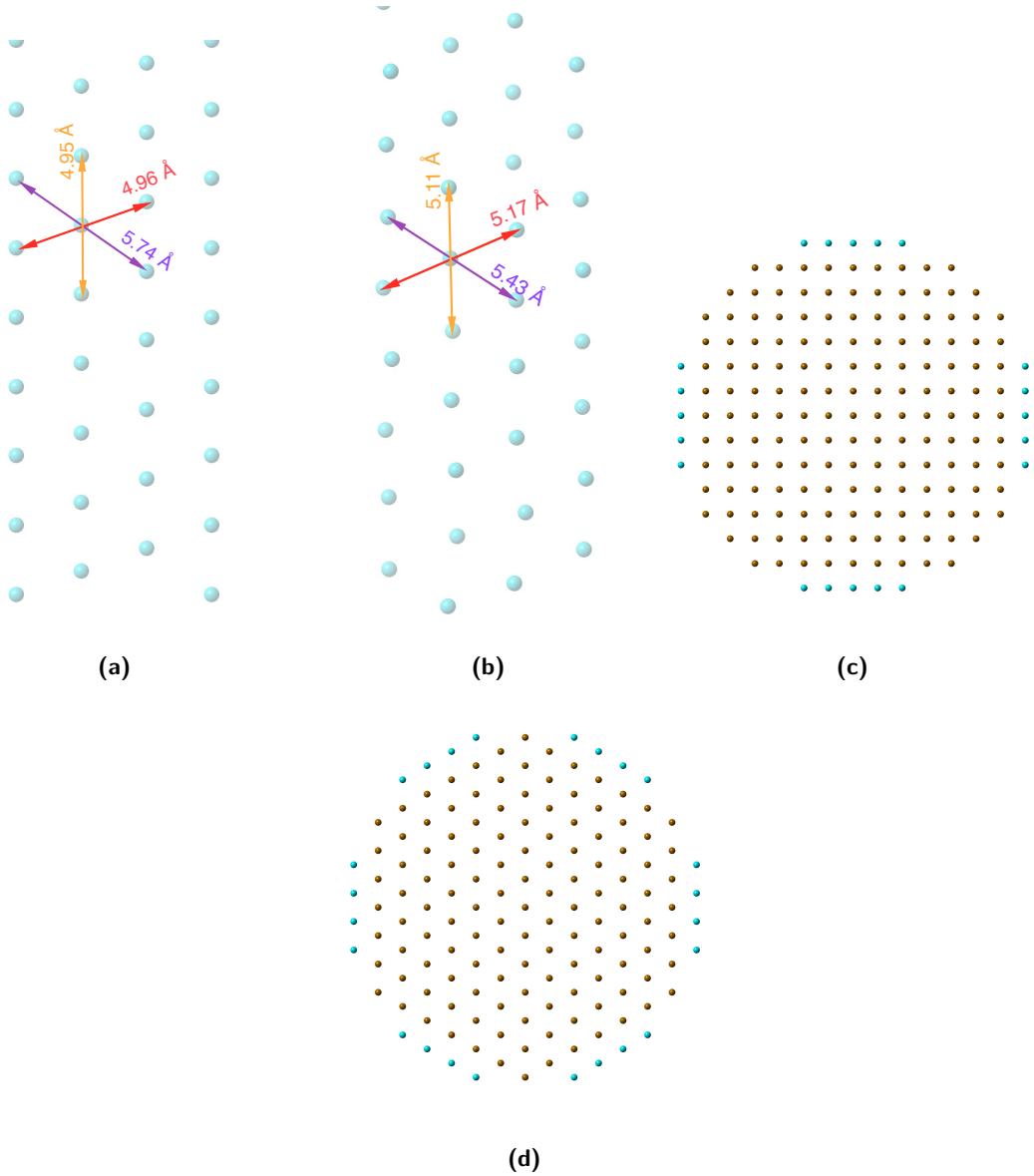

Figure 3.11: A region of the outermost atomic layer of the $30\,\text{Å}$ α-Fe nanowire with $\langle 111 \rangle$ along the z direction, viewed down the x axis, before (a) and after (b) the simulation. The bottom atoms belong to the tip of the nanowire. The hexagonal ordering sees a transition from a slightly distorted to a more regular 2D hexagonal lattice. View down the z axis of the $30\,\text{Å}$ diameter nanowire initial configurations, with $\langle 100 \rangle$ (c) and $\langle 111 \rangle$ (d) along the z direction. The atoms coloured in blue mark the set of planes $\langle 110 \rangle$ or symmetrically equivalent, that present the distorted hexagonal lattice ordering, shown in (a). The surface area presenting this arrangement is maximised in the second case, figure (d).

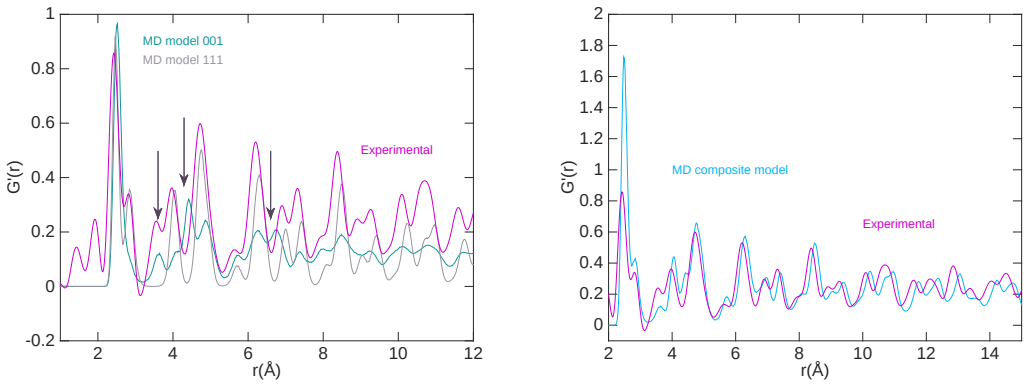

Figure 3.12: a) Comparison between the experimental x-ray G'(r) of the flower data and the MD simulations results of the 50 Å nanowires with ⟨001⟩ or ⟨111⟩ along z. The arrows refers to points of disagreement between the ⟨111⟩ MD model and the data, while instead some corresponding peaks are found in the ⟨001⟩ MD model. b) Adding up the two models produces a composite model that reproduce most of the features of the real data.

to the bulk α-Fe (apart from the previously mentioned shape effect). This has been confirmed performing `GULP` calculations of the α-Fe phase, using a grid of $5 \times 5 \times 5$ in k-space, as seen in figure 3.13 a. On the other hand, the nanowires with ⟨100⟩ along z present a largely different structure: the second, third and fourth nearest neighbour distances of α-Fe have been lost completely or partially and we observe the appearance of new peaks, absent in the other case. The PDF obtained from `GULP` calculations of the γ-Fe phase presents peaks, that are in similar positions to those exhibited by the 100 MD model.

Moreover, at the end of the simulation, the configuration with the ⟨100⟩ direction along z present a distorted arrangement of the atoms; looking at sections of the cylinder selected at different depths along the z axis, it is possible to observe that near the ends of the tube the 2D square lattice is retained (figure 3.13 b). However, moving towards intermediate and mid regions of the tube, the appearance of a 2D hexagonal pattern is observed (figure 3.13 b). This could reflect either the arrangement found in the (110) plane of the bcc phase or in the (111) plane of the the fcc phase.

The latter seems a more plausible interpretation, since the PDF has lost the second nearest neighbour peak, characteristic of the bcc phase. The first nearest neighbour peak of the bcc correspond in fact to the interatomic distance between the atoms at the corner and the one at the centre (found at the same position of the first nearest neighbour distance of the fcc phase) and the next is between atoms at the corners of the unit cell. Thus the loss of that peak indicates the overall loss of the body centred feature of the pair distribution function. In other words, the 100 model seems to present a vertical transition from the bcc to the fcc and back to the bcc phase, resulting in a sort of hybrid local ordering, that is effectively reflected by the disorder in

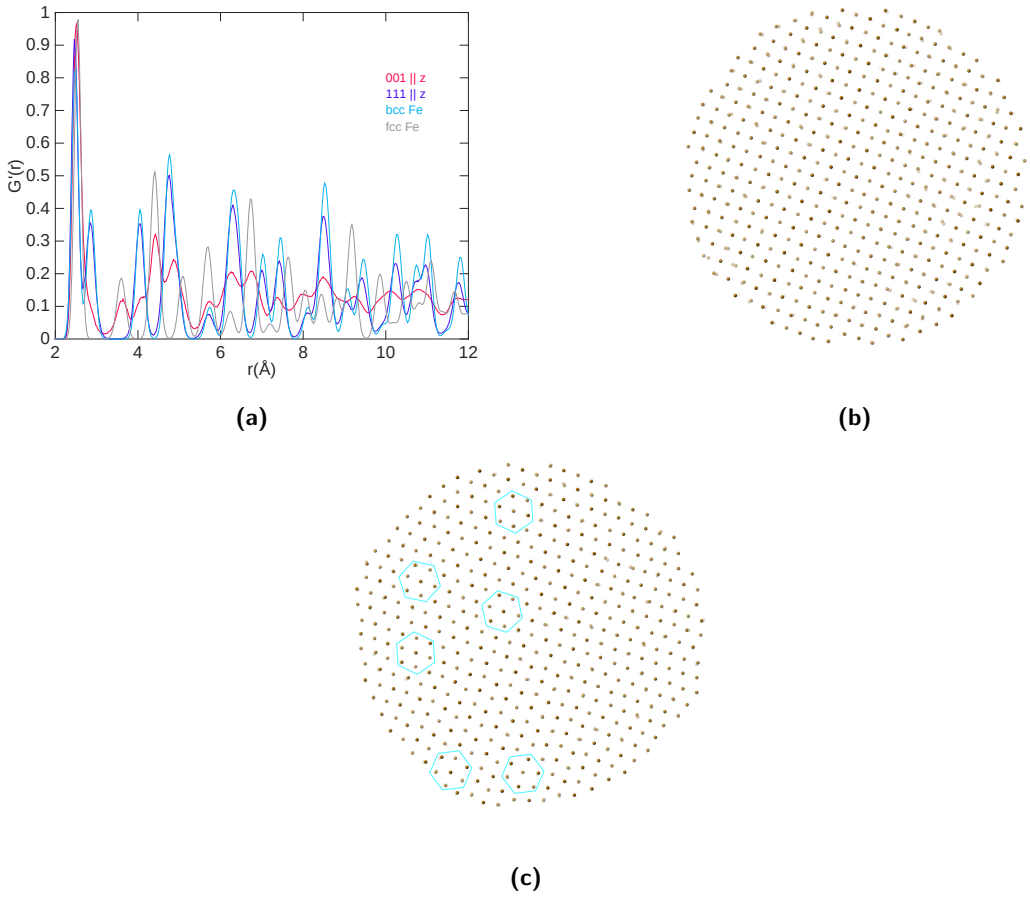

Figure 3.13: The final configuration of the 30 Å nanowire with the ⟨111⟩ direction pointing along the z axis. The near-end region of the tube (a) retains the 2D square ordering, while the regions closer to the centre (b) distort forming a pseudo-hexagonal 2D lattice (some hexagonal arrangements of atoms are marked by cyan hexagons).

the pdf function.

Returning to the comparison between the experimental data and the MD models (figure 3.12), the fact that the data seem to partially reflect both models, may imply the coexistence in the nanowire of regions with α and others with γ iron. This is consistent with what previously observed by TEM analysis: the fcc reflections are often observed at the tip of the nanowires or where there are bending points or constrictions in the nanowire.

3.3.3.3 Iron nanowires of infinite length: results and implications for the local ordering of the structure

Simulations of iron nanowires with 80 Å diameter and one of the crystallographic directions ⟨111⟩, ⟨110⟩ and ⟨100⟩ aligned along the z axis (z is parallel to main axis of the cylinder) were performed. Periodic boundary conditions were applied and the nanowires were cut along the z direction close to the x and y edges of the box, in such a way that they resulted continuous

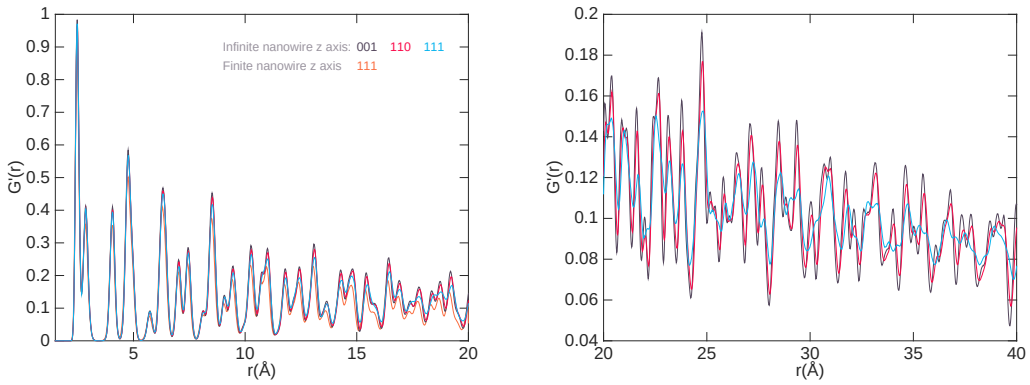

Figure 3.14: $G'(r)$ of MD simulations of infinite nanowires with diameter of $80\,\text{Å}$ and the z axis parallel to the main axis of the cylinder and the crystallographic direction of the α-Fe phase, as specified in the label (grey $z \parallel \langle 001 \rangle$, red $z \parallel \langle 110 \rangle$, blue $z \parallel \langle 111 \rangle$). In a) these are compared to the $G'(r)$ of the MD simulation of the finite nanowire with $50\,\text{Å}$ diameter and $z \parallel \langle 111 \rangle$. b) Medium range order of the infinite nanowries.

along z. More specifically, expanding the cell along z, the distance between the atoms on one extremity of the nanowire and the ones on the other extremity is approximately equal to the average bond distance. This is effectively equivalent to produce a nanowire of virtually infinite length and diameter $80\,\text{Å}$. The choice of the $80\,\text{Å}$ diameter was made based on the observation of the faster fall of the PDF intensities of the $50\,\text{Å}$ nanowire compared to the X-ray PDF of the flower structure, observed in figure 3.12 b.

In the previous section it was observed that the direction of the crystallographic axis with respect to the z-axis has a strong impact on the local ordering of the Fe atoms, leading to the formation a hexagonal arrangement of the surface atoms and perpendicularly to the z direction in nanowires with $\langle 100 \rangle \parallel z$. Interestingly, the behaviour observed in the case of infinite length nanowires is different to what is seen in the case of finite length nanowires. The local structure of the nanowires is not significantly affected by the orientation of the crystallographic axis with respect to z, remaining consistent with the bcc structure in all three cases. This finding shows that the size of the nanowire is crucial in determining the local arrangement of the Fe atoms, since the formation of a hybridised bcc-fcc type of structure is observed only if the nanowire is finite, when $\langle 100 \rangle \parallel z$.

Interestingly, as already mentioned, both collaborators Filippo Boi and Ibrar Muhammad observed by means of TEM imaging and diffraction, that γ domains forms in regions close to the end of a nanowire or in presence of a bending or a constriction. This has been often interpreted in the literature as a result of the pressure applied locally by the elastic walls of the CNT on the Fe, which leads to the local crystallisation of Fe in the γ-Fe phase. However, recent studies by Ibrar Muhammad on several samples of Fe@MWCNTs urchin, presenting a relative abundance of γ-Fe larger than that observed in the flower and urchin structures analysed in this chapter,

showed that the reason behind the formation of the γ-Fe may have to be found in the local rearrangement of the Fe atoms.

Previous studies of bulk γ-Fe showed that the intercalation of C atoms in the octahedral sites of γ-Fe leads to the stability of the phase even at room temperature. The intercalation of C atoms is likely to happen in interfacial regions between the Fe core and the CNT walls thus leading to the formation of room temperature stable γ-Fe [159]. On the other hand, the MD simulations performed at room temperature and without addition of interstitial C showed that a distortion of the local rearrangement of the lattice towards a fcc type of structure can occur in finite length iron nanowire depending on the orientation of the axis with respect to the nanowire. Thus, it can be inferred that the formation of γ-Fe can occur as a consequence of both these factors: C intercalation and spatial confinement of nanowire with specific orientation of the crystallographic axis.

3.3.4 Modelling the carbon content

MD simulations including the CNTs capsule were performed to investigate the role that the spacial confinement has in determining the structure of the iron core and the ordering of C and Fe atoms in interfacial regions. However for the C–C interaction, a distinction between intralayer and interlayer interactions has to be made. Moreover since this system comprises several components, the potentials were tested individually on each component, starting from a graphene sheet to the move to SWCNTs and subsequently to MWCNTs. Finally the CNTs can be assembled together with the iron component to perform model of the whole system (this part will be treated in section 3.3.4.2).

3.3.4.1 MD of graphene and SWCNT

The C–C intralayer interaction was modelled by means of a modified Morse potential with addition of an angular term. The potential was taken from a study where this was used to test the Young's modulus of SWCNTs as a function of their diameter and chirality [160]. The potential energy has the form $V = V_r + V_\theta$, with the first term representing the bond stretching energy and the second the C–C–C bond angle energy. These terms are given by:

$$V_r = D_e\{[1 - e^{-\beta(r-r_0)}]^2 - 1\}$$
$$V_\theta = \frac{1}{2}k_0(\Delta\theta)^2[1 + k_s(\Delta\theta)^4]$$

where $D_e = 6.031\,05 \times 10^{-10}\,\mathrm{N\,nm}$ is the dissociation energy, $\beta = 26.25\,\mathrm{nm}^{-1}$ a fitting parameter, $r_0 = 0.139\,\mathrm{nm}$ the equilibrium length, $k_0 = 0.9 \times 10^{-18}\,\mathrm{N\ m\ rad}^2$, $\Delta\theta = \theta - \theta_0$ with $\theta_0 = 2.094\,\mathrm{rad}$ and $k_s = 0.754\,\mathrm{rad}^{-4}$ (as reported in the study of reference).

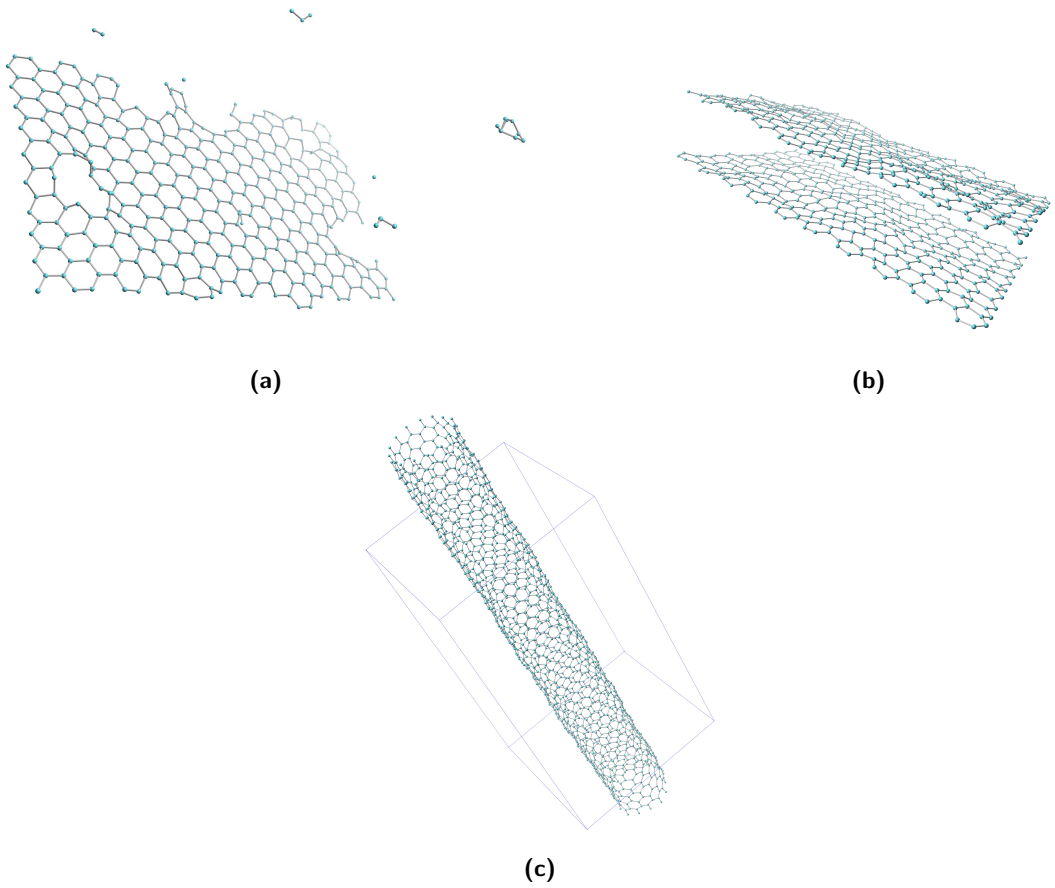

Figure 3.15: (a) The result of the MD on a graphene sheet when using a modified Morse potential for the C–C interaction. Some C atoms escapes the sheet as a consequence of 2D melting. (b) The C atoms stay in place and the bonds are preserved when using a harmonic instead of a Morse potential. c) The result of the MD on a SWCNT, showing the supercell and the continuity of the bonds beyond the edges in the z-direction as a result of the use of periodic boundary conditions.

The potential was initially tested in the modelling of a graphene sheet. Interestingly this first attempt led to the result shown in figure 3.15 a, where the breaking of some of the bonds is observed, with some C atoms escaping the graphene sheet. This result is a consequence of the phenomena of 2D melting, due to the density of states of phonon frequencies in a 2D system [90]. The mean-square displacement of the atoms in a crystal can be written in the high-temperature limit as

$$\langle \mathbf{u} \cdot \mathbf{u} \rangle = \frac{k_{\mathrm{B}} T}{N m} \int \frac{1}{\omega^2} g(\omega) \mathrm{d}\omega \tag{3.5}$$

where k_{B} is the Boltzmann constant, T the temperature, N the number of moles, m the mass of the atom (assuming a monoatomic system), ω the phonon frequency and $g(\omega)$ the density of states or distribution of phonon frequencies. In a 3D system $g(\omega)$ is proportional to ω^2, thus $g(\omega)/\omega^2$ is a constant and the mean-square displacement is finite. However in a nD system $g(\omega)/\omega^2 \propto \omega^{(n-1)}$ and the integral diverges logarithmically [90]. As a side comment, this has

implications for the possible existence of a real 2D system, since from these considerations it can be inferred that it would behave as a liquid rather than a solid.

The use of a harmonic potential to replace the Morse potential prevents the 2D melting from happening. The final harmonic bond stretch and angular terms have the form:

$$U_r = \frac{1}{2}k(r - r_0)^2$$
$$U_\theta = \frac{1}{2}k_\theta(\theta - \theta_0)^2$$

where k is calculated by means of the relationship $k = 2D_e\beta^2$, between the Morse and harmonic fitting parameters. Since the units chosen to perform the MD are eV for the energy, Å for distances and degrees for angles, the parameters were converted to comply with these units. So, the final values of the parameters used in the MD are $k = 25.9384\,\mathrm{eV\AA^{-2}}$, $r_0 = 1.39\,\mathrm{\AA}$, $k_\theta = 5.625\,\mathrm{eV\AA^{-2}}$ and $\theta_0 = 120°$.

The conversion leads to a stable result, as shown in figure 3.15 b, since it forces the atoms to oscillate around their equilibrium positions, so that they can no longer escape the graphene sheet. The harmonic potential provides a description of the interatomic forces that is sufficient for the aim of our simulation, since the objective is that of studying the behaviour of the CNT acting as a capsule interacting with the outermost layer of the iron core. Thus the main concern is to have a shell where the C atoms are free to oscillate but remain in place preserving the hexagonal network.

The potential was subsequently tested for the case of a SWCNT, showing good results also in this case, figure 3.15 c. The initial configuration was made rolling a graphene sheet using the program `CrystalMaker`; it was ensured that the edges of the supercell along the z direction (length of the cylinder) were cut in such a way to allow the C bonds to be properly formed between the two ends of the SWCNT, when applying periodic boundary conditions in the MD simulation. This is equivalent to test the potential on a SWCNT of virtually infinite length.

3.3.4.2 MD of SWCNTs filled with iron

Despite the wealth of information that it is possible to obtain already from the iron nanowire models, especially with respect to the role played by the shape and orientation in determining the local structure, the confinement due to the C capsule around it is expected to play also a crucial role. For this reason MD simulations of iron nanowires surrounded by SWCNT and MWCNTs were performed. The results from the models of iron nanowires can provide a guidance for the choice of size and orientation in assembling the composite models.

The potentials used in the MD iron nanowires and empty SWCNT/MWCNTs can be combined and used in the simulation of the system. However, we have to again choose and test an appropriate potential for the Fe–C interaction. A classic many-body potential from the

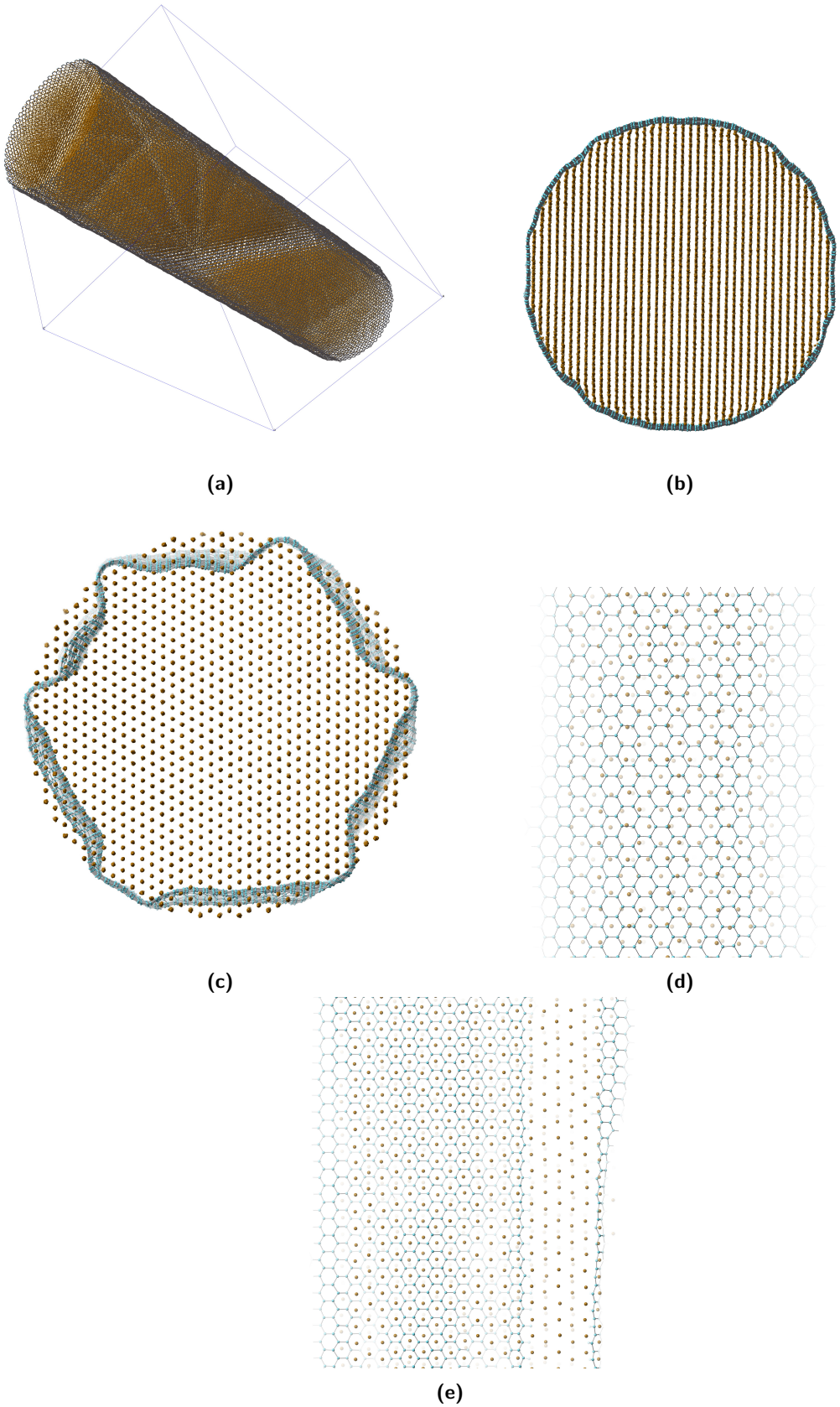

Figure 3.16: The final atomic configurations of the MD performed on a SWCNT filled with α-Fe. (a) Fe@SWCNT with the $< 110 > \| z$ and its section in direction perpendicular to z shown in (b). (c) Vertical section of Fe@SWCNT with the $< 111 > \| z$ and lateral section of the same configuration in correspondence of one of the directions where the Fe atoms (in brown) have diffused through the SWCNT. (e) Lateral section of the Fe@SWCNT with the $\langle 110 \rangle \parallel z$.

literature, originally used to model the growth of CNTs from metal clusters of Fe, Co and Ni, was chosen to model the C–Fe interaction [161] since it is expected to accurately describe this interaction. In the study, the parameters of the Morse-type potential are calculated by fitting to the binding energy from Density Functional Theory. The potential has the form:

$$
\begin{aligned}
E &= V_{\mathrm{R}} - V_{\mathrm{A}} \\
V_{\mathrm{R}} &= \frac{D_{\mathrm{e}}}{S-1} \exp\{-\beta\sqrt{2S}(r - R_{\mathrm{e}})\} \\
V_{\mathrm{A}} &= B^* \frac{D_{\mathrm{e}} S}{S-1} \exp\{-\beta\sqrt{2/S}(r - R_{\mathrm{e}})\} \\
B^* &= \{1 + b(N^C - 1)\}^{\delta}
\end{aligned}
$$

where V_{R} and V_{A} are the repulsive and attractive terms respectively, D_{e} and R_{e} the binding energy and equilibrium bond length respectively. S, β, b and δ are the potential parameters. The term B^* takes into account the many body potential effect and is expressed in function of the carbon coordination number of a given Fe atom, N^C. The latter is defined by means of a cut-off function $f(r)$ such that

$$
\begin{aligned}
f(r) &= \begin{cases} 1, & r \le R_1 \\ (1 + \cos\frac{r-R_1}{R_2-R_1}\pi)/2, & R_1 \le r \le R_1 \\ 0, & r > R_2 \end{cases} \\
N_i^C &= 1 + \sum_{k \neq j} f(r_{ik})
\end{aligned}
$$

The values of the fitted parameters are $D_e = 3.3249\,\mathrm{eV}$, $S = 1.3$, $\beta = 1.5284\,\mathrm{\AA}^{-1}$, $R_{\mathrm{e}} = 1.7304\,\mathrm{\AA}$, $R_1 = 2.7\,\mathrm{\AA}$, $R_2 = 3\,\mathrm{\AA}$, $b = 0.0656$ and $\delta = -0.4279$. In the case of our system we can assume the number of C nearest neighbours to be approximately 6, corresponding to a Fe in the proximity of a hexagonal graphene ring.

The results of the MD simulations show that the interaction between the SCWNT wall and the Fe core is strongly dependent on the direction of the crystallographic axis of α–Fe with respect to z. As an example, we can consider the case of $z \parallel \langle 110 \rangle$ and $z \parallel \langle 111 \rangle$.

In the first case the structure remains quite stable preserving (apart from thermal motion effects) the original structure, figure 3.16 a and b. Comparison of the neutron PDF with that of the infinite nanowire with the same orientation of the crystallographic axis shows that the structure remains almost unchanged except for the appearance of peak at 1.4 Å corresponding to the first C–C interatomic distance and a small feature at 3.66 Å corresponding to the fourth C–C distance, figure 3.17 a. Comparing the X-ray PDF, the already minimal C contribution in the neutron data is reduced to a negligible level, and it can be seen that the ordering of the

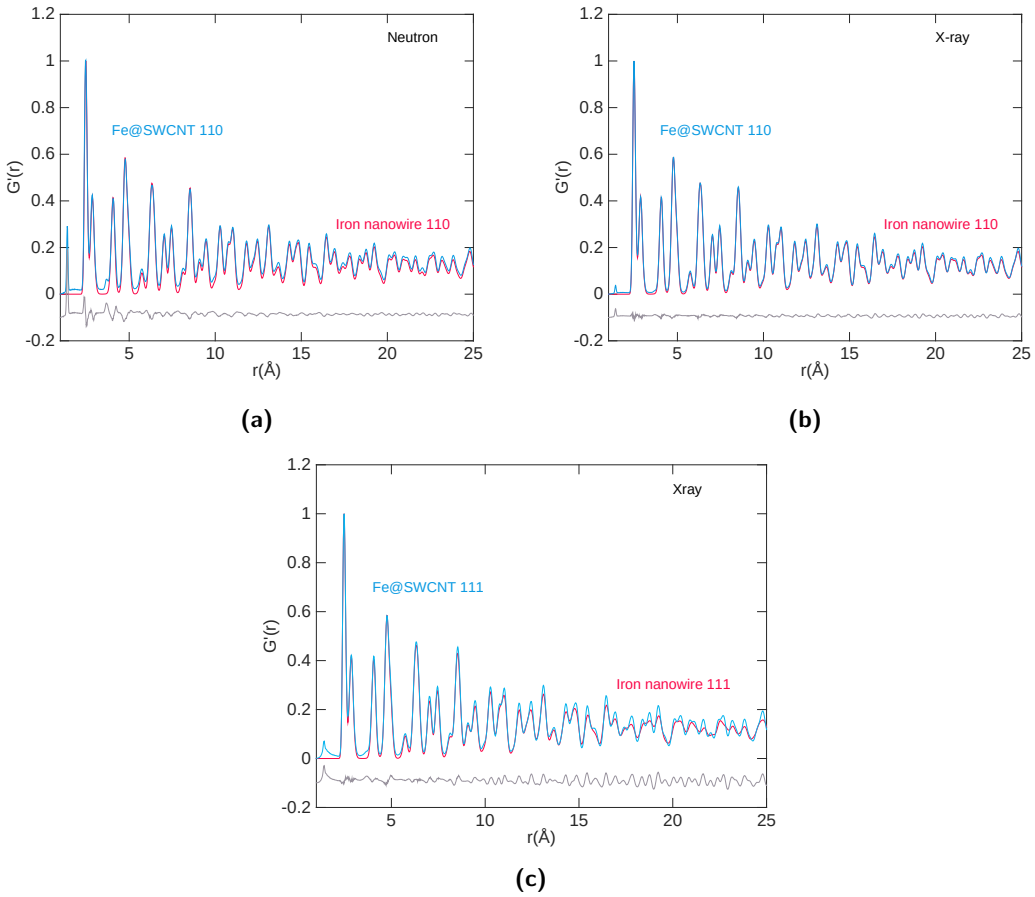

Figure 3.17: Neutron (a) and X-ray (b) $G'(r)$ of the MD configuration of Fe@SWCNT (blue line) compared to the infinite iron nanowire structure, both with $\langle 110 \rangle \parallel z$, with the difference between the two functions is the grey line. (c) X-ray $G'(r)$ of the MD configuration of Fe@SWCNT compared with $\langle 111 \rangle \parallel z$, compared to the equivalent infinite MD iron model.

nanowire is unaltered, figure 3.17 b.

In the case of the Fe@SWCNT with $z \parallel \langle 111 \rangle$, the interaction between the Fe and the SWCNT deforms the walls of the SWCNT and diffusion of some of the outermost Fe atoms through the hexagonal rings occur, figure 3.16 c. Looking at a lateral section of the $\langle 111 \rangle$ configuration, in direction perpendicular to z, it is possible to observe that the Fe adjacent to the walls of the SWCNT are forming an hexagonal lattice, with the Fe atoms sitting in the middle of the hexagonal C rings (figure 3.16 e). However, this result is unphysical and is likely to be an artefact of the simulation. It should be observed in fact that it is generally difficult to generate potentials that can accurately describe metals interaction, owing to the complexity of the electronic distribution in the the d and f orbitals [162]. It is then possible that the potentials used do not provide a realistic representation of the Fe–C interaction.

Notwithstanding the fact that the result is unphysical, it is still worth noticing that the iron atoms diffuse through the SWCNT only in one case (i.e. $z \parallel \langle 111 \rangle$) and not in the other

($z \parallel \langle 110 \rangle$). The effect of the Fe/C interaction on the local ordering of the iron is reflected by mild differences between the PDF function of the Fe@SWCNT and that of the infinite iron nanowire model, figure 3.17 c. It was already observed that positioning $z \parallel \langle 111 \rangle$ maximises the surface of the α-Fe cylinder presenting the pseudo-hexagonal arrangement, figure 3.11 a, and that after the simulation this arrangement tends towards a more regular hexagonal ordering, figure 3.11 b. Interestingly, the presence of such ordering on the surface of the Fe core greatly affects the SWCNT shell and determines the behaviour of the C atoms. Moreover, it was also observed that the infinite iron nanowires with this orientation of the crystallographic axis present a more disordered structure in the medium-long range order compared to the other orientations, figure 3.14 b, which could be associated with the tendency of the system to relax towards more disordered configurations.

3.3.5 Considerations on the ordering of the structure and the self-assembling formation process of iron filled MWCNTs

The results of the MD analysis have shown that the orientation of the crystallographic axis of α-Fe with respect to the main axis of the nanowire affects the local and medium range order of the structure in ways that depend on the diameter and length of the nanowire, with repercussion on the ordering of the SWCNT, when this in included.

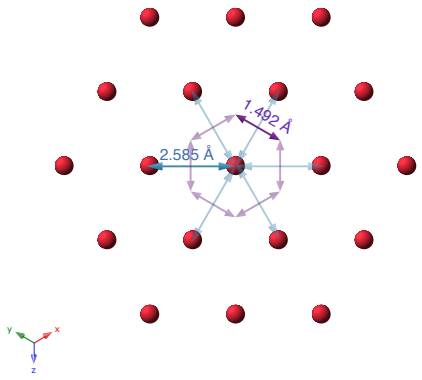

Figure 3.18: Projection of the $\langle 111 \rangle$ direction of the ideal gamma phase of iron showing in blue the distances between Fe atoms (in magenta) and in violet the distances between centroids of triangles, where the energy has local minima and the C atoms would position forming the hexagonal network. The distance between centroids of triangles is very close to the ideal C–C distance.

The atomic ordering of the iron nanowire and the MWCNTs is expected to be linked to the dynamics that governs the self-assembly of these nanostructures in the CVD synthesis. A previous study [161] (incidentally this is also the study of reference for the Fe–C potential described in the previous section) analysed the formation process of graphitic layers around small clusters of transition metal atoms (either Fe, Co or Ni) by classical molecular dynamics (MD) simulation.

The study reports the formation of 2D closed-packed facets in the transition metal clusters. The simulation shows that these facets act as templates, layers on top of which which the hexagonal carbon network starts forming, owing to the potential energy surface formed by the 2D closed-packed facets, that affect and facilitate the growth of the nanotubes. The interatomic

distance between Fe atoms on the facet is of 2.585 Å, corresponding to a distance between the centroids of the triangle formed by the metal atoms on the facet approximately of 1.492 Å, very close to the carbon covalent bonding distance (figure 3.18). In the positions corresponding to the corners of the hexagon formed by the centroid of the triangle (the hexagon marked with violet arrows figure 3.18), the field generated by the Fe lattice exhibits points of local minimina where the C atoms would position themselves in the growth process, representing the most energetically favourable configuration.

This shows that the formation of hexagonal facets is fundamental in the formation process of MWCNTs and we may expect the local ordering of the Fe nanowire to determines and, at the same time, be largely affected by the synthesis process. Structural features of the nanowire, such as orientation of the crystallographic axis, degree of disorder and arrangement of the atoms at the surface are all expected to be intimately connected with the dynamics that governs the reaction.

3.4 Summary

The work in this chapter represents a contribution to the understanding of the atomic structure of a class of MWCNTs continuously filled with iron, nanomaterials of great technological interest for their many potential applications. X-ray and neutron total scattering experiments were complemented by information from experimental techniques, such as SEM, TEM imaging and diffraction and Bragg diffraction. The combination of experimental methods with theoretical modelling techniques, such as `PDFgui` refinement, `GULP` calculations and MD simulations is pivotal for an understanding of these structures.

The iron nanowire of the samples analysed was found to be mainly composed of α-Fe. MD simulation showed that the orientation of the crystallographic axis of α-Fe with respect to the nanowire dimensions greatly determines the local ordering of the iron, in the case of cylinder of finite length. A composite model, combining the PDF calculated from the final MD configurations of the iron nanowires with the $\langle 100 \rangle$ and the $\langle 111 \rangle$ directions parallel to the main axis of the cylinder z, matches well the experimental X-ray PDF. Comparison of the MD results with `GULP` calculations shows that when z is parallel to the $\langle 100 \rangle$ direction, the structure exhibits a local ordering in between that of α-Fe and γ-Fe. This behaviour does not occur for nanowire of infinite length, where only the medium-long range order is affected by the orientation of the crystallographic axis relative to the dimensions of the nanowire. MD of SWCNT filled with iron showed that the interaction between the SWCNT wall and the iron core is greatly dependent on the orientation of the crystallographic axis of the α-Fe core. Deformation of the SWCNT and diffusion of some Fe atoms through the walls were observed when the $\langle 111 \rangle$ is parallel to the z direction. This result is however unphysical and likely to be an artefact due to the difficulty in

modelling the metal component of the system. This interaction as well as the higher stability of the ⟨111⟩ direction compared to the ⟨100⟩ (in the case of finite iron nanowire) are linked to the pseudo-hexagonal arrangement of the Fe atoms on the surface of the nanowires, that is maximised when this direction is chosen.

More generally, the result of this work shows once again how reductive a description of such complex nanostructures is, if done solely in terms of a unit cell and an average structure. The use of the PDF analysis combined with modelling techniques allowed us to achieve an understanding of the local atomic ordering inside these materials, that would have otherwise been difficult to determine.

Chapter 4

Prussian blue

The work in this chapter concerns the study of the local structure of a framework material, Prussian blue (chemical formula $Fe_4^{III}[Fe^{II}(CN)_6]_3$) in nanoparticulate and bulk form, by means of total neutron and X-ray scattering. The structure presents vacancies at $Fe^{II}(CN)_6$ sites, that can be occupied by water molecules in the pores and coordinated to the Fe^{III} centres.

The first section gives an overview of the properties and applications of this class of materials, as well as the previous studies where these were studied by means of total scattering.

The second section describes the samples analysed, the synthesis procedure and complementary experimental techniques used in the analysis. Elemental analysis and infrared spectroscopy measurements were used to obtain information about the atomic composition of the samples and the presence in the nano-particulate samples of polyvinylpyrrolidone, a polymer used in the synthesis. Moreover, in the case of the bulk sample, the infrared spectroscopy measurement provided a tool for determining the oxidation state of the Fe centres, owing to the sensitivity of the C–N stretching modes to their local environment.

The third section present an overview of the total neutron and X-ray scattering data collected. In the fourth section, the modelling techniques used in the analysis of the total scattering and PDF data are described. These include a bespoke least squares modelling procedure of the low-r peaks in the PDF used to identify the fraction of water and PVP found in the samples and `PDFgui` refinements of the Prussian blue unit cell against the experimental PDF.

In order to study the role played by the vacancies and water molecules on the ordering of the structure, atomic configurations of size $5 \times 5 \times 5$ unit cell swith random spatial distribution of the vacancies and different starting allocation of the water molecules in the pores were created. These were used as starting configurations to refine against the data using the program `RMCProfile`.

4.1 Brief history, properties and applications of Prussian blue and its analogues

Prussian blue (PB) was one of the first coordination materials to be discovered. The discovery was in fact accidental and it was made by a Berlin draper, Heinrich Diesbach, in 1706, while he was combining the distillate of animal carcasses with potassium carbonate [163]. The original PB, Iron(III) hexacyanoferrate(II), has chemical formula $Fe_4^{III}[Fe^{II}(CN)_6]_3$ and adopts a face-centred cubic structure (fcc) in the $Fm\bar{3}m$ space group, where the iron(III) ions form a network bridged by ferricyanide ions, with a cell parameter of 10.13 Å, figure 4.1 [164].

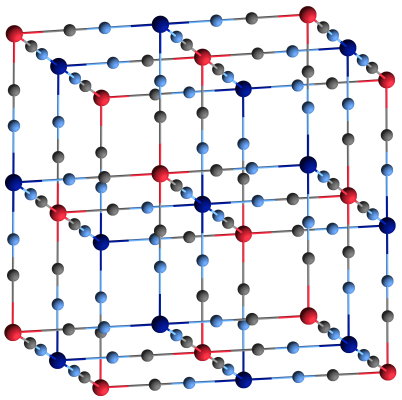

Figure 4.1: Crystal structure of PB: C atoms are coloured in grey, N cyan, Fe^{2+} blue and Fe^{3+} red. The structure is characterised by stoichiometric vacancies, with 25% of the $Fe_4[Fe(CN)_6]_3$ sites empty.

The first publication on PB appeared in 1710 in the *Miscellanea Berolinensia* where the remarkable properties of PB as a paint were discussed [165]. What was not known at the time of its discovery is that the intense blue colour, that made it originally popular among painters (figure 4.2) and printers, is the visible manifestation of a physical-chemical process, whereby electron transfer occurs between metallic centres through the cyanide bridges, owing to the weak electron delocalisation, with characteristic excitation at around 700 nm (corresponding to orange-red light being absorbed) [166]. The electron delocalisation is also responsible for the superexchange interaction between the high spin Fe^{III} centres, which produces ferromagnetic order below 5.2 K [164, 166].

Being porous, the PB framework can accommodate water molecules or gases, making it particularly suitable for use in gas storage [167–170], as e.g H_2 for energy storage applications [171]. The structure is also characterised by the presence of vacancies; in particular, if we rewrite the chemical formula of PB as $Fe^{III}[Fe^{II}(CN)_6]_{3/4}$, it becomes apparent that a quarter of the $[Fe^{II}(CN)_6]$ sites has to be empty, in order to maintain the charge balance. These vacancies can be occupied by water molecules and thus the chemical formula can be more generally written as $Fe_4^{III}[Fe^{II}(CN)_6]_3{\cdot}nH_2O$, where n is the number of water molecules per unit cell, some of which may be coordinated to the $Fe_3{}^+$ (e.g. the O atoms sit in the empty N sites) and others may occupy the pores in the framework. In any case the number of coordinated water molecules cannot exceed 6 per unit cell (this is equivalent to the number of vacancies left by the missing $Fe^{II}(CN)_6$ group). The total number of molecules in standard conditions (e.g. room temperature and atmospheric pressure) has generally been observed to be in the range $14 < n < 16$ [164].

Figure 4.2: *Starry night over the Rhône*, Vincent Van Gogh, 1888. Prussian blue is one of the pigments used in the painting to give the intense blue colour.

As most transition metal cyanides, PB presents also negative thermal expansion (NTE, i.e. contraction upon rising of the temperature) properties [172–174], owing to the high flexibility of the M–CN–M network [93]. The NTE properties can vary also depending on the concentration of guest molecules inside the pores since the guests greatly affect the flexibility of the framework [167, 171].

The original PB is the progenitor of a long list of compounds, known as PB analogues (PBAs), that have been synthesised by researchers substituting some or all of the Fe atoms with other transition metals, often aiming at the designing of PBAs exhibiting room temperature ferromagnetic behaviour. Among the PBAs, an interesting example is the Fe/Co system $A_xCo_y^{II}[Fe^{III}(CN)_6]_3 \cdot nH_2O$ (A: alkali metal ion), which shows tuneable magnetic and optical properties, owing to the thermally and photo-induced electron transfer occurring between the metal ions [166]. The electron transfer induces also a spin transition in this material, with the Co switching from a high spin configuration to a low-spin one. Because of these tuneable properties, many groups have worked in the direction of producing low dimensionality networks of this analogue, for applications in quantum computing and medicine [166].

4.1.1 Previous studies

To our knowledge, the original PB compound has never been investigated by means of total scattering, neither in its bulk nor nanoparticulate form. However, there are some studies in the literature concerning the application of the pair distribution function and total scattering technique to the study of PB analogues [168, 171, 175–177]. An area where this has proven particularly useful is in the understanding of the interaction between guest molecules and the PB framework. In particular, some studies have used differential pair distribution analysis, where the difference between the PDF of the sample before and after absorption of the guest molecules can be used to probe the local structure of specific components of the system. This method has been used for analysing the modifications in the local structure of a PB analogue, $Mn_3^{II}[Co^{III}(CN)_6]_2$, upon absorption of N_2 [175] and H_2/D_2 [171].

In the N_2 loaded sample case, the differential PDF was analysed using a model based on the results of the Rietveld refinement of the vacant framework corrected by some factors to account for lattice expansion and with addition of a Gaussian distribution of electron densities around the pore centres to represent the guest molecules. However the model does not give a representation of the structure that is coherent across multiple length scales, failing to refine properly the correlation between guest and metal in the immediately surrounding unit cells. Indeed the authors envisage a possible solution to the problem in the use of the reverse Monte Carlo refinement approach.

The study on H_2/D_2 loaded samples shows that, contrarily to what was postulated in other

studies, there is no evidence for guest molecules coordination to the Mn^{II} ions, presenting neighbouring vacant sites. In fact, there is not any sharp feature in the X-ray and neutron differential PDFs at values of r in the range of a hypothetical H_2/D_2 to Mn^{II} binding distance; moreover, both X-ray and neutron PDF are described more accurately by a model consistent with van der Waals interaction, where the guest is located at the centre of the pore (1/4, 1/4, 1/4) as in the case of the N_2 loaded sample, rather than a model with short range binding interactions. The material also exhibits NTE at temperatures between 30 K and 77 K. This applies to both vacant and loaded samples, with the only difference that the coefficient of NTE is smaller in the second case owing to the dampening of the transverse cyanide vibrations (caused by the presence of the guest molecules in the pores) that are responsible for the NTE behaviour of the material.

It should also be noted that in both these experiments (N_2 and H_2 loaded) the samples were first desolvated to eliminate the water in the framework, leaving an empty PBA network. In a previous study [168] it was shown that coordinated and non-coordinated water molecules can be both removed heating the sample at 350 K and 425 K, respectively.

An interesting study on the same PBA combines the PDF technique and diffuse reflectance infrared (IR) spectroscopy [167]. The IR is used to distinguish the different rates at which coordinated and non-coordinated water are liberated and the PDF shows how the structure changes and relaxes as the water is lost. The coordinated water molecules are liberated at higher temperature compared to the non-coordinated ones; this is proven by the loss at different temperatures (lower and higher respectively) of some of the broad features in the IR spectrum (attributed to water in the pores) compared to some of the sharp ones (attributed to coordinated water). The structural disorder increases as the coordinated water is released, owing to the higher degree of flexibility of the framework that is a consequence of the change in the local environment surrounding the Mn atoms, with a transition from a octahedrally coordinated to a distorted 4-coordinated geometry, as a consequence of the loss of 2-coordinated water molecules; this also reflected by the increased intensity of the C–N stretching modes in the IR spectrum.

These observations are consistent with earlier neutron diffraction studies [164], that had shown that the water-free original PB compound presents a contracted unit cell compared to the hydrated sample. Even in this case the contraction was identified as being driven by the distortion of the octahedral sites, with the Fe–C–N angle being 164°. The Rietveld refinement of the data shows that the pores of the hydrated sample contain 8 uncoordinated water molecules, with average positions (1/4, 1/4, 1/4) and (0.34, 0.34, 0.34). Interestingly, the first was identified as the position of the water molecules that are unable to form hydrogen bonds with the coordinated water, since they occupy a pore with no vacancies (corresponding to an octant with 4 Fe^{II} atoms in positions 4a (0,0,0), configuration that has a probability of $0.75^4 = 0.316$ to be found. On the other hand, the second is the position occupied by the water molecules in octant presenting one

Fe^{II} missing (whose probability, 0.422, is the highest amongst the five possible configurations), since this position corresponds to the distance that allows the formation of the hydrogen bonding with coordinated water molecules; in this case, the second configuration is in fact energetically favourable.

In another study, the differential PDF technique, combined with nuclear magnetic resonance studies, is used to analyse the structure of nanoparticles of sodium nitroprusside embedded in a an amorphous silica matrix [176]; this PBA has structure $Na_2[Fe(CN)_5NO]\cdot 2\,H_2O$, where one of the cyanide ligands is substituted by nitric oxide. This compound is often used as a drug in the cure of cardiovascular diseases and its use in nanoparticulate form can enhance the absorption of the drug. It was found that the nanoparticles are spherical, with a 5 nm diameter and that isolated molecules of the compound occupy smaller pores (approximately 1 nm) in the matrix.

There are few examples in the literature where the RMC refinement method combined with total scattering data has been used for gaining insight in the local structure of PBA. This is the case e.g. of the compounds $M_{3/2}[Cr(CN)_6]\cdot zH_2O$ (M=Fe and Co) [177]; according to the result of the Rietveld refinement performed against the X-ray and neutron Bragg profiles, the structure is face-centred cubic with space group $Fm\bar{3}m$. However the neutron diffraction data show the presence of a broad Bragg peak, 100 reflection, forbidden in this space group, which in fact is not refined by the Rietveld refinement. The structural model resulting from RMC analysis provides a good representation of the diffuse scattering components, as well as of the forbidden peak, which is found to be a consequence of the correlation of oxygen atoms at empty $Cr(CN)_6$ sites.

4.2 Samples: bulk, solid and hollow nanoparticles

When approaching the study of this class of materials, the variety of morphologies, chemical compositions and the wide range of applications therein associated, can make it hard to choose which particular analogue should be studied. In this thesis, it was decided to analyse the archetypical PB structure, that is the original PB compound. Although this compound has been extensively studied, most researches have focused on the study of the average bulk structure via Bragg diffraction and analysis of chemical, magnetic and optical properties. However to our knowledge there have not been studies on the local structure of the original PB compound, in particular using the total scattering technique.

Moreover some recent works focused on the synthesis of cubic PB nanoparticles [178, 179] in two variants (nanoparticles with a solid core and nanoparticles with a hollow interior), providing a clear synthesis route that leads to the formation of uniformly sized and shaped nanocrystals, offering the opportunity for a comparative study of bulk and nanostructured PB.

For these reasons total scattering experiments were conducted on these three forms of PB:

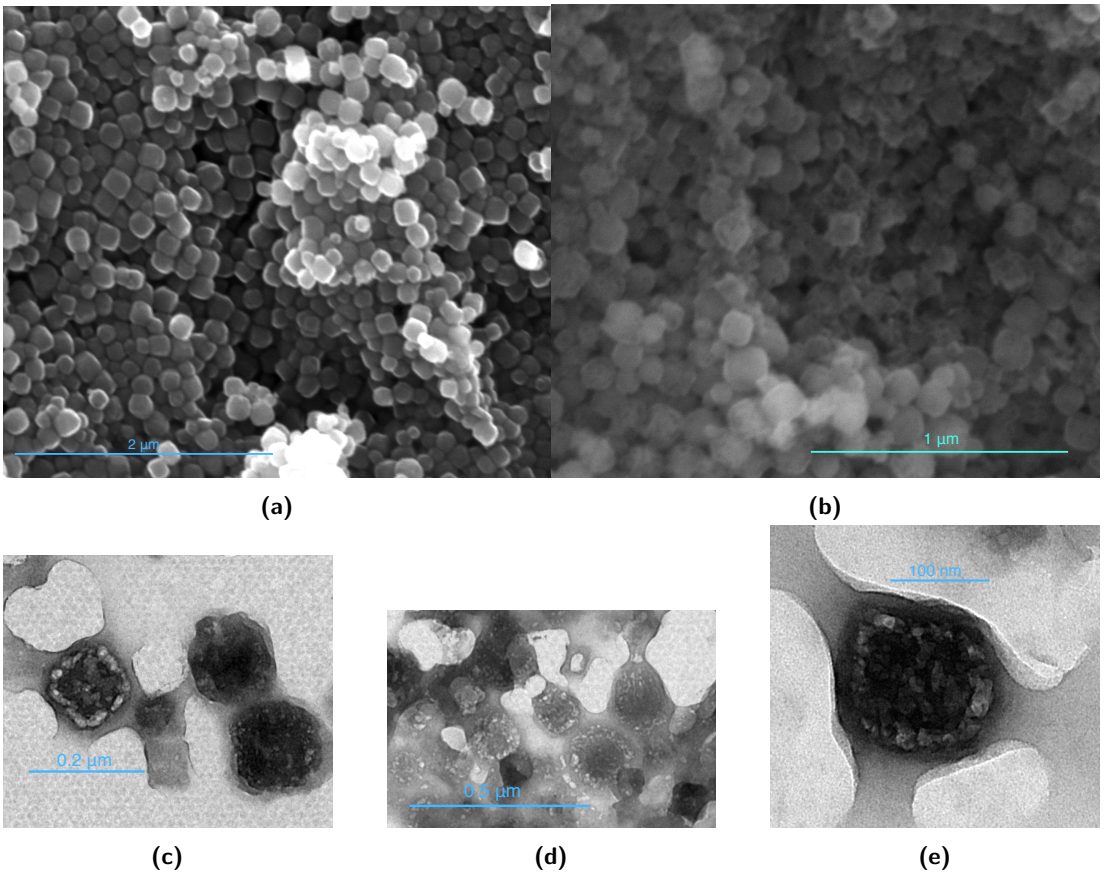

Figure 4.3: SEM images of (a) a PB solid nanoparticles sample and (b) a hollow nanoparticles sample. (c), (d), (e) TEM images of the hollow nanoparticles sample.

bulk, solid and hollow nanoparticles. The objective is comparing the structure of PB in its bulk form with the nanoparticles and in particular understanding the effect of the transition from bulk to nano on the local structure and the vacancies.

4.2.1 Synthesis technique

The synthesis techniques used were implemented by Hu *et* al. [178]. In order to test the replicability of the procedures, the synthesis were first performed in small batches, using H_2O and HCl. Cu-anode X-ray diffraction and scanning electron microscopy were used to confirm that the samples had the right crystal structure, morphology and size of the nanocrystals.

After the successful completion of these preliminary tests, in order to be able to perform neutron experiments, the syntheses were repeated using deuterated chemicals to reduce the concentration of hydrogen found in the samples; moreover the quantity of chemicals were scaled up (compared to what is reported in [178]) and the synthesis performed in several batches, since, as already mentioned, neutron experiments require large amount of samples in order to obtain an acceptable intensity of the scattering signal. Ideally, in a neutron experiment the sample

mass should be above 500 mg; in our case the nature of the equipment used and other practical factors limited the yield to approximately 200 mg for the case of the bulk and solid nanoparticles samples and to as little as approximately 21 mg in the case of hollow nanoparticles, owing to loss of a fraction of the yield in the various steps involved in the synthesis.

The possibility of increasing the concentration of precursors in order to maximise the yield was considered. However previous reports from Hu *et* al. have shown that the morphology and size of the nanocrystals is highly affected by the concentration of the precursors [180] and that higher homogeneity in size and shape is obtained using the procedure given in [178]. In this case it was decided to opt for optimising the quality rather than the quantity of the samples, since the atomic structure is expected to be highly dependent on size and morphology of the nanocrystals.

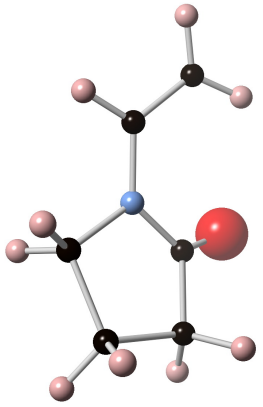

Figure 4.4: Crystal structure of a monomer of PVP, vinylpyrrolidone. The atoms in black are C, pink H, blue N and red O.

The synthesis and formation of the nanocrystals is driven by the polymer Poly(vinylpyrrolidone) (PVP) (figure 4.4), that acts as surface stabiliser, thus fixing the size of the nanoparticles, and as reducing agent. The stabilising abilities of PVP are due to the presence of a hydrophilic component (the pyrrolidone moiety) and a hydrophobic group (the alkyl group) [181, 182]. The hydrophobic group prevents the aggregation of the nanoparticles.

Previous studies have also shown that the nanoparticles form by a non-classical crystallisation process [179], whereby the formation of the final nanoparticle (mesocrystal) occur as a multi-step process. Small-sized nanoparticles first nucleate in the liquid and subsequently aggregate to form larger structure, to minimise the surface energy until equilibrium is reached. In the case of the synthesis here reported the stabilising action of PVP fix the size of the particles. Precursor and PVP concentrations, as well as pH values, are all parameters that determine the size, morphology and porosity of the final nanoparticles [179].

Here the synthesis technique is reported; the quantities are those used in the making of some of the samples synthesised for the neutron experiment. The chemicals, Poly(vinylpyrrolidone) (PVP, K30, average $M_w = 40000$), $K_3Fe(CN)_6$, D_2O, 10 mol aq. HCl and DCl, were purchased from Sigma Aldrich, Ltd.

Solid nanocrystals: 30 g of PVP and 1.3107 g of $K_3Fe(CN)_6$ were added to 400 ml of a 0.01 mol DCl solution under magnetic stirring until a clear solution was obtained after 30 min. The vial was then transferred into an oven and heated at 80 °C for 20 h. The solution was centrifuged at 13 000 min^{-1} several times; at each time the supernatant was disposed of and the

precipitate washed with D_2O, in order to minimise the amount of PVP remaining in the final precipitate. After drying in the oven at 50 °C for 12 hours, the sample was then transferred in a Nitrogen glove box and sealed in a container where it has been kept until the day of the neutron experiment. Finally at ISIS the sample were further dried in an Argon atmosphere furnace at 50 °C over night and then transferred in a nitrogen glove box where the sample has been loaded in an indium sealed vanadium cylindrical can. The last steps were aimed at preventing the absorption of H_2O from moisture in the air that would partially compromise the results of the total scattering measurements.

Hollow nanocrystals: 0.123 g of nanocrystals (synthesised following the procedure given above) and 600 mg of PVP were added to 123 ml of a 1 mol DCl solution in a Teflon vessel under magnetic stirring. After two hours the solution was transferred inside twelve 50 ml volume digestion bombs and heated at 140 °C for 4 h in an electric oven. The solution was centrifuged at 30 000 min^{-1} several times and washed with D_2O, as for the previous sample. The sample was dried in an argon atmosphere furnace at 50 °C over night and then transferred into a nitrogen glove box and loaded in an indium sealed vanadium cylindrical can, as in the case of the previous sample.

Bulk powder: 1.6809 g of $K_3Fe(CN)_6$ was added to 400 ml of a 0.1 mol DCl solution under magnetic stirring for 5 min, when a clear solution was obtained. The vial was then transferred into an oven and heated at 80 °C for 20 h. The precipitates were collected by centrifugation at 5000 min^{-1} and the same drying and storing procedure as for the case of the solid nanocrystal was applied in this case.

4.2.2 Elemental analysis

Elemental analysis were performed on the bulk and hollow nanoparticles samples by MEDAC Ltd, in order to estimate the concentration of C, N and H/D by combustion analysis and Fe by inductively coupled plasma mass spectroscopy.

The remaining mass percentage, that was not directly measured, was attributed to the presence of O (assuming no other impurities are present in the sample). However, since the samples were exposed to air between the neutron experiments and the elemental analysis measurement, it cannot be excluded that additional O_2 and H_2O may have been absorbed in the framework after the experiment. As a consequence, the measured H and calculated O concentrations, obtained from these measurements, are not entirely reliable. Further methods were applied for this reason to estimate the concentration of D_2O and H_2O present in the samples at the time of the experiment (as shown in section 4.4.1).

The elemental analysis was used to indirectly evaluate the PVP concentration remaining in the nanoparticle samples or if it had been entirely eliminated during the centrifugation

Table 4.1

Sample	Fraction	H/D	C	N	Fe	O*
Hollow nanoparticles	Mass	4.44	33.24	16.15	1.56	44.61
	Atomic*	618.06	693	228.84	7	698.60
Bulk	Mass	1.97	22.54	26.30	28.27	20.92
	Atomic	15.13	25.95	25.96	7	18.08

* Atomic fractions are calculated from mass fractions and normalised with respect to 7 Fe atoms.
* O mass fraction was not measured directly. It is an estimate based on the assumption that no other elements are found in the sample.

and washing steps. Moreover, while by direct observation the nanoparticle samples had the well-known intense blue colour, typical of the original PB, the bulk tended towards a greener shade, so we wanted to check whether this was due to a concentration of $Fe^{II}(CN)_6$ vacancies lower than 25%. In this case, although the compound retains the same crystal structure, some of the Fe^{II} sites are now occupied by Fe in a higher oxidation state, Fe^{III}. If all the sites are in their oxidised form the compound has chemical formula $Fe^{III}Fe^{III}(CN)_6$ [183]. The PB analogues that present less than 25% vacancies or none at all are called Berlin green, owing to the green colour of the sample.

The results of the elemental analysis are shown in table 4.1. The composition was provided in mass percentages and converted to atomic fractions. The atomic fraction of element i, x_i, normalised to 7 Fe atoms (in order to get an estimate of the number of atoms i found in the sample per unit cell) was calculated as $x_i = 7\frac{m_i/M_i}{m_{Fe}/M_{Fe}}$, where m_i is the weight fraction of element i, M_i its atomic mass and analogously for the Fe terms.

In the ideal PB structure with 25% vacancies, for every 7 Fe atoms there would be 18 C and N atoms, as well as 6 water molecules occupying the vacancies and m (usually $6 < m < 10$) in the pores. The PVP has chemical formula $(C_6H_9NO)_n$ ($n \approx 360$ in the compound used in the synthesis), so that in the nanoparticles samples an excess of C and N (compared to the case where all the C and N atoms are part of the PB molecule) can be attributed to the presence of PVP not entirely eliminated during the washes.

The bulk sample, on the other hand, does not contain any PVP so that all the C and N detected by means of the elemental analysis should be attributed to the PB itself. However the elemental analysis show that for every 7 Fe atoms there are approximately 26 C and N atoms or 3.7 for 1 Fe atom. If the material does not present any vacancies and all the Fe are in the oxidation state Fe^{III}, as in the case of the ideal Berlin green structure, for 1 Fe atom there are 3 C and N atoms, so that in this case there is an excess of 0.7 C and N atoms, that may be due to free CN^- ions or HCN trapped in the pores. This partially confirms that the bulk sample presents either the structure of the fully oxidised Berlin green or something in between that and the classic PB structure, with some vacancies in the network but in smaller percentage

compared to PB.

The hollow sample contains a much larger number of C and N atoms, compared to the expected 18. In this case it is assumed that the framework presents the classical PB stoichiometry with 25% vacancies in the structure (assumption based in first instance on the intense blue colour of the sample), so that the remaining C and N concentration is entirely attributed to the residual PVP in the sample. Based on this assumption, it can be argued that the washing and centrifugation procedure did not eliminate the PVP completely, since for every unit cell of PB (or 7 Fe atoms), there are approximately 100 (C_6H_9NO) groups in the sample. The washing procedure in the case of the hollow sample proved in fact to be more difficult than for the solid nanoparticle case. This was likely due to the higher porosity of the nanoparticles that made it easier for them to remain embedded in the PVP viscous matrix. This was observed visually during the washing procedure, since it was quite hard to throw away the supernatant completely without loosing some of the precipitate. Thus a small fraction of solution was left at the bottom of the centrifugation tube at each washing. This may have caused a larger fraction of PVP, compared to the solid sample, to remain in the final dried yield.

Despite the fact that we did not take elemental analysis measurements on the solid nanoparticle sample, the different amount of PVP left in the two samples is also reflected in the neutron data. It was proved difficult in fact to achieve good corrections on the neutron total scattering data of the hollow nanoparticle sample. This is probably a consequence of the large amount of H found in the sample, due to the PVP content, and small size of the sample. For this reason the neutron data of the hollow nanoparticle are not treated in this chapter, since we are still working on ways to improve their corrections.

Finally, since the O and the D mass concentrations were not measured, the result of this elemental analysis are not exhaustive so a bootstrapping procedure was used to extrapolate the atomic concentration. In order to evaluate the atomic composition from the information we hold, we start from the first certain information that we have and that is that for every 7 Fe atoms there needs to be at least 18 C and N atoms.

4.2.3 Infrared spectroscopy measurements

Infrared spectroscopy measurements were performed on a portion of each of the three samples (since part of the samples had been previously used for elemental analysis), as well as on the PVP, using a BRUKER Tensor 27 FTIR spectrometer. The spectra, measured between $600\,\mathrm{cm}^{-1}$ and $4000\,\mathrm{cm}^{-1}$, are shown in figure 4.5 a. The PVP spectrum provides a reference for the presence of residual PVP in the nanoparticles samples. The spectrum of the bulk sample provides, on the other hand, a reference for the Prussian Blue IR intensities, since the amount of impurities in this sample (if any) should be negligible. In fact, a first check confirms that the features of the

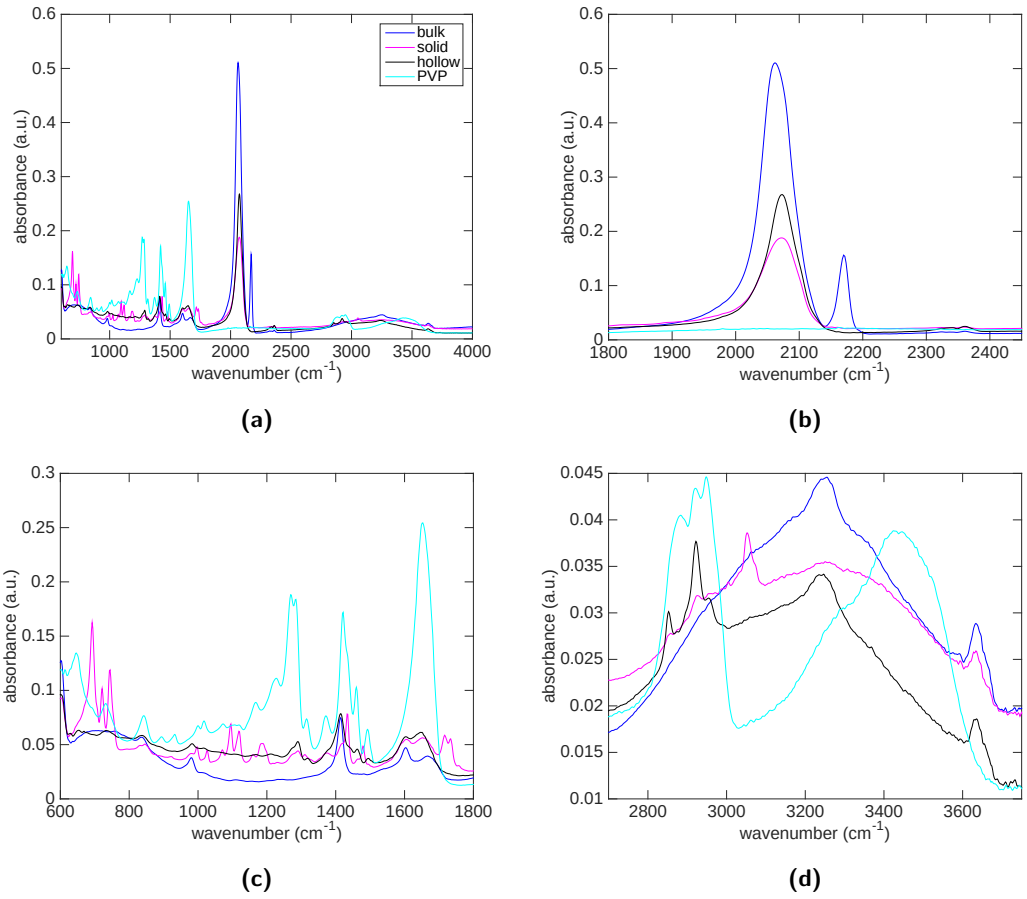

Figure 4.5: (a) FTIR spectrum of the three PB samples and of PVP. The blue line refers to the bulk sample, magenta to the solid nano, black to the hollow nano and light blue to PVP. (b) Stretching band originating from the CN, with maximum intensity located at approximately $2070\,\mathrm{cm}^{-1}$. The second peak at $2170\,\mathrm{cm}^{-1}$ in the bulk sample is due to the presence of $Fe^{III}-CN-Fe^{III}$ bonds in the network. (c) Mid-IR region, where most of the PVP peaks are observed, and (d) far-IR region, where the stretching modes of H_2O are located.

IR spectrum of the bulk sample correspond to values previously reported in the literature [184].

It is possible to identify very clearly the peak arising from the C≡N bond stretch in all the three samples, as shown in figure 4.5 a. However while in the case of the nanoparticles samples there is only one peak whose maximum falls at approximately $2072\,\mathrm{cm}^{-1}$, the bulk sample has also another feature at $2170\,\mathrm{cm}^{-1}$, figure 4.5 b. The C≡N bond stretching modes are in fact very sensitive to their surrounding environment [178, 185, 186] and the two peaks correspond to the CN group being in either of the $Fe^{II}-CN-Fe^{III}$ or the $Fe^{III}-CN-Fe^{III}$ moiety, respectively. This confirms, as inferred through observation of the green shade of the colour, that the bulk sample presents a lower number of vacancies in the framework compared to the nanoparticles with some of the Fe^{2+} sites in their oxidised form.

The literature reports a ratio of extinction coefficients of approximately 3:1 for the the mixed valence stretch with respect to the oxidised cyanide stretch [185]. The extinction coefficient k is related to the absorption coefficient α, through $\alpha = \frac{4\pi\nu k}{c}$, where ν is the frequency of the

incoming wave and c the speed of light in vacuum [187].

Thus, the ratio of extinction coefficients can be used to estimate the fraction of the two moieties in the sample. This is simply done by calculating the ratio of the area under the peak at $2072\,\mathrm{cm}^{-1}$ to the area under the peak at $2170\,\mathrm{cm}^{-1}$ and dividing it by 3. The calculation returns a concentration of approximately $3.5:1$ of $\mathrm{Fe^{II}}-\mathrm{CN}-\mathrm{Fe^{III}}$: $\mathrm{Fe^{III}}-\mathrm{CN}-\mathrm{Fe^{III}}$. The fact that the $\mathrm{Fe^{III}}-\mathrm{CN}-\mathrm{Fe^{III}}$ moiety is present in the sample indicates that the average number of vacancies found in the sample (and hence water molecules) must be lower than the number found in the original PB compound (where 6 empty sites can be occupied by coordinated water molecules).

Most of the peaks characteristic of PVP are located in the mid-IR region below $1800\,\mathrm{cm}^{-1}$, figure 4.5 (c). Both the solid and hollow nanoparticle samples present some features that are probably due to the presence of residual PVP in the sample. The relatively sharp feature at $1415\,\mathrm{cm}^{-1}$ of the bulk sample spectrum is also observed in the nanoparticles ones, but in the latter the width and shape of the peak are altered by the presence of a superimposed neighbouring peak at $1425\,\mathrm{cm}^{-1}$, that arises from the residual PVP. Analogously, the peak at $1605\,\mathrm{cm}^{-1}$ is present in all the three samples, but in the nanoparticle data there is also a broad feature at approximately $1655\,\mathrm{cm}^{-1}$, corresponding to the stretching vibration of the C=O in the PVP amide unit [188]. However, it should be noted that the H_2O bending modes fall between $1600\,\mathrm{cm}^{-1}$ and $1700\,\mathrm{cm}^{-1}$ [167], so these are also expected to give a contribution to the broad features in this region. The stretching modes of H_2O are instead located in the far-IR region above $2800\,\mathrm{cm}^{-1}$, as shown in figure 4.5 d [167].

Below $1400\,\mathrm{cm}^{-1}$ the intensities of the nanoparticles spectra can be mostly attributed to PVP (typical of PVP is e.g. the absorption band at $1285\,\mathrm{cm}^{-1}$). Only few peaks, signature of the PB compound, can be observed in this region: the low intensity peaks at $980\,\mathrm{cm}^{-1}$ and $835\,\mathrm{cm}^{-1}$, some broad features below $800\,\mathrm{cm}^{-1}$ and the right end of a peak with maximum at roughly $603\,\mathrm{cm}^{-1}$ (the left side not being visible since the data are measured down to $600\,\mathrm{cm}^{-1}$). All these peaks are characteristic of the PB spectrum. The nanoparticle samples present in this region a series of low intensity features that are probably due to the remaining PVP.

A slight shift or change in the PVP intensities observed in the nanoparticles data, compared to the pure PVP sample [189], is justified by the interaction between the nanoparticle and the polymer, that can affect the vibration modes of the latter. Previous studies of nanoparticles coated in PVP show that the FTIR intensities are affected by the interaction between the atoms on the surface of Ag and Au nanoparticle and the PVP [188, 190, 191]. In particular, in the study on Ag nanoparticles [190], it is observed that this interaction causes a variation of the C=O stretching feature at around $1700\,\mathrm{cm}^{-1}$.

Another possible contribution to the IR spectrum could be due to the presence of some DCN trapped in the pores that may give rise to the features between $600\,\mathrm{cm}^{-1}$ and $800\,\mathrm{cm}^{-1}$ in the

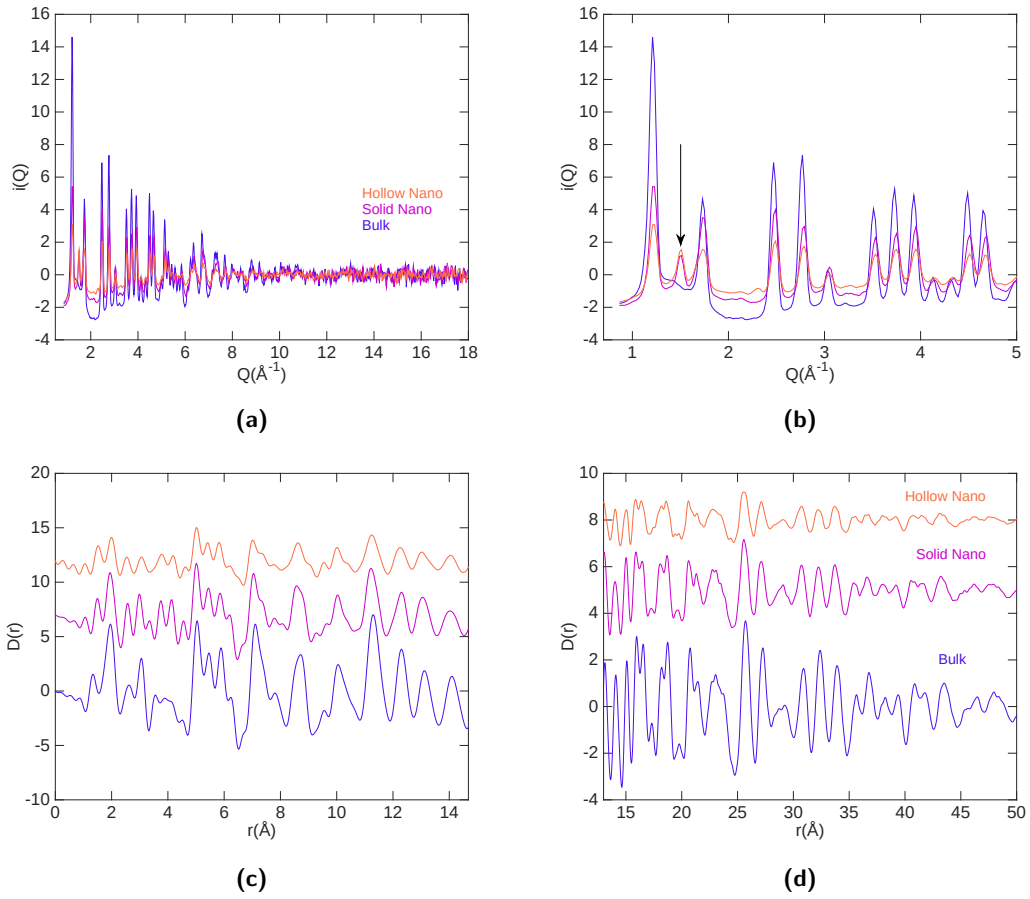

Figure 4.6: (a) Room temperature X-ray total scattering data of the three PB samples. (b) The peak, indicated by an arrow at $1.51\,\text{Å}^{-1}$, in the nanoparticle data, but absent in the bulk, corresponds to the 112 reflection that can be associated with ordering of the water in the pores. (c)-(d) Low and medium r range of the respective PDF functions. The hollow sample doesn't present any sharp feature beyond $35\,\text{Å}$ and the peaks are overall broader and less intense.

solid nanoparticles spectrum. The IR spectrum of HCN reported in the literature includes a doubly degenerate bending at $712.1\,\text{cm}^{-1}$ [192, 193]. However the lack of a peak of comparable intensity at $2630\,\text{cm}^{-1}$ [192], corresponding to the C–D stretch of DCN, invalidate partially this hypothesis.

4.3 Studies of the atomic structure

4.3.1 X-ray and neutron total scattering measurements

The X-ray data were collected on the three samples at room temperature, while the neutron data were collected at five temperatures (298 K, 220 K, 150 K, 100 K and 20 K). The two probes are used to focus the attention on the heavier and lighter atoms separately (X-ray and neutrons respectively), as in the case of the materials presented in the previous chapter. In particular, the contribution coming from water molecules or PVP content in the samples are minimised

in the X-ray data, while the contribution coming from PB framework is much more relevant (owing to the Fe content). The ratio of the intensities of the PDF peaks at 1.98 Å and 1.15 Å, that arise from Fe–N pairs and C−N pairs, respectively, is proportional to

$$\frac{n_{\mathrm{FeN}}\, c_{\mathrm{N}}\, c_{\mathrm{Fe}}\, Z_{\mathrm{N}}\, Z_{\mathrm{Fe}}}{n_{\mathrm{NC}}\, c_{\mathrm{N}}\, c_{\mathrm{C}}\, Z_{\mathrm{N}}\, Z_{\mathrm{C}}} = 4.3333 \tag{4.1}$$

where the X-ray scattering factors are approximated by the atomic numbers, Z. This ratio is even higher if calculated for the Fe–N peak to D–O peak (found at 0.98 Å) , giving 16.3798. Hence, the contribution from D and/or H is minimal in the X-ray data. However the Fe–O and O–O pairs are still going to contribute significantly with intensities comparable to the pairs containing C and N (since the atomic numbers of these elements are very close).

The room temperature X-ray total scattering data (figure 4.6 a) show that the structure of the three samples is relatively crystalline, owing to the presence of well-defined diffraction peaks. However the decrease of the intensity of the peaks and simultaneous increase of their widths, moving from the bulk to the solid and then hollow nano samples, indicate an increasing level of structural disorder. This confirms what is expected since the transition from bulk to nano and then from nanocrystals to hollow nanostructures, with the consequent presence of higher surface area, affect the local ordering of the atoms.

The appearance of a peak in the solid and hollow nanoparticle data at $Q = 1.51$ Å, absent in the bulk, is associated with the emergence of structural features in the nanocrystalline samples that are lacking in the bulk sample, figure 4.6 b. The peak corresponds to the reflections from the set of planes {112}, that are systematically absent in the $Fm\bar{3}m$ space group. Hence, it indicates a loss of face centring, that could be a consequence of a regular arrangement of the vacancies in the PB framework.

The nanoparticle data overall exhibit a loss of crystallinity, visible also in the real-space PDF data, figures 4.6 c and d. Although most peak positions are analogous in the three structures, the hollow sample does not present any sharp feature beyond 35 Å and the peaks are broader and less intense.

A first look at the neutron total scattering data of the solid nanoparticle and bulk samples (figures 4.7 a and 4.8 a respectively) does not show any significant difference between the various temperatures, except for an increase in the intensity of some of the reflections with decreasing temperature. However, it can be readily observed that the intensity of the peaks in the total scattering function (that were normalised with respect to $\langle b^2 \rangle$) is significantly higher for the bulk sample compared to the solid nanoparticles. This is natural, since the bulk phase is expected by definition to be more crystalline than any nanocrystalline phase of the same material.

On the other hand, the PDF functions (figures 4.7 c, d and 4.8 c, d) show some variations with temperature, especially in the low-r region, whose features are not easily observed by eye

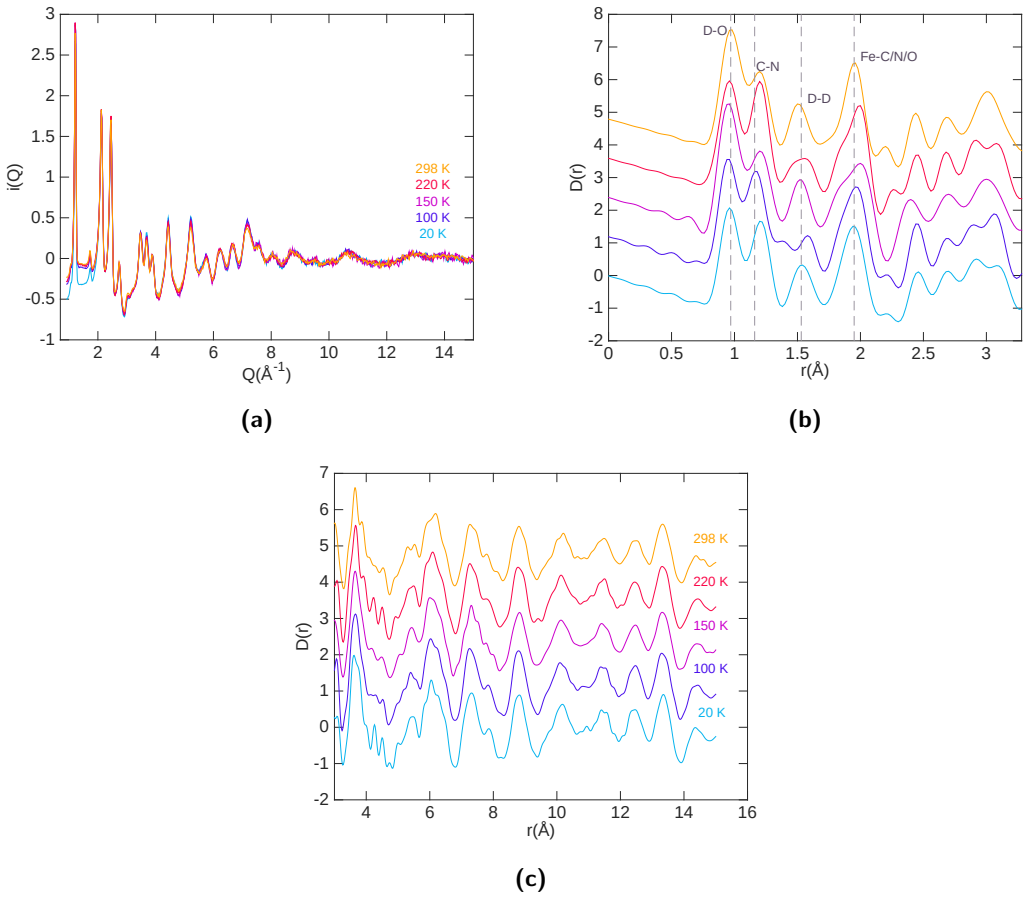

Figure 4.7: (a) Neutron total scattering functions of the solid nanoparticle data at different temperatures. (b) Low-r range of the PDF functions at each temperature, showing the average positions and corresponding atomic pairs of the first four peaks. (c) Medium range-order of the PDF.

in the scattering function $i(Q)$. The origin of these differences is explored using the Reverse Monte Carlo technique in the following sections. However, this may be mainly due to variations in the degree of disorder of the PB framework and to the ordering of coordinated and free water molecules. Interestingly, the variations of the first and second water peaks (D–O and D–D) in both samples seem to follow the same temperature dependence (which also reduced the possibility of these features being due to spurious effects arising from noise and data corrections). In particular the intensity and width (linked to the the structural ordering) of these peaks follow an oscillatory behaviour, decreasing when going from temperature 298 K to 220 K, increasing at 150 K, to then decrease and increase again at the lower temperatures.

A comparison between the solid nanoparticle and bulk PDF data (figure 4.9 b) shows that the relative intensities of the first two peaks, D–O and C–N are inverted in the two samples (i.e. the D–O is more intense than the C–N peak in the nanoparticle PDF while the opposite is observed in the bulk). This is consistent with the conclusions inferred based on the colour of the bulk sample, the analysis of the IR spectrum and elemental analysis: the bulk structure

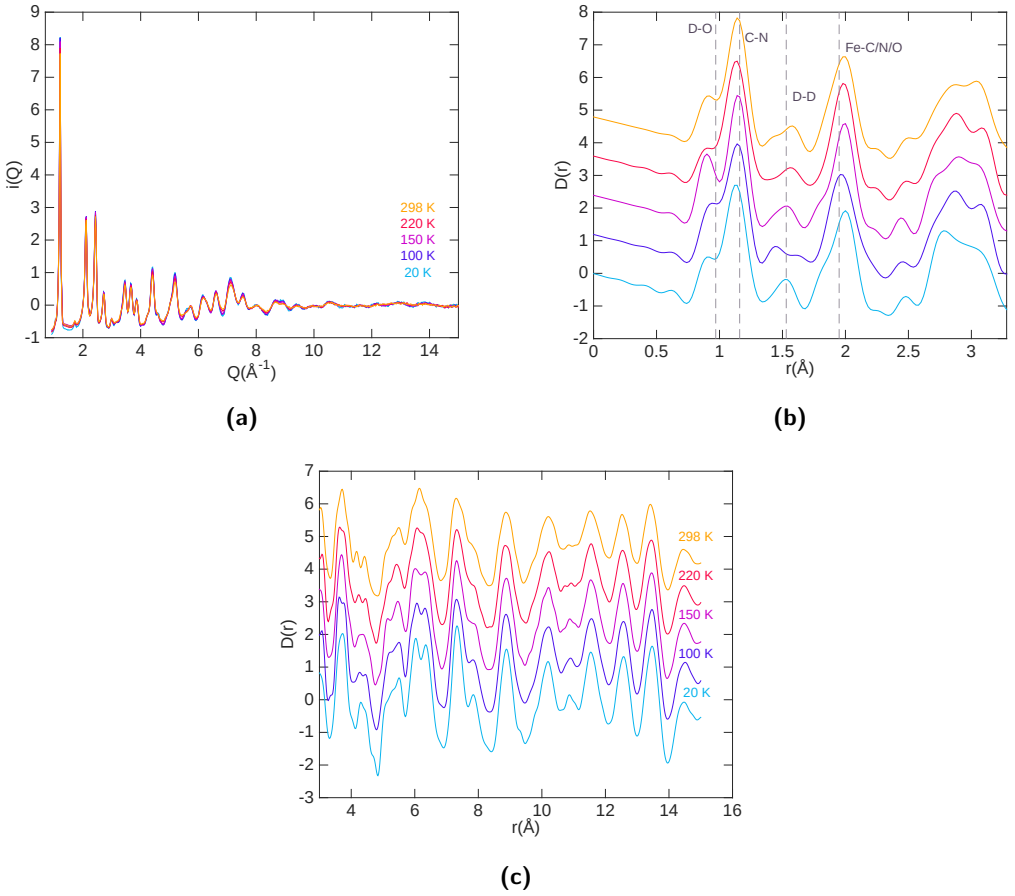

Figure 4.8: (a) Neutron total scattering data of the bulk sample at different temperatures. (b) The short and (c) medium range order of the corresponding PDF functions.

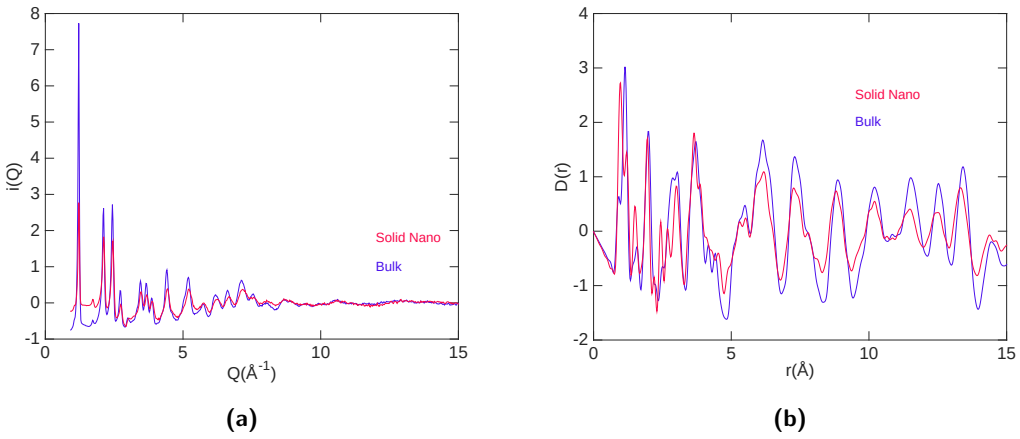

Figure 4.9: a) Room temperature neutron total scattering functions of the bulk and solid nano samples and b) corresponding PDF functions.

presents a lower number of vacancies compared to the case of the original PB structure and therefore less water can be accommodated in the pores, resulting in a decrease of the relative intensity of the first peak. It can also be observed that the first peak appears slightly shifted to lower r, with average position at 0.92 Å. This could be due to a difference in the local ordering of the water molecules in this structure. This distance is shorter than what has been observed in previous studies of heavy water by 0.05 Å, so it is not excluded the possibility of the presence of low-r spurious effects due to high-Q truncation reflected in the Fourier transform. However its consistency across the various temperatures offers evidence for the reliability of this peak. Finally, the slightly higher low-Q level of the solid nano data is probably a signature of the higher H content (due to the PVP remaining in the sample), owing to the recoil of the H atoms.

4.3.2 Data correction

Owing to the high intensity of the noise in the data collected by the different banks of NIMROD detectors, we were obliged to exclude some of the banks and use $Q_{\max} \approx 31\,\text{Å}^{-1}$ for the calculations and corrections in `GudrunN`. Most of the low angle banks were not included in the data correction and the high Q range ($Q > 20\,\text{Å}^{-1}$) was included from only few of the high angle banks. The modified Lorch parameters described in section 2.3.3 were used to get rid of spurious truncation ripples in the PDF functions.

The exact composition (in particular the exact amount of water and PVP) and density of the samples were also uncertain. This problem was overcome by combining information from the elemental analysis and the IR spectrometry with a bespoke modelling procedure of the first few peaks of the $G(r)$ function, that was used to determine the concentrations of the elements and the overall density (section 4.4.1).

The X-ray data also presented a relatively high amount of noise, owing to truncation ripples generated by the limited Q-range. Moreover, although the data were collected up to approximately 21.5 Å it was decided to include the points only up to $Q_{\max} = 18.5\,\text{Å}^{-1}$, $18.2\,\text{Å}^{-1}$ and $18\,\text{Å}^{-1}$ for the bulk, solid and hollow nano samples respectively, since there were no usable data beyond these maxima.

4.4 Modelling

4.4.1 The water and PVP content: least squares fitting

The neutron PDF shows the presence of a positive peak at approximately 1 Å. This interatomic distance is likely to be associated with the presence of D_2O located in the vacancies and interstitially in the pores, since, as previously mentioned, all the steps in the synthesis were performed using deuterated chemicals. This does not however exclude the possibility of the

presence of a small percentage of H_2O relative to the D_2O content. The water content is quite hard to estimate through elemental analysis; moreover, once the sample is exposed to the atmosphere, it can easily release/absorb water molecules, owing to the porous nature of the framework, resulting in changes in the effective composition of the sample.

The information about the water (deuterated or not) content in the samples at the time of the measurements are contained in the PDF functions themselves; even though what is obtained Fourier transforming the total scattering data is the overall pair distribution function of the sample, we can estimate the partial PDFs, from which the concentrations of atomic species in the sample at the time of measurement can be evaluated.

The procedure used involves performing a least squares fitting of the experimental $G(r)$ by adding together Gaussian functions that reproduce the contribution from peaks arising from individual pairs of atoms. The fitting was performed in the low-r region, including distances below 2.13 Å. In this region we find interatomic distances corresponding to the D/H–O and O–O bonds of $D_{/}H_2O$ (i.e. the first and second nearest neighbour of water) and intermolecular O−$D_{/}$H hydrogen bonds, the distances corresponding to C–N and Fe–C/N of $Fe_4(Fe(CN)_6)_3$, as well as Fe–O (i.e. the distances between Fe and coordinated O molecules). Several peaks corresponding to interatomic distances in the PVP monomer are also found in this region (details are given in the following sections). Previous studies [194, 195] have shown that heavy water is a more structured liquid than light water: the former presents in fact longer and more symmetric intermolecular hydrogen bonds compared to the latter, with average distance 1.81 Å, as well as more symmetric and shorter intramolecular D−O distance, with average distance 0.9687 Å. Moreover the number of hydrogen bonds per water molecule in heavy water is higher than in light water, being 3.76 ± 0.1 and 3.62 ± 0.1 respectively [195].

Since the theoretical mean position and the coordination number of each peak are known, this information can be used to parametrise and constrain the fitting of the functions to the data; similarly the molecular concentrations can be used to apply constraints to the fit.

4.4.1.1 The method used in the determination of the composition and density

Since as already mentioned the corrections for these data sets present a series of challenges, the least square fitting procedure was used in an iterative process (going back and forth from `Gudrun` to the fit, written in `Matlab`) until an acceptable agreement between `Gudrun` and the results of the fit was achieved. The work-flow for this process is schematically shown in the flow chart in figure 4.10.

The procedure can be summarised in few steps. Firstly, initial guess values for the atomic fractions and density are used to perform the first `Gudrun` corrections. Once the `Gudrun` corrections produce output functions with the correct merged differential cross section values (the tweak factor is also modified accordingly), the $G'(r)$ function is calculated. Details of this function

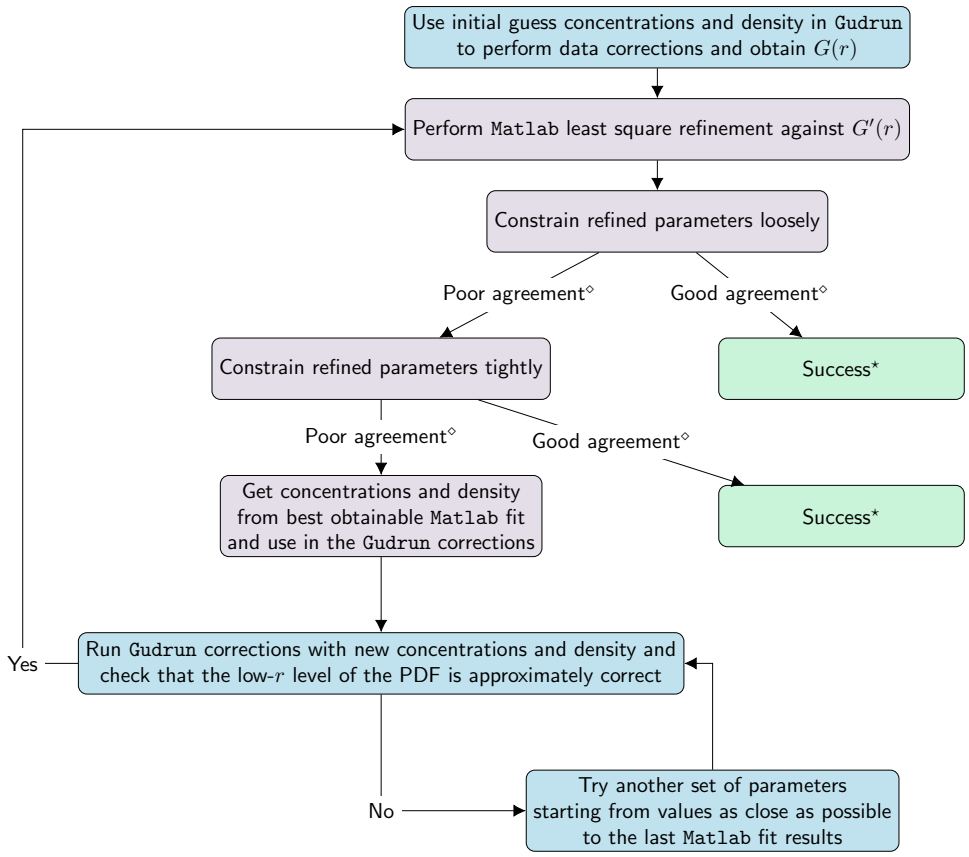

◇ Agreement between the data and the model, as well as between the values of the atomic composition and density used in Gudrun and those obtained through the Matlab least square refinement.

⋆ The composition and density values obtained through the Matlab least square refinement are accepted and used as final values in the corrections.

Figure 4.10: Flow-chart explaining the iterative process used for determining the correct composition and density of the samples. This involves the use of Gudrun and of the Matlab least square fitting code. The different colours of the boxes refer to operations performed in Gudrun ■, Matlab ■ or termination of the process ■.

will be given in the following section, but for now it is enough to know that it is a normalised $G(r)$ with low-r limit equal to zero.

Subsequently, a model $G'(r)$ function is refined against the data in the region of interest, through a bespoke least squares refinement code written in Matlab. The model $G'(r)$ function is calculated from the sum of a series of Gaussians that represent the contribution to the total function arising from individual pairs of atoms. Considering the Gaussian i corresponding to a specific peak of the partial pair distribution function of the pair of atoms n and m, the Gaussian depends on c_n and c_m, atomic fractions of the two elements, and on σ_i, its standard deviation. So c_n, c_m and σ_i are the refined parameters for each Gaussian. Some constraints, based on the stoichiometry of the compound, are applied.

The means of the Gaussians are instead fixed to values known from the literature, with, in some cases a deviation < 0.1 Å from the reported value depending on where the maximum of a

peak is observed in our data. Moreover, each Gaussian is also multiplied by a factor dependent on ρ, the average atomic density of the material, which is dependent upon the atomic fractions c_j of all the elements j involved in the fitting. This is the case also for the normalisation factor that the model $G'(r)$ is multiplied by.

Firstly loose conditions are applied to the parameters, using a wide window $\Delta x = x_u - x_l$ of possible values that the parameter x can take, where x_u is the upper limit and x_l the lower limit. This is done in order to check whether the model is able to produce a refinement of the data, consistent with the concentrations and density used in `Gudrun`, without application of tight conditions. If this process is successful the values used in `Gudrun` are accepted as the corrected composition and density.

Otherwise, tighter constraints are applied. If the refinement gives a good agreement with the data and initial parameters, the value of the composition and density obtained are accepted. Alternatively, the values of composition and density from the best fit to the data are used as parameters to perform a new `Gudrun` correction run.

The regularity of the levels of the $G(r)$ and $D(r)$ below the minimum of the first peak was among the factors used to judge whether the composition and density used in `Gudrun` were correct: the first minimum of the functions beyond the first interatomic peak (i.e. a distance $r > r_{\max_1}$ where no interatomic distances are expected to occur, so that $g(r) \approx 0$) has to sit approximately on the direction drawn by the level (in the case of $G(r)$) or gradient (for $D(r)$) of the data below the first peak ($r > r_{\min_1}$).

4.4.1.2 The choice of the parameters and Gaussian functions refined in the fit

Owing to the uncertainty in the exact composition of the nanoparticles samples two main possibilities were considered: the case where the PVP content can be approximated to zero or where the PVP is still present in the sample and it represents a substantial fraction of the composition. In both situations the cases where some H_2O (as well as HDO) is present in the samples (owing to exchange between D and H) or where no H is present in the sample were also considered, with D and H referring to the two isotopes of hydrogen, ^{2}H and ^{1}H. The situation where some PVP is present was considered only in the case of the solid nanoparticles sample, since the synthesis of the bulk does not involve its use.

The four models used can be summarised, depending on the PVP and ^{1}H content, as:

1. no PVP, no ^{1}H
2. no PVP, ^{1}H present in H_2O
3. PVP but no ^{1}H present otherwise
4. PVP, and ^{1}H also present in H_2O

and we will refer to each of these by the respective number in the list.

The assumption that no H_2O is present in the sample is realistic since all the syntheses were performed in deuterated chemicals, except for the PVP that was used in its hydrogenated form. The only two sources of H that could substitute the D in the D_2O molecules are the moisture in the air and the PVP; however, the first eventuality was minimised by keeping the samples in oven under vacuum or under Ar flow, as well as manipulated in nitrogen glove boxes, between the synthesis and the neutron experiments. The second is more likely to happen when the samples are still in solution, since, once the nanoparticles are formed, the PVP is located on the surface, with the amide unit bonding to the iron ions, and the likelihood of exchange becomes lower (being in some way proportional to the surface to volume ratio of the nanoparticles, $0.05\,\mathrm{nm}^{-1}$). In any case, the concentration of H (from PVP) is significantly lower than the D number ratio. In the synthesis of the solid nanoparticles, where the highest concentration of PVP is used, the ratio of H to D is approximately 1:13.4. So, even in this case the likelihood of hydrogenated molecules of water forming and being absorbed in the PB framework is very low.

The refinements performed including light water, either in the presence or not of PVP contributions (i.e. models 2. and 4.), returned results that are not compatible with the concentration of elements used in the synthesis procedure. Moreover, when the estimated concentrations were used as input parameters for the `Gudrun` corrections, the resulting PDF did not have the correct low-r level. The H percentage returned as a result of the fit was greater than what would be expected, based on the composition of the solution; the fits returned D:H ratios of approximately 2:1, while, as previously mentioned, this ratio is 13:1 in the nanoparticle solution.

However, when H was not included in the composition (model 1), the `Gudrun` corrections were very unstable. The values of the tweak factor needed for the level of the merged differential cross section to be correct were close to or smaller than 1, which, for a powder sample, is not realistic if not even unphysical. The low-r level of the PDF function also appeared to be largely incorrect (see figure 4.11 a).

The IR measurements show that, even if in low concentration, some PVP has remained in the nanoparticles samples. So the H contribution to the scattering is most likely coming from the PVP. For these reasons, after several attempts, the fit including peaks from PVP and D_2O and excluding the presence of light water (i.e. model 3) was chosen and the fit and correction repeated until a good agreement was achieved. Hence model 3 was used for fitting to the nanoparticle data and model 1 to the bulk data (since the bulk sample does not contain PVP).

It was mentioned that the water absorbed in the pores of the PB framework is expected to present some degree of correlation that goes beyond the intramolecular distances (even more so since heavy water is expected to dominate), with hydrogen bonds forming between neighbouring water molecules. However, being segregated in the pores of the structure, not all atoms will be

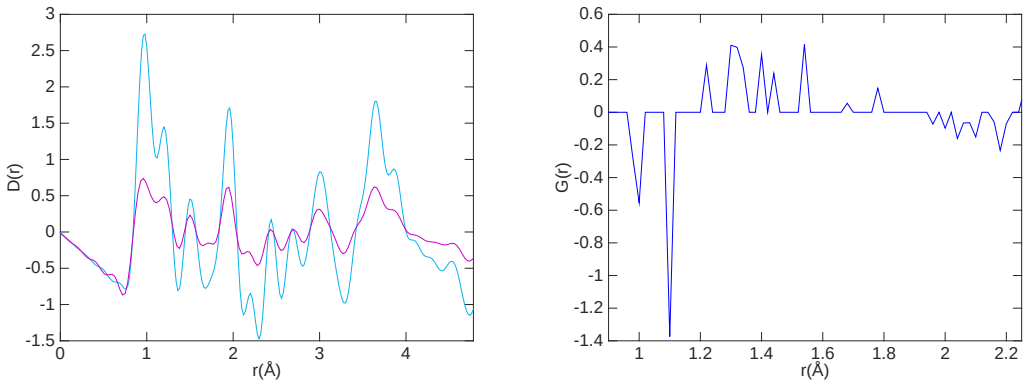

(a) (b)

Figure 4.11: (a) The solid nanoparticle room temperature neutron PDF function, including H in the composition (cyan curve) or not (magenta). When H is not included the scale of the PDF is substantially affected, showing a large discrepancy between the low r limit of the function and its baseline beyond the first peak, indicating a lack of consistency in the concentration and density values used in the data correction. (b) Reference PDF function from the theoretical structure of a monomer of PVP, vinylpyrrolidone (shown in figure 4.4). The PDF presents a dense forest of negative and positive peaks in the range of distances considered.

involved in intramolecular bonds. For this reason, the peak for the intramolecular D–O and H–O interaction is included in the least square fitting procedure adding a scale factor to account for the fraction of atoms that do not form hydrogen bonds; this was set to $0.684 = 1 - 0.316$, since 0.316 is the fraction of atom that is likely to sit in pores that do not contain vacancies (section 4.1.1).

While the water and PB PDFs present well defined isolated peaks, the theoretical structure of the PVP monomer has a dense distribution of low intensity peaks in the range between 1 and 2.2 Å as can be seen from the PDF calculated from the theoretical structure of vinylpyrrolidone, figure 4.11 b. For the purpose of this modelling, some of the peaks were grouped in one broader peak and were assigned the respective weightings based on the scattering length of the atoms involved.

At the beginning of this section, it was mentioned that the low-r level of the PDF was among the methods used to judge the reliability of the parameters used in `Gudrun`. However, we bore in mind that in the case of the nanoparticles, since the PVP contributes to the PDF with a series of distances that are spread across the whole range analysed, it is also expected that the low-r levels of the $G(r)$ and $D(r)$ will mot match exactly the tangent to any of the local minima of the first few peaks, but they will be slightly lower; in fact, even where there is a local minimum, there are still low intensity contributions due to the PVP content (i.e. $g(r) \neq 0$).

4.4.1.3 The formalism used for the fitting procedure

We recall here for convenience equation 2.35:

$$\mathcal{N}_{nm}(r_{\min}, r_{\max}) = \frac{c_m}{c_n} \quad \mathcal{N}_{mn}(r_{\min}, r_{\max}) \tag{4.2}$$

This defines the relationship between the number of atoms of type m coordinated to an atom n at the origin $\mathcal{N}_{nm}(r_{\min}, r_{\max})$ and the number of atoms of type n coordinated to an atom m at the origin, $\mathcal{N}_{mn}(r_{\min}, r_{\max})$. As an example, considering $\mathcal{N}_{\mathrm{FeC}}$, the number of atoms C in PB, at a distance between approximately $r_{\min} = 1.70\,\text{Å}$ and $r_{\max} = 2.15\,\text{Å}$ from a Fe atom

$$\mathcal{N}_{FeC}(r_{\min}, r_{\max}) = \frac{c_C}{c_{Fe}}\mathcal{N}_{CFe}(r_{\min}, r_{\max}) = \frac{18}{7} = 2.5714 \tag{4.3}$$

since $N_{CFe} = 1$, being every C atom coordinated to one Fe atom, while not all Fe are surrounded by six C atoms, since some are coordinated to N and others to O or a vacancy. Equation 4.2 can be applied to all the atomic pairs in the sample.

As already mentioned, a normalised $G(r)$ function is used in the fit. `Gudrun` offers several choices for the normalisation of the PDF and total scattering data. In this work we use the normalisation with respect to $\left(\sum_{i=1}^{m} c_i b_i\right)^2$, that, since $\lim_{r\to 0} G(r) = -\left(\sum_{i=1}^{m} c_i b_i\right)^2$, has the effect of producing a function whose low-r limit is -1. We then add 1 in order to produce a function, sometimes called normalised $G'(r)$, with $\lim_{r\to 0} G'(r) = 0$ [124], which is easier to manipulate for the purpose of our fit. The script used for the least square refinement is shown in appendix A.3. Hence, the model function refined against the data has the following form:

$$G'(r) = \left(\sum_{i=1}^{m} c_i b_i\right)^{-2} \sum_{i,j\geq i}^{m,n} c_i c_j b_i b_j g_{ij}(r) \tag{4.4}$$

and in the fitting procedure, each element of the sum is computed individually. From 2.34, which we recall here is given by

$$\mathcal{N}_{mn}(r_{\min}, r_{\max}) = 4\pi c_n \rho \int_{r_{\min}}^{r_{\max}} r^2\, g_{mn}(r)\, \mathrm{d}r \tag{4.5}$$

we can also write

$$g_{mn}(r) = \frac{\mathcal{N}_{mn}(r)}{4\pi\rho_n r^2}. \tag{4.6}$$

Incidentally, recalling that $\rho_n = c_n\rho$, we can rewrite this equation as:

$$g_{mn}(r) = \frac{\mathcal{N}_{mn}(r)}{4\pi c_n \rho r^2} = \frac{\mathcal{N}_{mn}(r)}{4\pi r^2 \mathcal{N}_n / V} = \frac{\mathcal{N}_{mn}(r)}{\frac{\mathcal{N}_n}{V/4\pi r^2}} = \frac{\mathcal{N}_{mn}(r)}{\overline{\mathcal{N}}_n(r)} \tag{4.7}$$

where $\mathcal{N}_{mn}(r)$ are the number of particles of type n between distances r and $r + \mathrm{d}r$ from a

particle of type m and $\overline{\mathcal{N}}_n(r)$ is the average number of atoms of type n in a volume $4\pi r^2 \mathrm{d}r$. This expression shows that this function is a density distribution, as anticipated from the methodology section.

In the modelling procedure it is assumed that, since the range of r values, e.g. $\Delta r = r_{\max} - r_{\min}$, covered by one single peak, is relatively small, equation 4.6 can be rewritten in a finite approximated form, that defines $g(r)$ in this range as:

$$g_{mn}(r)\big|_{(r_{min},r_{max})} = \frac{\mathcal{N}_{mn}(r_{min}, r_{max})}{4\pi\rho_n \bar{r}^2 \Delta r}\mathcal{G}(r) \tag{4.8}$$

where $\bar{r}$ is the mid-point of the distribution (e.g. the average distance between atoms m and n); $\mathcal{G}(r)$ is a Gaussian function (with area normalised to 1) i.e.:

$$\mathcal{G}(r) = \frac{1}{\sigma\sqrt{2\pi}} \exp\left[-\frac{1}{2}\left(\frac{r-\bar{r}}{\sigma}\right)^2\right] \tag{4.9}$$

since, as already mentioned, the distribution of atomic positions around the average is approximated by a Gaussian. As a consequence in 4.8 the substitution $\Delta r \approx 6\sigma$ can also be made, since this corresponds approximately to the width of the Gaussian and is approximately equal to the distance interval of relevance.

From equation 2.31 the $g_{mn}(r)$ and $g_{nm}(r)$ components are identical (as one would also expect intuitively), so they can be paired up together, i.e. $c_n c_m b_n b_m (g_{nm}(r) + g_{mn}(r)) = 2c_n c_m b_n b_m g_{nm}(r)$ and expressed as a function of $\mathcal{N}_{mn}(r_{\min}, r_{\max})$ as above (equation 4.8).

So, from equations 2.32, 4.3 and 4.8 the atom pair Fe–C will contribute the following term to the PDF function:

$$\begin{aligned} G'(r)_{\mathrm{FeC}} &= \left(\sum_{i=1}^{m} c_i b_i\right)^2 2c_{\mathrm{C}} c_{\mathrm{Fe}} b_{\mathrm{C}} b_{\mathrm{Fe}} g_{\mathrm{FeC}}(r) \\ &= \left(\sum_{i=1}^{m} c_i b_i\right)^2 2c_{\mathrm{Fe}} b_{\mathrm{C}} b_{Fe} \frac{\mathcal{N}_{\mathrm{FeC}}(r_{\min}, r_{\max})}{4\pi\rho\bar{r}^2 6\sigma}\mathcal{G}(r) = \\ &= \left(\sum_{i=1}^{m} c_i b_i\right)^2 2c_{\mathrm{C}} b_{\mathrm{C}} b_{\mathrm{Fe}} \frac{\mathcal{N}_{\mathrm{CFe}}(r_{\min}, r_{\max})}{4\pi\rho\bar{r}^2 6\sigma}\mathcal{G}(r). \end{aligned} \tag{4.10}$$

$G'(r)_{\mathrm{FeC}}$ is the function used in the least square refinement fit to model the partial pair distribution function peak corresponding to the pair of atoms Fe–C. The other functions used for the refinement of the other PDF peaks are defined analogously. In the refinement, the means of the gaussian functions, $\bar{r}$, were fixed to values known from the literature, while the standard deviations and the concentrations of the elements (σ_i, c_n and c_m) were refined subject to some constraints. The parameters refined in the fit are listed in table 4.2.

The number of parameters was minimised applying the following conditions to the concen-

trations:

$$c_{\mathrm{O}} = \frac{1}{2}(\mathrm{c}_{\mathrm{D(D_2O)}} + \mathrm{c}_{\mathrm{H(H_2O)}}) \tag{4.11a}$$

$$c_{\mathrm{C(PB)}} = c_{\mathrm{N(PB)}} \tag{4.11b}$$

$$c_{\mathrm{Fe(PB)}} = \frac{7}{18} c_{\mathrm{C(PB)}} \tag{4.11c}$$

$$c_{\mathrm{N(PVP)}} = c_{\mathrm{O(PVP)}} \tag{4.11d}$$

$$c_{\mathrm{H(PVP)}} = 9c_{\mathrm{O(PVP)}} \tag{4.11e}$$

$$c_{\mathrm{C(PVP)}} = 6c_{\mathrm{O(PVP)}} \tag{4.11f}$$

The least square fit produces refined atomic fractions, whose sum is normalised to approximately 1. The fractions are then converted to number of atoms (or molecules) of each species per unit cell, starting from the assumption that one unit cell contains 18 C and N and 7 Fe atoms (i.e. the material has the PB structure) in the case of the nanoparticle sample and 24 C and N and 8 Fe atoms in the case of the bulk.

As an example, in the solid nanoparticle case, given a concentration x of C atom from the PB framework and y concentration of D atom, the number d of D atoms per unit cell is calculated as $d = \frac{18y}{x}$ (analogously for the other elements/molecules). The density of the sample (calculated as number of atoms per unit cell) is dependent on the refined concentrations, so it is recalculated at each time and used in the calculation of the partial pdfs.
The formulas used for the calculation of the density are the following:

$$\rho_1 = \left[\frac{18}{c_{C_{\mathrm{PB}}}} 1.5 c_D + 43\right] / V_{\mathrm{PB}} \tag{4.12a}$$

$$\rho_2 = \left[\frac{18}{c_{C_{\mathrm{PB}}}} 1.5 (c_D + c_H) + 43\right] / V_{\mathrm{PB}} \tag{4.12b}$$

$$\rho_3 = \left[\frac{18}{c_{C_{\mathrm{PB}}}} (1.5 c_D + 17 c_{N_{\mathrm{PVP}}}) + 43\right] / \left[18 c_{N_{\mathrm{PVP}}} V_{\mathrm{vinyl}} / c_{C_{\mathrm{PB}}} + V_{\mathrm{PB}}\right] \tag{4.12c}$$

$$\rho_4 = \left[\frac{18}{c_{C_{\mathrm{PB}}}} (1.5 (c_D + c_H) + 17 c_{N_{\mathrm{PVP}}}) + 43\right] / \left[18 c_{N_{\mathrm{PVP}}} V_{\mathrm{vinyl}} / c_{C_{\mathrm{PB}}} + V_{\mathrm{PB}}\right] \tag{4.12d}$$

depending on whether the model 1, 2, 3 or 4 (as described in the previous section) are used, respectively. V_{PB} is the volume of the PB unit cell and V_{vinyl} is the volume occupied by a vinyl monomer ($V_{\mathrm{PB}} = 10.13^3 \text{Å}^3$ and $V_{\mathrm{vinyl}} = 5.62^3 \text{Å}^3$), 43 is the number of atoms contained in a PB unit cell with 25% vacancies and 17 is the number of atoms in a PVP monomer. The volume of a single vinyl monomer was estimated starting from the density of the material reported in the literature. Analogous are the expression for the bulk case, excluding the PVP content

and changing the number of atoms in a PB unit cell and number of C and N atoms to the appropriate values.

Table 4.2

Type of parameters	Refined parameters and corresponding number					
Atomic fractions	$c_{\mathrm{C/N_{PB}}}$	c_{D}	$c_{\mathrm{O_{PVP}}}$			
Parameter number*	5	6	8			
Standard deviations of PB and D_2O peaks	$\sigma_{\mathrm{D-O}}$	$\sigma_{\mathrm{C-N}}$	$\sigma_{\mathrm{D-D}}$	$\sigma_{\mathrm{D-O}^{*}_{i}}$	$\sigma_{\mathrm{Fe-C/N/O}^{\dagger}}$	
Parameter number*	1	2	3	7	4	
Standard deviations of PVP peaks	$\sigma_{\mathrm{C-H}^{\bullet}_{1}}$	$\sigma_{\mathrm{C-H}^{\bullet}_{2}}$	$\sigma_{\mathrm{C-N/O/C}^{\dagger}}$	$\sigma_{\mathrm{C-C}}$	$\sigma_{\mathrm{H-H}}$	$\sigma_{\mathrm{H-C/N}^{\dagger}}$
Parameter number*	11	9	10	13	12	14

The table reports the parameters used in the fit performed including PVP and water only as D_2O (i.e. no H_2O). The parameters number from 1 to 7 (i.e. all those corresponding to peaks arising from PB and D_2O) are the same used in the fit of the bulk sample. The subscripts of the σ are consistent with the peaks labels shown in figures 4.12 c and 4.13 c.

* These numbers correspond to those used to represent the parameters in the correlation matrix in figures 4.12 b and 4.13 b.

* Intermolecular hydrogen bond.

† These refer to gaussians where several peaks are included in one.

$^{\bullet}$ The two C−H peaks of PVP at $r_1 = 1\,\text{Å}$ and $r_2 = 1.1\,\text{Å}$ are represented by separate Gaussians.

Table 4.3

Solid nanoparticles least square fit results						
Temperature (K)	298	220	150	100	20	% agreement*
D atoms†	27.2	25.5	26.9	31.4	20	15.5 %
Density (atoms/Å^3)	0.081	0.073	0.087	0.080	0.079	0.1%
PVP monomers†	1.1	1.33	1.19	2.1	1.2	21.3 %

The data were corrected in `Gudrun`, assuming 25% vacancies in the PB framework, 15 D_2O molecules and 1.4 PVP, thus using the overall composition Fe 7, C 26.4, N 19.4, D 30, H 12.6 O 16.4 and the density $\rho = 0.0837$atoms/Å^3. The tweak factors used were between 2.44 and 2.52.
* Determined according to equation 4.13.
† Number of atoms or monomers per unit cell (assuming 7 Fe atoms in one unit cell). The corresponding number of O and D_2O molecule is given by the number of D atoms divided by 2.

4.4.1.4 The results of the refinements

The results of the final refinements for neutron data of the solid nanoparticle and the bulk samples are reported in table 4.3 and 4.4, respectively. Since the neutron experiments were performed at temperatures between 20 K and 298 K, the concentration of water in the pores is expected to remain almost constant (the temperature is not high enough for the sample to be desolvated or loose the uncoordinated water molecules). In the data correction and least square refinement analysis, it was assumed that the water content is approximately constant across all temperatures. Thus, a mean percent agreement between the parameter used as `Gudrun` input and its estimated value across the various temperatures was calculated as:

$$\frac{2\sum_{i=1}^{5}|y_i - a|/5}{a + \sum_{i=1}^{5} y_i/5} \tag{4.13}$$

where the sum comprises five elements, one for each temperature, y_i is the refined parameter (i.e. number of D atoms, of PVP monomers or density, ρ) calculated at temperature i, a is the

Table 4.4

Bulk least square fit results						
Temperature (K)	298	220	150	100	20	% agreement*
D atoms†	10.3	6.5	9.5	8.9	8.2	15.4 %
Density (atoms/Å^3)	0.0761	0.065	0.069	0.068	0.067	0.07%

The data were corrected in `Gudrun` using the composition Fe 7.7, C 23, N 23, D 10, O 5, H 4. The density $\rho = 0.0699$atoms/Å^3 and tweak factors between 2.3 and 2.4.
* Determined according to equation 4.13.
† Number of atoms per unit cell (assuming 7.7 Fe atoms in one unit cell). The corresponding number of O and D_2O molecule is given by the number of D atoms divided by 2.

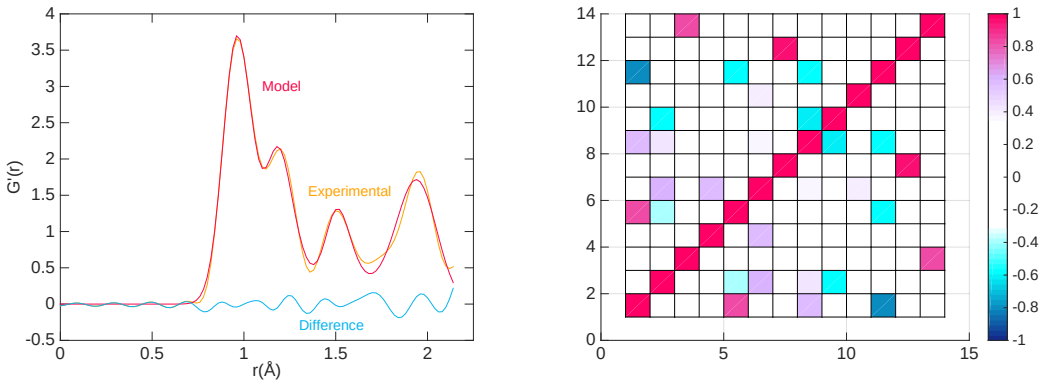

(a) (b)

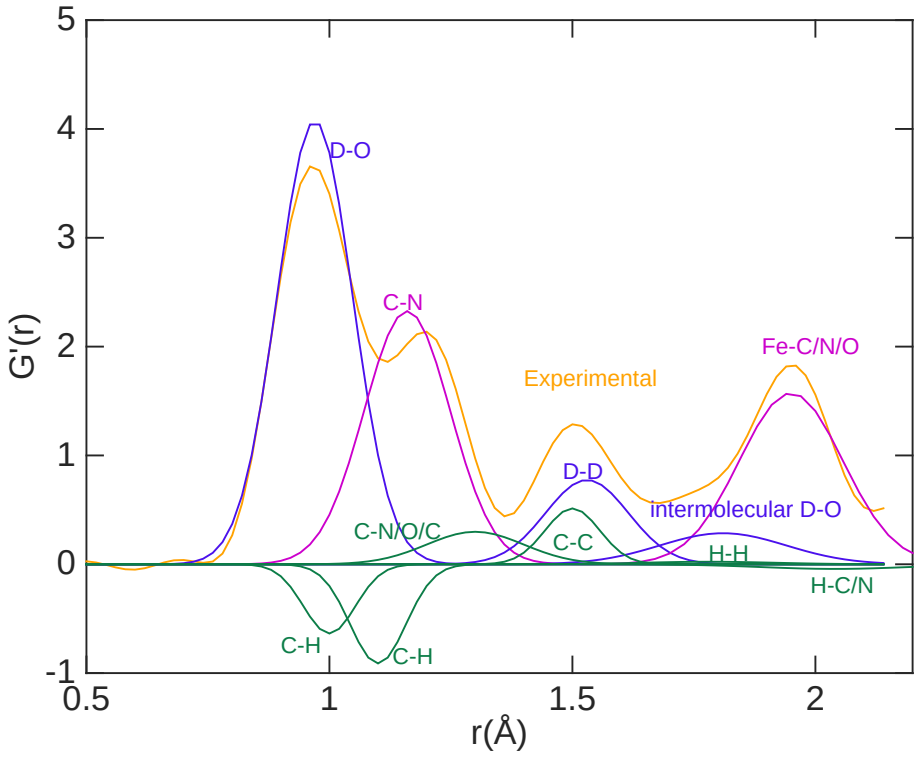

(c)

Figure 4.12: (a) Comparison between the gaussian model function and the room temperature neutron data. (b) Correlation matrix of the parameters refined in the fit, including the Gaussians standard deviations and the concentration of the elements. The parameters corresponding to the numbers in the matrix are listed in 4.2. (c) Gaussian functions corresponding to individual pairs, used in the refinement, with the peaks due to D_2O contributions coloured in blue, to the PB framework in magenta and PVP in green.

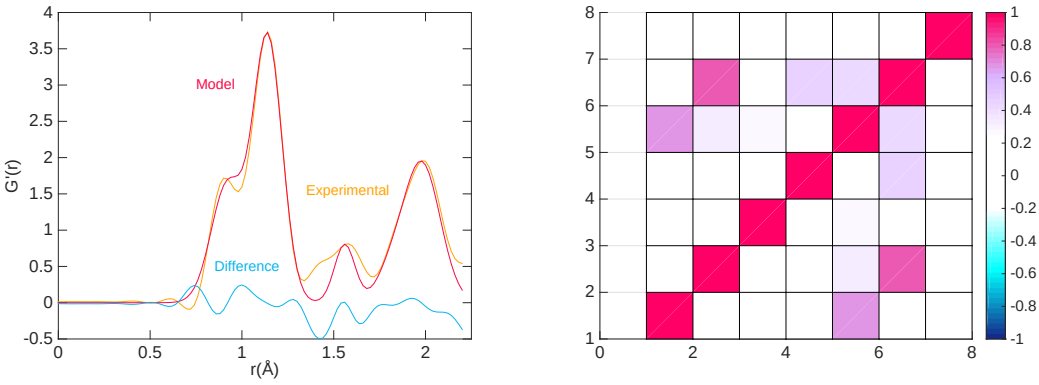

(a) (b)

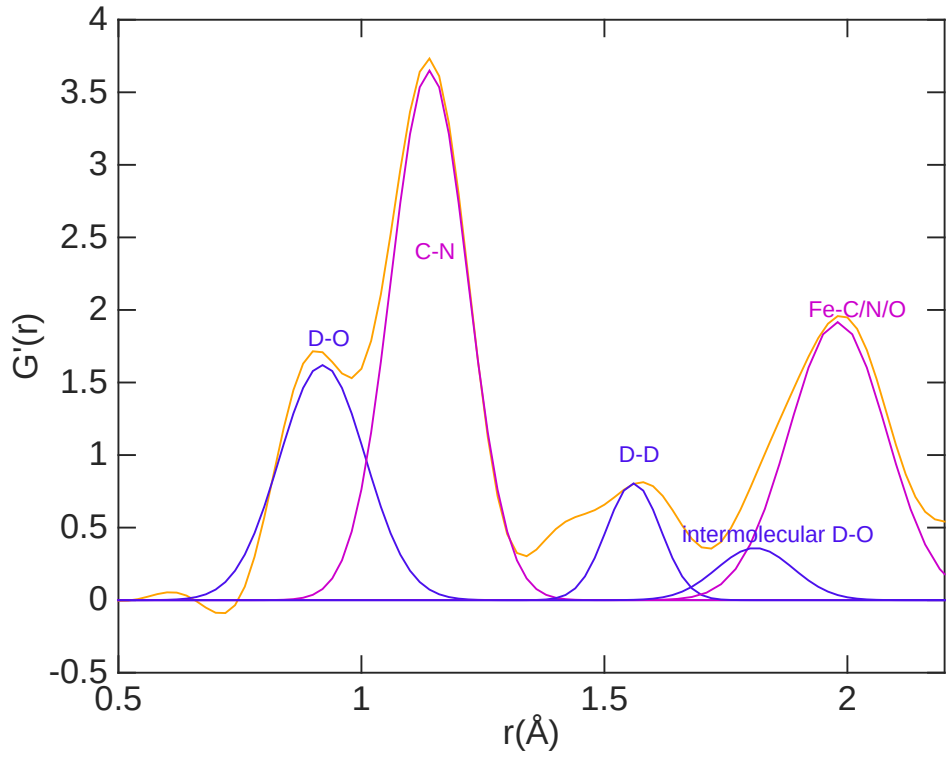

(c)

Figure 4.13: (a)Comparison between the least square fit model and the 298K bulk sample neutron data. (b) Correlation matrix of the parameters refined in the fit, including the gaussians standard deviations and the concentration of the elements. The parameters corresponding to the numbers in the matrix are listed in 4.2. c) Peaks used in the fitting procedure.

value of the corresponding parameter used in the final `Gudrun` corrections.

Figure 4.12 a shows a representative fit against the 298 K solid nanoparticle PDF function (as given in equation 4.4). The model PDF is in good agreement with the data in the region included in the fit. The only regions where it shows a relatively poor agreement are around 1.35 Å and 1.65 Å; these are regions where the function depends upon several contributions as it can be seen in figure 4.12 c. This may be due to the fact that all the peaks were approximated by Gaussian functions and that some of the peaks arising from the PVP were grouped in single peaks. These factors introduce a degree of uncertainty in the fit, implying that not all features of the function can be exactly reproduced. On the other hand, grouping some of the peaks of the PVP in one Gaussian function is a way of avoiding over-parametrising the fit.

Figure 4.12 b shows the correlation matrix of the parameters refined in the fit to the solid nanoparticle data, including the Gaussians standard deviations and the concentration of the elements, constrained as per equations 4.11 and 4.12. The numbers in the correlation matrix correspond to the refined parameters, according to the values shown in table 4.3. The correlation matrix was calculated as $\mathrm{corr}(x) = (\mathrm{diag}\mathbf{\Sigma}(\mathbf{x}))^{-1/2}\mathbf{\Sigma}(\mathbf{x})(\mathrm{diag}\mathbf{\Sigma}(x))^{-1/2}$ where $\mathrm{diag}\mathbf{\Sigma}(x)$ is the vector formed by the elements of the diagonal of $\mathbf{\Sigma}(\mathbf{x})$, the covariance matrix. The last is in turn calculated from the Jacobean of the system as: $\Sigma = (\mathbf{J_f}(x)^T\mathbf{J_f}(x))^{-1}$. The Jacobian matrix, $\mathbf{J_f}(x)$ of a vector function $f = [f_1(x_1, ..., x_m), ..., f_n(x_1, ..., x_m)]$ is the matrix of the partial derivatives of f with respect to x.

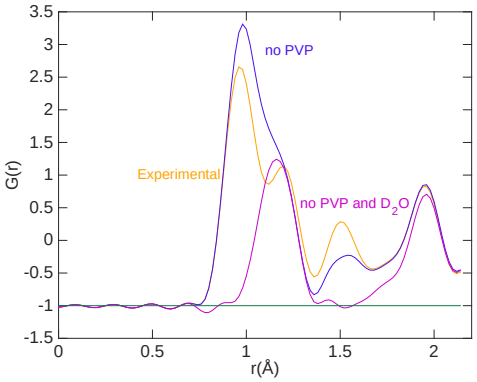

Figure 4.14: (a) The three curves show the experimental $G(r)$, the same function after subtraction of the calculated PVP contribution and after subtraction of both the calculated PVP and D_2O contributions. The baseline of the $G(r)$ after elimination of the PVP and D_2O contributions matches the green line.

The highest correlation is observed between the parameters 1 and 11 and parameters 7 and 12. The first two are the standard deviations of the Gaussian functions corresponding to the pair D−O and C−H (i.e. $\sigma_{\mathrm{D-O}}$ and $\sigma_{\mathrm{C-H_1}}$), whose averages fall both approximately around 1 Å, so the negative correlation is to be expected. The other two are the standard deviations of the intermolecular D−O pair and H−H respectively (i.e. $\sigma_{\mathrm{D-O}_i}$ and $\sigma_{\mathrm{H-H}}$).

It should be noted that for each phase contributing to the fit (i.e. D_2O, PB and PVP), only one atomic fraction parameter is refined, since the other atomic fractions are linked to the refined one through the constraints in equation 4.11. However from equations 4.8 and 4.12d, it can be seen that, owing to the density term, the concentrations of the various components contribute a factor to each gaussian. Still, the correlation matrix shows that the respective parameters

remain almost independent from each other, confirming the reliability of the fit.

As shown in table 4.3, the final atomic fractions used in the `Gudrun` corrections of the solid nanoparticle data are PB with 25% vacancies (i.e. 18 C, N and 7 Fe), 15 D_2O and 1.4 PVP monomer. The results of the refinement of the D concentration (and hence water) at the various temperatures agree with these values within 15.5%. In fact, excluding the lowest temperature data, the agreement is within 9.8%. This corresponds approximately to an uncertainty of ± 2 water molecules or a total number of water molecules between 13 and 17. The low temperature data refinement, on the other hand, returned a significantly lower value of D_2O molecules (approximately 10); this may be a consequence of the inability of the Gaussian model to reproduce the features of the local ordering of the water at low temperature.

For the PVP concentration the fit returned values within a 21.3% agreement, corresponding to a number of PVP monomers per PB unit cell between 1.1 and 1.7; in fact except for the 100 K data set, that returned a concentration of PVP equal to 2.1, the other data sets are in agreement by 14% (PVP between 1.2 and 1.6).

Figure 4.14 shows the comparison between the experimental PDF and those obtained subtracting the peaks calculated as arising from interatomic distances of PVP, as well as both PVP and D_2O. These can be written as:

$$G(r)_{\mathrm{noPVP}} = G(r) - \sum_i G'(r)_{PVP_i} \tag{4.14a}$$

$$G(r)_{\mathrm{noPVP/D_2O}} = G(r) - \sum_i G'(r)_{\mathrm{PVP}_i} - \sum_j G'(r)_{\mathrm{D_2O}_j} \tag{4.14b}$$

respectively. Once both PVP and D_2O peaks are eliminated, the function assumes the value $G(r) = -1$ (magenta line) at the minimum ($r = 1.41$ Å), beyond the first nearest neighbours interatomic distance, since $g(r)$ falls to zero.

In the first two cases (blue and orange lines), the multiple interatomic distances involved in the PDF prevent the $g(r)$ function from assuming the value zero at any point in the range considered. On the other hand, once the PVP and water contribution are eliminated the function present a region where no interatomic distances are observed, which is between the C−N and the Fe–C/N/O peaks, thus falling as expected to zero.

Figure 4.13 a shows a representative fit of the Gaussian model against the room temperature neutron data of the bulk sample. A moderately poorer agreement, compared to the solid nanoparticles fit, is observed in the region of the D–D peak. This could be due to some local short-range ordering that is not possible to capture with this simple model. However the result of the fit are consistent with the infrared spectroscopy measurements and calculated number of vacancies. In fact it was found that owing to the presence of Fe^{III}−CN−Fe^{III} moiety, the average fraction of vacancies per unit cell is reduced in the bulk sample. Thus an overall number

of water molecules (free plus coordinated) lower than the one found in the case of the solid nanoparticle sample is expected. The best agreement between the `Gudrun` corrections and the `Matlab` fit was found using a composition that includes 10 D_2O, 23 C and N atoms and 7.7 Fe. However, it was necessary to include 4 additional H atoms in order to produce a PDF with the correct low-r baseline. This H could be present in small quantities either as part of HCN impurities or exchanged in some of the D_2O molecules. Still, it was decided not to include the H component in the form of H_2O, since when we tried the fit produced unrealistically large values of H and D atomic fractions. In the case of the HCN, it would be very hard to separate the partial PDF from the overall contribution and in any case we do not hold evidences for its presence in the sample.

Either ways the fit provides a good indication of the amount of water found in the sample, as shown also by the good agreement of 15.4% between the refined D atomic fraction and the one used in the final `Gudrun` correction (table 4.4), as well as the above mentioned agreement with the IR results.

The Gaussians corresponding to single pairs are shown in figure 4.13 c and the correlation matrix is shown in 4.13 b. Very low level of correlations are observed for most of the parameters, confirming the reliability of the fit. The highest correlation is observed for parameter 2 and 6, D concentration and standard deviation of the C–N peak, respectively (table 4.2).

Finally, in both the solid nanoparticle and bulk fits the refined values of the density parameter show an exceptionally good agreement of the order of 0.1% with the value used in the `Gudrun` corrections.

4.4.2 `PDFgui` refinements

Systems characterised by porosities and vacancies like the ones here studied cannot be easily represented in terms of a unit cell. However, even though the small box modelling approach can only provide a partial description of the material, it can represent a good reference and starting point to compare against the results obtained through the big box modelling approach. In our case it can in fact be used to estimate overall average quantities, such as lattice parameters, phase compositions and atomic displacement parameters.

The refinement was first performed using the standard PB framework unit cell with 25 % vacancies. Once the best possible agreement between the data and the model was achieved, other two phases including water in vacancies and/or pores, as shown in figure 4.15, were added to the refinement sequentially (i.e. the third phase was added once a good agreement between the data and the two phases model was achieved). The two configurations with water consist of a PB framework with water molecules in the pores at positions (1/4, 1/4, 1/4), figure 4.15 a, and one with a vacancy in the centre of the unit cell (i.e. a $Fe^{II}(CN)_6$ is missing) with both coordinated

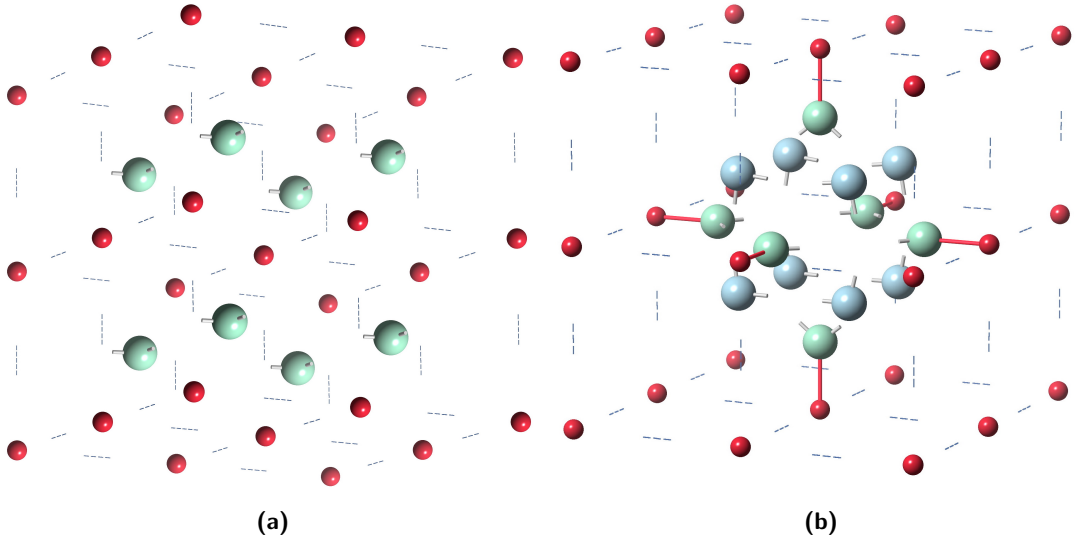

Figure 4.15: (a) Unit cell of PB with water molecules (O atoms in green) in the pores at position (1/4, 1/4, 1/4). The Fe atoms are coloured in magenta and the C−N groups are represented as dashed lines for clarity. (b) Unit cell with six coordinated water molecules (O in green) and 8 uncoordinated ones (O in cyan). The latter are at positions (0.34, 0.34, 0.34), so that the O−O distance is approximately 2.8 Å, compatible with the formation of hydrogen bonds.

and uncoordinated water molecules, figure 4.15 b. These were generated using bespoke `Python` codes, similar to those written for generating the RMC supercell (that will be discussed in the next section) and reported in appendix A.4.

These different types of unit cell account for the three locally ordered configurations that are likely to be found in the PB framework. These three can coexist in different percentages in the material and can be refined either singularly or benefitting from the multiphase functionality available in the program, thus giving an estimate of the fractional contribution of the various phases to the fitting.

A representative fit of the room temperature neutron data of the bulk sample is shown in figure 4.16. The refinement confirmed the consistency of the data with the structural model of the PB framework, as shown by the overall good agreement between the two. However poor agreement is observed at low-r (figure 4.16 b). This is not surprising since it is in this region that the water molecules are expected to give a significant contribution to the distribution of atomic distances. In fact, the inclusion in the fit of the configuration shown in figure 4.15 a visibly improves the low-r agreement (figure 4.16 d) even though the model does still not exactly reproduce the data. The refinement returns a phase composition of approximately 4:1 (for the PB framework and the configuration with water in the pores respectively). This, however, is not in agreement with the water content expected based on the analysis exposed in the previous section and the IR analysis. Hence the unit cell with water in the pores cannot be considered as an exhaustive representation of the structure, thus implying the necessity of a more complex modelling approach.

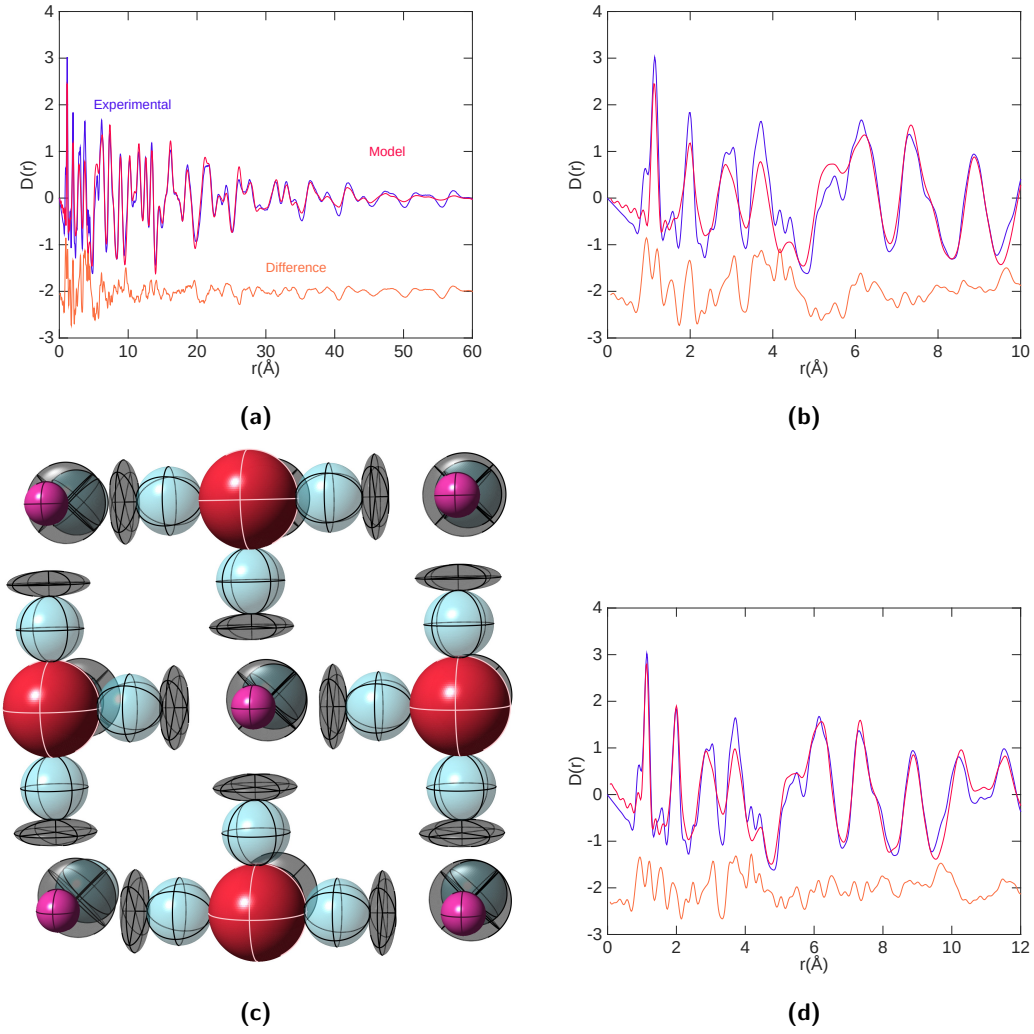

Figure 4.16: (a) PDFgui refinement of the neutron data collected on the bulk sample at room temperature against the PB framework phase (i.e. no water is included in the fit), reduced $\chi^2 = 0.030$ and $Rw = 0.364$; however, as seen in (b) the model can't fit the low-r features. (c) Thermal ellipsoids resulting from the refiniment of the ADPs, where the red corresponds to Fe^{III}, magenta to Fe^{II}, cyan to N and black to C. (d) Fit of the same data against two phases: the PB framework and the unit cell with water in the pores, as shown in figure 4.15 a (reduced $\chi^2 = 0.076$ and $Rw = 0.324$). Including water improves the agreement in the low-r region.

The atomic displacement parameters (ADPs) were refined applying the symmetry constraints of the $Fm\bar{3}m$ space group. The lattice parameters and ADPs obtained through refinement of the PB framework without water were used as starting parameters for the configurations with water. Figure 4.15 c shows the thermal ellipsoids obtained through the refinement of the PB unit cell with 25 % vacancies. The shape of the thermal ellipsoid is consistent with what is expected based on the chemical bonding between the atoms: the Fe^{II}–C bond is a stronger covalent bond than the Fe^{III}–N, thus the thermal ellipsoids of Fe^{II} and C are smaller, indicating a more confined motion. In the case of the C atoms the resulting ellipsoids have oblate shape indicating that the motion along the direction of the Fe^{II}–C bond is very limited, while they have more freedom to move in the other two directions. The Fe^{III} and N atoms have instead very large quasi-spherical ellipsoids indicating that thermal motion happens in all directions and the weaker bonds allow them to move more freely compared to the Fe^{II} and C bond.

4.4.3 Atomic structure modelled using `RMCProfile`.

To our knowledge, this is the first study where modelling of the original PB structure is attempted using `RMCprofile`, both in its bulk and nanoparticulate form. Moreover, very few studies report the use of the RMC refinement method for modelling against NIMROD data. To our knowledge only one previous study has used the RMC approach in the modelling of NIMROD data [196]. The reason why data collected on the NIMROD diffractometer are not studied using the RMC technique is linked to the nature of the materials analysed: most are in fact nanomaterials or complex composite structures for which an appropriate analysis route is not yet implemented in the `RMCProfile` code. Thus different modelling approaches are generally adopted depending on the system analysed.

Ideally a full analysis of the NIMROD data would include also the low-Q data, i.e. the small angle scattering region. However, tools for analysis of the SAS scattering are not included in the `RMCprofile` code, thus we exclude this region for the purpose of this analysis.

In this study, owing to the relatively large size of the nanoparticles (compared to the size of a standard supercell used in the RMC refinement procedure, usually a box with edges of approximately 50 Å), the material was treated as bulk for the purpose of the refinement and supercell of size of $5 \times 5 \times 5$ unit cells were created.

In a first approximation, in the case of the nanoparticle sample, it was assumed that the contribution from the PVP in the nanoparticle data are negligible when it comes to the modelling of the structure. The PDF of the PVP is in fact going to be characterised by a broad component at low r, corresponding to a lack of any strong reflection in the scattering function.

Moreover since the density of a vinyl monomer and of a PB unit cell with approximately 15 water molecules in the pores are very close, not taking into account the PVP contribution does

Table 4.5

Bond stretch potentials		
Atomic pair	D(eV)	r_0(Å)
C–N	8.317	1.216
D–O	3.6	0.967
Bending potential		
Atomic pair	k(eV)	$\theta_0(^\circ)$
O–D–D	3.5	104.0
Distance windows		
Fe–C	Fe–N	Fe–O
1.4-2.4 Å		

not alter the low-r level of the PDF.

Each configuration was refined against $D(r)$, $G(r)$, $i(Q)$ and Bragg profile. Different weighting of the functions relative to each other were attempted.

4.4.3.1 Initial RMC configurations

Different configurations were generated accounting for various possible ordering of the water molecules in the framework. The two main options are that the water is either located in the vacancies or is distributed across the whole network, even in pores with no vacancies. The second option is in agreement with previous studies [164, 171], as mentioned in section 4.1.1. Still, also the first of the two possibilities was explored to analyse how it affects the structure locally.

Moreover, configurations with two different types of ordering of the water molecules in the pores were generted. The configuration in figure 4.17 b has 6 coordinated water molecules in each vacancy and a water cluster (as the one shown in figure 4.17 a), placed at the centre of each vacancy. The configuration in figure 4.18 a has instead a more ordered structure with the 6 coordinated water molecules as in the previous case, but the O of the other molecules in the vacancy have the O atom in position $(0.34, 0.34, 0.34)$, as shown in figure 4.18 b. Moreover more water molecules are positioned in the centre of octants with no vacancies.

The supercell has dimensions $50.65\,\text{Å} \times 50.65\,\text{Å} \times 50.65\,\text{Å}$ and volume $\approx 130 \times 10^3 \text{Å}^3$. The number of atoms in a configuration depends on the amount of water inserted in the pores. The procedure used for building the starting configurations is described in appendix A.4 and the relevant bespoke `Python` codes are shown in the appendix A.4.1 and A.4.2.

In order to explore possible correlations between the local ordering and the positions of the pores and vacancies, several configurations with different initial random substitution of Fe atoms were generated. This resulted in a variety of possible random distributions of the vacancies.

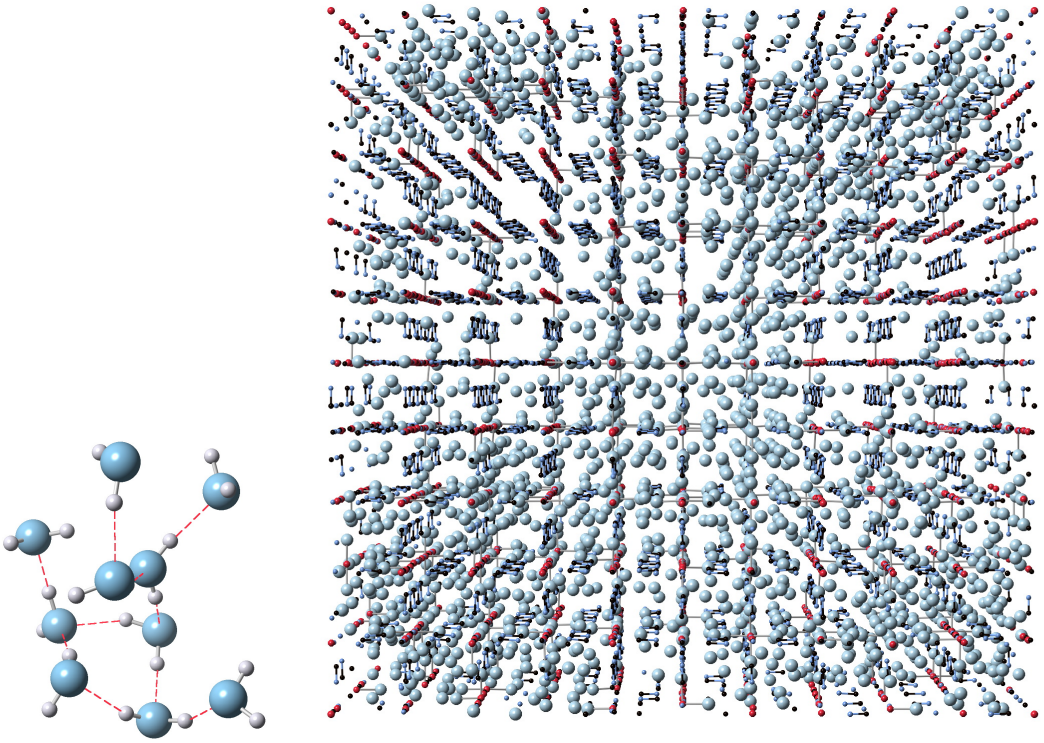

(a) (b)

Figure 4.17: (a) A cluster of 10 water molecules, obtained from MD simulations at ambient conditions using the TIP4P potential; the red dotted lines show the intermolecular hydrogen bonds. (b) Representative PB supercell with 25% vacancies occupied by water molecules coordinated to the Fe atoms and 10 molecules in each pore; the O atoms are coloured in light blue and the D and H atoms are omitted for clarity.

4.4.3.2 RMC restraints

Bond stretching and bending potentials were applied, in order to ensure that the resulting structure was chemically sensible. Distance windows were applied in cases where the average local ordering needed to be preserved, but without forcing the atoms in specific positions to allow for octahedral distortion (as in the case of distances involving the Fe atom). Finally also minimum distances parameters were applied in cases where no other restraints were in place to prevent the atoms from getting close to each other at unphysical distances. The list of parameters is provided in table 4.5.

The low-r peaks of the C–N and D–O pairs are very close in the PDF function and the first is characterised by an interatomic potential significantly stronger than the second. In such case, `RMCProfile` can generate a distorted distribution of distances, where the peak corresponding to the pair whose interaction is weaker can present a distribution with two peaks forming around the average r_0. In order to prevent this from happening, an artificial $G'(r)$ consisting in a Gaussian peak representing the first D–O distance was created and added to the list of functions that the configuration is refined against. Neutron coefficients were specified, setting all

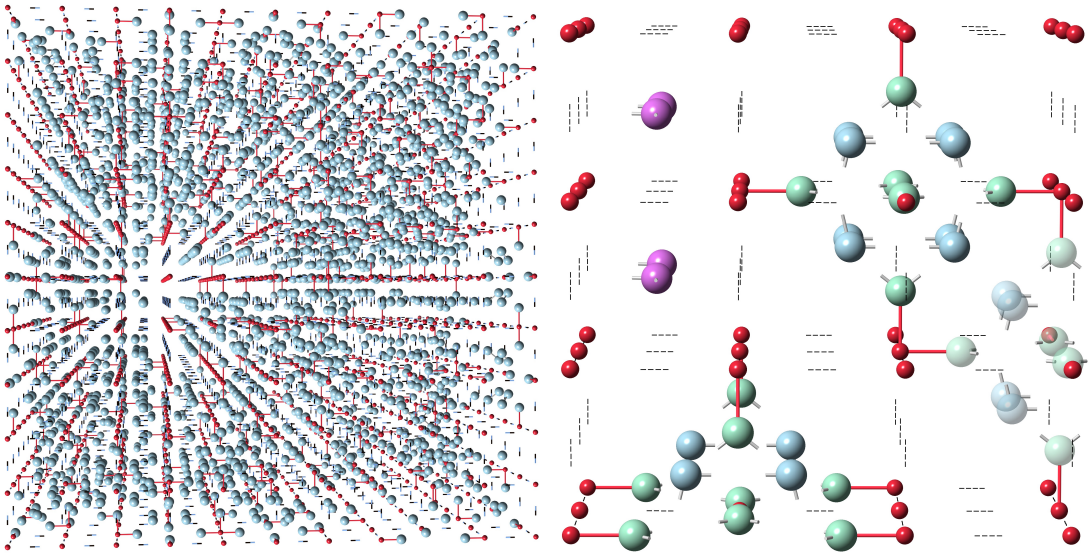

(a) (b)

Figure 4.18: (a) A $5 \times 5 \times 5$ PB supercell with 25% vacancies occupied by water molecules coordinated to the Fe atoms and 8 molecules in each pore; the O atoms are coloured in light blue and the D atoms are omitted for clarity, while the C≡N groups are represented as black and blue sticks. Compared to figure 4.17 b the water molecules are now more homogeneously distributed, since also the octants with no vacancies contain one molecule. This can be seen in (b) that shows an area selected from the configuration in (a) where the purple are O atoms sitting in pores at position $(1/4, 1/4, 1/4)$, the green are O coordinated to the Fe atoms (in magenta), the red bonds represent the coordination between the O and the Fe and the blue atoms are O at position $(0.34, 0.34, 0.34)$ in unit cells occupied by a vacancy. D, C and N atoms are omitted for clarity.

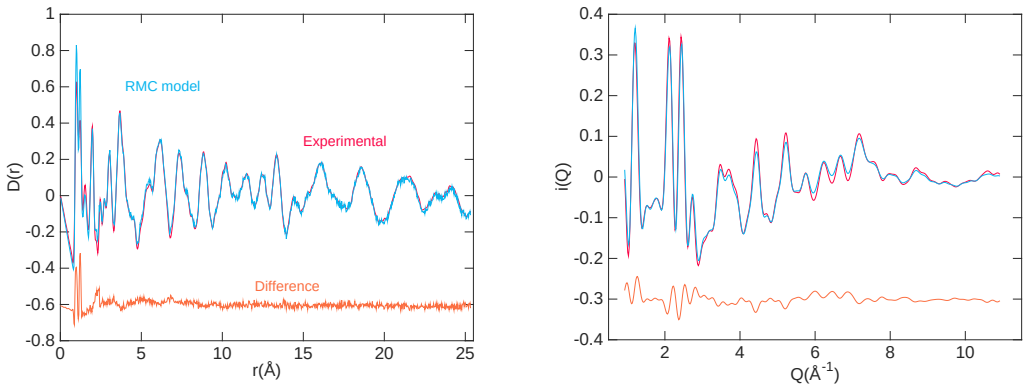

(a) (b)

Figure 4.19: (a) Comparison between the PDF of the RMC model and the experimental data and (b) corresponding $i(Q)$ functions.

Faber-Ziman factors (i.e. $\sum_{ij} c_i c_j b_i b_j$) to zero, except the one corresponding to the D–O pair.

4.4.3.3 Representative fits: towards a realistic RMC model

A representative RMC fit of the solid nanoparticles room temperature data is shown in figure 4.19. The agreement between the model and the experimental $D(r)$ is overall very good except

for the difference in intensities of the first two peaks. However, it should be noted that this model was performed before the optimal atomic ratios and density including the PVP contribution were calculated through the least square refinement procedure, as explained in the previous sections. Thus, it is expected for the model not to represent exactly the low-r region since this is where the PVP component will give the strongest contribution. The atomic ratios and density used in the correction of the experimental data shown in figure 4.19 and in the making of the starting configuration were yes calculated through the `Matlab` least square procedure; however, while a fraction of H_2O was included, the necessity to account for PVP contributions was not considered, assuming it to be entirely negligible.

Interestingly, the mismatch between the intensity of the first two peaks (together with the IR analysis) is what hinted at the necessity to include in the `Matlab` least square fit also the contributions arising from PVP. In fact the intensities of the two experimental PDF peaks is lower than the model ones, thus suggesting that a negative contribution is required (as the one given by the PVP peaks in this region, figure 4.12 c). Hence, the data were subsequently corrected with the new calculated atomic fractions and density (results reported in section 4.4.1.4), which also resulted in a more realistic low-r level of the PDF.

Moreover, despite the good agreement between the model and experimental $D(r)$ and $i(Q)$ (figure 4.19), the model Bragg profile provided a very poor match to the the data. This observation implied that although the atomic ordering of the final configuration is a coherent representation of the local ordering, the same is not true for the average structure. From this came the realisation that a more ordered starting configuration was required, such as the one shown in figure 4.18, in order to try to generate a model coherent across multiple length scales.

Several RMC refinements of these configurations against the data at various temperatures were attempted, although a model consistent with both PDF and Bragg data has not been achieved yet. However the results from these preliminary models showed that the final RMC configuration, refined applying the restraints in the previous section, was locally consistent with the expected structure and provided chemically sensible results (figure 4.20). The starting configuration for this RMC refinement was created as shown in figure 4.17, by inserting a water cluster in the vacancies.

In the final configuration, a deviation of the Fe–C–N and Fe–N–C bonds from linearity is observed, as consistent with the literature (section 4.1.1). However compared to the literature that reports the value of 164°, the angles in the final configuration are in a range that includes significantly smaller values, i.e. $100° < \theta < 170°$. This can be improved adding bending potentials for C–N–Fe and N–C–Fe to the restraints used.

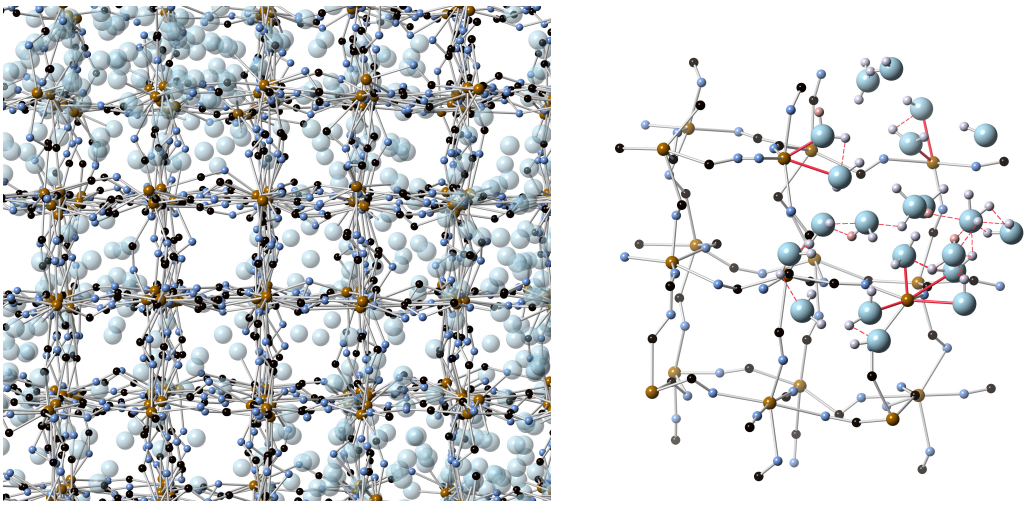

(a) (b)

Figure 4.20: (a) A representative image of the final configuration, where the O atoms are the big light blue atoms (D and H are omitted for clarity), brown Fe atoms, black C and blue N. (b) A closer look at a section of the configuration. The D atoms are shown in light gray and H in pink; red dashed lines mark distances between H/D and O consistent with the formation of intermolecular hydrogen bonding and the red sticks are Fe–O bonds (i.e. water molecules coordinated to Fe^{III}).

4.5 Summary

The work exposed in this chapter builds the foundation for an accurate analysis and modelling of X-ray and neutron total scattering data collected on Prussian blue, in bulk and nano-particulate form.

The infrared spectroscopy measurements provided information about the oxidation state of the Fe centres, linked to the average number of vacancies per unit cell, and about the presence of residual PVP in the nanoparticle samples. The first point was particularly important in the case of the bulk sample, since it was found that it presents a ratio $Fe^{II}-CN-Fe^{III}$:$Fe^{III}-CN-Fe^{III}$ equal to 3.5:1. As a consequence, the bulk has a lower number of vacancies per unit compared to the standard PB case. The information about the PVP content is important in the case of the nanoparticle data, since on this depends the approach taken in the modelling of the total scattering data.

It was demonstrated that through a bespoke least square fitting procedure of the first few peaks in the PDF function, it is possible to obtain information concerning the water and PVP content in the samples, in terms of atomic ratios. More generally, the procedure here used can be applied to any system where individual peaks can be assigned to specific pairs of atoms based on prior theoretical knowledge of the system studied.

It was shown that the `PDFgui` refinement of the standard Prussian blue unit cell against the bulk neutron PDF produces a good representation of the structure. Moreover, the resulting atomic displacement parameters are consistent with the bond strengths of the pair of atoms in

the system, confirming the validity of the fit. It was also shown that in the low-r region the fit is improved by addition of a second phase in the fit consisting of the Prussian blue unit cell with water in the pores at position $(1/4, 1/4, 1/4)$.

The information about the water content obtained through the least squares refinement, on the number of vacancies in the bulk through the IR measurements and from prior knowledge were used to guide the making of atomic configurations with vacancies randomly allocated. Water molecules, arranged either in clusters or in a more ordered configuration (both consistent with the presence of intermolecular hydrogen bonding) were located in the vacancies, together with additional molecules in octants with no vacancies and coordinated to the the free Fe^{III} centres. We performed `RMCProfile` refinements, starting from the atomic configurations created, and obtained a model of the structure, consistent with the solid nanoparticle PDF and total scattering data, chemically sensible and in agreement with the previous literature.

Chapter 5

Analysis of the structure of CaO nanoparticles for CO_2 capture applications

This chapter presents the results of a study performed on a series of CaO and $CaCO_3$ nanoparticles that have undergone carbonation through absorption of CO_2 and/or calcination.

By comparing the total scattering data with model PDF functions of the CaO and $CaCO_3$ phases, calculated from the spectrum of phonon frequencies of the bulk materials using the program `GULP`, the phase content of the samples analysed can be determined qualitatively. Moreover the comparison provides information about the long-range order in the structure and its degree of crystallinity.

Additionally, small angle scattering analysis is used to study the porosity of the materials, that it is directly linked to their ability to absorb CO_2 and undergo the carbonation process.

5.1 Application of CaO nanoparticles in CO_2 capture

Climate change is one of threats that humanity faces today. Its main cause is identified by the scientific community as the continuous emission of greenhouse gases in the atmosphere, as a consequence of human activity [197].

In order to reduce these emissions, it is necessary to operate at several different levels; in particular, the achievement of a significant curbing of CO_2 emission is strongly dependent on improvements in energy efficiency, decarbonisation of the electricity and fuel supplies, combined with the use of biological storage as well as capture of CO_2 from the atmosphere [198–201].

Among these, the decarbonisation can be either achieved by shifting the energy production towards clean sources (i.e. free of CO_2 emissions, such as renewable and nuclear energy) or by carbon capture and storage (CCS) [2]. Although, the first may seem like a more effective

solution, the fact that a large fraction of the energy used globally is still generated by means of fossil fuels imposes the urge to implement new technologies for preventing the release of CO_2 produced in the combustion process in already existing power plants. In fact 41% of the electricity produced globally in 2008 was obtained by coal combustion [202]. Coal-fired plants contributed the 50% of the total power generated nationally in the United States [203] in 2009, corresponding to 30% of the total CO_2 emissions. This value dropped to 33% in 2015 [204], but more needs to be done to stabilise the CO_2 atmospheric concentration below 550 ppm, the target threshold set for year 2050 [198].

The use of CCS technology can help achieving a significative reduction of the emission, preventing up to 90% of the CO_2 from reaching the atmosphere [198]. The most mature technology for post-combustion capture is amine scrubbing, that makes use of a liquid solvent [203]. However, this technique presents a substantial energy penalty, a loss of 11%-40% of the energy produced by power plants when operated without use of CO_2 capture systems; this is due to the large amount of heat required in the regeneration process of the liquid sorbent [205, 206].

A possible alternative involves the use of high temperature absorption looping, consisting of the reversible reaction of a solid material with gaseous CO_2 [202]. The theoretical energy penalty in this case is limited between 6% and 8%, significantly lower than that of amine scrubbing. The high temperature absorption looping technique involves the reaction of the sorbent with CO_2 in the flue gas (carbonation) and subsequent regeneration (calcination) at higher temperatures to recover the original material. An ideal sorbent would undergo this process for thousands of times reforming the original structure at each time and without loosing efficiency.

Among the solid sorbents, the CaO-$CaCO_3$ system represents a natural choice and has the advantage of being a clean and highly available material [207]. The reversible calcination (endothermic) and carbonation (exothermic) reactions are given by:

$$CaCO_3 \rightleftharpoons CaO + CO_2, \qquad \Delta H = \pm 182.1\,\mathrm{kJ\ mol^{-1}} \tag{5.1}$$

These are performed in the temperature ranges 750–950 °C and 600–700 °C, respectively [207]. When used in its nano-particulate rather than bulk form, the sorbent presents the advantage of a highly increased surface area available for the absorption of CO_2 and hence the carbonation process to occur.

5.1.1 Challenges and how understanding the local structure can help

One of the main problems associated with the use of solid sorbents concerns the deactivation of the material after several cycles, as a consequence of sintering that leads to a loss of porosity and subsequently of CO_2 absorption efficiency. In the case of natural limestone, the capture

capacity can fall by 90 mol% after 20 carbonation-regeneration (calcination) cycles. Studies of the local structure provide insight about the origin of this drastic decrease in efficiency and the cause of the deterioration of the sorbent.

The work exposed in this chapter is part of a study performed in collaboration with Matthew Dunstan and Clare Grey (University of Cambridge) [2], involving the use of several local probes to understand the response of a variety of CaO-$CaCO_3$ systems to the carbonation and regeneration process after different carbonation times and/or several cycles. The use of total X-ray and neutron scattering was combined with in-situ X-ray diffraction studies of the samples under CO_2 flow (with and without addition of steam) and X-ray tomography to achieve a better understanding of the changes occurring both from the atomic and morphological point of view. As a whole, the study provides information that can help answer questions concerning the carbonation reaction process and the parameters that control the capacity of this class of materials to absorb CO_2.

Moreover, this study is part of a wider project carried out by Dunstan aimed at the optimisation of the performance and efficiency of materials for high-temperature CO_2 looping. This was performed by means of a theoretical structural screening that led to the identification of 640 structures suitable for use in CCS.

Among these a novel CCS material, $Ba_4Sb_2O_9$ was tested for use in CO_2 absorption, thus being the first perovskite structure to undergo reversibly the carbonation-calcination process [208]. The study showed that the its high absorption capacity and stability is linked to the ability of the structure to retain its porosity; this is in turn a consequence of the existence of an inert chemical framework of Sb polyhedra, demonstrating the intimate connection between the structural properties of this material and its ability to preserve the CO_2 absorption efficiency.

As mentioned, the loss of porosity upon carbonation and regeneration is one of the main problems associated with CaO sorbent. Understanding the causes of this deterioration from a structural point of view can help optimising the performances of CaO sorbent with addition of impurities to tailor the behaviour of the system starting from its local structure. Moreover, it can guide the choice of new unexplored sorbents suitable for CO_2 capture, starting from the knowledge of the key characteristics that determine the efficiency of a material and the prediction of the structural and morphological modifications they would undergo under CO_2 absorption.

5.2 The samples

The total scattering experiments were conducted on three classes of samples. The three classes consist of four samples that have undergone carbonation and/or calcination for different lengths of time. In all three cases, the carbonation was performed at 600 °C and the calcination at

Table 5.1

Series	CaO			
Precursor	CaO*			
Sample name	Ca O 0	CaO 2	CaO 5	CaO 10
Carbonation time (min)	0	2	5	10

* Partially converted to $Ca(OH)_2$ owing to absorption of moisture from the air.

Table 5.2

Series	CaO–AlMg			
Precursor	$CaO^{*}{\cdot}xAl_2O_3{\cdot}yMgO^{\star}$			
Sample name	CaO–AlMg 0	CaO–AlMg 3	CaO–AlMg 5	CaO–AlMg 10
Carbonation time (min)	0	3	5	10

* Partially converted to $Ca(OH)_2$ owing to absorption of moisture from the air. * $3\% < x < 6\%$ and $1\% < y < 3\%$ (weight fractions).

Table 5.3

Series	limestone			
Precursor	$CaCO_3$			
Sample name	limestone 0	limestone fresh	limestone 2	limestone 5
Carbonation time (min)	0	0	2	5
Calcination†		✓	✓	✓

† Undergoes calcination prior to carbonation.

900 °C. The starting material or precursor of the three series is in each case different. In the first case it is nominally CaO and this class will be called CaO series, table 5.1. The precursor of the second series is CaO with addition of some Al_2O_3 and MgO impurities and it will be called CaO–AlMg series, table 5.2. In the case of the last series the precursor is limestone $CaCO_3$, called limestone series, table 5.3.

The synthesis of these samples was performed by collaborators of Dunstan according to the following procedures. The CaO series samples were prepared from CaO spherical nanoparticles (98%, diameter < 160 nm, Sigma Alrich), the limestone series from calcined Purbeck limestone and the CaO–AlMg series from CaO nanopowders with some Al_2O_3 and MgO impurities.

Specifically, the CaO series consists of four samples of CaO nanoparticles which have undergone carbonation for different amounts of time: 0, 2, 5 and 10 minutes and we will refer to these samples as CaO 0, 2, 5 and 10, respectively. The powder was pelletised to be able to react in a fluidised bed reactor (FBR), and was then carbonated in the FBR at 1023 K under a 15% CO_2 flow.

The same procedure was used for synthesising the CaO−AlMg series, with the only difference that the second sample was carbonated for 3 minutes. Analogously to the previous case these samples will be called CaO–AlMg 0, 3, 5 and 10, respectively.

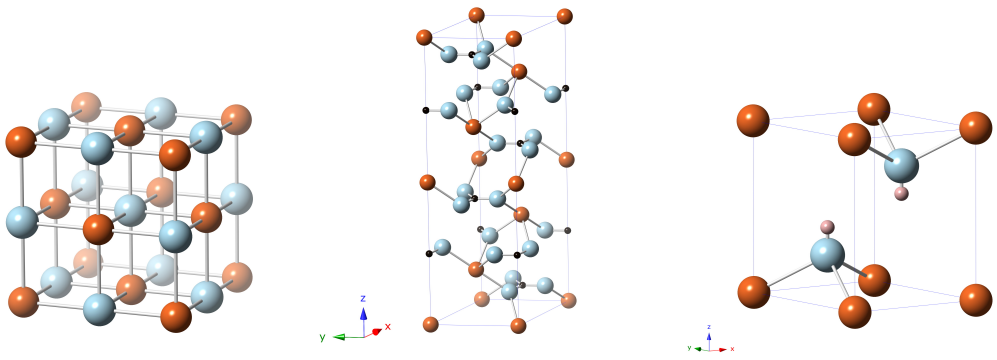

Figure 5.1: The unit cell of the CaO (a), $CaCO_3$ (b) and $Ca(OH)_2$ (c) phases, with the C atoms in dark orange, O atoms in light blue and H in pink. (a) CaO has the fcc structure (space group $Fm\bar{3}m$, $a = 4.81$ Å), (b) calcite, $CaCO_3$, presents the rhombohedral structure (space group $R\bar{3}c$, $a = 4.99$ Å, $c = 17.06$ Å), but the picture is drawn with respect to the non primitive trigonal unit cell. (c) $Ca(OH)_2$ is trigonal (space group $P\bar{3}m1$, $a = 3.59$ Å, $c = 4.89$ Å).

The limestone series of samples consists of a sample of the precursor limestone (limestone fresh), a sample that has only undergone calcination (limestone 0) and then a further two samples calcined and then carbonated for 2 and 5 minutes respectively (limestone 2 and 5).

These samples can be used to study how the structure of CaO evolves after undergoing carbonation for different times (CaO series), as well as the effect that the addition of some impurities has on the capacity of the material to absorb CO_2 (CaO−AlMg series) and the response to carbonation of samples that have already undergone calcination previously (limestone series).

The main phases found in the samples are CaO and $CaCO_3$, as well as the $Ca(OH)_2$ phase in some of the samples 5.1. CaO presents the fcc structure (space group $Fm\bar{3}m$), while $Ca(OH)_2$ is trigonal (space group $P\bar{3}m1$), figure 5.1. $CaCO_3$ has several polymorphs: calcite (figure 5.1), aragonite (orthorhombic, space group Pmcn) and vaterite (hexagonal, space group $P6_3/mmc$) [209] as well as in various amorphous phases [131]. An interesting example found in nature, where the variety of phases that $CaCO_3$ can form plays a crucial role, it is that of biomineralization (i.e. bone formation, sea urchin, crabs etc.) [210]. The hard skeletal structures of many marine invertebrate organisms is formed by $CaCO_3$. In the growth stage, the $CaCO_3$ presents an amorphous structure, that allows the formation of complex shapes, that would not be possible in the presence of long-range order, which would favour instead the growth in specific crystallographic directions [131, 210]. As the organism grows, the amorphous phase becomes unstable, leading to the formation of crystalline phases of $CaCO_3$ [210]. Bivalves shells contains two polymorphs of $CaCO_3$, aragonite in the inner part and calcite externally [211].

In the samples studied, $CaCO_3$ is expected to be found mainly as calcite, since most limestone occurs as calcite [207]. This is confirmed by the analysis exposed in section 5.4.

5.3 Studies of the local structure

5.3.1 X-ray and neutron total scattering data

Room temperature X-ray and neutron total scattering measurements were performed on the three series of samples. As in the case of the other materials analysed in this thesis work, X-ray and neutron measurements provide complementary information due to the differences in contrast between atomic scattering factors: neglecting the Q dependence of X-ray scattering factors, $f_{\mathrm{C}} = 6$, $f_{\mathrm{O}} = 8$ and $f_{\mathrm{Ca}} = 20$, while the corresponding neutron coherent scattering lengths are more comparable, being $b_{\mathrm{C}} = 6.6460\,\mathrm{fm}$, $b_{\mathrm{O}} = 5.803\,\mathrm{fm}$ and $b_{\mathrm{Ca}} = 4.70\,\mathrm{fm}$. Among the three elements, particularly important in this case is the difference between the C X-ray scattering factor and neutron scattering length, since it allows us to differentiate the contribution in the X-ray data arising from the CaO phase from those arising from $CaCO_3$. As an example we can consider the ratio of the X-ray scattering intensities arising from the pairs Ca–O of CaO and C–O of $CaCO_3$, that is given by:

$$x = \frac{c_{\mathrm{Ca}} c_{\mathrm{O}} f_{\mathrm{Ca}} f_O n_{\mathrm{Ca}}}{c_{\mathrm{C}} c_{\mathrm{O}} f_{\mathrm{C}} f_{\mathrm{O}} n_{\mathrm{C}}} = 13.9 \tag{5.2}$$

where at numerator the c_{Ca} and c_O are the concentrations of Ca and O in CaO and at the denominator c_C and c_O are the concentrations in $CaCO_3$, $n_{Ca} = 6$ and $n_C = 3$ the number of O nearest neighbours with respect to Ca in CaO and to C in $CaCO_3$, respectively. Hence, while in a neutron experiment the scattering intensities arising from these two contributions would be comparable, in a X-ray experiment the Ca contribution dominates.

The neutron total scattering data of the CaO and CaO–AlMg series (figures 5.2 a and c, respectively) show the variations happening in the structure upon carbonation, already from a first observation. These are also reflected by the differences between the PDF functions (figures 5.2 b and d for the CaO and CaO−AlMg series, respectively).

The reflections found in the $i(Q)$ function and interatomic distances in the $D(r)$ function corresponding to $Ca(OH)_2$, $CaCO_3$ and CaO are marked in the figures by solid red lines, dashed green lines and black solid lines, respectively. The corresponding hkl values (reciprocal space) and atom pairs (real space) are written for simplicity just in figures 5.2 a and b, respectively. The presence of the $Ca(OH)_2$ phase, in the CaO 0 and CaO–AlMg 0 samples (table 5.1 and 5.2 for details about the samples), was identified firstly owing to the higher level of the intensities of the merged scattering cross section (compared to the other samples in the series), accompanied by the presence of a slope at low-Q, both signatures of the presence of hydrogen in the sample. Secondly, some isolated reflections (001 and 011) that do not correspond to either of the two phases were identified as corresponding to $Ca(OH)_2$ reflections.

This would indicate that $Ca(OH)_2$ may form initially on the CaO surface due to reaction

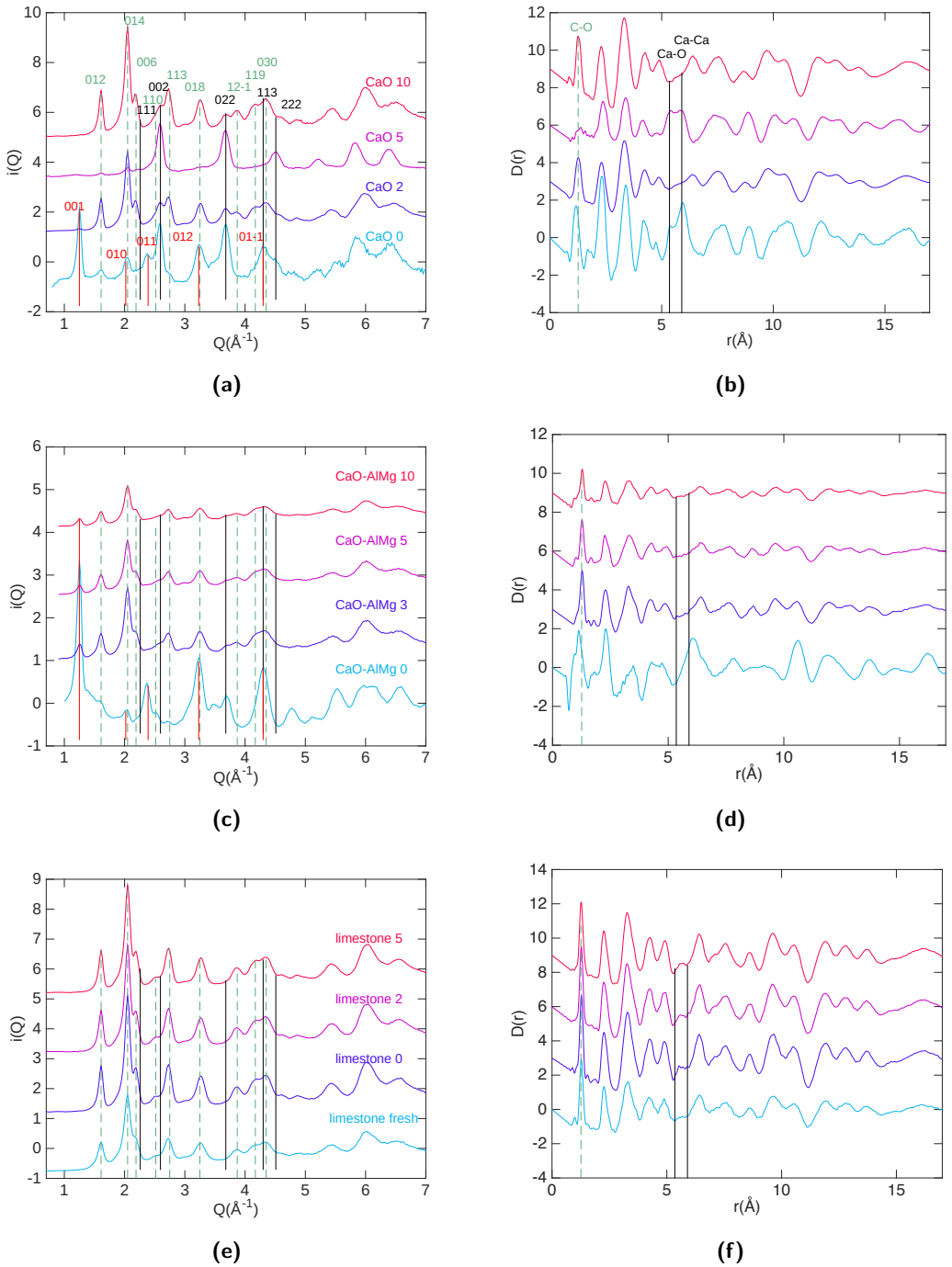

Figure 5.2: The total neutron scattering data (a)-(c)-(e) and corresponding PDF functions (b)-(d)-(f) of the CaO, CaO-AlMg and limestone series respectively. The vertical lines indicate reflections (in the $i(Q)$ function) and interatomic distances (in the $D(r)$ function) corresponding to different phases differentiated by colour: red for $Ca(OH)_2$, green dashed for $CaCO_3$ and black for CaO. The corresponding reflections (in the $i(Q)$) and atomic pairs (in the $D(r)$) are marked for simplicity only in the CaO series data, figures (a) and (b).

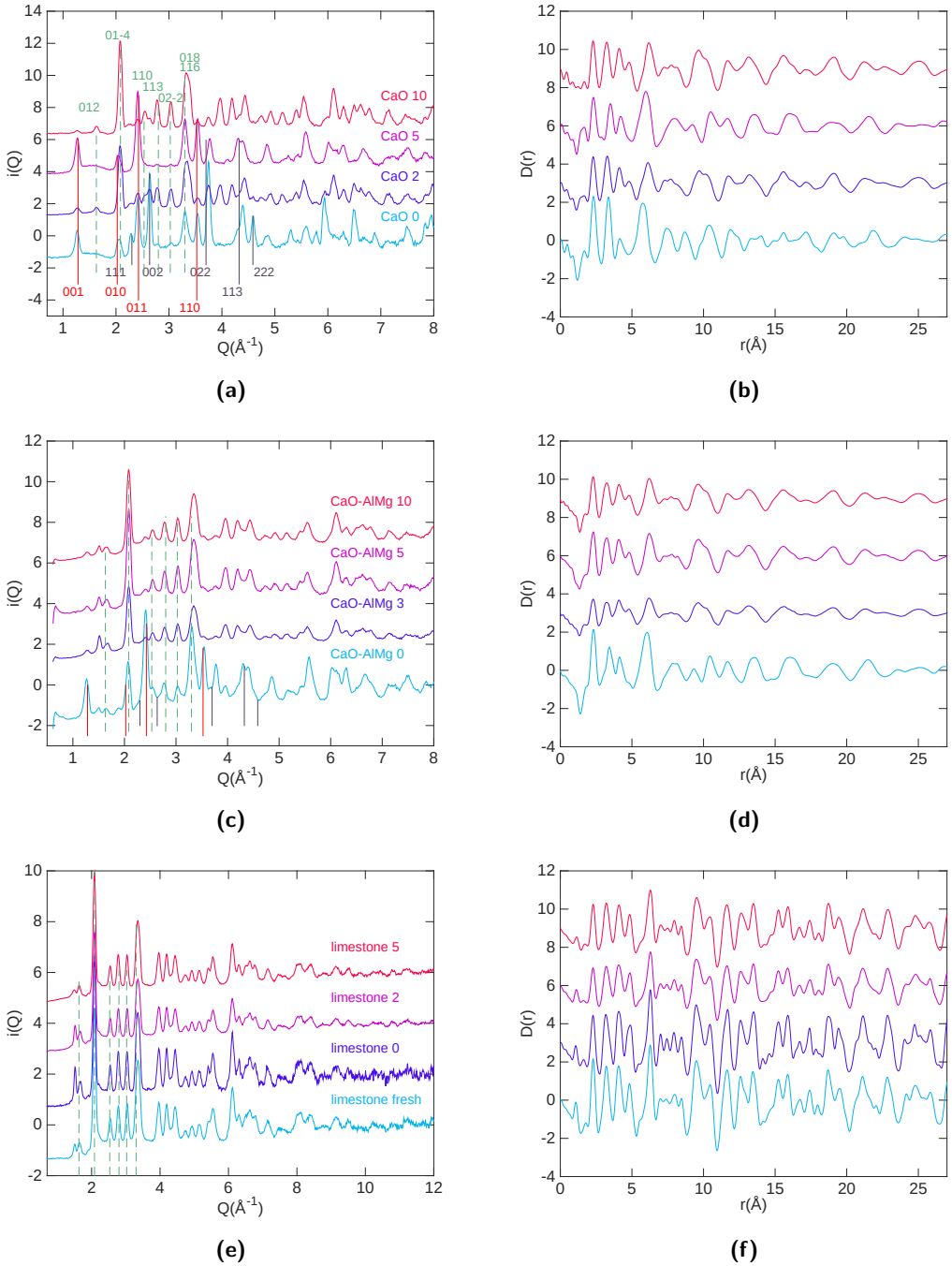

Figure 5.3: The total X-ray scattering data (a)-(c)-(e) and corresponding PDF functions (b)-(d)-(f) of the CaO, CaO-AlMg and limestone series respectively. The vertical lines indicate reflections (in the $i(Q)$ function) corresponding to different phases differentiated by colour: red for $Ca(OH)_2$, green dashed for $CaCO_3$ and grey for CaO. The corresponding reflections (in the $i(Q)$) are marked for simplicity only in the CaO series data, figure (a)).

with moisture in the atmosphere, but after carbonation does not form on the surface of the carbonated particles. Furthermore, at low temperatures $Ca(OH)_2$ would undergo carbonation to form additional $CaCO_3$. This also explains why, even in the two non carbonated sample, (012) reflections that can be unambiguously attributed to the $CaCO_3$ phase are observed. On the other hand, the fact there is still CaO in the non carbonated samples (i.e. not all was converted into $Ca(OH)_2$) is confirmed by the presence of the (002) and (022) reflections. The latter in particular can be clearly distinguished from other reflections.

Among the CaO series, the sample CaO 5 presents an unexpected result. The diffraction pattern does not contain any strong reflections that can be attributed to the $CaCO_3$ phase. In fact the only visible reflections correspond to those belonging to the CaO phase. Based on this observation, we could argue that some errors may have taken place during the synthesis procedure, i.e. the CO_2 flux was inadvertently switched off or the density of CO_2 lowered, so that the carbonation didn't happen at all or only partially; on the other hand, the high temperature would have still caused the conversion of the $Ca(OH)_2$ into CaO resulting in a sample containing only or mainly the latter. It is hard to know whether this is effectively the case; a clear answer can be obtained only repeating the synthesis and the measurements. The PDF data (figure 5.2 d) presents a very low intensity and noisy feature in correspondence of the first interatomic distance of $CaCO_3$, C–O, but it is hard to tell whether the peak is a genuine feature or not. In any case, the CaO 5 sample can be useful if used as a reference for the structure of nanoparticles comprising mainly CaO.

The total scattering functions of the two other samples of the series, CaO 2 and 10, are mainly characterised by $CaCO_3$ reflections with only a relatively small CaO contribution. This observation anticipates that the carbonation of the sample happens mainly in the first couple of minutes and the structure does not change significantly afterwards. Incidentally this would also confirm the hypothesis that the CaO 5 sample was not carbonated during the synthesis.

Moving now back to the CaO-AlMg series, we can observe that the $Ca(OH)_2$ component seems more significant in the CaO-AlMg 0 sample compared to the CaO 0. The conversion of surface CaO to $Ca(OH)_2$ due to absorption of moisture in the air, may be here facilitated by the presence of the oxides impurities. The presence of a low intensity 001 reflection shows that some $Ca(OH)_2$ is left in the samples even after carbonation. This may possibly imply that the formation of $Ca(OH)_2$ does not happen solely on the surface of the pellet, but also in the core.

As in the case of the CaO series the carbonation seems to happen all in the first few minutes since there are not visible differences between the diffraction patterns of the samples 3, 5 and 10. However, the broader width and lower intensity of the peaks in the $i(Q)$ implies that the carbonation process affects the crystallinity of the sample of this series more significantly, leading to a higher level of disorder. Moreover, the disorder appears also to increase with carbonation time.

The samples of the limestone series show very similar $i(Q)$ patterns (figure 5.2 e), with most reflections being mainly consistent with the $CaCO_3$ structure. Analysis of the limestone 0 sample data reveals that the calcination process does not affect greatly the structure, since the real and reciprocal space data are very similar to those of the limestone fresh sample. This indicates that the conversion of $CaCO_3$ to CaO was only minimal or did not occur at all.

The limestone data do not contain reflections that can be attributed to the $Ca(OH)_2$ phase (as expected since it forms starting from CaO) and consequently did not show the low-Q slope in the $i(Q)$ typical of hydrogen-containing samples.

It should be noticed at this point that, while in the neutron reciprocal space data it is possible to attribute unambiguously some reflections to specific phases, based on their theoretical structure, it is not equally obvious to identify atomic pairs in the real space data, since these are often overlapping, as well as very densely distributed in the case of the $CaCO_3$ and $Ca(OH)_2$ phases. For this reason only the first peak of $CaCO_3$ at 1.25 Å (i.e. the C–O distance), since it is the only peak that can be found at that given distance, and the CaO peaks at 5.35 Å (i.e. the Ca–O distances) have been marked. Modelling can help in providing a better interpretation of the PDF as well as of the total scattering data, as shown in section 5.4.

Moving now our attention to the X-ray, it can be observed that the total scattering data present several relatively sharp reflections. This is due to the previously mentioned higher sensitivity of X-rays to the Ca component and simultaneous reduction of the intensities due to the C and O, resulting in a more defined diffraction pattern. The total scattering data of the CaO, CaO-AlMg and limestone series are shown in figure 5.3 a, c and e, respectively. In figure 5.3 b, d and f the corresponding PDF functions are shown. As for the case of neutrons the main reflections that can be assigned to one of the phases are marked in the $i(Q)$ plots by vertical lines: red for $Ca(OH)_2$, green dashed for $CaCO_3$ and grey for CaO.

The X-ray data are consistent with the neutron data. In the CaO series, the peaks corresponding to the (110), (113) and $(02\bar{2})$ reflections of $CaCO_3$ in the CaO 2 and 10 samples, but absent in the other two samples of the series, confirms that the carbonation has occurred. However they are more intense and sharper in the CaO 10 sample, thus showing that the carbonation is not completed after 2 minutes. The $(01\bar{4})$ reflection of $CaCO_3$ is present in the form of a mild peak also in the CaO 0, confirming that some carbonation has already occurred.

The $Ca(OH)_2$ reflections, (001), (010), (011) and (110), are well defined in the CaO 0 and 5 samples. In the case of the CaO 0 sample this is in agreement with neutron data, however in the case of the CaO 5, we didn't observe any reflection that could be attributed to this phase. This could be due to the fact that the X-ray data were collected some time after the neutron experiments, thus the CaO 5 samples could have absorbed moisture from the air, leading to the formation of a fraction of $Ca(OH)_2$.

The X-ray data of the CaO-AlMg series are in agreement with the neutron data, with the

CaO-AlMg 0 presenting a mixture of $Ca(OH)_2$, $CaCO_3$ and CaO reflections and the other three samples presenting mainly a calcite component. The lower intensity of the reflections compared to the CaO series confirms that the structure of this series presents a higher degree of disorder.

Similarly, the $i(Q)$ functions of the samples of the limestone series are characterised by reflections that can be attributed almost exclusively to $CaCO_3$. However an interesting feature that does not appear in the neutron data is the splitting of the (012) reflection in two components. This double feature is not observed in the theoretical structure of $CaCO_3$ and may indicate the formation of a local ordering peculiar to these nanostructures. The presence of sharp peaks in the PDF data up to higher distances compared to the other two series, show that the structure of the samples of the limestone series is more ordered.

5.3.1.1 Data correction

As for the other samples studied in this thesis, the data correction presented some degree of complexity. The composition, density and packing fraction of the materials need to be known with a certain accuracy in order to perform appropriate corrections.

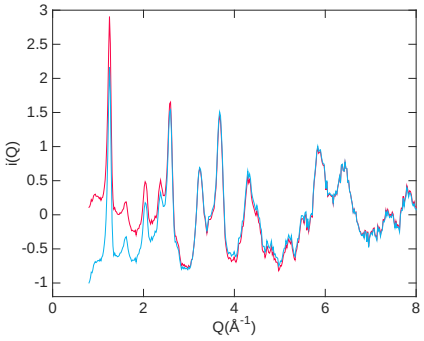

Figure 5.4: The total scattering function of the sample CaO 0 before application of the exponential function corrections in red (only top hat corrections applied) and after applying the exponential function using amplitude and decay parameters $A = 1$ and $\gamma = 5$, respectively.

The composition of the samples was firstly measured by collaborators of Dunstan by means of X-ray fluorescence elemental analysis; however, owing to the low sensitivity of the technique to light elements, it was not possible to detect the C content and hence the $CaCO_3$ concentration could not be determined. On the other hand, the elemental analysis allowed us to get an estimate of the concentration of Al_2O_3 and MgO in the CaO−AlMg series. The composition used in the `Gudrun` corrections was chosen to give good agreement specifically with three factors: the high-Q limit of the merged differential cross section, low-r limits of the $D(r)$ and $G(r)$ functions and prior knowledge of the composition based on the synthesis procedure. In order to reduce the uncertainty of this procedure, the density of the samples was measured experimentally using a pycnometer. The packing fractions were calculated from the ratio between the density of the samples at the time of the neutron experiment (in turns calculated as mass of sample inside the TiZr flat-plate can over volume of the can) and the density measured with the pycnometer. The measured densities are all in the range between $2.3\,\mathrm{g\ cm^{-3}}$ and $2.8\,\mathrm{g\ cm^{-3}}$, with exception of the limestone 2 and 5 samples, whose density was approximately $3.5\,\mathrm{gcm^{-3}}$.

In the correction of the neutron data, it was observed that the low-Q signal had very high intensity, as a consequence of a strong contribution to the scattering arising from the large surface area available. The low-Q component of the scattering arises predominantly from neutrons with long wavelengths. This signal was strong enough to conceal the local and medium range structural features when including all neutron wavelengths in the correction. For this reason, only wavelengths between 0.05 Å and 4.5 Å were used in the corrections of the total scattering data, while for the SAS studies wavelengths up to 10 Å were used in the analysis. This conclusion was not trivial to reach and it required a careful analysis of the data collected from individual detector banks of the instrument NIMROD.

As pointed out in the previous section, both samples CaO 0 and Ca–AlMg 0 contained hydrogen, due to the presence of some $Ca(OH)_2$ in the samples. This was evident throughout the correction procedure since the total scattering function of both materials presented higher intensities compared to the other samples, as well as a steep slope in the low-Q region, a signature of the recoil of the hydrogen atoms. To correct for this effect the exponential parameters described in section 2.3.3 were used, figure 5.4.

Different values of $Q_{\max}$ and Lorch parameters were used depending on the level of noise of the total scattering function at high-Q. The $Q_{\max}$ values were between 17.3 $Å^{-1}$ and 21.3 $Å^{-1}$ for the X-ray data and between 35.6 $Å^{-1}$ and 50 $Å^{-1}$ for the neutron data.

5.4 GULP models for determination of the phase content

In section 5.3.1 we showed that the reflections in the total scattering functions can provide some indications about the phase content of the samples. We also noticed, however, that the peaks in the PDF functions are not as easy to identify. Considerations based on the broad width of the peaks (in both real and reciprocal space) and the loss of strong correlations in the PDF beyond 25 Å in the CaO and CaO-AlMg series hints at the existence of a high level of disorder in the structure. One may hence ask the question of how close the structure of these nanostructures is to the bulk phase of the two main phases of interest for the carbonation applications (CaO and $CaCO_3$). On the other hand, the limestone series present a higher level of order as evidenced by correlations in the PDF beyond 25 Å.

Models based on PDF and total scattering functions of the two phases calculated starting from the spectrum of phonon frequencies using the program `GULP` are used in this chapter as a comparison to the total scattering data to explore the structure and phase composition of these materials. While some of the results that are in this section were already partially anticipated by the observations in section 5.3.1 through identification of the reflections in the $i(Q)$ functions, the `GULP` calculations give a full description of both real and reciprocal data. Being calculated from the phonon frequencies, the model PDFs provide a realistic and qualitative comparison

for identifying the contribution that each of the two phases gives to the experimental PDFs calculated for our samples.

5.4.1 Method

Theoretical neutron PDFs of bulk CaO and $CaCO_3$ were calculated from structural models, simulated on the basis of previously reported potentials and phonon spectra [212], using the software `GULP`. Phonons were sampled on a $5 \times 5 \times 5$ grid in reciprocal space for $CaCO_3$ and a $10 \times 10 \times 10$ grid in the case of CaO.

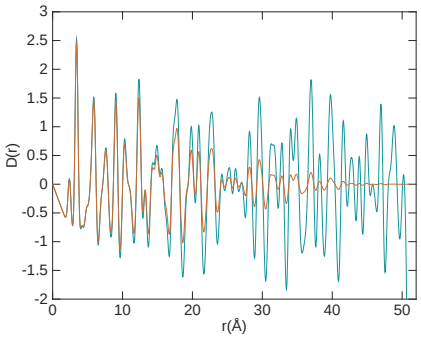

Figure 5.5: The $D(r)$ `GULP` function before (green) and after (orange) multiplication by the sinc function.

The program produces the neutron $D(r)$ and the radial distribution functions of individual pairs of atoms, $g_{ij}(r)$. Specifically, for the $CaCO_3$ phase these are the radial distribution functions $g_{\mathrm{CaCa}}(r)$, $g_{\mathrm{CaO}}(r)$, $g_{\mathrm{OO}}(r)$, $g_{\mathrm{CaC}}(r)$, $g_{\mathrm{CO}}(r)$ and $g_{\mathrm{CC}}(r)$, while for the CaO phase these are $g_{\mathrm{CaCa}}(r)$, $g_{\mathrm{CaO}}(r)$ and $g_{\mathrm{OO}}(r)$.

Thus the X-ray $D(r)$ were calculated using the radial distribution function, making the approximation that the X-ray scattering factors are constant and equal to the atomic number Z. $D(r)$ can be written in terms of the $g_ij(r)$ functions:

$$D(r) = 4\pi\rho r \sum_{ij \geqslant i} c_i c_j Z_i Z_j (g_{ij}(r) - 1) \tag{5.3}$$

where c_i and c_j are the concentrations of atoms i and j, respectively, and ρ is the density of the theoretical crystal structure of the material used in the phonon calculations. These are $0.0718\,\text{Å}^{-3}$ for CaO and $0.0815\,\text{Å}^{-3}$ for $CaCO_3$.

The model neutron and X-ray $i(Q)$ functions were calculated with a bespoke `Matlab` code, that involves three steps. Firstly, a cubic spline interpolation is performed on the real space data to increase the number of data points (or equivalently reduce Δr). After the interpolation the data are multiplied by a cardinal sine function defined as

$$\mathrm{sinc} = \frac{\sin(\pi r / r_{\max})}{\pi r / r_{\max}} \tag{5.4}$$

with $r_{\max} = 51\,\text{Å}$ in this case, equal to the cut-off values for the calculation of the `GULP` PDFs. The sinc function is applied to smooth the high-r data, in order to reduce termination ripples. Incidentally this produces the PDF of a theoretical pseudo-nanoparticle, figure 5.5. The PDF function is also padded with zeroes up to approximately $r = 300\,\text{Å}$, beyond the maximum

$r = 51$ Å, prior to Fourier transforming. This corresponds to an interpolation between points in Q space, which has the result of producing a smoother Fourier transform.

The resulting function is finally sine-Fourier transformed to produce the function $Qi(Q)$, which is divided by Q to obtain $i(Q)$. The Q array needs to be calculated starting from the resolution of the interpolated $D(r)$, Δr_i, and the number of points, n_{r_i} . The conversion is performed applying the following formulas:

$$\begin{aligned} \Delta Q &= 2\pi \frac{1}{(2n_{r_i}\Delta r_i)} \\ Q &= \Delta Q[0 : n_{r_i} - 1] \end{aligned} \tag{5.5}$$

The experimental PDFs are broadened by the experimental resolution and by the smoothing functions applied to remove truncation ripples; in order to be able to reproduce these, the simulations were therefore performed at artificially high temperature. For comparison with the neutron and X-ray PDF data a temperature of 1000 K was used in the `GULP` calculations.

As previously mentioned the work in this chapter has been in part published [2]. The `GULP` calculations included in the publication were all performed at the temperature of 3000 K. The data were corrected, applying a higher degree of smoothing, compared to those reported in this chapter, through the revised Lorch function parameters available in `Gudrun`, thus a higher temperature was required for reproducing the broadening. However subsequent corrections of the data showed that using lower Lorch parameters and the steps described in the methodology section 2.3.3 the noise and termination ripples in the data equally successfully compensated. This does not invalidate the analysis presented since of qualitative nature, aimed mainly at identifying the phase composition of the samples, thus reliable even when a higher degree of broadening is applied. Moreover, as already mentioned, in the case of the sample CaO 0 and CaO–AlMg 0 the exponential parameters were used for improving the neutron correction of the low-Q region due to the hydrogenous component, while in the CaO 0 published data these were not used.

In the case of the $Ca(OH)_2$ phase `GULP` calculations were not performed. However, X-ray and neutron PDF functions were produced using equation 5.3 (Z was substituted by b in the case of neutron), starting from the partial radial distributions calculated from the theoretical structure of $Ca(OH)_2$ using the program `RMCCreate`. A Gaussian broadening (full width at half maximum approximately 0.2 Å) was applied to the PDF to reproduce the broadening due to experimental resolution. The neutron and X-ray $i(Q)$ were calculated applying the same procedure as above.

The $Ca(OH)_2$ model is not expected to reproduce all the features of the experimental data reliably (particularly in the case of the real space data), since it was calculated from the model of the perfectly crystalline unit cell and it cannot account for thermal motion and correlated motion of the atoms. However it still provides a very good reference for identify unambiguously

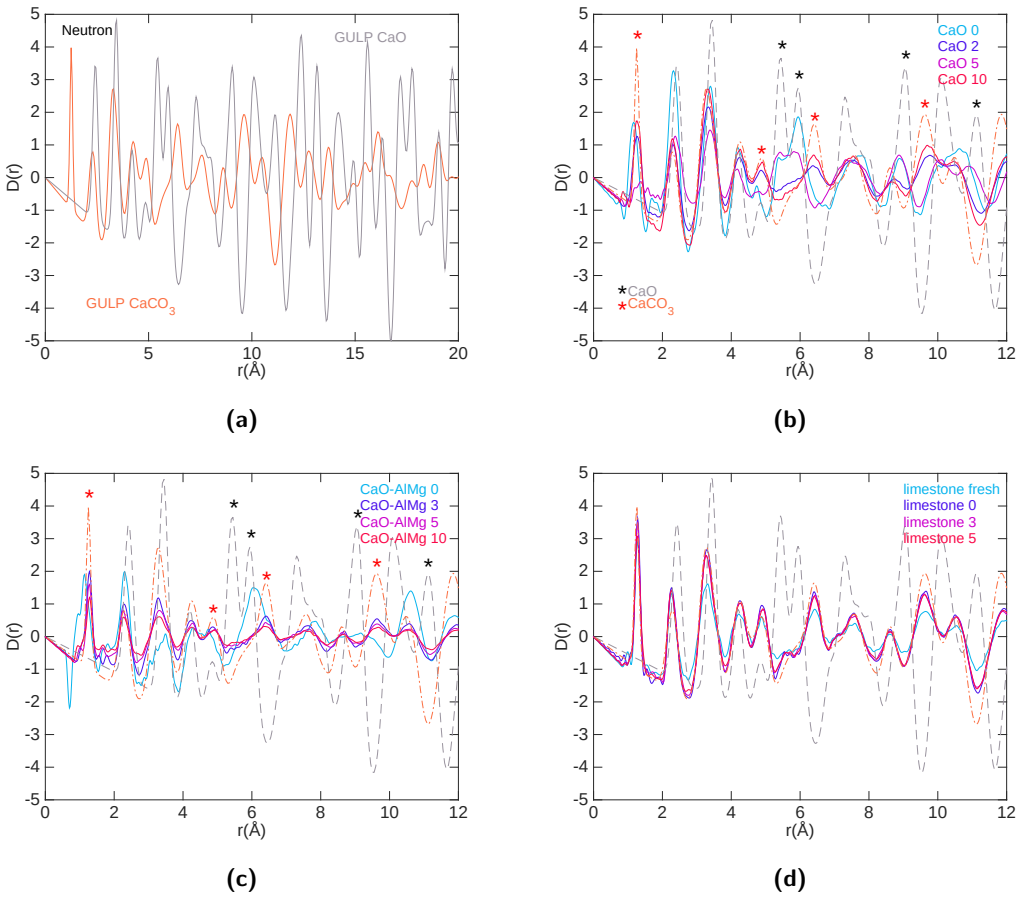

Figure 5.6: (a) GULP model neutron $D(r)$ functions produced from the bulk structure of CaO and $CaCO_3$. Comparison with the neutron PDF of the CaO series (b), CaO–AlMg series (c) and limestone series (d). The GULP model $D(r)$ are the orange ($CaCO_3$) and grey (CaO) dashed lines. The black and red asterisks mark isolated peaks that can be used to identify CaO and $CaCO_3$, respectively.

the presence of the phase of interest.

5.4.2 Analysis of the neutron data

The theoretical neutron $D(r)$ functions of bulk $CaCO_3$ and CaO are shown in figure 5.6 a. While several peaks in the two functions are overlapping, there are a few isolated peaks; these are the C–O peak of the $CaCO_3$, centred on 1.3 Å, and the two Ca–O peaks of the CaO at around 5.4 Å and 5.9 Å. Two other relatively isolated peaks in the $CaCO_3$ phase can be observed at 6.4 Å and 9.6 Å and another one for the CaO phase at 9 Å, but they cannot be assigned to a single pair of atoms since several interatomic distances in the theoretical structure contribute to these two peaks. These peaks (marked in figures 5.6 b and c by asterisks, red for $CaCO_3$ and black for CaO) can be used to identify the two phases, since at the given positions only one of the two will contribute to the histogram of interatomic distances and hence to the total $D(r)$.

Figure 5.6 b shows the comparison between the PDFs of the CaO series and the calculated

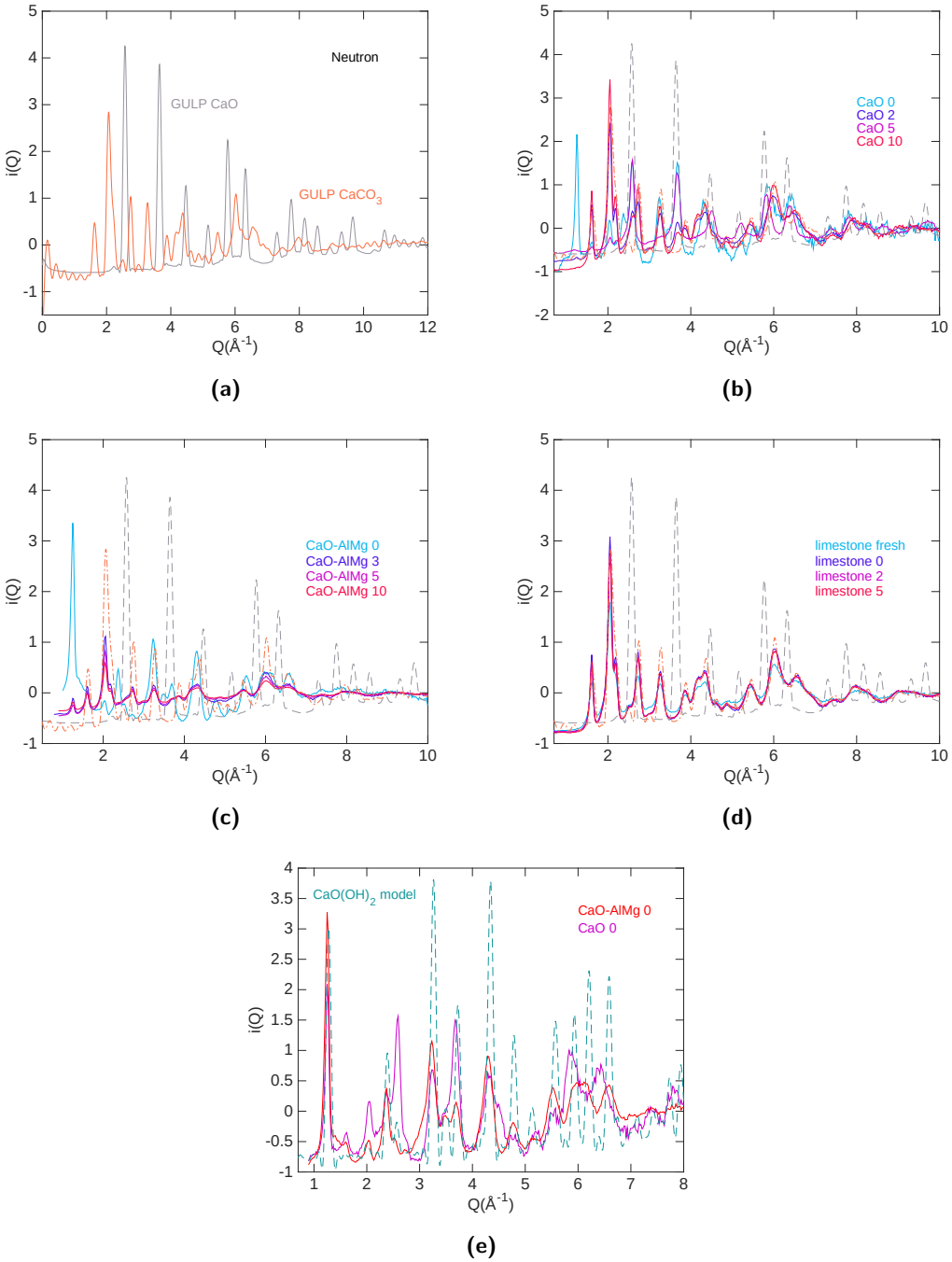

Figure 5.7: (a) GULP model neutron $i(Q)$ functions calculated by sine-Fourier transformation of the $D(r)$ in figure 5.6 a. In (b)-(d) the GULP model $i(Q)$ functions, orange and grey dashed lines ($CaCO_3$ and CaO, respectively), are compared with the neutron $i(Q)$ functions (experimental and model $Ca(OH)_2$). Comparison with (b) the neutron $i(Q)$ of the CaO series, (c) CaO–AlMg series and (d) limestone series. (e) Comparison between the $i(Q)$ calculated from the $Ca(OH)_2$ model and the CaO 0 and CaO–AlMg 0 data.

ones. As observed in section 5.3.1 the C–O peak at 1.3 Å is present in all the CaO series samples, with exception of the CaO 5, as discussed above. The presence of this peak in the CaO 0 sample indicates that there is $CaCO_3$ in the sample even before carbonation, which may be due to slow carbonation in the atmosphere before the experiment. However the gradual increase of the calcite component in samples CaO 2 and 10 is more evident observing the peaks at 9.6 Å and 6.4 Å. The CaO content is reduced drastically even after only 2 minutes of carbonation, as indicated by the lack of the CaO peaks at 5.4 Å and 5.9 Å, as well as by the depletion of all the other peaks signature of CaO (black asterisks in the figure). Features in the CaO 0 sample that deviate from either of the $D(r)$ of the two phases can be identified as arising from the $Ca(OH)_2$ contribution, as i.e. the higher intensity of the peak at 5.9 Å relatively to the one at 5.4 Å, when compared to the CaO model. Interestingly the CaO 5 sample $D(r)$ is the closest to the CaO model $D(r)$ confirming that the carbonation may have not occurred in this sample.

The CaO–AlMg series also shows a gradual increase of carbonation with time, even though already after 3 minutes the sample is mainly composed of $CaCO_3$. This is confirmed by the similarities of the $D(r)$ of $CaCO_3$ with the three samples CaO-AlMg 3, CaO-AlMg 5 and 10. However, a high level of disorder is observed in this structures as evidenced by the broadening of the calcite peaks already at 4 Å. The CaO-AlMg 0 sample lacks of features that could be unambiguously associated with CaO (black asterisks), but has a contribution from the $CaCO_3$ phase, as observed from the presence of the first peak marked with the red asterisk. All the other features in the PDF reflect the structure of $Ca(OH)_2$ rather than the CaO, as the single peaks at 6 Å and at 10.5 Å that correspond to a collection of interatomic distances found in theoretical crystal structure of $Ca(OH)_2$.The presence of a significant hydrogenous component in the sample would explain why it was difficult to achieve good corrections in the case of this sample.

Finally, all the samples in the limestone series match very well the PDF of the $CaCO_3$ model. In the case of the limestone 0 sample this shows that the calcination did not have any effect on the structure, i.e. the CaO was not reformed. It is hard then to know whether in the case of the limestone 2 and 5 sample the calcitic component is simply due to the original limestone fresh precursor, that, during the calcination and carbonation reaction, did not undergo any structural and chemical changes, or if in the case of these samples the calcination did have an effect and the final calcite composition was reformed upon carbonation. Based on the result on limestone 0, the first of the two possibilities is the most likely.

The reciprocal space data calculated from the `GULP` PDF functions reflect the results obtained in real space, figure 5.7. It can be observed that the peak at 1.28 $Å^{-1}$ in the non carbonated samples, CaO 0 and CaO–AlMg 0 does not find any corresponding peak in the model i(Q) functions. This peak was identified as the (001) reflection of crystalline $Ca(OH)_2$. This is confirmed by comparison of the two sets of data with the $i(Q)$ calculated from the model PDF

of the $Ca(OH)_2$ unit cell, as observed in figure 5.7 e.

It should be noted that, since the intensities of the functions of the `GULP` models and $Ca(OH)_2$ model are arbitrary, they were scaled using the first peak of the $D(r)$ and $i(Q)$ limestone series samples as reference for the $CaCO_3$ phase model. The CaO was then scaled accordingly, since there isn't a well defined and localised intensity that can be associated exclusively to CaO, as in the case of the first peaks of the $D(r)$ and $i(Q)$ of $CaCO_3$. For the $Ca(OH)_2$ model the first peak of the $i(Q)$ of CaO–AlMg 0 was used as reference.

5.4.3 Analysis of the X-ray data

Comparison of the CaO and $CaCO_3$ X-ray model PDF and $i(Q)$ functions with the total X-ray PDF and scattering data (figure 5.8 and 5.9) leads to conclusions analogous to those achieved through analysis of the neutron data.

However a difference is observed in the case of the CaO 0 and CaO 5 samples of the CaO series. The CaO component is not as well defined as in the neutron data, as evidenced from the presence in the PDF of a unique broad peak at around 5.8 Å, rather than the two split peaks observed in the CaO model (black asterisks), and another peak at 10.5 Å. This is instead in agreement with interatomic distances observed in the $Ca(OH)_2$ theoretical structure, as shown in figure 5.8 e (where we also plotted the CaO–AlMg 0 PDF since the $Ca(OH)_2$ phase is found also in this sample). Comparison of the X-ray PDF function of the CaO-AlMg 0 sample with those of the CaO 0 and CaO 5 samples show that the features at 5.8 Å and 10.5 Å are observed also in the CaO–AlMg 0 sample. It was observed in the case of the neutron data that this sample presents features in the PDF and $i(Q)$ that are not in agreement with either of the two model phases, but can be associated with the presence of a significant $Ca(OH)_2$ component.

Analogously to the neutron data of the CaO–AlMg 0 sample, that reflects the presence of a strong hydrogenous component, the formation of $Ca(OH)_2$ happens as a consequence of absorption of moisture in the air. This implies, as already anticipated in section 5.3.1, that between the neutron and X-ray experiments the two samples CaO 0 and 5 absorbed water from the air, leading to the formation of more $Ca(OH)_2$. This in turn also implicitly confirms that, in order to be able to form $Ca(OH)_2$, the CaO 5 sample was composed mainly of CaO at the time of the neutron experiment. The presence of a remaining CaO component in the CaO 0 sample can be inferred based on the peak at approximately 7.5 Å, very broad and shifted to higher r in the CaO 5 sample. Moreover the feature at 5.8 Å is located in between the two CaO peaks (figure 5.8 b), while shifted on the right in the CaO 5 sample, indicating that not all CaO has reacted to form $Ca(OH)_2$.

The strong similarity of the $i(Q)$ functions of CaO–AlMg 0 and CaO 5 samples with the model $i(Q)$ of $Ca(OH)_2$ (figure 5.9 d) confirms what observed in real space. On the other hand,

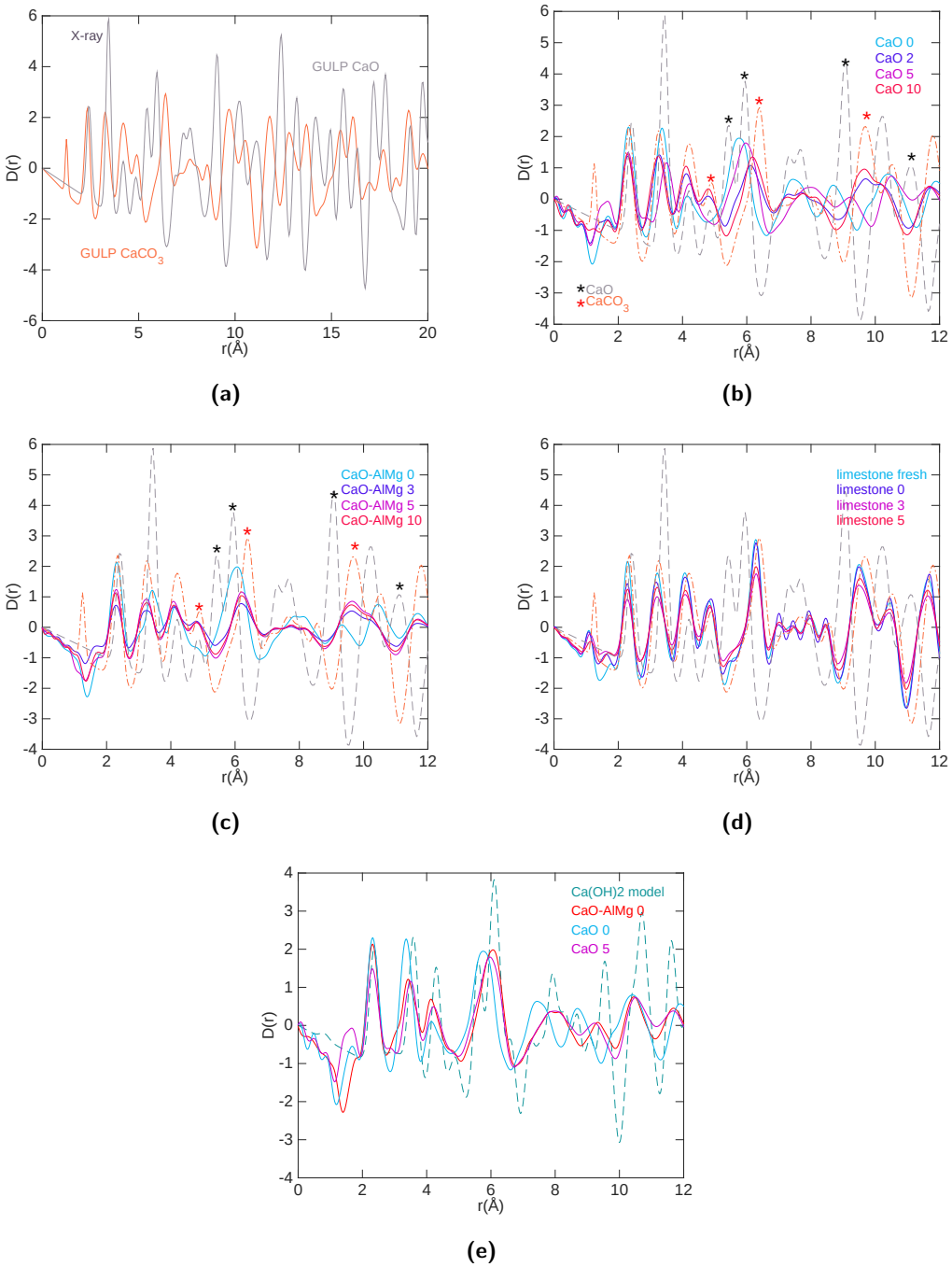

Figure 5.8: (a) Model X-ray $D(r)$ functions calculated from the GULP partial $g_{ij}(r)$ of the bulk structure of CaO and $CaCO_3$. Comparison with the X-ray PDF of the CaO series (b), CaO–AlMg series (c) and limestone series (d). The GULP model $D(r)$ are the orange ($CaCO_3$) and grey (CaO) dashed lines. The black and red asterisk mark isolated peaks that can be used to identify CaO and $CaCO_3$, respectively. (e) Model $D(r)$ calculated from the unit cell of $Ca(OH)_2$ compared to the CaO–AlMg 0, CaO 0 and CaO 5 data.

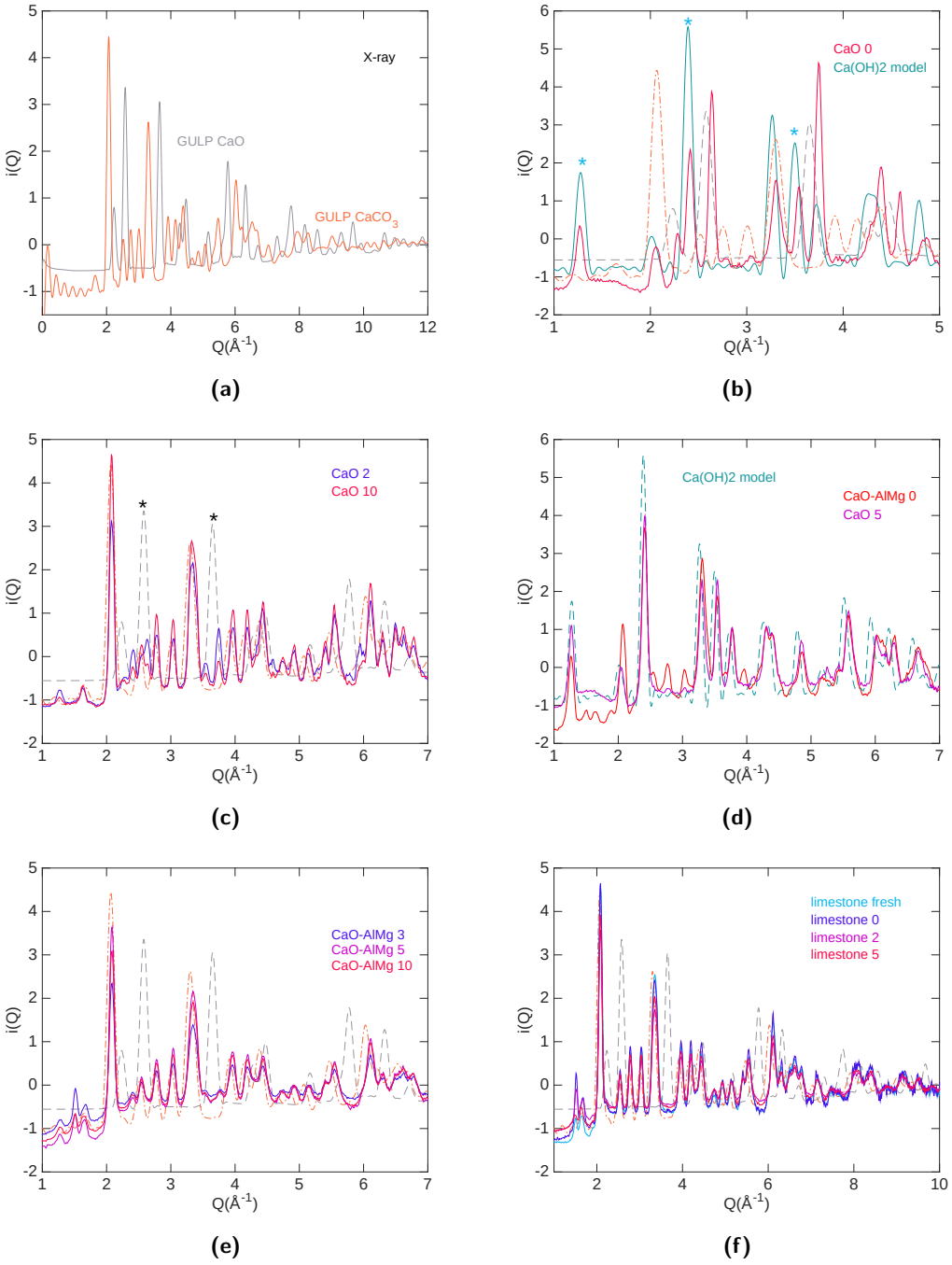

Figure 5.9: (a) GULP model X-ray $i(Q)$ functions calculated by sine-Fourier transformation of the $D(r)$s in figure 5.8 a. In (b)-(f) the GULP model $i(Q)$ functions, orange and grey dashed lines ($CaCO_3$ and CaO, respectively), are compared with the X-ray $i(Q)$ functions (experimental and model $Ca(OH)_2$) . Comparison with: (b) the $i(Q)$ of the CaO O sample and the model $Ca(OH)_2$, (c) the CaO 2 and CaO 10 samples, (d) the $i(Q)$ of the two samples containing the highest fraction of the $Ca(OH)_2$ phase (CaO 5 and CaO–AlMg) and the model $Ca(OH)_2$ $i(Q)$ functions, (e) the $i(Q)$ of the three carbonated samples of the CaO–AlMg series and (f) the $i(Q)$ of the samples of the limestone series.

the presence of a mixture of phases in the CaO 0 sample is observed in figure 5.9 b, where the peaks that can be used to identify the contribution from the $Ca(OH)_2$ component are marked by light blue asterisks. Other peaks arise predominantly from the contribution due to the CaO phase.

The other carbonated samples of CaO and CaO–AlMg show relatively good agreement with the $CaCO_3$ phase model, both in real and reciprocal space (figures 5.8 b and c, 5.9 c and e). In the CaO series, the gradual increase in carbonation is evidenced particularly in the real space data, where some minor features associated with a CaO contribution in the CaO 2 sample are observed. These correspond to the (002) and (022) reflections and are marked in figure 5.9 c by black asterisks. The carbonated samples of the CaO–AlMg series doesn't show visible changes in the PDF and $i(Q)$ upon carbonation (figures 5.8 c and 5.9 e), indicating that most of the carbonation occurs in the first 3 minutes and the structure remains stable after that.

Finally, the very good agreement of the PDF and $i(Q)$ data of the limestone series samples with the $CaCO_3$ model confirms, as observed in the case of the neutron data, the strong calcitic component of the samples.

5.4.4 Long-range order

We have observed in the previous section that the short range order of most carbonated samples is in good agreement with the model bulk $CaCO_3$ structure. A comparison of the medium and long range order in the PDF of the most carbonated samples of the three series (CaO 10, CaO–AlMg 10 and limestone 5) data with the model PDF of $CaCO_3$ shows that the structure is not represented at all by the model in this region (figures 5.10 a and b). A strong drop in the intensities of the neutron PDF data is observed beyond 20 Å. Similarly in the X-ray data, although in this case the limestone 5 sample appears to have a much more ordered structure compared to the other two samples, since sharp peaks are observed up to 30 Å. Not only do the intensities fall off beyond these distances, but they also become very broad. In the case of the neutron data of the CaO–AlMg no correlation is observed beyond 30 Å.

These observations show that the structure presents a very high level of disorder and a lack of long range order. Thus, the bulk `GULP` model is a qualitative representation of the local order in the structure and overall phase composition.

It was mentioned earlier that prior to perform the Fourier transform the data to calculate the $i(Q)$ model functions, we need to multiply the model $D(r)$ by a sinc function (section 5.4.1) . The functions resulting from the multiplication of the sinc function with the neutron and X-ray model PDF are shown in figures 5.10 c and d and compared with the experimental data. The application of the sinc function causes a gradual dampening of the PDF intensities, that go to zero at the desired cut-off distance. The effect of this function is similar to that obtained when

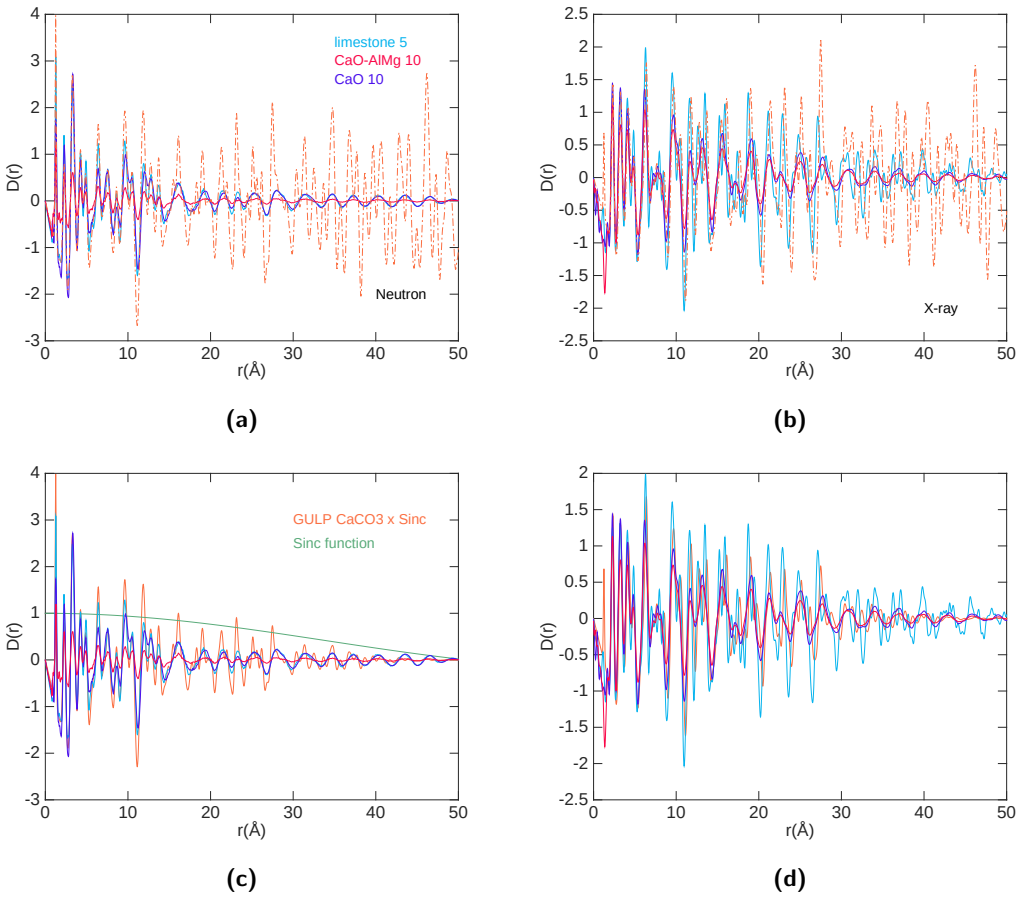

Figure 5.10: The short and medium range order of the most carbonated samples of the three series compared to the GULP model of $CaCO_3$, neutron data (a) and X-ray data (b). The correlations in the experimental data fades at much lower r compared to the bulk model. (c) The GULP model of $CaCO_3$ multiplied by the sinc function (equation 5.4), shown in green, compared to the neutron data.

multiplying the data by a shape function that accounts for the shape of a nanoparticle. As a result this creates a model PDF that is closer, at least in intensities, to the experimental PDF. The $i(Q)$ functions resulting from the Fourier transform of the sinc multiplied PDF functions are thus expected as a consequence to be closer in relative intensities to the experimental $i(Q)$ data.

5.5 Small angle scattering

In the case of the materials studied in this chapter, further insight into the morphology of the nanoparticles can be obtained through analysis of the small angle scattering region. We recall here that the diffractometer NIMROD can measure Q as low as $0.02\,\text{Å}^{-1}$, thus accessing in this case the Porod region, which corresponds to dimensions smaller than the scattering object [213]. The Porod region provides information about the local morphology of a single nanoparticle, such as pores or tortuosity of the material. In particular, the Porod plot, consisting

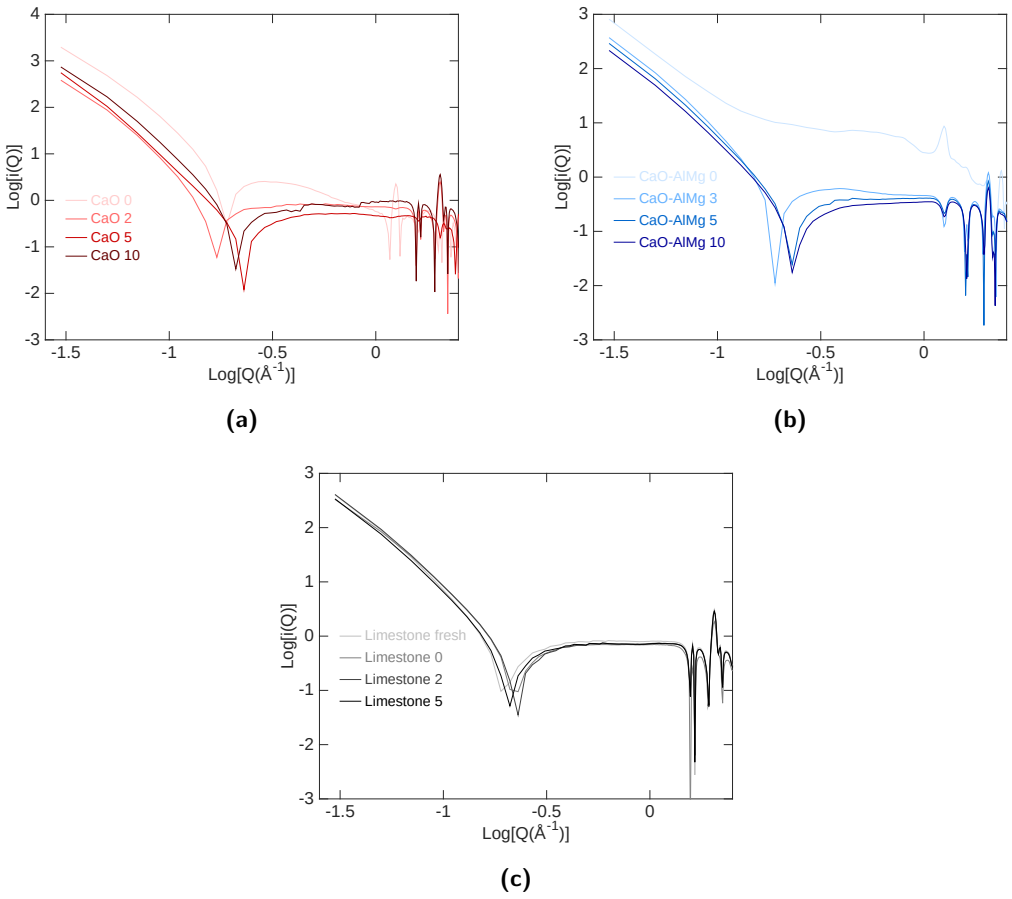

Figure 5.11: Porod plot of the small angle scattering region of the CaO series (a), CaO-AlMg series (b) and limestone series (c). $Q_{\min} = 0.02\,\text{Å}^{-1}$ was used in the correction and wavelengths up to 10 Å were included.

of a $\log_{10}(Q)$ vs $\log_{10}(iQ)$ plot, yields information about fractal dimensions. In fact, in this region:

$$I(Q) = \frac{A}{Q^n} + B, \tag{5.6}$$

which can be rewritten as

$$\log_{10}[I(Q) - B] = \log_{10} A - n \log_{10} Q \tag{5.7}$$

where A and B are constants and $n = 6 - D$, where D is the fractal dimension. If $n \approx 4$ then the nanoparticles are 3D objects with smooth surfaces, whereas a slope with $3 < n < 4$ characterises rough interfaces of fractal dimension D [213].

The Porod plots for the three series of samples are shown in figure 5.11. A least squares linear fit to the SAS curves was performed in the region $-1.53 < \log_{10}(Q) < -0.89$, the corresponding dimension probed being $49\,\text{Å} < d < 213\,\text{Å}$. The results of the fit are shown in table 5.4. In the case of the CaO samples we observe a loss of porosity upon carbonation, as evidenced by the

Table 5.4

Porod plot results			
CaO 0	CaO 2	CaO 5	CaO 10
3.412 ± 0.007	3.905 ± 0.014	3.847 ± 0.003	3.646 ± 0.006
CaO-AlMg 0	CaO-AlMg 3	CaO-AlMg 5	CaO-AlMg 10
$2.676 \pm 0.001^{\star}$	3.491 ± 0.005	3.387 ± 0.003	3.323 ± 0.002
Limestone fresh	Limestone 0	Limestone 2	Limestone 5
3.197 ± 0.003	3.509 ± 0.004	3.335 ± 0.002	3.402 ± 0.003

The values reported in the table are $n + \sigma^2$, resulting from a linear least squares fit to the SAS in the region $-1.53 < \log_{10}(Q) < -0.89$. The variance σ^2 is given by $\frac{1}{N-1}\sum_{i=1}^{N} |A_i - \mu|^2$ where μ is the mean of A.
* This value is not entirely reliable since there is a strong signal due to the inelastic scattering from the H atoms.

increased values of n of the carbonated samples compared to the CaO 0 sample. The values of n for the CaO 2 and CaO 5 samples in particular is very close to 4 indicating that the surface of the nanoparticles is almost completely smooth. This loss of porosity is likely to be linked to the sintering mechanism mentioned earlier that causes the depletion of the CO_2 absorption capacity of CaO upon several carbonation cycles.

The value of n obtained for the CaO–AlMg 0 sample is not entirely reliable, since, as can be seen in figure 5.11 b, the signal is altered by the incoherent component of the scattering due to the high H content in the sample. The other three samples of the series all have values of n in between 3.3 and 3.5, indicating object with fractal dimensions between 2.5 and 2.7.

In the case of the limestone series a gradual loss of porosity is observed upon calcination since n goes from approximately 3.2 to 3.5. The values decrease slightly upon further carbonation (samples limestone 2 and 5). Overall, however, strong changes are not observed.

Despite the fact that the SAS provides an additional source of information, it should be noted that the number of data points in the region of interest is scarce. In fact the fit was performed with respect to only 6 data points.

5.6 Summary

The work presented in this chapter is a contribution to the understanding of the structure of $CaO/CaCO_3$ nanoparticles, a class of materials of great technological interest for applications in CO_2 capture. We demonstrated that the PDF and total scattering data can be used for identifying the carbonation state of the samples after various carbonation time. We calculated model PDFs of the CaO and $CaCO_3$ bulk phases, based on the spectrum of phonon frequencies using the program `GULP`. Model total scattering functions were calculated from the model PDFs and used, together with the PDFs, as a means of comparison to the data. This allowed us to identify the phase contribution to the data of the various samples.

Hence, it was shown that in CaO samples and CaO with Al_2O_3 and MgO impurities, the carbonation process occurs mainly in the first two minutes of carbonation, since the structure does not show significant changes after further carbonation time. Moreover we showed that the calcination of the limestone sample does not produce a structure consistent with CaO rather the sample retains the $CaCO_3$ structure, thus implying that this material (in the form here studied) is not suitable for applications in carbonation-calcination looping.

Finally, the small angle scattering region of the data provided some information about the fractal dimensions of these nanoparticles. In particular, a loss of porosity was observed in the CaO samples upon carbonation. This factor is likely to affect the CO_2 absorption efficiency of these nanostructures.

Chapter 6

Conclusions

In this thesis work the total scattering technique was combined with a variety of modelling techniques to study the local atomic structure of three different classes of nanomaterials and their phase composition, when information about the latter was not easily accessible through other techniques. All of the three classes of nanomaterials studied multiwalled carbon nanotubes continuously filled with iron (Fe@MWCNTs), Prussian blue $Fe[Fe(CN)_6]_3$ in solid and hollow form and $CaO/CaCO_3$ with various degree of carbonation are novel materials of great technological interest since they present a large number of potential applications, depending on their properties. This study is the first attempt at studying the structure of these novel nanomaterials by means of total scattering. These nanomaterials are more structurally complex than those previously studied by total scattering.

The differences between these nanostructures are many more than their similarities. The latter can be reduced to them being all nanoparticles and presenting properties that stem from their size. The differences, on the other hand, arise from several factors.

From the morphological point of view, they all present different shapes, characterised in some cases by local alterations. The Fe@MWCNTs can be described as cylindrical one-dimensional nanostructures, with various degrees of distortion from the perfectly cylindrical geometry depending on the tortuosity of the single wire. The Prussian blue nanoparticles are cubic nanoparticles and in the case of the hollow morphology they can be described as cubic shells, created by the internal cavity. The $CaO/CaCO_3$ nanoparticles are spherical and characterised by porosities.

These nanostructures are all multiphase systems, composed of a combination of phases, but none of these are in common between the different classes. The spatial distribution of such phases in the nanostructures is also very case-dependent, being determined at times by factors of physical, chemical or morphological origin.

The local ordering in these nanostructures is determined by factors that are due to the spatial confinement in the case of Fe@MWCNTs, of chemical nature being due to the presence

of $[Fe(CN)_6]^{-4}$ vacancies in Prussian blue and the morphology in the case of $CaO/CaCO_3$ nanoparticles owing to the presence of pores.

Notwithstanding the high level of complexities and the differences between these three classes of nanostructures, we were able, by use of the total scattering method combined with a variety of modelling techniques, to answer several questions concerning their structure. This study represents an example of the many approaches that, starting from total scattering data, can be taken to solve questions that concern the structure and properties of nanomaterials. These approaches are case dependent and always involve the combination of experimental and modelling techniques, the latter being guided and directed by an initial understanding of the nanomaterials, based on prior knowledge and complementary experimental techniques. This study also demonstrates that the combined use of both neutrons and X-rays as total scattering probes is often pivotal for achieving an understanding of complex multiphase systems, either in nanoparticulate or bulk form.

6.1 Modelling methods: to each nanoparticle its own

In this thesis work a variety of modelling methods was used to complement and make the most of the information contained in the total scattering data, depending on the material studied. The modelling and structural refinement techniques used include: Rietveld refinement, `PDFgui` refinement, MD simulations, `GULP` calculations, bespoke modelling of the low-r peaks in the PDF, `RMCProfile` modelling and small angle scattering analysis.

The choice of the analysis or modelling technique used depended on the nature of the nanomaterials analysed and the questions we were trying to answer. The approach taken in this work can be generalised to the study of other nanomaterials and some of the overarching principles that underlie the choice of a specific method in spite of another can be stated.

In case of nanostructures whose diffraction pattern presents sharp Bragg peaks, it is useful to perform complementary powder diffraction measurements. If the phases contained in the sample are known, the unit cell of these phases can be refined against the Bragg data through Rietveld refinement. The Rietveld refinement can provide some initial information about the weight fractions of the various phases and indicative lattice parameters. However if the structure has a high degree of disorder some peaks in the diffraction pattern may be absent or very broad, thus running the risk of underestimating the presence of some of the phases refined and generating a fit to the data that is not robust.

We showed that for analysis of the PDF and total scattering data different approaches can be taken. Firstly the program `PDFgui` can be used in the case of nanomaterials whose structure is close enough to that of a bulk material. `PDFgui` is very useful in the case of spherical nanoparticles of small dimensions (i.e. $< 10\,\text{nm}$) containing a single phase, since in this case

it is possible to use the shape function to get a realistic estimate of the average size of the nanoparticles. Even in the case of larger nanoparticles (as the Fe@MWCNTs and Prussian blue) it can still provide information about the average expansion of the lattice parameters compared to the theoretical structure, phase content and atomic displacement parameters.

However, in order to study nanoparticles where the local structure is affected by the large surface to volume ratio and spatial confinement (e.g. Fe@MWCNTs) or the presence of defects (e.g. Prussian blue) or when we are interested in the morphology of the nanoparticles (e.g. $CaO/CaCO_3$ system) we need to use more complex and exhaustive modelling approaches that can take into account these factors. This can be done modelling the structure by means of MD simulations, `RMCProfile` refinements and `GULP` calculations.

MD simulations are very useful for testing the local changes that occur in a nanoparticle under desired conditions (temperature and pressure). Provided appropriate interatomic potentials are used, the MD simulation approach can give a great wealth of information, especially about surface effects, interaction between different phases at interfaces and spatial confinement effects. Moreover they offer the advantage of a great flexibility, providing the ability to build and test potentially any sort of nanoparticle. The PDF can be calculated from the final atomic configuration and compared with the experimental data to confirm the validity of the model.

The `RMCProfile` method can be used when it is possible to build a starting configuration that is very close to the real expected structure of the material. Hence, in the case of nanomaterials, the use of the technique will often require some other preliminary analysis that can guide the making of realistic atomic configurations. This is the case of the study of Prussian Blue, where the stoichiometry and dislocation of the vacancies of the initial configuration for use in RMC modelling were decided based on results from elemental analysis, infrared spectroscopy analysis and a least squares fitting procedure of the first few peaks of the PDF of the material. However, at the current stage, `RMCProfile` deals only with bulk configurations (i.e. supercells with periodic boundary conditions applied), thus it cannot be used to model the structure of small nanoparticles (section 6.2.4).

`GULP` calculations are useful for determining the phase content of a nanomaterial, in cases where other techniques such as `PDFgui` do not provide robust results. In order to apply this method one must be able to identify peaks in the PDF and/or total scattering data that can be unambiguously attributed to one single phase, based on the prior knowledge of the theoretical structure. An extensive example of the use of this method is the study of the $CaO/CaCO_3$ system. Another case where `GULP` calculations are very useful is to identify the similarities between the PDF of a theoretical structure and the PDF calculated from the final configuration of a MD simulation. In the case of the study of the iron nanowire in the Fe@MWCNTs systems this method allowed us to identify the formation of a hybrid structure in between that of γ and α-Fe.

The small angle scattering technique provides information about shape, size and morphology of the nanoparticles. In the case of the $CaO/CaCO_3$ nanoparticles, we could access the Porod region, where objects of size smaller than the nanoparticles themselves are probed. Thus this gave us information about the pores and the surface roughness of the nanoparticles. This information are particularly useful in cases where the morphology affects the properties and structure of the nanoparticles. In the case of our system, the porosity is linked to the efficiency of this material as filter for CO_2 capture, thus representing a fundamental bit of information.

6.2 Current and future work

6.2.1 Fe@MWCNTs

To further develop the model of the iron-filled multi-walled carbon nanotubes we have started working on MD simulations of Fe@MWCNTs (rather than Fe@SWCNT). A van der Waals type of potential can be used to model the interlayer interactions, as the one reported by Hasegawa and Nishidate [214]. The **a** and **b** crystallographic axes of a CNT can be oriented parallel to the a and b axis of the neighbouring CNTs or at an angle. It is useful to explore different possible orientations of the axis of the CNTs relative to each other. Previous studies [155] have in fact reported the formation of regular facets, where the interlayer distance is locally increased, depending on the relationship between the chiral angle of adjacent nanotubes. This is a consequence of the local atomic stacking of neighbouring layers. The local structure is expected to be highly affected by the interplay between the formation of facets and the interaction between the innermost nanotubes layer and the iron core, depending on the orientation of the crystallographic axis of Fe with respect to the nanowire (as shown in section 3.3.4.2). The results of the MD of Fe@MWCNTs can then be compared with the total scattering and PDF data.

We have also started working on MD simulations of iron nanowires containing different phases. In particular we have created configurations with γ-Fe located at the tip of a α-Fe nanowire. Other possibilities can include a concentric arrangement of the phases (e.g. an α-Fe core surrounded by a γ-Fe shell), or alternating phases along the axis of the cylinder. Other models can also include the Fe_3C phase that is found in some of the materials treated.

Differential neutron total scattering analysis can be performed to observe changes in the total scattering data that could arise from the antiferromagnetic-paramagnetic phase transition of γ-Fe and its interaction with the ferromagnetic α-Fe. The magnetic signal (if any) appears in our case masked by the C contribution to the scattered intensities. The differential neutron data can be caclulated subtracting normalised neutron total scattering data collected from empty MWCNTs from the Fe@MWCNTs data. The empty MWCNTs can be synthesised by CVD and the parameters of the synthesis adjusted so that the MWCNTs present a number of walls closed to those found in the Fe@MWCNTs studied.

In any case, in the modelling and study of these structures by means of total scattering, it is always necessary to combine different techniques (such as TEM imaging and diffraction, SEM imaging, Bragg diffraction and magnetometry), in order to both guide the choices made in performing the modelling and confirm its consistency with other experimental observations.

6.2.2 Prussian Blue

Several `RMCProfile` refinements of both the solid nanoparticle and bulk data have been attempted. We are still working on these, trying to improve the consistency of the model with the various sets of data (i.e. $D(r)$, $i(Q)$ and Bragg profile). Ideally, to fully benefit from the availability of both neutron and X-ray data these should be refined together in one unique `RMCprofile` refinement (i.e. including both X-ray and neutron $D(r)$ and $i(Q)$). This can be done with `RMCProfile 6.5`.

The X-ray total scattering data of the nanoparticle samples show the presence of an additional peak absent in the bulk data, that is forbidden in the $Fm\bar{3}m$ space group. We mentioned that this it is probably an indication of the breaking of the symmetry as a consequence of systematic defects in the structure. It is possible that this could arise as a consequence of vacancies regularly rather than randomly allocated in the structure. We could then create starting configurations for RMC refinement containing ordered vacancies.

We have observed that there is a residual PVP component in the nanoparticle sample which is reflected by a weak signal underlying in the first peak of the PDF, as shown in the least square fitting procedure 4.4.1.4. We have started working on performing `GULP` calculations of the PVP monomer, in order to produce a PDF and its Fourier transform that can be then subtracted, after appropriate normalisation, from the solid nanoparticle data.

Another possible route, that would be firstly useful for confirming the contribution to the PDF arising from the PVP, would involve collection of additional total scattering data on NIMROD on PVP powder. Secondly, this data could be subtracted from the solid nanoparticle data (instead of the calculated `GULP` PDF) to subsequently perform analysis of the differential PDF.

An approach that could be taken in a future neutron experiment on PB would involve heating the samples to 450 K to remove coordinated and non-coordinated water molecules [168] and observe the structural changes as the water is released.

6.2.3 CaO

Further insight on the carbonation process of the CaO nanoparticles and how it affects the structure can be obtained performing MD simulations. Matthew Dunstan and Martin Dove performed MD simulations of spherical core-shell ($CaCO_3$@CaO) nanoparticles, with variable

diameters for the CaO core and the $CaCO_3$ shell. This was performed hypothesising a carbonation process that affects the surface of the CaO nanoparticles homogeneously.

However the tomography and small angle scattering analysis showed that the carbonation happens starting from pores in the CaO nanoparticles [2]. Thus MD simulations with pores randomly distributed across the CaO nanoparticle would provide a better understanding of the structure and behaviour of the system. Ideally the simulation would be performed flowing CO_2 molecules in the simulation box implementing chemical reaction in the simulation, to observe the CO_2 carbonation process happening. This would be performed at the typical carbonation temperature, pressure and CO_2 flow rate of industrially used sorbents [207]. The carbonation would then be followed by a MD simulation of the calcination process, by interrupting the CO_2 flow and applying appropriate temperature to the carbonated system obtained from the previous step.

However, a simpler start would involve coating the pores of the CaO nanoparticles with $CaCO_3$ and let the system relax the under desired temperature and pressure. This model would give some more information about the sintering process and could be used as a comparison to the total scattering data. Moreover, these configurations could be used in an RMC refinement performed treating the material as bulk.

6.2.4 Considerations on the use of `RMCProfile` for modelling of nanoparticles

The RMC refinement of the structure of PB was performed treating the material as bulk, i.e. a supercell was created and periodic boundary conditions were applied to the box. This approximation is realistic for nanoparticles of sizes in the order of few tens of nanometers or more. However when it comes to the analysis of smaller nanoparticles treating the material as a bulk is reductive.

As an example from this thesis, it is not possible to model the structure of Fe@MWCNTs using this approach. Still, using the MD model of the Fe@MWCNTS as starting configuration of a RMC refinement against the data would provide further insight in the understanding of the structure of these materials. For this reason we have started working towards implementing functionalities in `RMCProfile` that would allow the modelling of nanoparticles against total scattering data. This step involves the use of a different formalism compared to that used in the modelling of bulk configurations.

Particularly important in this context it is how the density of the supercell containing the nanoparticle is defined, since this affects the behaviour of the $D(r)$ function at high-r. An approach that we have considered so far involves the use of a local density function. Compared to the shape function approach largely used in the literature and in `PDFgui` [215] this would not require the use of a bulk model as starting point of the refinement.

6.2.5 Sample preparation

A final remark concerns the synthesis techniques used for the preparation of the nanoparticle for total scattering measurements. In order to simplify the analysis process of the total scattering and PDF data, it is important to consider ahead (i.e. at the synthesis stage) which experimental method can be used to minimise the presence of impurities, polymers or any other additional compound used in the synthesis. Usually, these components are not of interest for the analysis of the atomic structure of the nanoparticles, while they add a further level of complexity in the steps involved in the data correction and modelling procedure. This was observed in the case of the study of the PB nanoparticles where the remaining PVP in the sample affected the ability to model the data.

On the other hand, the synthesis of nanoparticles often involves the use of some additional catalytic or stabilising compound and, in some cases, the formation of byproducts of the synthesis (e.g. oxides in the Fe@MWCNTs samples). Where possible, it is thus advisable to consider ahead the available synthesis route that can be taken and experimental methods that can be used to clean the samples, in order to produce nanoparticles as pure as possible. The higher the purity of the nanoparticles, the simpler the data analysis and processing are, providing at the same time a more solid ground for building models of the atomic structure consistent with the data.

Appendix A

Coding

A.1 Code for making nanoparticles of different shapes in solid and hollow form

This Fortran subroutine is part of the `RMCCreate` code. I have added the functionalities to make nanoparticles of different shapes, such as cylindrical, rectangular and ellipsoidal (apart from the pre-existing spherical option). Moreover the nanoparticles can be either in solid form or hollow. The hollow nanoparticles can then be used either as they are or combined with other configurations to create core-shell types of nanoparticles.

If the `rotate` flag and the `nanoparticle` flag are invoked together, the supercell is first rotated by means of the subroutine in appendix A.2 and subsequently cut to form the desired shape. As an example, a typical command line to generate an α-Fe nanoparticle of hollow cylindrical shape with 111 crystallographic direction parallel to z will look like:

`./RMCCreate -cif -rotate[45 54.70 0] -nano[30 30 100] -shape cylinder -hollow[10 10 50] α-Fe.cif` where the numbers in brackets after the `rotate` flag are the Euler angles

of rotations, after `nano` the dimensions of the cylinder in the three orthogonal directions (i.e.

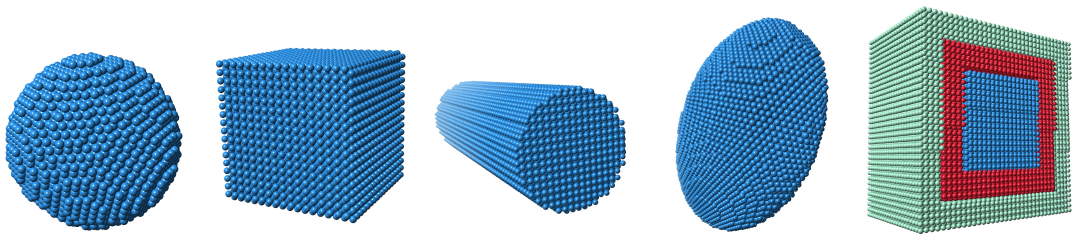

Figure A.1: The subroutine operated in the framework of the `RMCcreate` code can be used to generate nanoparticles of various shapes, as shown in the first four pictures, as well as hollow nanoparticles, that can be then assembled together to form core-shell type of structure as shown in (e).

diameter along x and y and length of cylinder along z) and analogously for the hollow flag (i.e. they specify the size of the cavity). Specifying the diameter in both x and y direction gives the possibility to create where requested distorted cylindrical structures (this applies also to the other shapes, where the appropriate flags are used).

```
  subroutine nanoparticle
!   ======================

!------------------------------
!
!     This subroutine creates a nanoparticle of a chosen shape from the expanded
!     configuration
!
!------------------------------

    use structure_data
    use arguments

    implicit none

    integer :: i,j,newatoms,iel
    integer, allocatable :: atom_typet(:),atom_labelt(:),rnumt(:),rcellt(:,:)
    double precision,allocatable :: xft(:),yft(:),zft(:),xot(:),yot(:),zot(:)
    double precision :: rcentre(3),rsq,r,rx,ry,rz
    character(len=10), allocatable :: catom_labelt(:)
    character(len=4), allocatable :: atom_namet(:)
    logical, allocatable :: lwithin(:)

    allocate(xft(natoms),yft(natoms),zft(natoms))
    allocate(xot(natoms),yot(natoms),zot(natoms))
    allocate(atom_namet(natoms))
    allocate(atom_typet(natoms))

    allocate(atom_labelt(natoms))
    allocate(rnumt(natoms),rcellt(natoms,3))

    if(lrotate) then
      xft = xf(1:natoms)
      yft = yf(1:natoms)
      zft = zf(1:natoms)
      xot = xrot(1:natoms)
      yot = yrot(1:natoms)
      zot = zrot(1:natoms)
    else
      xft = xf(1:natoms)
      yft = yf(1:natoms)
      zft = zf(1:natoms)
      xot = xo(1:natoms)
      yot = yo(1:natoms)
      zot = zo(1:natoms)
    end if

    atom_namet = atom_name(1:natoms)
```

```
49      atom_typet = atom_type(1:natoms)
50
51      atom_labelt = atom_label(1:natoms)
52      rnumt = reference_number(1:natoms)
53      rcellt = reference_cell(1:natoms,:)
54      if (allocated(xf)) deallocate(xf,yf,zf)
55      if (allocated(xo)) deallocate(xo,yo,zo)
56      if (allocated(atom_name)) deallocate(atom_name)
57      if (allocated(atom_type)) deallocate(atom_type)
58      if (allocated(atom_label)) deallocate(atom_label)
59      if (allocated(catom_label)) deallocate(catom_label)
60      if (allocated(reference_number)) deallocate(reference_number)
61      if (allocated(reference_cell)) deallocate(reference_cell)
62
63      rcentre(1) = (cell(1,1) + cell(2,1) + cell(3,1))/2.0d0
64      rcentre(2) = (cell(1,2) + cell(2,2) + cell(3,2))/2.0d0
65      rcentre(3) = (cell(1,3) + cell(2,3) + cell(3,3))/2.0d0
66      allocate(lwithin(natoms))
67      lwithin = .false.
68      newatoms = 0
69
70      do i = 1,natoms
71        select case(trim(cshape))
72          case('sphere')
73           if(lhollow) then
74            rx = xot(i) - rcentre(1)
75            ry = yot(i) - rcentre(2)
76            rz = zot(i) - rcentre(3)
77            rsq = rx**2 + ry**2 + rz**2
78            r = sqrt(rsq)
79            if ((rhollow(1)/2.0d0<=r).and.(r<=rnano(1)/2.0d0)) then
80            lwithin(i) = .true.
81            newatoms = newatoms + 1
82            end if
83           else
84            rx = xot(i) - rcentre(1)
85            ry = yot(i) - rcentre(2)
86            rz = zot(i) - rcentre(3)
87            rsq = rx**2 + ry**2 + rz**2
88            r = sqrt(rsq)
89            if (r<=rnano(1)/2.0d0) then
90            lwithin(i) = .true.
91            newatoms = newatoms + 1
92            end if
93           end if
94          case('cube')
95           if(lhollow) then
96            rx = xot(i) - rcentre(1)
97            ry = yot(i) - rcentre(2)
98            rz = zot(i) - rcentre(3)
99            if ((abs(rx)<=rnano(1)/2.0d0).and.(abs(ry)<=rnano(2)/2.0d0).and.(abs(rz)<=rnano(3)
                  ↪ /2.0d0).and.&
100           ((rhollow(1)/2.0d0<=abs(rx)).or.(rhollow(2)/2.0d0<=abs(ry)).or.(rhollow(3)/2.0d0<=
                  ↪ abs(rz))))then
101           lwithin(i) = .true.
```

```
102             newatoms = newatoms + 1
103             end if
104            else
105             rx = xot(i) - rcentre(1)
106             ry = yot(i) - rcentre(2)
107             rz = zot(i) - rcentre(3)
108             if ((abs(rx)<=rnano(1)/2.0d0).and.(abs(ry)<=rnano(2)/2.0d0).and.(abs(rz)<=rnano(3)
                    ↪ /2.0d0)) then
109             lwithin(i) = .true.
110             newatoms = newatoms + 1
111             end if
112            end if
113           case('cylinder')
114            if(lhollow) then
115             rx = xot(i) - rcentre(1)
116             ry = yot(i) - rcentre(2)
117             rz = zot(i) - rcentre(3)
118             rsq = rx**2 + ry**2
119             r = sqrt(rsq)
120             if ((abs(rz)<=rnano(3)/2.0d0).and.(r<=rnano(1)/2.0d0).and.&
121             (abs(rz)>=rhollow(3)/2.0d0).and.(r>=rhollow(1)/2.0d0)) then
122             lwithin(i) = .true.
123             newatoms = newatoms + 1
124             end if
125            else
126             rx = xot(i) - rcentre(1)
127             ry = yot(i) - rcentre(2)
128             rz = zot(i) - rcentre(3)
129             rsq = rx**2 + ry**2
130             r = sqrt(rsq)
131             if ((abs(rz)<=rnano(3)/2.0d0).and.(r<=rnano(1)/2.0d0)) then
132             lwithin(i) = .true.
133             newatoms = newatoms + 1
134             end if
135            end if
136           case('rectangle')
137            if(lhollow) then
138             rx = xot(i) - rcentre(1)
139             ry = yot(i) - rcentre(2)
140             rz = zot(i) - rcentre(3)
141             if ((abs(rx)<=rnano(1)/2.0d0).and.(abs(ry)<=rnano(2)/2.0d0).and.(abs(rz)<=rnano(3)
                    ↪ /2.0d0).and.&
142             ((rhollow(1)/2.0d0<=abs(rx)).or.(rhollow(2)/2.0d0<=abs(ry)).or.(rhollow(3)/2.0d0<=
                    ↪ abs(rz)))) then
143             lwithin(i) = .true.
144             newatoms = newatoms + 1
145             end if
146            else
147             rx = xot(i) - rcentre(1)
148             ry = yot(i) - rcentre(2)
149             rz = zot(i) - rcentre(3)
150             if ((abs(rx)<=rnano(1)/2.0d0).and.(abs(ry)<=rnano(2)/2.0d0).and.(abs(rz)<=rnano(3)
                    ↪ /2.0d0)) then
151             lwithin(i) = .true.
152             newatoms = newatoms + 1
```

```
153             end if
154            end if
155           case('ellipsoid')
156            if(lhollow) then
157             rx = xot(i) - rcentre(1)
158             ry = yot(i) - rcentre(2)
159             rz = zot(i) - rcentre(3)
160             if (((rx**2/(rnano(1)/2.0d0)**2)+(ry**2/(rnano(2)/2.0d0)**2)+(rz**2/(rnano(3)/2.0
                    ↪ d0)**2)<=1).and.&
161             ((rx**2/(rhollow(1)/2.0d0)**2)+(ry**2/(rhollow(2)/2.0d0)**2)+(rz**2/(rhollow(3)
                    ↪ /2.0d0)**2)>=1)) then
162           lwithin(i) = .true.
163           newatoms = newatoms + 1
164         end if
165            else
166             rx = xot(i) - rcentre(1)
167             ry = yot(i) - rcentre(2)
168             rz = zot(i) - rcentre(3)
169             if ((rx**2/(rnano(1)/2.0d0)**2)+(ry**2/(rnano(2)/2.0d0)**2)+(rz**2/(rnano(3)/2.0d0
                    ↪ )**2)<=1) then
170             lwithin(i) = .true.
171             newatoms = newatoms + 1
172             end if
173            end if
174         end select
175       end do
176       write(6,'(a,i0)') 'Number of atoms within nanoparticle is ',newatoms
177
178       allocate(xo(newatoms),yo(newatoms),zo(newatoms))
179       allocate(xf(newatoms),yf(newatoms),zf(newatoms))
180       allocate(atom_name(newatoms))
181       allocate(atom_type(newatoms))
182       allocate(atom_label(newatoms))
183       allocate(reference_number(newatoms))
184       allocate(reference_cell(newatoms,3))
185       cell = 0.0d0
186       cell(1,1) = 4.0d0*rnano(1) ; cell(2,2) = 4.0d0*rnano(2) ; cell(3,3) = 4.0d0*rnano(3)
187       a = 4.0d0*rnano(1) ; b = 4.0d0*rnano(2) ; c = 4.0d0*rnano(3)
188       alpha = 90.0d0 ; beta = 90.0d0 ; gamma = 90.0d0
189       j = 0
190       do i = 1,natoms
191         if (lwithin(i)) then
192           j = j + 1
193           xo(j) = xot(i) ; yo(j) = yot(i) ; zo(j) = zot(i)
194           atom_name(j) = atom_namet(i)
195           atom_type(j) = atom_typet(i)
196           atom_label(j) = atom_labelt(i)
197           reference_number(j) = rnumt(i)
198           reference_cell(j,:) = rcellt(i,:)
199         end if
200       end do
201       xo = xo - sum(xo)/dble(newatoms) + cell(1,1)/2
202       yo = yo - sum(yo)/dble(newatoms) + cell(2,2)/2
203       zo = zo - sum(zo)/dble(newatoms) + cell(3,3)/2
204       xf = xo/cell(1,1) ; yf = yo/cell(2,2) ; zf = zo/cell(3,3)
```

```
205
206
207     if (allocated(xft)) deallocate(xft,yft,zft)
208     if (allocated(xot)) deallocate(xot,yot,zot)
209     if (allocated(atom_namet)) deallocate(atom_namet)
210     if (allocated(atom_typet)) deallocate(atom_typet)
211     if (allocated(atom_labelt)) deallocate(atom_labelt)
212     if (allocated(catom_labelt)) deallocate(catom_labelt)
213     if (allocated(rnumt)) deallocate(rnumt)
214     if (allocated(rcellt)) deallocate(rcellt)
215
216     if (ldiag) then
217       write(main_output,*)
218       write(main_output,'(a)') 'Output from nanoparticle'
219       write(main_output,'(a)') ' === New structure ==='
220       write(main_output,'(a)') ' New lattice vectors'
221       write(main_output,*) cell(:,1)
222       write(main_output,*) cell(:,2)
223       write(main_output,*) cell(:,3)
224       do i = 1,newatoms
225          write(main_output,'(i5,2x,a4,2x,6f10.5,4i4)') i,atom_name(i),  &
226                   xf(i),yf(i),zf(i),xo(i),yo(i),zo(i), &
227                   reference_number(i),reference_cell(i,:)
228       end do
229     end if
230
231     natoms = newatoms
232
233     call assign_elements
234     ntypes = 0
235     if (allocated(numoftype)) then
236       do iel = -1,nelements
237         if (n_elements(iel)>0) then
238           ntypes = ntypes + 1
239           numoftype(ntypes) = n_elements(iel)
240         end if
241       end do
242     end if
243
244     if (lsort) call sort_structure
245
246     return
247
248   end subroutine nanoparticle
```

A.2 Option to rotate the axis of a crystal structure or nanoparticle

I have added this Fortran subroutine to the `RMCCreate` code, in order to be able to generate structure where the crystallographic axis can be oriented in specific direction with respect to the cartesian orthogonal axis that defines the supercell. This is particularly useful for nanoparticle studies where often the direction of the crystallographic axis with respect to some orientations

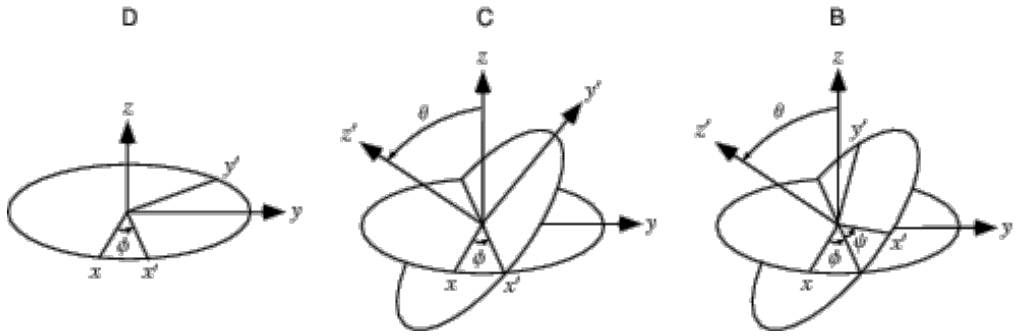

Figure A.2: Schematic representation of the three rotations performed using the Euler angles, θ, ϕ and ψ [216].

of the nanoparticle can largely affect the structure and the properties of the material.

The rotation is performed using the Euler angles [216]. The Euler rotation theorem states that any rotation can be described using three angles, θ, ϕ and ψ. The three corresponding rotations are shown in figure A.2.

A rotation is expressed in the form of a matrix A

$$A = BCD \tag{A.1}$$

which is given by the product of three rotation matrices B, C and D, corresponding to each of the three individual rotations shown in the figure.

The first is a rotation around the z-axis by the angle ϕ, the second rotation is by an angle θ in $[0, \pi]$ about the former x-axis (now x') and the third rotation is by an angle ψ about the former z-axis (now z'). The elements of the matrix A are given by

$$\begin{aligned}
a_{11} &= \cos\psi\cos\phi - \cos\theta\sin\phi\sin\psi \\
a_{12} &= \cos\psi\sin\phi + \cos\theta\cos\phi\sin\psi \\
a_{13} &= \sin\psi\sin\theta \\
a_{21} &= -\sin\psi\cos\phi - \cos\theta\sin\phi\cos\psi \\
a_{22} &= -\sin\psi\sin\phi + \cos\theta\cos\phi\cos\psi \\
a_{23} &= \cos\psi\sin\theta \\
a_{31} &= \sin\theta\sin\phi \\
a_{32} &= -\sin\theta\cos\phi \\
a_{33} &= \cos\theta
\end{aligned}$$

In our code (shown below), the angle θ is called *csi* (which stands for the Greek letter ξ!).

```
 subroutine rotate_structure
!   ===============================
!-----------------------------------
!
!     This subroutine rotates the expanded configuration about three chosen
!     angles. The nanoparticles will be then chopped from the rotated
!     expanded configuration
!-----------------------------------
    use structure_data
    use arguments

    implicit none


    double precision :: euler(3,3), rcentre(3), pi
    double precision, allocatable :: xtemp(:),ytemp(:),ztemp(:)
    integer :: i

    pi = 2.0d0*dacos(0.0d0)

    psi = psi*pi/180
    fi = csi*pi/180
    csi = csi*pi/180

    euler(1,1) = cos(psi)*cos(fi)-cos(csi)*sin(fi)*sin(psi)    !These are the elements of
        ↪ the euler rotation matrix
    euler(1,2) = cos(psi)*sin(fi)+cos(csi)*cos(fi)*sin(psi) !Fi is the angle of rotation
        ↪ about the z axis
    euler(1,3) = sin(psi)*sin(csi)                              !csi about the former x axis
    euler(2,1) = -sin(psi)*cos(fi)-cos(csi)*sin(fi)*cos(psi)   !Psi about former z axis
    euler(2,2) = -sin(psi)*sin(fi)+cos(csi)*cos(fi)*cos(psi)   !They are provided by the
        ↪ user in square brackets after -rotate
    euler(2,3) = cos(psi)*sin(csi)
    euler(3,1) = sin(csi)*sin(fi)
    euler(3,2) = -sin(csi)*cos(fi)
    euler(3,3) = cos(csi)

    allocate (xtemp(natoms),ytemp(natoms),ztemp(natoms))
    allocate (xrot(natoms),yrot(natoms),zrot(natoms))

    rcentre(1) = (cell(1,1) + cell(2,1) + cell(3,1))/2.0d0
    rcentre(2) = (cell(1,2) + cell(2,2) + cell(3,2))/2.0d0
    rcentre(3) = (cell(1,3) + cell(2,3) + cell(3,3))/2.0d0

    xtemp = xo - rcentre(1)
    ytemp = yo - rcentre(2)
    ztemp = zo - rcentre(3)

    xrot = euler(1,1)*xtemp + euler(1,2)*ytemp + euler(1,3)*ztemp + rcentre(1)
    yrot = euler(2,1)*xtemp + euler(2,2)*ytemp + euler(2,3)*ztemp + rcentre(2)
    zrot = euler(3,1)*xtemp + euler(3,2)*ytemp + euler(3,3)*ztemp + rcentre(3)

```

```
50      if (ldiag) then
51        write(main_output,'(/a)') 'Output from rotate_structure'
52        write(main_output,'(a/)') '==================================='
53        write(main_output,'(/a/)') 'Coordinates xrot yrot zrot'
54        write(main_output,'(/a/)') 'Element, label, rotated coordinates'
55        do i = 1,natoms
56          write(main_output,'(a,3f12.4)') element(atom_type(i)),xrot(i),yrot(i),zrot(i)
57        end do
58      end if
59
60      return
61
62    end subroutine rotate_structure
```

A.3 Code for least square fitting

This `Matlab` code was written in order to perform the least square refinements of Gaussians functions with respect to the first peaks of the PDF of Prussian blue (as seen in chapter 4).

```
1  cd /Volumes/Transcend/ownCloud/Documents/Documents/NeutronData&Analysis/PBdataNimrod/4Jan17/
       ↪ Solid_Nano/log_binning
2
3  Gr_1_2 = dlmread('NIMROD00028497.mgor01','','B5..B76'); %read values till the minimum
       ↪ between 4th peak and next
4  r_1 = dlmread('NIMROD00028497.mgor01','','A5..A76');
5
6  Gr_1_2_new = Gr_1_2+1; %adding 1 in order to work with funtion with lim(0)-> 0
7  r_0 = [0.97 1.18 1.5 1.94 1.81 1.09 1.35 1 1.74 1.5 2.1]; %average bond distances for D-O, C
       ↪ -N, D-D, Fe-C/Fe-N, O-D intermolecular; PVP: C-H, C-H, C-N/O/C, H-H, C-C, H-C/N
       ↪ respectively
8
9  b = [0.6671 0.6646 0.9360 0.5803 0.9540 -0.3739]; %Neutron scattering Lengths, in the order:
       ↪  D, C, N, O, Fe, H
10
11 prob_hbond = 1 - 0.316; % probability for water molecules in pores to form hydrogen bonds
       ↪ with neighrbouring water molecules
12
13 n = [2 1 1 2.5714 prob_hbond];  %coordination numbers D-O/H-O, C-N, D-D/H-H, Fe-C/Fe-N, H/D-
       ↪ O
14
15 V_PB = (10.25)^3; %volume of PB unit cell
16 V_Vynil = 177.4573; %volume occupied by vynil monomer, density of vynil=1.04 g/cm^3
17
18 x0 = [0.08 0.08 0.08 0.08 0.144 0.256 0.08 0.016 0.08 0.08 0.08 0.08 0.08 0.08 0.05 0.05];%
       ↪ first 4 7 and 9-14 are Gaussian's sigmas, 5 concentration of C/N, 6 of D, 8 PVP conc,
       ↪  15 fraction of D/H in DOH molecules, 16 conc of H
19
20 fun = @(x, r_1) (x(6)*b(1)+b(4)*(x(6))/2+x(5)*(b(2)+b(3))+x(5)*(7/18)*b(5)+x(8)*(b(4)+b(3)
       ↪ +9*b(6)+6*b(2)))^(-2)*((2*n(1)/(4*pi*((18/x(5))*(x(6))*1.5+43+18*x(8)*(2+9+6)/x(5))/(
       ↪ x(8)*V_Vynil+V_PB)*6*x(1)*r_0(1)^2))*b(4)*((x(6)*b(1)/2+x(16)*b(6)/2)*x(15)/4)*(x(1)*
       ↪ sqrt(2*pi))^(-1)*exp(-(r_1-r_0(1)).^2/(2*x(1)^2))+(2*n(2)/(4*pi*((18/x(5))*(x(6))
       ↪ *1.5+43+18*x(8)*(2+9+6)/x(5))/(x(8)*V_Vynil+V_PB)*6*x(2)*r_0(2)^2))*x(5)*b(2)*b(3)*(x
```

```
    ↪ (2)*sqrt(2*pi))^(-1)*exp(-(r_1-r_0(2)).^2/(2*x(2)^2))+(n(3)/(4*pi*((18/x(5))*(x(6))
    ↪ *1.5+43+18*x(8)*(2+9+6)/x(5))/(x(8)*V_Vynil+V_PB)*6*x(3)*r_0(3)^2))*(x(6)*(1-x(15)/x
    ↪ (6))*b(1)^2+x(16)*(1-x(15)/x(16))*b(6)^2+2*x(15)*b(1)*b(6))*(x(3)*sqrt(2*pi))^(-1)*
    ↪ exp(-(r_1-r_0(3)).^2/(2*x(3)^2))+(2*n(4)/(4*pi*((18/x(5))*(x(6))*1.5+43+18*x(8)
    ↪ *(2+9+6)/x(5))/(x(8)*V_Vynil+V_PB)*6*x(4)*r_0(4)^2))*b(5)*x(5)*(7/18)*(b(2)+b(3)
    ↪ +6/(7*n(4))*b(4))*(x(4)*sqrt(2*pi))^(-1)*exp(-(r_1-r_0(4)).^2/(2*x(4)^2))+(2*n(5)/(4*
    ↪ pi*((18/x(5))*(x(6))*1.5+43+18*x(8)*(2+9+6)/x(5))/(x(8)*V_Vynil+V_PB)*6*x(7)*r_0(5)
    ↪ ^2))*b(4)*(x(6)*b(1)+x(16)*b(6))*(x(7)*sqrt(2*pi))^(-1)*exp(-(r_1-r_0(5)).^2/(2*x(7)
    ↪ ^2))+(2*1/(4*pi*((18/x(5))*(x(6))*1.5+43+18*x(8)*(2+9+6)/x(5))/(x(8)*V_Vynil+V_PB)*6*
    ↪ x(9)*r_0(6)^2))*(2/3)*x(8)*9*b(6)*b(2)*(x(9)*sqrt(2*pi))^(-1)*exp(-(r_1-r_0(6))
    ↪ .^2/(2*x(9)^2))+(1/(4*pi*((18/x(5))*(x(6))*1.5+43+18*x(8)*(2+9+6)/x(5))/(x(8)*V_Vynil
    ↪ +V_PB)*6*x(10)*r_0(7)^2))*(x(8)*2*b(2)^2+2*2*x(8)*b(3)*b(2)+2*x(8)*b(2)*b(4))*(x(10)*
    ↪ sqrt(2*pi))^(-1)*exp(-(r_1-r_0(7)).^2/(2*x(10)^2))+(2*1/(4*pi*((18/x(5))*(x(6))
    ↪ *1.5+43+18*x(8)*(2+9+6)/x(5))/(x(8)*V_Vynil+V_PB)*6*x(11)*r_0(8)^2))*(1/3)*x(8)*9*b
    ↪ (6)*b(2)*(x(11)*sqrt(2*pi))^(-1)*exp(-(r_1-r_0(8)).^2/(2*x(11)^2))+(1/(4*pi*((18/x(5)
    ↪ )*(x(6))*1.5+43+18*x(8)*(2+9+6)/x(5))/(x(8)*V_Vynil+V_PB)*6*x(12)*r_0(9)^2))*8*x(8)*b
    ↪ (6)^2*(x(12)*sqrt(2*pi))^(-1)*exp(-(r_1-r_0(9)).^2/(2*x(12)^2))+(1/(4*pi*((18/x(5))*(
    ↪ x(6))*1.5+43+18*x(8)*(2+9+6)/x(5))/(x(8)*V_Vynil+V_PB)*6*x(13)*r_0(10)^2))*(x(8)*4*b
    ↪ (2)^2+2*x(8)*b(3)*b(2))*(x(13)*sqrt(2*pi))^(-1)*exp(-(r_1-r_0(10)).^2/(2*x(13)^2))
    ↪ +(1/(4*pi*((18/x(5))*(x(6))*1.5+43+18*x(8)*(2+9+6)/x(5))/(x(8)*V_Vynil+V_PB)*6*x(14)*
    ↪ r_0(11)^2))*x(8)*(9*b(6)*b(2)+3*b(6)*b(3))*(x(14)*sqrt(2*pi))^(-1)*exp(-(r_1-r_0(11))
    ↪ .^2/(2*x(14)^2))); %function to fit data, as sum of 11 Gaussians
21
22  lb=[0.05 0.05 0.05 0.05 0.1 0.1 0.013 0 0 0 0 0 0 0 0 0]; %lower limit for parameters
    ↪ fitting
23  ub=[0.1 0.1 0.1 0.1 0.3 0.5 0.15 0.15 0.1 0.15 0.1 0.15 0.15 0.15 1 0.1]; %upper limit for
    ↪ parameters fitting
24
25  [x, resnorm, residual, exitflag, output, lambda, jacobian] = lsqcurvefit(fun,x0,r_1,
    ↪ Gr_1_2_new, lb, ub);
26
27  norm=(x(6)*b(1)+b(4)*(x(6))/2+x(5)*(b(2)+b(3))+x(5)*(7/18)*b(5)+x(8)*(b(4)+b(3)+9*b(6)+6*b
    ↪ (2)))^(-2); %normalisation function (sum(c_i b_i))^-2
28
29  V= (x(8)*V_Vynil+V_PB); %volume per unit cell weighted with respect to PVP percentage, e.g.
    ↪ x(8)*V_vynil is the volume occupied by the PVP per one PB unit cell
30
31  rho = ((18/x(5))*(x(6)*1.5+x(8)*(2+9+6))+43)/V; %density --> everything is normalised with
    ↪ respect to 18/x(5), since one unit cell contains 18 C/N
32
33  %Gaussians are rewritten below for plotting
34  Gauss1 = norm*(2*n(1)/(4*pi*rho*6*x(1)*r_0(1)^2))*b(4)*(x(6)*b(1)/2+x(16)*b(6)/2)*(x(1)*sqrt
    ↪ (2*pi))^(-1)*exp(-(r_1-r_0(1)).^2/(2*x(1)^2));
35  Gauss2 = norm*(2*n(2)/(4*pi*rho*6*x(2)*r_0(2)^2))*x(5)*b(2)*b(3)*(x(2)*sqrt(2*pi))^(-1)*exp
    ↪ (-(r_1-r_0(2)).^2/(2*x(2)^2));
36  Gauss3 = norm*(n(3)/(4*pi*rho*6*x(3)*r_0(3)^2))*(x(6)*(1-x(15)/x(6))*b(1)^2+x(16)*(1-x(15)/x
    ↪ (16))*b(6)^2+2*x(15)*b(1)*b(6))*(x(3)*sqrt(2*pi))^(-1)*exp(-(r_1-r_0(3)).^2/(2*x(3)
    ↪ ^2));
37  Gauss4 = norm*(2*n(4)/(4*pi*rho*6*x(4)*r_0(4)^2))*b(5)*x(5)*(7/18)*(b(2)+b(3)+6/(7*n(4))*b
    ↪ (4))*(x(4)*sqrt(2*pi))^(-1)*exp(-(r_1-r_0(4)).^2/(2*x(4)^2));
38  Gauss5 = norm*(2*n(5)/(4*pi*rho*6*x(7)*r_0(5)^2))*b(4)*(x(6)*b(1)+x(16)*b(6))*(x(7)*sqrt(2*
    ↪ pi))^(-1)*exp(-(r_1-r_0(5)).^2/(2*x(7)^2));
39  Gauss6 = norm*(2*1/(4*pi*rho*6*x(9)*r_0(6)^2))*(2/3)*x(8)*9*b(6)*b(2)*(x(9)*sqrt(2*pi))^(-1)
    ↪ *exp(-(r_1-r_0(6)).^2/(2*x(9)^2));
```

```
Gauss7 = norm*(1/(4*pi*rho*6*x(10)*r_0(7)^2))*(x(8)*2*b(2)^2+2*2*x(8)*b(3)*b(2)+2*x(8)*b(2)*b(4))*(x(10)*sqrt(2*pi))^(-1)*exp(-(r_1-r_0(7)).^2/(2*x(10)^2));
Gauss8 = norm*(2*1/(4*pi*rho*6*x(11)*r_0(8)^2))*(1/3)*x(8)*9*b(6)*b(2)*(x(11)*sqrt(2*pi))^(-1)*exp(-(r_1-r_0(8)).^2/(2*x(11)^2));
Gauss9 = norm*(1/(4*pi*rho*6*x(12)*r_0(9)^2))*8*x(8)*b(6)^2*(x(12)*sqrt(2*pi))^(-1)*exp(-(r_1-r_0(9)).^2/(2*x(12)^2));
Gauss10 = norm*(1/(4*pi*rho*6*x(13)*r_0(10)^2))*(x(8)*4*b(2)^2+2*x(8)*b(3)*b(2))*(x(13)*sqrt(2*pi))^(-1)*exp(-(r_1-r_0(10)).^2/(2*x(13)^2));
Gauss11 = norm*(1/(4*pi*rho*6*x(14)*r_0(11)^2))*x(8)*(13*b(6)*b(2)+3*b(6)*b(3))*(x(14)*sqrt(2*pi))^(-1)*exp(-(r_1-r_0(11)).^2/(2*x(14)^2));

Gauss=Gauss1+Gauss2+Gauss3+Gauss4+Gauss5+Gauss6+Gauss7+Gauss8+Gauss9+Gauss10+Gauss11;

diff = Gauss - Gr_1_2_new;


for i = 1:100
    if i<72
    r_2(i)=r_1(i);
    else
        r_2(i)=r_2(i-1)+0.03;
    end
end

Gauss4 = norm*(2*n(4)/(4*pi*rho*6*x(4)*r_0(4)^2))*b(5)*x(5)*(7/18)*(b(2)+b(3)+6/(7*n(4))*b(4))*(x(4)*sqrt(2*pi))^(-1)*exp(-(r_2-r_0(4)).^2/(2*x(4)^2));
Gauss11 = norm*(1/(4*pi*rho*6*x(14)*r_0(11)^2))*x(8)*(9*b(6)*b(2)+3*b(6)*b(3))*(x(14)*sqrt(2*pi))^(-1)*exp(-(r_2-r_0(11)).^2/(2*x(14)^2));

figure(50)
plot(r_1, Gauss1, r_1, Gauss2, r_1, Gauss3, r_2, Gauss4, r_1, Gauss5, r_1, Gauss6, r_1, Gauss8, r_1, Gauss7,  r_1, Gauss9, r_1, Gauss10, r_2, Gauss11, r_1, Gr_1_2_new)
xlabel(['r(' char(197) ')']);
ylabel('G(r)');
legend('D-O','C-N','D-D','Fe-C/N/O', 'intermolecular O-D', 'PVP C-H', 'PVP C-H', 'PVP C-N C-O C-C',  'PVP H-H', 'PVP C-C', 'PVP H-C H-N');
xlim([0 2.55]);


figure(51)
plot(r_1, Gauss, r_1, Gr_1_2_new, r_1, diff)
xlabel(['r(' char(197) ')']);
ylabel('G(r)');
legend('Model','Experimental', 'Difference');
xlim([0 2.25]);


J_T_PVP = transpose(jacobian);
cov_PVP = J_T_PVP * jacobian; %covariance matrix
corr_PVP = diag(diag(cov_PVP.^(-1/2)))*cov_PVP*diag(diag(cov_PVP.^(-1/2))); %correlation matrix
fc_PVP = full(corr_PVP);

figure(52)
surf(fc_PVP);
```

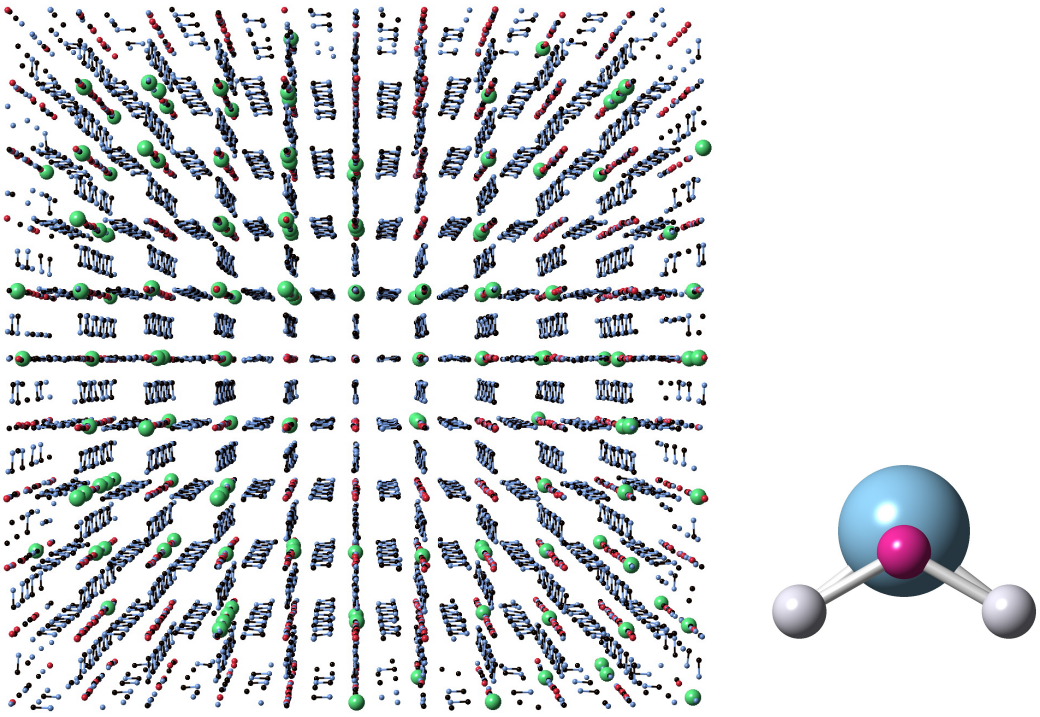

Figure A.3: (a) A $5x5x5$ PB supercell with 25% of the Fe^{II} atoms (Fe atoms in magenta) substituted by dummy atoms (green), after a few seconds long RMC run. C atoms are coloured in black and N in blue. b) A water molecule with the O atoms coloured in blue and the D in grey and an additional dummy atom in magenta for use of the TIP4P potential in MD simulations of liquid water.

```
85  view(2);
```

A.4 Making the Prussian Blue configurations

The procedure for generating the configurations used as starting configuration for modelling with `RMCProfile` involves few steps. I explain first the steps involved in the creation of a supercell with water located only in unit cells containing vacancies (the code can be found in the following section A.4.1). Firstly a $5 \times 5 \times 5$ supercell of the standard PB network is generated, starting from a unit cell with no vacancies as the one shown in figure 4.1. Using the flag `-replace` included in the `RMCCreate` code, a desired percentage of Fe^{II} atoms randomly selected is replaced by dummy atoms, i.e. Ni atoms (in order to create the classic PB network as described above we need to replace 25% of the atoms). A short (few seconds long) RMC refinement was run on this configuration, in order to produce the file containing information about the bonds (.bonds file); the resulting configuration is shown in figure A.3 a. This step is needed to identify the C and N atoms bonded to the dummy atoms.

The dummy atoms are subsequently deleted, together with the neighbouring 6 cyanides

group, that are replaced with D_2O; the O atoms are placed in the positions previously occupied by the N atoms, while the O–D bonds sit on the planes of the cyanide bonds, with the O−D bonds pointing towards the dummy atoms coordinates.

Subsequently, a heavy water cluster (figure 4.17 a) containing a chosen number of molecules is inserted in the pores using the coordinates of the dummy atoms as centre for positioning the cluster. When requested, a desired percentage of the D atoms can be replaced by H atoms (using the `-replace` flag as before), resulting in water molecules found in either of the three forms: D_2O, H_2O and DHO.

The water cluster was selected from a water configuration output from a MD simulation at ambient pressure, performed using the TIP4P potential for water, where an additional negatively charged dummy atom, as shown in figure A.3 a, is added to improve the charge distribution around the water molecule [217]. The MD simulation was carried out by Chenxing Yang (Queen Mary). The decision to start with a water cluster selected from a configuration that had undergone an MD simulation came from the attempt to reproduce the ordering due to the intermolecular hydrogen bonding.

The procedure for generating the supercell containing water molecules in both pores and vacancies is analogous (the code is found in section A.4.2). The difference is that the water molecules are now initially placed at position $(1/4, 1/4, 1/4)$ in pores with no vacancies, while where there are vacancies there are water molecules with the O in the position previously occupied by the N atoms (as per previous case) and others located at $(0.34, 0.34, 0.34)$; as a result, the distance between the oxygens in coordinated water molecules and those in uncoordinated ones is approximately 2.75 Å, which is compatible with formation of intermolecular hydrogen bonds. However the the D atoms were not positioned along the line joining the two O atoms, but slightly away from it, relying on the ability of the RMC method to reproduce such ordering where this was present. A representative configuration is shown in 4.18.

A.4.1 Configuration with water cluster in vacancies

The following Python code was used to create the supercell with water in the vacancies: six water molecules coordinated to the Fe^{III} and a cluster of water molecules, taken from the output configuration of a MD simulation of water, in each vacancy.

```
1
2 from numpy import *
3
4 import numpy as np
5
6 from StringIO import StringIO
7
8 with open('prussianblue.bonds') as b_file:
```

```
    bond_file = [s[:-1] for s in b_file.readlines()[10:]]

bond_list = [b.split()[0:-2] for b in bond_file]

all_Ni = [b for b in bond_list if b[1] == 'Ni' and b[2] == '4'] #find Ni atoms to remove
C_to_remove = [Ni[4::3] for Ni in all_Ni] #list of C atoms to remove written as strings of 6 elements
C_to_remove_flat = [C for sublist in C_to_remove for C in sublist] #write as list rather than strings of 6 elements

all_N = [b for b in bond_list if b[1] == 'N' and b[2] == '1' and b[4] in C_to_remove_flat] # find N atom bonded to C to remove
N_to_remove = [Ind[0] for Ind in all_N] #write their indeces as list

with open('prussianblue.rmc6f') as r_file:
    rmc_file = [s for s in r_file.readlines()[21:]]

rmc_list = [r.split() for r in rmc_file]

with open('WaterClusterCoordinates.txt') as w_file:
    water_file = [w for w in w_file.readlines()[18:]]

water_list = [w.split() for w in water_file]

from copy import deepcopy

new_list = []

for a in rmc_list:
    if a[0] in C_to_remove_flat or a[1] == 'Ni':
        continue # do nothing, so remove this atom
    elif a[0] in N_to_remove:
        new_atom = deepcopy(a)
        new_atom[1] = 'O'  #replace N atoms in vacancies with O, coordinated to Fe
    else:
        new_atom = a
    new_list.append(new_atom)

d = 3.14 #distance between Ni and N
l = 0.9687 #O-D distance
alpha = 103.78/2*pi/180 #103.78 = DOD angle
S = 10.13*5 # length of edge 5x5x5 Prussian blue supercell


for a in [a for a in rmc_list if a[1] == 'Ni']: #now add the D using the Ni coordinates as reference
    for H_coords in [(-d+l*cos(alpha), l*sin(alpha), 0), #12 coordinates for 12 D atoms, corresponding to six O occupying the vacant N sites
                     (+d-l*cos(alpha), l*sin(alpha), 0),
                     (-d+l*cos(alpha), -l*sin(alpha), 0),
                     (+d-l*cos(alpha), -l*sin(alpha), 0),
                     (l*sin(alpha), -d+l*cos(alpha), 0),
                     (l*sin(alpha), +d-l*cos(alpha), 0),
                     (-l*sin(alpha), -d+l*cos(alpha), 0),
                     (-l*sin(alpha), +d-l*cos(alpha), 0),
```

```
                    (0, l*sin(alpha), +d-l*cos(alpha)),
                    (0, l*sin(alpha), -d+l*cos(alpha)),
                    (0, -l*sin(alpha), +d-l*cos(alpha)),
                    (0, -l*sin(alpha), -d+l*cos(alpha))]:
        new_atom = deepcopy(a)
        new_atom[0] = '9000'
        new_atom[1] = 'D'
        new_atom[3] = str(float(new_atom[3]) + H_coords[0]/S)
        new_atom[4] = str(float(new_atom[4]) + H_coords[1]/S)
        new_atom[5] = str(float(new_atom[5]) + H_coords[2]/S)
        new_list.append(new_atom)

h=15.56513/S  #conversion factor for fractional coordinates; 15.56513 size of cell of the
    ↪ original water cluster configuration

for a in water_list: #copy water cluster in the centre of the vacancy
    for b in [b for b in rmc_list if b[1] == 'Ni']:
        new_atom = deepcopy(b)
        new_atom[0] = '9100'
        new_atom[1] = a[0]
        new_atom[3] = str(float(new_atom[3])+(float(a[2])-1)*h)
        new_atom[4] = str(float(new_atom[4])+(float(a[3])-1)*h)
        new_atom[5] = str(float(new_atom[5])+(float(a[4])-1)*h)
        new_list.append(new_atom)

formatString =  "{:4s} "*3 + "{:10.8s} "*3 + "{:4s}"*4

outfile = open('PB', 'w') #test for printing date in file

final_list = [] #write the list in rmc6f format
for i, atom in enumerate(new_list, 1):
    final_atom=deepcopy(atom)
    final_atom[0] = str(i)
    final_atom[1:10] = atom[1:10]
    final_list.append(final_atom)
print final_list[-10:-1]

for atom in final_list:
    outfile.write(str(formatString.format(*atom))+ ' ')
    outfile.write('\n')
outfile.close()
```

A.4.2 Modifications to add water in different positions depending on pore type

The following are the modifications made to the code, reported in the previous section, to add water in different positions in the unit cells, depending on the pore type (with vacancy or no vacancy).

```

from decimal import *
getcontext().prec = 6

```

```
5  all_Fe = [Fe for Fe in rmc_list if Fe[1]=='Fe']
6
7  d=0.100000;
8
9  Ni_list = [Ni for Ni in rmc_list if Ni[1]=='Ni']
10
11 list_translation = []
12 for Ni in Ni_list:
13     for Fe_trans in [(-d, 0, 0),   #8 Fe atoms in one unit cell, only 7 in case of vacancy
14                      (0, -d, 0),
15                      (0, 0, -d),
16                      (-d, -d, 0),
17                      (-d, 0, -d),
18                      (0, -d, -d),
19                      (-d, -d, -d)]:
20         new_coord = deepcopy(Ni)
21         new_coord[0] = '9000'
22         new_coord[1] = 'Fe'
23         new_coord[3] = ("%.6f" % round(Decimal(float(new_coord[3]))  + Decimal(Fe_trans[0])
               ↪ ,6))
24         new_coord[4] = ("%.6f" % round(Decimal(float(new_coord[4]))  + Decimal(Fe_trans[1])
               ↪ ,6))
25         new_coord[5] = ("%.6f" % round(Decimal(float(new_coord[5])) + Decimal(Fe_trans[2])
               ↪ ,6))
26         list_translation.append(new_coord)
27
28
29 Fe_vacancy = []
30 for f in all_Fe:
31     for l in list_translation:
32         if f[3:6]==l[3:6] and f not in Fe_vacancy:
33            Fe_vacancy.append(f)
34
35 Fe_no_vacancy = [f for f in all_Fe if f not in Fe_vacancy];
36
37 new_list = []
38
39 for a in rmc_list:
40     if a[0] in C_to_remove_flat or a[1] == 'Ni': # adding O in vacant N sites
41         continue # do nothing, so remove this atom
42     elif a[0] in N_to_remove:
43         new_atom = deepcopy(a)
44         new_atom[1] = 'O'
45     else:
46         new_atom = a
47     new_list.append(new_atom)
48
49 d = 3.14 # angstrom; distance between N and Ni
50 l = 0.9687 # O-D bond distance
51 alpha = 103.78/2*pi/180 # 103.78 = DOD angle
52 S = 10.13*5 # edge of 5x5x5 supercell
53 g = 0.16*10.13 # from 0.16=(0.5-0.34) --> frac coordinate to subtract from Ni coordinates to
       ↪  get O to sit in (0.34,0.34,0.34) position
54 beta = 13.78*pi/180 # 13.78=103.78 - 90 -->  angle chosen for direction of one of the OD
       ↪ bond
```

```
55 n = 0.25*10.13 # cartesian coordinate corresponding to 1/4 fractional coordinate in one unit
       ↪  cell
56
57 for a in [a for a in rmc_list if a[1] == 'Ni']: # place O atoms at (0.34 0.34 0.34)
       ↪ positions
58     for O_coords in [(+g, -g, +g),
59                      (-g, -g, +g),
60                      (+g, -g, -g),
61                      (-g, -g, -g),
62                      (+g, +g, +g),
63                      (-g, +g, +g),
64                      (-g, +g, -g),
65                      (+g, +g, -g)]:
66         new_atom = deepcopy(a)
67         new_atom[0] = '8000'
68         new_atom[1] = 'O'
69         new_atom[3] = str(float(new_atom[3]) + O_coords[0]/S)
70         new_atom[4] = str(float(new_atom[4]) + O_coords[1]/S)
71         new_atom[5] = str(float(new_atom[5]) + O_coords[2]/S)
72         new_list.append(new_atom)
73
74 for a in Fe_no_vacancy: #now add the O in pores with no vacancies at position (1/4, 1/4,
       ↪ 1/4)
75     new_atom = deepcopy(a)
76     new_atom[0] = '7000'
77     new_atom[1] = 'O'
78     new_atom[3] = str(float(new_atom[3]) + n/S)
79     new_atom[4] = str(float(new_atom[4]) + n/S)
80     new_atom[5] = str(float(new_atom[5]) + n/S)
81     new_list.append(new_atom)
82
83
84
85 for a in [a for a in rmc_list if a[1] == 'Ni']: #now add the D
86     for H_coords in [(-d+l*cos(alpha), l*sin(alpha), 0), # Hydrogens bonded to O in N
           ↪ position
87                      (+d-l*cos(alpha), l*sin(alpha), 0),
88                      (-d+l*cos(alpha), -l*sin(alpha), 0),
89                      (+d-l*cos(alpha), -l*sin(alpha), 0),
90                      (l*sin(alpha), -d+l*cos(alpha), 0),
91                      (l*sin(alpha), +d-l*cos(alpha), 0),
92                      (-l*sin(alpha), -d+l*cos(alpha), 0),
93                      (-l*sin(alpha), +d-l*cos(alpha), 0),
94                      (0, l*sin(alpha), +d-l*cos(alpha)),
95                      (0, l*sin(alpha), -d+l*cos(alpha)),
96                      (0, -l*sin(alpha), +d-l*cos(alpha)),
97                      (0, -l*sin(alpha), -d+l*cos(alpha)),
98                      (+g, g-l, +g), # Hydrogen parallel to y perp. to x and z, bonded to O
                            ↪ in pores, O at (0.34 0.34 0.34)
99                      (-g, g-l, +g),
100                     (+g, -g+l, -g),
101                     (-g, -g+l, -g),
102                     (+g, -g+l, +g),
103                     (-g, -g+l, +g),
104                     (+g, +g-l, -g),
```

```
105                     (-g, +g-l, -g),
106                     (+g, g+l*sin(beta),g-l*cos(beta)), # Hydrogen bonded to O in pores,
                            ↪ bond parallel to z-y plane, forming angle beta with z direction
107                     (-g, g+l*sin(beta),g-l*cos(beta)),
108                     (+g, -g-l*sin(beta),g-l*cos(beta)),
109                     (-g, -g-l*sin(beta),g-l*cos(beta)),
110                     (+g, -g-l*sin(beta),-g+l*cos(beta)),
111                     (-g, -g-l*sin(beta),-g+l*cos(beta)),
112                     (+g, +g+l*sin(beta),-g+l*cos(beta)),
113                     (-g, +g+l*sin(beta),-g+l*cos(beta))]:
114         new_atom = deepcopy(a)
115         new_atom[0] = '9000'
116         new_atom[1] = 'D'
117         new_atom[3] = str(float(new_atom[3]) + H_coords[0]/S)
118         new_atom[4] = str(float(new_atom[4]) + H_coords[1]/S)
119         new_atom[5] = str(float(new_atom[5]) + H_coords[2]/S)
120         new_list.append(new_atom)
121
122 for a in Fe_no_vacancy: # Hydrogen bonded to oxygen in pores at (1/4, 1/4, 1/4)
123     for H_coords in [(+n-l, +n, +n),
124                     (+n+l*sin(beta), +n-l*cos(beta), +n)]:
125         new_atom = deepcopy(a)
126         new_atom[0] = '9000'
127         new_atom[1] = 'D'
128         new_atom[3] = str(float(new_atom[3]) + H_coords[0]/S)
129         new_atom[4] = str(float(new_atom[4]) + H_coords[1]/S)
130         new_atom[5] = str(float(new_atom[5]) + H_coords[2]/S)
131         new_list.append(new_atom)
```

Bibliography

[1] F. S. Boi, S. Maugeri, J. Guo, M. Lan, S. Wang, J. Wen, G. Mountjoy, M. Baxendale, G. Nevill, R. M. Wilson, Y. He, S. Zhang, G. Xiang, *Appl. Phys. Lett.* **2014**, *105*, 243108.

[2] M. T. Dunstan, S. A. Maugeri, W. Liu, M. G. Tucker, O. O. Taiwo, B. Gonzalez, P. K. Allan, M. W. Gaultois, P. R. Shearing, D. A. Keen, A. E. Phillips, M. T. Dove, S. A. Scott, J. S. Dennis, C. P. Grey, *Farad. Discuss.* **2016**, *192*, 217–240.

[3] K. Autumn, Y. A. Liang, S. T. Hsieh, W. Zesch, W. P. Chan, T. W. Kenny, R. Fearing, R. J. Full, *Nature* **2000**, *405*, 681–685.

[4] T. S. Kustandi, V. D. Samper, D. K. Yi, W. S. Ng, P. Neuzil, W. Sun, *Adv. Funct. Mater.* **2007**, *17*, 2211–2218.

[5] A. Hartland, J. R. Lead, V. Slaveykova, D. O'Carroll, E. Valsami-Jones, *Nature Edu. Knowled.* **2013**, *4*, 7.

[6] S. Wagner, A. Gondikas, E. Neubauer, T. Hofmann, F. von der Kammer, *Angew. Chem. Int. Edit.* **2014**, *53*, 12398–12419.

[7] S. Iijima, *Nature* **1991**, *354*, 56–58.

[8] M. Shatruk, A. Dragulescu-Andrasi, K. E. Chambers, S. A. Stoian, E. L. Bominaar, C. Achim, K. R. Dunbar, *J. Am. Chem. Soc.* **2007**, *129*, 6104–6116.

[9] K. Ariga, K. Minami, M. Ebara, J. Nakanishi, *Polym. J.* **2016**, *48*, 371–389.

[10] C. Q. Sun, *Prog. Solid State Ch.* **2007**, *35*, 1–159.

[11] R. Daw, **2012**, `https://www.theguardian.com/nanotechnology-world/nanotechnology-is-ancient-history`.

[12] I. Freestone, N. Meeks, M. Sax, C. Higgitt, *Gold Bull* **2007**, *40*, 270–277.

[13] A. Li, B. T. Draine, *ApJ* **2002**, *564*, 803.

[14] M. E. Borges, M. C. Alvarez-Galvn, P. Esparza, E. Medina, P. Mart.n-Zarza, J. L. G.Fierro, *Energy Environ. Sci.* **2008**, *1*, 364–369.

[15] V. K. Sharma, J. Filip, R. Zboril, R. S. Varma, *Chem. Soc. Rev.* **2015**, *44*, 8410–8423.

[16] M. Labrenz, G. K. Druschel, T. Thomsen-Ebert, B. Gilbert, S. A. Welch, K. M. Kemner, G. A. Logan, R. E. Summons, G. D. Stasio, P. L. Bond, B. Lai, S. D. Kelly, J. F. Banfield, *Science* **2000**, *290*, 1744–1747.

[17] K. Autumn, A. M. Peattie, *Integr. Comp. Biol.* **2002**, *42*, 1081–1090.

[18] M. Buscema, H. Deyhle, T. Pfohl, S. E. Hieber, A. Zumbuehl, B. Mller, *Bioinspir. Biomim.* **2016**, 97970S.

[19] S. Bugna, M. Buscema, S. Matviykiv, R. Urbanics, A. Weinberger, T. Meszaros, J. Szebeni, A. Zumbuehl, T. Saxer, B. Mller, *Nanomedicine* **2016**, *12*, 845–849.

[20] P. Walter, E. Welcomme, P. Hallgot, N. J. Zaluzec, C. Deeb, J. Castaing, P. Veyssire, R. Brniaux, J.-L. Lv.que, G. Tsoucaris, *Nano Letters* **2006**, *6*, 2215–2219.

[21] P. Wilkinson, The Royal Institution - Science Lives Here, **2014**, `http://www.rigb.org/our-history/iconic-objects/iconic-objects-list/faraday-gold-colloids`.

[22] L. A. Polette-Niewold, F. S. Manciu, B. Torres, M. Alvarado Jr., R. R. Chianelli, *J. Inorg. Biochem.* **2007**, *101*, 1958–1973.

[23] A. V. Crewe, M. Isaacson, D. Johnson, *Rev. Sci. Instrum.* **1969**, *40*, 241–246.

[24] E. Ruska, `http://www.nobelprize.org/nobel_prizes/physics/laureates/1986/ruska-lecture.html`.

[25] Nano.gov National Nanotechnology Initiative, `http://www.nano.gov/nanotech-101/what/seeing-nano`.

[26] M. Faraday, *Phil. Trans. R. Soc. Lond.* **1857**, *147*, 145–181.

[27] J. Tyndall, J M Dent & Co, **1861**, 304 pp.

[28] P. Wilkinson, `http://www.rigb.org/our-history/iconic-objects/iconic-objects-list/tyndall-blue-sky`.

[29] J. Hutchings, Engineering and Science, **1960**, `http://resolver.caltech.edu/CaltechES:23.5.0`.

[30] S. J. Billinge, *J. Solid State Chem.* **2008**, *181*, 1695–1700.

[31] A. P. Alivisatos, *J. Phys. Chem.* **1996**, *100*, 13226–13239.

[32] M. Haruta, *Nature* **2005**, *437*, 1098–1099.

[33] J. Ding, L. Bu, S. Guo, Z. Zhao, E. Zhu, Y. Huang, X. Huang, *Nano Lett.* **2016**, *16*, 2762–2767.

[34] L. Pasquato, P. Pengo, P. Scrimin, *J. Mater. Chem.* **2004**, *14*, 3481–3487.

[35] V. G. Yarzhemsky, E. N. Murav'ev, M. A. Kazaryan, Y. A. Dyakov, *Inorg. Mater.* **2012**, *48*, 1075–1077.

[36] D. Bera, L. Qian, T.-K. Tseng, P. H. Holloway, *Materials* **2010**, *3*, 2260–2345.

[37] C. Noguez, *J. Phys. Chem. C* **2007**, *111*, 3806–3819.

[38] X. Huang, I. H. El-Sayed, W. Qian, M. A. El-Sayed, *J. Am. Chem. Soc.* **2006**, *128*, 2115–2120.

[39] H. Kroto, J. Heath, S. Obrien, R. Curl, R. Smalley, *Nature* **1985**, *318*, 162–163.

[40] T. Murakami, K. Tsuchida, *Mini-Rev. Med. Chem.* **2008**, *8*, 175–183.

[41] S. R. Plant, M. Jevric, J. J. L. Morton, A. Ardavan, A. N. Khlobystov, G. A. D. Briggs, K. Porfyrakis, *Chem. Sci.* **2013**, *4*, 2971–2975.

[42] R. Partha, L. R. Mitchell, J. L. Lyon, P. P. Joshi, J. L. Conyers, *ACS Nano* **2008**, *2*, 1950–1958.

[43] A. D. Yoffe, *Adv. Phys.* **2001**, *50*, 1–208.

[44] Y. Zhang, O. Ersoy, A. Karatutlu, W. Little, A. Sapelkin, *J. Synchrotron Radiat.* **2016**, *23*, 253–259.

[45] P. Alivisatos, *Nat. Biotechnol.* **2004**, *22*, 47–52.

[46] M. N. O'Brien, M. R. Jones, C. A. Mirkin, *Proc. Natl. Acad. Sci. U. S. A.* **2016**, *113*, 11717–11725.

[47] S. J. Frost, D. Mawad, J. Hook, A. Lauto, *Adv. Healthc. Mater.* **2016**, *5*, 401–414.

[48] S. Iijima, *Physica B* **2002**, *323*, 1–5.

[49] F. S. Boi, G. Mountjoy, R. M. Wilson, Z. Luklinska, L. J. Sawiak, M. Baxendale, *Carbon* **2013**, *64*, 351–358.

[50] M. V. Kharlamova, *Prog. Mater. Sci.* **2016**, *77*, 125–211.

[51] S. Scalese, V. Scuderi, D. DAngelo, M. M. G. Buscema, S. Libertino, R. A. Puglisi, M. Miritello, V. Privitera, *Mater. Sci. Semicond. Process.* **2016**, *42, Part 1*, 45–49.

[52] S. C. Benjamin, A. Ardavan, G. A. D. Briggs, D. A. Britz, D. Gunlycke, J. Jefferson, M. A. G. Jones, D. F. Leigh, B. W. Lovett, A. N. Khlobystov, S. A. Lyon, J. J. L. Morton, K. Porfyrakis, M. R. Sambrook, A. M. Tyryshkin, *J. Phys. Condens. Matter* **2006**, *18*, S867–S883.

[53] A. P. Shpak, S. P. Kolesnik, G. S. Mogilny, Y. N. Petrov, V. P. Sokhatsky, L. N. Trophimova, B. D. Shanina, V. G. Gavriljuk, *Acta Mater.* **2007**, *55*, 1769–1778.

[54] X. Huang, C. Tan, Z. Yin, H. Zhang, *Adv. Mater.* **2014**, *26*, 2185–2204.

[55] K. S. Novoselov, A. K. Geim, S. V. Morozov, D. Jiang, Y. Zhang, S. V. Dubonos, I. V. Grigorieva, A. A. Firsov, *Science* **2004**, *306*, 666–669.

[56] X.-L. Wang, S. X. Dou, C. Zhang, *NPG Asia Mater.* **2010**, *2*, 31–38.

[57] K. S. Novoselov, A. K. Geim, S. V. Morozov, D. Jiang, M. I. Katsnelson, I. V. Grigorieva, S. V. Dubonos, A. A. Firsov, *Nature* **2005**, *438*, 197–200.

[58] X. Huang, Z. Yin, S. Wu, X. Qi, Q. He, Q. Zhang, Q. Yan, F. Boey, H. Zhang, *Small* **2011**, *7*, 1876–1902.

[59] N. P. Funnell, Q. Wang, L. Connor, M. G. Tucker, D. O'Hare, A. L. Goodwin, *Nanoscale* **2014**, *6*, 8032–8036.

[60] C. Wu, X. Lu, L. Peng, K. Xu, X. Peng, J. Huang, G. Yu, Y. Xie, *Nat. Commun.* **2013**, *4*, 2431.

[61] H. Z. Zhang, B. Gilbert, F. Huang, J. F. Banfield, *Nature* **2003**, *424*, 1025–1029.

[62] A. E. Nel, L. Mdler, D. Velegol, T. Xia, E. M. V. Hoek, P. Somasundaran, F. Klaessig, V. Castranova, M. Thompson, *Nat. Mater.* **2009**, *8*, 543–557.

[63] J. Schweitzer, `https://www.purdue.edu/ehps/rem/rs/sem.htm`.

[64] `http://www.nobelprize.org/educational/physics/microscopes/tem/index.html`.

[65] A. I. Lopez-Lorente, B. Mizaikoff, *TrAC Trends Anal. Chem.* **2016**, *84*, 97–106.

[66] L. A. Feigin, D. I. Svergun, *Nature* **1928**, *121*, 501–502.

[67] `https://www2.warwick.ac.uk/fac/cross_fac/sciencecity/programmes/internal/themes/am2/booking/particlesize/intro_to_dls.pdf`.

[68] `http://teaching.shu.ac.uk/hwb/chemistry/tutorials/molspec/nmr1.htm`.

[69] `http://www.rsc.org/learn-chemistry/wiki/Introduction_to_NMR_spectroscopy`.

[70] A. T. M. Anishur Rahman, P. Majewski, K. Vasilev, *Contrast Media Mol. Imaging* **2013**, *8*, 92–95.

[71] L. E. Marbella, J. E. Millstone, *Chem. Mater.* **2015**, *27*, 2721–2739.

[72] Y. Liu, J. Luo, Y. Shin, S. Moldovan, O. Ersen, A. Hebraud, G. Schlatter, C. Pham-Huu, C. Meny, *Nat. Commun.* **2016**, *7*, DOI `10.1038/ncomms11532`.

[73] A. I. Frenkel, A. Yevick, C. Cooper, R. Vasic, *Annu. Rev. Anal. Chem.* **2011**, *4*, 23–39.

[74] D. E. Sayers, E. A. Stern, F. W. Lytle, *Phys. Rev. Lett.* **1971**, *27*, 1204–1207.

[75] W. Bragg, *Pro. Cambridge Philos. Soc.* **1913**, *17*, 43–57.

[76] M. T. Dove, M. G. Tucker, D. A. Keen, *Eur. J. Mineral.* **2002**, *14*, 331–348.

[77] L. A. Bendersky, F. W. a. Gayle, **2001**, *106*, 997–1012.

[78] L. A. Feigin, D. I. Svergun, Plenum Press, New York, **1987**, 335 pp.

[79] H. M. Rietveld, *Acta Crystallogr.* **1967**, *22*, 151–152.

[80] P. Juhs, D. M. Cherba, P. M. Duxbury, W. F. Punch, S. J. L. Billinge, *Nature* **2006**, *440*, 655–658.

[81] A. Karatutlu, M. Song, A. P. Wheeler, O. Ersoy, W. R. Little, Y. Zhang, P. Puech, F. S. Boi, Z. Luklinska, A. V. Sapelkin, **2015**, *5*, 20566–20573.

[82] V. Petkov, S. J. L. Billinge, P. Larson, S. D. Mahanti, T. Vogt, K. K. Rangan, M. G. Kanatzidis, *Phys. Rev. B* **2002**, *65*, 092105.

[83] S. J. L. Billinge, T. Egami, *Vol. 16*, Elsevier, Second, **2013**.

[84] S. J. L. Billinge, M. G. Kanatzidis, *Chem. Commun.* **2004**, 749–760.

[85] A. L. Patterson, *Phys. Rev.* **1939**, *56*, 978–982.

[86] P. Scherrer, **1918**, *1918*, 98–100.

[87] A. Cervellino, C. Giannini, A. Guagliardi, M. Ladisa, *Phys. Rev. B* **2005**, *72*, 035412.

[88] K. Page, T. Proffen, H. Terrones, M. Terrones, L. Lee, Y. Yang, S. Stemmer, R. Seshadri, A. K. Cheetham, *Chem. Phys. Lett.* **2004**, *393*, 385–388.

[89] T. Proffen, *JOM* **2012**, *64*, 112–116.

[90] M. T. Dove, *Mater. Today* **2003**, *6*, 59.

[91] T. Proffen, S. J. L. Billinge, T. Egami, D. Louca, *Z. Kristall.* **2003**, *218*, 132–143.

[92] T. Proffen, H. Kim, *J. Mater. Chem.* **2009**, *19*, 5078–5088.

[93] C. A. Young, A. L. Goodwin, *J. Mater. Chem.* **2011**, *21*, 6464–6476.

[94] R. Harrington, R. B. Neder, J. B. Parise, *Chem. Geol.* **2012**, *329*, 3–9.

[95] L. Pusztai, R. L. McGreevy, *Physica B Condens. Matter.* **1997**, *234*, 357–358.

[96] M. G. Tucker, D. A. Keen, M. T. Dove, A. L. Goodwin, Q. Hui, *J. Phys. Condens. Matter* **2007**, *19*, 335218.

[97] C. L. Farrow, P. Juhas, J. W. Liu, D. Bryndin, E. S. Bozin, J. Bloch, T. Proffen, S. J. L. Billinge, *J. Phys. Condens. Matter* **2007**, *19*, 335219.

[98] S. J. L. Billinge, T. Dykhne, P. Juhas, E. Bozin, R. Taylor, A. J. Florence, K. Shankland, *CrystEngComm* **2010**, *12*, 1366–1368.

[99] S. J. L. Billinge, I. Levin, *Science* **2007**, *316*, 561–565.

[100] M. W. Terban, M. Johnson, M. D. Michiel, S. J. L. Billinge, *Nanoscale* **2015**, *7*, 5480–5487.

[101] S. S. M. Bhat, D. Swain, M. Feygenson, J. C. Neuefeind, A. K. Mishra, J. L. Hodala, C. Narayana, G. V. Shanbhag, N. G. Sundaram, *Inorg. Chem.* **2017**, *56*, 5525–5536.

[102] D. A. Keen, A. L. Goodwin, *Nature* **2015**, *186*, 012010.

[103] G. H. Vineyard, *J. Chem. Phys.* **1954**, *22*, 1665–1667.

[104] P. Debye, *Ann. Phys.* **1915**, *351*, 809–823.

[105] L. Gelisio, P. Scardi, *Acta Crystallogr. Sect. A* **2016**, *72*, 608–620.

[106] G. Dalba, *Acta Crystallogr. Sect. A* **2016**, *72*, 591–607.

[107] P. Debye, *Phys. Z.* **1930**, *31*, 419–428.

[108] F. Zernike, J. A. Prins, *Phys. Z.* **1927**, *41*, 184–194.

[109] T. Egami, *IUCrJ* **2015**, *2*, 479–480.

[110] H. R. Marchbank, A. H. Clark, T. I. Hyde, H. Y. Playford, M. G. Tucker, D. Thompsett, J. M. Fisher, K. W. Chapman, K. A. Beyer, M. Monte, A. Longo, G. Sankar, *ChemPhysChem* **2016**, *17*, 3494–3503.

[111] U. P. Gawai, B. N. Dole, *RSC Adv.* **2017**, *7*, 37402–37411.

[112] E. D. Bojesen, B. B. Iversen, *Crystengcomm* **2016**, *18*, 8332–8353.

[113] R. Setton, P. Bernier, S. Lefrant, CRC Press, **2002**, 510 pp.

[114] W. I. F. David, R. M. Ibberson, J. C. Matthewman, K. Prassides, T. J. S. Dennis, J. P. Hare, H. W. Kroto, R. Taylor, D. R. M. Walton, *Nature* **1991**, *353*, 147–149.

[115] K. H. Michel, D. Lamoen, W. I. F. David, *Acta Crystallogr. Sect. A* **1995**, *51*, 365–374.

[116] R. Lyndenbell, K. Michel, *Rev. Mod. Phys.* **1994**, *66*, 721–762.

[117] V. M. Nield, D. A. Keen, Oxford University Press, **2000**, 334 pp.

[118] D. A. Keen, M. T. Dove, *J. Phys.: Condens. Matter* **1999**, *11*, 9263.

[119] D. S. Sivia, Oxford University Press, **2011**, 200 pp.

[120] M. T. Dove, *Eur. J. Mineral.* **2002**, *14*, 203–224.

[121] A. K. Soper, E. R. Barney, *J. Appl. Crystallogr.* **2011**, *44*, 714–726.

[122] `http://www.isis.stfc.ac.uk`.

[123] D. T. Bowron, A. K. Soper, K. Jones, S. Ansell, S. Birch, J. Norris, L. Perrott, D. Riedel, N. J. Rhodes, S. R. Wakefield, A. Botti, M.-A. Ricci, F. Grazzi, M. Zoppi, *Rev. Sci. Instrum.* **2010**, *81*, 033905.

[124] D. A. Keen, *J. Appl. Crystallogr.* **2001**, *34*, 172–177.

[125] A. K. Soper, Report RAL-TR-2011-013, **2011**.

[126] I. Todorov, W. Smith, `ftp://ftp.dl.ac.uk/ccp5/DL_POLY/DL_POLY_4.0/DOCUMENTS/USRMAN4.pdf`.

[127] R. L. McGreevy, L. Pusztai, *Mol. Simul.* **1988**, *1*, 359–367.

[128] D. A. Keen, R. L. McGreevy, *Nature* **1990**, *344*, 423–425.

[129] R. L. McGreevy, *J. Phys. Condens. Matter* **2001**, *13*, R877.

[130] M. G. Tucker, M. T. Dove, D. A. Keen, *J. Appl. Crystallogr.* **2001**, *34*, 630–638.

[131] A. L. Goodwin, F. M. Michel, B. L. Phillips, D. A. Keen, M. T. Dove, R. J. Reeder, *Chem. Mat.* **2010**, *22*, 3197–3205.

[132] M. G. Tucker, M. T. Dove, A. L. Goodwin, D. A. Keen, H. Playford, `http://www.rmcprofile.org/imagesFhj/b/ba/Rmcprofile_v6_manual.pdf`.

[133] C. L. Farrow, P. Juhas, J. W. Liu, D. Bryndin, E. S. Bozin, J. Bloch, T. Proffen, S. J. L. Billinge, `http://www.diffpy.org/doc/pdfgui/pdfgui.pdf`.

[134] T. Proffen, S. Billinge, `http://www.diffpy.org/doc/pdffit/pdf_man.pdf`.

[135] U. K. Gautam, P. M. F. J. Costa, Y. Bando, X. Fang, L. Li, M. Imura, D. Golberg, *Sci. Technol. Adv. Mater.* **2010**, *11*, 054501.

[136] F. S. Boi, G. Mountjoy, M. Baxendale, *Carbon* **2013**, *64*, 516–526.

[137] F. S. Boi, R. M. Wilson, G. Mountjoy, M. Ibrar, M. Baxendale, *Farad. Discuss.* **2014**, *173*, 67–77.

[138] R. Lv, S. Tsuge, X. Gui, K. Takai, F. Kang, T. Enoki, J. Wei, J. Gu, K. Wang, D. Wu, *Carbon* **2009**, *47*, 1141–1145.

[139] N. Grobert, W. K. Hsu, Y. Q. Zhu, J. P. Hare, H. W. Kroto, D. R. M. Walton, M. Terrones, H. Terrones, P. Redlich, M. Ruhle, R. Escudero, F. Morales, *Appl. Phys. Lett.* **1999**, *75:21*, 3363–3365.

[140] F. C. Dillon, A. Bajpai, A. Ko.s, S. Downes, Z. Aslam, N. Grobert, *Carbon* **2012**, *50*, 3674–3681.

[141] A. Leonhardt, M. Ritschel, D. Elefant, N. Mattern, K. Biedermann, S. Hampel, C. Mller, T. Gemming, B. Bchner, *J. Appl. Phys.* **2005**, *98*, 074315.

[142] H. Sato, A. Nagata, N. Kubonaka, Y. Fujiwara, *Jpn. J. Appl. Phys.* **2013**, *52*, 11NL03.

[143] P. Bruno in *Ferienkurse des Forschungszentrums Julich*, **1993**, pp. 24.1–24.27.

[144] S. V. Halilov, A. Y. Perlov, P. M. Oppeneer, A. N. Yaresko, V. N. Antonov, *Phys. Rev. B* **1998**, *57*, 9557–9560.

[145] C. Prados, P. Crespo, J. M. Gonzlez, A. Hernando, J. F. Marco, R. Gancedo, N. Grobert, M. Terrones, R. M. Walton, H. W. Kroto, *Phys. Rev. B* **2002**, *65*, 113405.

[146] M. U. Lutz, U. Weissker, F. Wolny, C. Mller, M. Lffler, T. Mhl, A. Leonhardt, B. Bchner, R. Klingeler, *J. Phys.: Conf. Ser.* **2010**, *200*, 072062.

[147] F. Wolny, U. Weissker, T. Mhl, A. Leonhardt, S. Menzel, A. Winkler, B. Bchner, *J. Appl. Phys.* **2008**, *104*, 064908.

[148] H. Mamiya, B. Jeyadevan, *Sci Rep* **2011**, *1*, DOI 10.1038/srep00157.

[149] R. Marega, F. De Leo, F. Pineux, J. Sgrignani, A. Magistrato, A. D. Naik, Y. Garcia, L. Flamant, C. Michiels, D. Bonifazi, *Adv. Funct. Mater.* **2013**, *23*, 3173–3184.

[150] J. Zhu, D. Liu, J. Wang, H. Yi, S. Wang, J. Wen, M. A. C..Willis, Y. Hou, J. Borowiec, F. S..Boi, *RSC Advances* **2017**, *7*, 20604–20609.

[151] F. Wolny, T. Mhl, U. Weissker, K. Lipert, J. Schumann, A. Leonhardt, B. Bchner, *Nanotechnology* **2010**, *21*, 435501.

[152] F. S. Boi, J. Guo, G. Xiang, M. Lan, S. Wang, J. Wen, S. Zhang, Y. He, *RSC Adv.* **2017**, *7*, 845–850.

[153] G. Xc, W. Jq, W. Kl, W. Wx, L. Rt, C. Jg, K. Fy, G. Jl, W. Dh, *Mater. Res. Bull.* **2008**, *43*, 3441–3446.

[154] F. S. Boi, J. Guo, S. Wang, Y. He, G. Xiang, X. Zhang, M. Baxendale, *Chem. Commun.* **2016**, *52*, 4195–4198.

[155] I. Leven, R. Guerra, A. Vanossi, E. Tosatti, O. Hod, *Nat. Nano.* **2016**, *11*, 1082–1086.

[156] X. D. Dai, Y. Kong, J. H. Li, B. X. Liu, *J. Phys.: Condens. Matter* **2006**, *18*, 4527.

[157] M. W. Finnis, J. E. Sinclair, *Philos. Mag. A* **1984**, *50*, 45–55.

[158] J. H. Rose, J. R. Smith, F. Guinea, J. Ferrante, *Phys. Rev. B* **1984**, *29*, 2963–2969.

[159] N. Ridley, H. Stuart, *Metal Science Journal* **1970**, *4*, 219–222.

[160] M. Meo, M. Rossi, *Compos. Sci. Technol.* **2006**, *66*, 1597–1605.

[161] Y. Shibuta, S. Maruyama, *Comput. Mater. Sci.* **2007**, *39*, 842–848.

[162] P. Li, K. M. Merz, *Chem. Rev.* **2017**, *117*, 1564–1686.

[163] H. Nakotte, M. Shrestha, S. Adak, M. Boergert, V. S. Zapf, N. Harrison, G. King, L. L. Daemen, *JSAMD* **2016**, *1*, 113–120.

[164] F. Herren, P. Fischer, A. Ludi, W. Haelg, *Inorg. Chem.* **1980**, *19*, 956–959.

[165] A. Kraft, G. GmbH, *Bull. Hist. Chem.*, *36*.

[166] D. Aguil, Y. Prado, E. S. Koumousi, C. Mathonire, R. Clrac, *Chem. Soc. Rev.* **2016**, *45*, 203–224.

[167] K. W. Chapman, K. A. Beyer, H. Zhao, P. J. Chupas, *CrystEngComm* **2013**, *15*, 9377–9381.

[168] K. W. Chapman, P. D. Southon, C. L. Weeks, C. J. Kepert, *Chem. Commun.* **2005**, 3322–3324.

[169] S. S. Kaye, J. R. Long, *Catal. Today* **2007**, *120*, 311–316.

[170] S. H. Ogilvie, S. G. Duyker, P. D. Southon, V. K. Peterson, C. J. Kepert, *Chem. Commun.* **2013**, *49*, 9404–9406.

[171] K. W. Chapman, P. J. Chupas, E. R. Maxey, J. W. Richardson, *Chem. Commun.* **2006**, 4013–4015.

[172] A. L. Goodwin, *Z. Kristall.* **2009**, 1–11.

[173] M. T. Dove, H. Fang, *Rep. Prog. Phys.* **2016**, *79*, 066503.

[174] K. W. Chapman, P. J. Chupas, C. J. Kepert, *J. Am. Chem. Soc.* **2006**, *128*, 7009–7014.

[175] K. W. Chapman, P. J. Chupas, C. J. Kepert, *J. Am. Chem. Soc.* **2005**, *127*, 11232–11233.

[176] E.-E. Bendeif, A. Gansmuller, K.-Y. Hsieh, S. Pillet, T. Woike, M. Zobel, R. B. Neder, M. Bouazaoui, H. E. Hamzaoui, D. Schaniel, *RSC Adv.* **2015**, *5*, 8895–8902.

[177] P. Bhatt, N. Thakur, M. D. Mukadam, S. S. Meena, S. M. Yusuf, *J. Phys. Chem. C* **2013**, *117*, 2676–2687.

[178] M. Hu, S. Furukawa, R. Ohtani, H. Sukegawa, Y. Nemoto, J. Reboul, S. Kitagawa, Y. Yamauchi, *Angew. Chem. Int. Ed.* **2012**, *51*, 984–988.

[179] H. Ming, N. L. K. Torad, Y.-D. Chiang, K. C.-W. Wu, Y. Yamauchi, *CrystEngComm* **2012**, *14*, 3387–3396.

[180] H. Ming, N. L. K. Torad, Y.-D. Chiang, K. C.-W. Wu, Y. Yamauchi, *CrystEngComm* **2012**, *14*, 3387.

[181] C. Y. Kao, T. C. Lo, W. C. Lee, *J. Appl. Polym. Sci.* **2003**, *87*, 1818–1824.

[182] K. M. Koczkur, S. Mourdikoudis, L. Polavarapu, S. E. Skrabalak, **2015**, *44*, 17883–17905.

[183] J. Yang, H. Wang, L. Lu, W. Shi, H. Zhang, *Cryst. Growth Des.* **2006**, *6*, 2438–2440.

[184] `http://lisa.chem.ut.ee/IR_spectra/paint/pigments/prussian-blue/`.

[185] D. M. Pajerowski, T. Watanabe, T. Yamamoto, Y. Einaga, *Phys. Rev. B* **2011**, *83*, 153202.

[186] S. Le Car, G. Vigneron, J. P. Renault, S. Pommeret, *Chem. Phys. Lett.* **2006**, *426*, 71–76.

[187] U. of Reading, `http://www.reading.ac.uk/ir-substrateopticaltheory-%5Cabsorptionandextinctioncoefficienttheory.aspx`.

[188] Z. H. Li, J. L. Zhang, T. C. Mu, J. M. Du, Z. M. Liu, B. X. Han, J. Chen, *Colloids Surf. A* **2004**, *243*, 63–66.

[189] R. P. DAmelia, S. Gentile, W. F. Nirode, L. Huang, *WJCE* **2016**, *4*, 25–31.

[190] R. Usman, A. Mihata, J. Kurawaki, *E-j. surf. sci. nanotechnol.* **2015**, *13*, 431–434.

[191] R. Seoudi, A. A. Fouda, D. A. Elmenshawy, *Physica B Condens. Matter.* **2010**, *405*, 906–911.

[192] C. R. Keedy, *J. Chem. Educ.* **1992**, *69*, A296.

[193] N. I. of Standard Technology, `http://webbook.nist.gov/cgi/cbook.cgi?ID=C74908%5C&Mask=80#IR-Spec`.

[194] A. K. Soper, *J. Phys.: Condens. Matter* **2007**, *19*, 335206.

[195] A. K. Soper, C. J. Benmore, *Phys. Rev. Lett.* **2008**, *101*, 065502.

[196] M. Schumacher, H. Weber, Y. Tsuchiya, T. G. A. Youngs, I. Kaban, R. Mazzarello, *Sci. Rep.* **2016**.

[197] IPCC, **2013**, `http://www.climatechange2013.org/images/report/WG1AR5_ALL_FINAL.pdf`.

[198] S. Pacala, R. Socolow, *Science* **2004**, *305*, 968–972.

[199] E. Beagle, E. Belmont, *Energy Pol.* **2016**, *97*, 429–438.

[200] D. W. Keith, *Science* **2009**, *325*, 1654–1655.

[201] F. C. Krebs, *Energy Environ Sci.* **2012**, *5*, 7238–7239.

[202] M. E. Boot-Handford, J. C. Abanades, E. J. Anthony, M. J. Blunt, S. Brandani, N. Mac Dowell, J. R. Fernandez, M.-C. Ferrari, R. Gross, J. P. Hallett, R. S. Haszeldine, P. Heptonstall, A. Lyngfelt, Z. Makuch, E. Mangano, R. T. J. Porter, M. Pourkashanian, G. T. Rochelle, N. Shah, J. G. Yao, P. S. Fennell, *Energy Environ. Sci.* **2014**, *7*, 130–189.

[203] G. T. Rochelle, *Science* **2009**, *325*, 1652–1654.

[204] U.S. Energy Information Administration, **2016**, `https://www.eia.gov/tools/faqs/faq.cfm?id=427%5C&t=3`.

[205] K. Z. House, C. F. Harvey, M. J. Aziz, D. P. Schrag, *Energy Environ. Sci.* **2009**, *2*, 193–205.

[206] A. B. Rao, E. S. Rubin, *Environ. Sci. Technol.* **2002**, *36*, 4467–4475.

[207] B. R. Stanmore, P. Gilot, *Fuel Process. Technol.* **2005**, *86*, 1707–1743.

[208] M. T. Dunstan, W. Liu, A. F. Pavan, J. A. Kimpton, C. D. Ling, S. A. Scott, J. S. Dennis, C. P. Grey, *Chem. Mater.* **2013**, *25*, 4881–4891.

[209] B. Jones, *Sediment. Geol.* **2017**, 64–75.

[210] S. Weiner, J. Mahamid, Y. Politi, Y. Ma, L. Addadi, *Front. Mater. Sci. China* **2009**, *3*, 104.

[211] X. Wang, L. Li, Y. Zhu, X. Song, X. Fang, R. Huang, H. Que, G. Zhang, *Mol. Biol. Rep.* **2014**, *41*, 7067–7071.

[212] T. D. Archer, S. E. A. Birse, M. T. Dove, S. A. T. Redfern, J. D. Gale, R. T. Cygan, *Phys. Chem. Min.* **2003**, *30*, 416–424.

[213] B. Hammouda, `https://www.ncnr.nist.gov/staff/hammouda/the_SANS_toolbox.pdf`.

[214] M. Hasegawa, K. Nishidate, *Phys. Rev. B* **2004**, *70*, 205431.

[215] C. L. Farrow, S. J. L. Billinge, *Acta Crystallogr. Sect. A* **2009**, *65*, 232–239.

[216] E. W. Weisstein, `http://mathworld.wolfram.com/EulerAngles.html`.

[217] J. L. F. Abascal, C. Vega, *J. Chem. Phys.* **2005**, *123*, 234505.